

# Welding Simulation and Fatigue Assessment of Tubular K-Joints in High-Strength Steel

THÈSE N° 6158 (2014)

PRÉSENTÉE LE 28 AVRIL 2014

À LA FACULTÉ DE L'ENVIRONNEMENT NATUREL, ARCHITECTURAL ET CONSTRUIT  
LABORATOIRE DE LA CONSTRUCTION MÉTALLIQUE  
PROGRAMME DOCTORAL EN GÉNIE CIVIL ET ENVIRONNEMENT

ÉCOLE POLYTECHNIQUE FÉDÉRALE DE LAUSANNE

POUR L'OBTENTION DU GRADE DE DOCTEUR ÈS SCIENCES

PAR

Farshid ZAMIRI AKHLAGHI

acceptée sur proposition du jury:

Prof. T. Keller, président du jury  
Prof. A. Nussbaumer, Dr J.-M. Drezet, directeurs de thèse  
Dr D. Carron, rapporteur  
Prof. M. Fontana, rapporteur  
Dr Th. Nitschke-Pagel, rapporteur



ÉCOLE POLYTECHNIQUE  
FÉDÉRALE DE LAUSANNE

Suisse  
2014



Le véritable voyage de découverte  
ne consiste pas à chercher de nouveaux paysages,  
mais à avoir de nouveaux yeux.  
— Marcel Proust

To Toktam and Parastoo ✨





# Acknowledgements

My gratitude firstly goes to Prof. Alain Nussbaumer (Steel Structures Laboratory, ICOM), director of my thesis, and MER Dr. Jean-Marie Drezet (Computational Materials Laboratory, LSMX), co-director. In particular, I express my deepest appreciation to Prof. Nussbaumer for his illuminating guidelines, patience, and numerous constructive discussions on a broad range of topics, and to MER Dr. Drezet for his support, and for insightful comments on my research. I would like to thank Prof. Jean-Paul Lebet, director of ICOM, for giving me the opportunity to do my research at ICOM, and for providing a work environment highly conducive to research and learning.

This research was part of the project P816 “Optimal use of hollow sections and cast nodes in bridge structures made of S355 and S690 steel”, supported financially and with academic advice by the Forschungsvereinigung Stahlanwendung e. V. (FOSTA), Düsseldorf. I would like to thank FOSTA for funding this thesis as well as Vallurec & Mannesman Tubes (Germany), Friedrich Wilhelms-Hütte (Germany), and Zwahlen & Mayr (Switzerland) for contributing the material and fabrication facilities.

I offer my sincere thanks to the examining committee for their comments and feedback on the final draft of this document: Prof. Mario Fontana, ETH Zurich, Dr.-Ing. Thomas Nitschke-Pagel, TU Braunschweig, Germany, Dr. Denis Carron, Université de Bretagne-Sud, France, and Prof. Thomas Keller (chairman), CCLAB, EPFL. I would like to thank Esther von Arx for her valuable assistance with administrative tasks.

During the course of this thesis I have received guidance and feedback from a number of experts in various research areas. I express my deepest appreciation to all of them. In this limited space, I would like to especially thank Dr. Laurent D’Alvise from GeonX, Belgium, Dr. Jean-Pierre Lefebvre and Dr. Josué Barboza from CENAERO, Belgium, for their advice on numerical simulation issues. Dr. Thilo Pirling, Institut Laue-Langevin, France, helped me for neutron diffraction measurements. I received valuable scientific help from Prof. Stefan Herion, Karlsruhe Institute of Technology, Germany, Prof. Jacqueline Lecomte-Beckers and Dr. Anne Mertens from University of Liege, Belgium, Dr. Hany Ahmed, ArcelorMittal, Luxembourg, Jörg Baumgartner, Fraunhofer LBF, Germany, Professor Norbert Enzinger, TU Graz, Austria. I deeply appreciate their contribution.

A major part of my research included experimental work in the structures laboratory. I am especially thankful to Gérald Rouge and Sylvain Demierre for their great help in the lab, and also for good humor. Also, I would like to thank Gilles Guignet, Frédérique Dubugnon, Patrice Gallay, Armin Krkic, and Roland Gysler. Willy Dufour (LMM), Cyril Dénéreaz (LMM), and Dr.

## Acknowledgements

---

Emmanuelle Boehm-Courjault (LSMX) greatly helped me with the material tests for which I am very thankful to them.

During the past four years, I have shared the office with Claire Acevedo and Claudio Baptista. We have had plenty of talks and critical discussions which I will always remind and appreciate. I have spent a memorable time at ICOM thanks to my friends Albano, Christian, Dimitrios, Gary, Gustavo, Jagoda, Luca, Manuel, Maria, Nariman, Raphaël, Santosh, Shyam, Valentin and also friends from other laboratories: Marina and Julien, Hadi, Moslem, Ehsan, Mark, Maléna, Sarah, Raluca, Alessandro, Francisco and the rest of my peers in doctoral school. My great thanks to all of them for the time we spent together at work and outside the work.

I would also like to thank the Master's students who helped me in this research: Janna Krummenacker, Katharina Rohr, and François-Joseph Contat.

Looking further back in time, I would like to send my appreciation to my Master's thesis supervisor, Prof. Mahammad Al-Emrani, Chalmers University of Technology, Sweden, for opening the door to the exciting research topic of "fatigue of weldments", and to Dr. Mladen Lukić, chairman of ECCS-TC6 committee, for introducing me to the outstanding ICOM research laboratory.

I offer my most sincere thanks to my family, specially my parents whose everlasting support and encouragement provided me valuable motivation. This work couldn't have been done without patience and unconditional support and love from my wife, Toktam, whom I am deeply grateful to. I also thank my daughter, Parastoo, for cheering me up with her charms and telling "daddy come home" at the end of some long work days.

*Lausanne, 10 April 2014*

F. Z.

# Abstract

Application of newly developed high strength steel hollow sections is increasing in construction industry – especially for bridge structures – due to their satisfactory material properties and fabrication advantages. These sections allow for longer spans, more slender structures. Savings in weight and volume of material compared to traditional steel grades increase sustainability of construction and compensate for part of higher unit cost of material. Nevertheless, use of high strength steels cannot be promoted unless potential fatigue issues are properly addressed.

Two fabrication methods are currently available for the planar Warren trusses made of circular hollow sections (CHS): welding the tubes together, or using cast steel nodes and connecting truss members to them by girth welds. Previous research on tubular bridge trusses indicates that the problematic fatigue cracking sites for the first fabrication method are located at weld toes in the gap region of the truss joints. For the second method, cracking occurs at the root of CHS–cast butt welds.

Fatigue performance of these two methods were investigated by constant amplitude fatigue testing of two full scale trusses made of steel grade S690QH and with a geometry similar to previous S355J2H investigation. Fatigue lives of K-joints were in agreement with current recommended code values. For CHS–cast welded connections, no visible cracking was observed up to  $2 \times 10^6$  cycles. Due to the effect of residual stresses, fatigue cracking was observed in compressive joints as well as tensile joints. Indeed, tensile welding residual stresses keep the crack open during all or part of the compressive load cycle. Their distribution and impact on fatigue life of tubular joints has not been fully investigated before for a complex detail such as Tubular K-joint made of high strength steel.

Experimental and numerical methods were utilized for assessment of welding residual stresses. Neutron diffraction experiments were conducted to evaluate the residual stress field in the gap region of K-joint, which was critical location for fatigue cracking. Transversal residual stresses of up to  $0.60 f_y$  nominal were registered at some depth from the surface of the chord. The  $\sigma_{res}/f_y$  ratio for the high strength steel S690QH was lower than similar measurements previously done by Acevedo (2011) on steel grade S355J2H. This is believed to be mainly due to welding with low heat input and solid-state phase transformations in high strength steel material. Microstructural changes in the heat affected zone (HAZ) for low alloy carbon steels favorably act in reducing tensile residual stresses by adding compressive residual stresses during part of cooling. These effects were modelled numerically using a coupled thermal-mechanical-metallurgical analysis of welding process. Welding sequence was registered and

## Acknowledgements

---

temperature data acquired during fabrication stage of the test trusses; they were employed for creation of calculation model.

There has been considerable progress in the methods and tools for computational weld modelling since early 90's, from 2D to 3D possibilities. Since welded details involved in structural engineering design have generally complex shapes, one major objective of this study was to apply the state of the art in weld modelling into a purposely-selected complex detail with several weld passes. This led to recommendations regarding modelling procedures and simplifying assumptions, as well as FEM practical issues that arise for the case of such intricate geometries. Investigated parameters include weld pass reduction by lumping, welding start/stop positions, and microstructural transformation assumptions.

Finally, an extended finite element model (XFEM) was used for fatigue crack propagation analysis in 3D in a K-joint under combined effect of external compressive loading and tensile residual stresses at crack site. Limitations of the utilized finite element code were identified and solutions suggested for improvement of 3D crack growth calculation in the presence of residual stress field.

**Keywords:** *tubular truss bridges, high-strength steel, HSLA, welding simulation, residual stress, phase transformation, neutron diffraction, fatigue, large-scale tests, crack propagation.*

## Résumé

L'utilisation de nouveaux profils en acier à haute résistance est en augmentation dans l'industrie de la construction — spécialement pour les ponts — en raison de propriétés des matériaux satisfaisantes et de leurs avantages lors de la fabrication. Les réductions de poids et de volume du matériau par rapport aux nuances d'acier traditionnelles augmentent la durabilité de la construction et compensent en partie le coût unitaire plus élevé du matériau. Néanmoins, l'usage d'aciers à haute résistance ne peut pas être promu tant que les problèmes potentiels de fatigue ne sont pas dûment pris en compte. Dans le cas des treillis plan de type Warren en profils creux circulaires (CHS), des recherches antérieures indiquent que les problèmes de fissuration en fatigue se situent en pied des cordons situés dans l'espace entre les diagonales dans les nœuds des treillis. Deux méthodes de fabrication pour les nœuds sont disponibles : le soudage des tubes, ou l'emploi de nœuds moulés en acier soudés aux éléments du treillis par des joints bout-à-bout.

Les performances en matière de fatigue de ces deux méthodes de fabrication ont été étudiées par des essais sur deux treillis en vraie grandeur en acier S690QH. La résistance à la fatigue des joints en K était en accord avec les valeurs actuelles recommandées des normes. Pour les assemblages bout-à-bout CHS–nœuds moulés, aucune fissure visible n'a été observée jusqu'à  $2 \times 10^6$  cycles. En raison de l'effet des contraintes résiduelles, la fissuration par fatigue a été observée dans les joints en compression et en traction.

Les contraintes résiduelles en traction résultant du soudage maintiennent la fissure ouverte pour toute ou pour une partie du cycle de charge en compression. Leur distribution et leur impact sur la résistance à la fatigue des joints tubulaires n'ont pas été étudiés de façon approfondie par le passé pour un détail complexe tel qu'un joint tubulaire en K en acier à haute résistance.

Des méthodes expérimentales et numériques ont été utilisées pour l'évaluation des contraintes résiduelles causées par le soudage. Des mesures par diffraction de neutrons ont été réalisées afin d'évaluer le champ de contraintes résiduelles dans la zone des joints en K, qui est l'emplacement critique pour la fissuration par fatigue. Des contraintes résiduelles transversales allant jusqu'à  $0.60 f_y$  nominal ont été enregistrées à une certaine profondeur dans le paroi de la membrure. Le rapport  $\sigma_{res}/f_y$  pour l'acier à haute résistance étudié était plus petit que lors de mesures similaires effectuées par Acevedo (2011) sur l'acier S355J2H. Cela est principalement dû en soudage avec faible apport de chaleur et aux transformations de phase à l'état solide de l'acier à haute résistance. Les changements de microstructure dans la zone affectée par la chaleur (ZAT) des aciers au carbone faiblement alliés agissent favorablement

dans la réduction des contraintes résiduelles en traction par l'ajout de contraintes résiduelles en compression. Les effets ont été modélisés numériquement pour une analyse couplée thermique-mécanique-métallurgique du procédé de soudage. Les données de la séquence de soudage et de la température acquises lors de la fabrication des treillis d'essai ont été employées pour la validation du modèle de calcul.

Des progrès considérables ont été faits dans les méthodes de calcul et outils de modélisation des soudures depuis le début des années 90. Étant donné que les détails soudés utilisés dans la pratique ont généralement des formes complexes, un objectif majeur de cette étude était d'appliquer l'état de l'art de la modélisation des soudures à un détail complexe comportant plusieurs passes de soudage. Ceci a conduit à déterminer des méthodes de modélisation et des hypothèses simplificatrices, ainsi qu'à résoudre des questions pratiques d'utilisation de la MEF qui se posent dans le cas de ces géométries complexes. Les paramètres étudiés comprenaient des réductions de passes par l'utilisation de passes équivalentes, les positions de début/fin de soudure, et des hypothèses de transformation de la microstructure.

Enfin, un modèle d'éléments finis étendus (XFEM) a été utilisé pour l'analyse de la propagation des fissures de fatigue des joints en K sous l'effet combiné de la charge de compression externe et des contraintes résiduelles de traction au niveau de la fissure. Les limites du code d'éléments finis utilisé ont été détectées et des solutions ont été proposées pour l'amélioration de la prévision de croissance de fissure en présence d'un champ de contraintes résiduelles.

**Mots-clés :** *ponts tubulaires, acier à haute résistance, aciers haute résistance faiblement alliés (HRFA), simulation de soudage, contraintes résiduelles, transformation de phase, diffraction de neutrons, fatigue, essais à vraie grandeur, propagation de fissures.*

# Contents

<b>Acknowledgements</b>	<b>v</b>
<b>Abstract (English/Français)/Persian</b>	<b>vii</b>
<b>List of figures</b>	<b>xv</b>
<b>List of tables</b>	<b>xxi</b>
<b>1 Introduction</b>	<b>1</b>
1.1 Background . . . . .	1
1.2 Problem statement . . . . .	2
1.3 Objectives . . . . .	3
1.4 Scope . . . . .	3
1.5 Structure of the dissertation . . . . .	4
<b>2 Background on welding residual stresses and simulation</b>	<b>5</b>
2.1 Introduction . . . . .	5
2.2 Description of phenomena . . . . .	6
2.2.1 Residual stresses . . . . .	6
2.2.2 Formation of welding residual stresses . . . . .	7
2.3 Computational welding simulation . . . . .	9
2.3.1 Subdomains . . . . .	9
2.3.2 Previous work . . . . .	9
2.3.3 Governing equations . . . . .	11
2.4 Evolution of microstructure . . . . .	12
2.4.1 Welding effects . . . . .	12
2.4.2 Multipass welds . . . . .	19
2.5 Summary . . . . .	21
<b>3 Fatigue assessment of tubular joints</b>	<b>23</b>
3.1 introduction . . . . .	23
3.2 High strength steel material . . . . .	23
3.3 Overview of fatigue assessment methods . . . . .	25
3.3.1 Structural hot-spot stress method . . . . .	26
3.3.2 Linear elastic fracture mechanics (LEFM) . . . . .	26

## Contents

---

3.4	Prediction of crack path . . . . .	27
3.4.1	Maximum Tangential stress criterion (MTS) (Erdogan and Sih, 1963) . . . . .	28
3.4.2	Maximum energy release rate (Nuismer, 1975) . . . . .	28
3.4.3	Minimum strain energy density (Sih, 1974) . . . . .	29
3.4.4	Zero $K_{II}$ criterion . . . . .	29
3.5	Conclusion . . . . .	29
<b>4</b>	<b>Residual stress measurements</b>	<b>31</b>
4.1	Introduction . . . . .	31
4.1.1	Residual stress measurement methods . . . . .	31
4.2	Theory . . . . .	33
4.2.1	Principles of residual stress measurement using neutron diffraction . . . . .	33
4.2.2	Calculation of stress components . . . . .	35
4.3	Method . . . . .	36
4.3.1	Specimens . . . . .	36
4.3.2	Apparatus . . . . .	40
4.4	Results . . . . .	41
4.4.1	Reference lattice spacing . . . . .	41
4.4.2	Estimation of full strain tensor (S7-355 specimen) . . . . .	43
4.4.3	Strain scanning measurements (S10-690 and S11-690 samples) . . . . .	45
4.5	Conclusion . . . . .	57
<b>5</b>	<b>Fatigue experiments</b>	<b>59</b>
5.1	Introduction . . . . .	59
5.2	Theory . . . . .	61
5.2.1	Alternative current potential drop (ACPD) . . . . .	61
5.3	Experimental method . . . . .	63
5.3.1	Fabrication of test trusses . . . . .	63
5.3.2	Temperature measurements . . . . .	72
5.3.3	Test setup . . . . .	77
5.3.4	Test procedure . . . . .	82
5.3.5	Measurement methods . . . . .	82
5.3.6	Repairs . . . . .	85
5.4	Results . . . . .	88
5.4.1	Static tests . . . . .	88
5.4.2	Crack propagation results . . . . .	95
5.4.3	Post-mortem examinations . . . . .	98
5.5	Discussion . . . . .	102
5.5.1	$S_{r,hs}-N$ Curves . . . . .	102
5.6	Conclusion . . . . .	104



<b>6 Modelling of welding</b>	<b>105</b>
6.1 Introduction . . . . .	105
6.2 Modelling simplifications and assumptions . . . . .	106
6.2.1 Weld pool modelling . . . . .	106
6.2.2 Modelling of weld metal deposition . . . . .	106
6.2.3 Weld pass reduction . . . . .	107
6.2.4 Symmetry in model . . . . .	108
6.2.5 Utilized units system . . . . .	109
6.3 Geometry of the model . . . . .	109
6.3.1 Weld torch trajectory . . . . .	110
6.4 Finite element meshes . . . . .	110
6.4.1 Convergence study . . . . .	111
6.5 Finite element analysis . . . . .	114
6.6 Thermophysical and mechanical material properties . . . . .	114
6.6.1 Two approaches in modelling material behaviour . . . . .	115
6.6.2 Thermal properties . . . . .	117
6.6.3 Mechanical properties . . . . .	120
6.6.4 Phase transformation kinetics . . . . .	128
6.6.5 Transformation plasticity (TRIP) . . . . .	132
6.7 Boundary conditions . . . . .	132
6.7.1 Initial and boundary conditions for thermal analysis . . . . .	132
6.7.2 Mechanical boundary conditions . . . . .	135
6.8 Results . . . . .	135
6.8.1 Model validation . . . . .	137
6.8.2 Comparison of residual stresses in K-joint and Y-joint . . . . .	140
6.8.3 Effect of start/stop points and torch speed . . . . .	145
6.8.4 Phase transformation effects . . . . .	145
6.9 Conclusion . . . . .	150
<b>7 Fatigue crack growth simulation</b>	<b>153</b>
7.1 Introduction . . . . .	153
7.2 The XFEM model . . . . .	154
7.3 Results . . . . .	155
7.3.1 Contact of crack faces . . . . .	156
7.4 Conclusion . . . . .	160
<b>8 Conclusion</b>	<b>161</b>
8.1 Determination of residual stress field in high-strength tubular K-joint . . . . .	161
8.2 Fatigue life assessment of welded high-strength tubular K-joints . . . . .	163
8.3 Future work . . . . .	163
<b>A Fabricator's welding procedure specifications for trusses</b>	<b>165</b>

## Contents

---

<b>B</b>	<b>Dimensions and instrumentation of test trusses</b>	<b>169</b>
<b>C</b>	<b>Summary of S-N data</b>	<b>175</b>
<b>D</b>	<b>Transformation kinetics calculations and input metallurgy data files</b>	<b>177</b>
<b>E</b>	<b>Results of principal residual stress measurements using neutron diffraction (S355J2H sample)</b>	<b>189</b>
	<b>Bibliography</b>	<b>193</b>
	<b>Curriculum Vitae</b>	<b>205</b>

# List of Figures

1.1	Traunstein (tree buttress) bridge with the detail of a cast node. Design R. J. Dietrich (Nussbaumer et al., 2010).	1
1.2	Two recent tubular bridges.	2
2.1	Three distinct types of residual stresses ( $\sigma^I$ , $\sigma^{II}$ , and $\sigma^{III}$ ) categorized based on their range of action; after Macherauch et al. (1973) according to Radaj (2003).	7
2.2	MIG/MAG welding (WMB, 2009) : 1.Shielding gas, 2.Electric arc, 3.Weld pool, 4.Solidified weld metal, 5.Welding torch, 6.Gas nozzle, 7.Wire feed, 8.Welding wire(solid or flux-cored), 9.Protective atmosphere, 10.Base material.	8
2.3	Subdomains of welding simulation including objectives of each subdomain and the coupling factors, (Karlsson, 1986; Radaj, 2003)	10
2.4	Interaction of temperature, mechanical and microstructural fields for the welding simulation, adapted from Radaj (2003)	13
2.5	Uncoupled sequential analysis procedure for thermo-mechanical analysis	14
2.6	Metallurgical zones in a single-pass weld categorized by maximum temperature at each region (Francis and Withers, 2011).	15
2.7	Iron–Carbon Phase diagram (Brandt and Warner (2009), Originally from Struers Inc.). Pearlite: two-phase, lamellar structure composed of $\alpha$ -iron (88 wt%) and cementite (12 wt%).	17
2.8	CCT diagrams for S690QL from literature.	18
2.9	Impact of different modelling assumptions on longitudinal stresses of a multipass plate weld (after Francis and Withers (2011)); Shaded area is the temperature range where transformations take place. $B_s$ and $B_f$ are bainite start and finish temperatures, respectively.	19
2.10	Schematic microstructure in a single pass weld (a) versus multipass weld (b) (Easterling, 1992).	19
3.1	Naming convention for locations and hot spots on K-joint.	23
3.2	Historical development of construction steel products and production processes (Samuelsson and Schröter, 2005)	24
3.3	Effect of grain refinement on toughness (DBTT: ductile to brittle transition temperature) (Ponge, 2005)	24

## List of Figures

---

3.4	evaluation of hot spot stress by extrapolation of surface stress (Zamiri Akhlaghi, 2009). . . . .	26
3.5	CIDECT (Wardenier et al., 2008) fatigue strength curves for CHS joints according to the hot-spot stress method. . . . .	27
3.6	Definition of the coordinate system and stress components in the vicinity of the crack (Richard et al., 2005). . . . .	28
4.1	Ranges of current capabilities of available techniques of residual stress measurement. The grey shaded areas indicate destructive methods (Withers et al., 2008). . . . .	32
4.2	Difference in the phase of the various rays of a coherent beam inciding a crystalline structure (Bragg's rule) (Hutchings et al., 2005) . . . . .	34
4.3	The fatigue tested truss and the extracted specimen. . . . .	37
4.4	Geometry of specimen used for the ND measurement (S7-355). The weld lines are only shown in the 3D rendering. . . . .	38
4.5	Measurement locations on the chord's weld toe (Specimen S7-355). . . . .	38
4.6	Illustration of neutron beam passing through the window cut on the specimen. . . . .	39
4.7	Geometry of specimens used for the ND measurement (S10-690 and S11-690). The weld lines are only shown in the 3D rendering. . . . .	39
4.8	Experiment setup for continuous neutron beam instrument (Webster, 2001) . . . . .	40
4.9	Hexapod platform with the specimen mounted on it. . . . .	41
4.10	Cube and Comb stress-free samples to measure $d_0$ . . . . .	42
4.11	Through-thickness profiles of the principal residual stresses at point M0; horizontal dashed lines indicate nominal yield stress value of S355. . . . .	44
4.12	Through-thickness profiles of the principal residual stresses at point M1; horizontal dashed lines indicate nominal yield stress value of S355. Measurements in 2.5mm depth were removed from dataset due to high measurement error at that location. . . . .	44
4.13	Through-thickness profiles of the principal residual stresses at point M2; horizontal dashed lines indicate nominal yield stress value of S355. . . . .	45
4.14	Measured residual stress ellipsoids on specimen S7-355 superposed on a wire-frame model of the joint. . . . .	46
4.15	Locations of measurements for the specimen S10-690 (Weld backing ring not shown in the drawing). . . . .	47
4.16	Nonlinear background function used for the peak-fitting. . . . .	47
4.17	Effect of selected background function on the result of peak-fitting. . . . .	48
4.18	Evaluated residual stress field components for specimen S10. . . . .	50
4.18	(Continued) Evaluated residual stress field components for specimen S10. . . . .	51
4.19	Evaluated residual stress field components for specimen S11. . . . .	52
4.19	(Continued) Evaluated residual stress field components for specimen S11. . . . .	53

4.20 Residual stress profiles for selected points on S10. Note that for the weld root measurements, the high background noise prevented getting reliable measurements. . . . .	54
4.21 High signal-to-noise ratio resulting in a poor peak fit for the left weld root. . . .	54
4.22 Residual stress profiles obtained from several neutron diffraction measurements. Shaded area shows the range of stresses proposed by the code (BS 7910, 2005). . . .	55
4.22 (Continued) Residual stress profiles obtained from several neutron diffraction measurements. . . . .	56
5.1 Principle of crack depth measurement using ACPD (Saguy and Rittel, 2005). . . .	62
5.2 Nominal dimensions of test trusses S10 and S11. . . . .	64
5.3 Dimensions of cast nodes used in fabrication of trusses S10 and S11; End preparation (bevels) is not shown (see figure 5.7). . . . .	65
5.4 Various parameters defining the gap and the weld geometry in K-Joints. . . . .	67
5.5 Stages for assembling and welding of the CHS profiles and cast nodes to fabricate truss chords. . . . .	70
5.6 Various cast joint details and their suggested detail categories, tested by Nussbaumer et al. (2010). $\Delta\sigma_{Cb}$ :detail category for bending, $\Delta\sigma_{Ct}$ :detail category for axial loading(strip specimens cut out of tubes), $\Delta\sigma_{CIL}$ :detail category for axial loading(tube specimens), $m$ : slope of S-N curve. . . . .	71
5.7 Weld gap details for cast node connections in trusses S10 and S11, conforming to details $b$ and $c$ in Figure 5.6. Tack welds ( $a=3$ mm) not shown. . . . .	72
5.8 Fabrication of trusses S10 and S11. . . . .	73
5.9 Geometry of weld gap for brace-to-chord connections in S10 and S11. The detail shows welding passes according to the welding procedure specifications. . . . .	74
5.10 Weld passes at crown toe identified from etched sample taken from trusses after testing. . . . .	74
5.11 Sequence of welding passes. Welding start and stop locations were off the crown toe and crown heel regions. . . . .	75
5.12 Installation of thermocouples on specimens and protecting them against preheating flame. . . . .	77
5.13 Position of thermocouples installed on the chord of the K-Joint to register welding temperatures. The weld toe lines on the chord are shown on the unrolled top view of K-joint. . . . .	78
5.14 Registered welding temperature histories for CHS – cast joint. Distance of each thermocouple from the edge of the weld gap is mentioned on the corresponding legend entry in each graph. First and second locations have a 90° angular distance. . . . .	79
5.15 Registered welding temperature histories for K-joint. Thermocouple numbering for the K-joint is given in Figure 5.13 . . . . .	80
5.16 Test setup. . . . .	81
5.17 ACPD probes locations on joints S10-J5N and S11-J2. . . . .	84
5.18 Setup on the truss joint for ACPD measurements. . . . .	84

## List of Figures

---

5.19	Repair of truss by prestressing the cracked joint. . . . .	86
5.20	Designed piece for mechanical anchorage of tendons. . . . .	86
5.21	Strain gage data for control of the symmetry in truss S10. Locations of strain gages are indicated in Figure B.2. . . . .	89
5.22	Nominal stress diagrams for K-joint in truss S10 (Units in MPa). . . . .	93
5.23	Nominal stress diagrams for cast nodes in truss S10 (Units in MPa). . . . .	93
5.24	S11-J2+ ACPD data, low-pass filtered with a moving average function. . . . .	96
5.25	Crack depth corrected to the final crack dimensions ( $d^*$ ), measured by opening the crack after the test. . . . .	97
5.26	Crack growth rates for joints S11-J2+ and S10-J5N-. . . . .	98
5.27	Evolution of Stress Intensity Factors with crack depth. . . . .	99
5.28	Cracking of joint S10-J3N (tensioned brace side). . . . .	99
5.29	Partially cracked(a) and fully cracked (b) joints. See Figure 5.30 for a close-up of partially cracked (marked) region of joint S11-J5S. . . . .	99
5.30	Close-up of cracking in S11-J5S. . . . .	100
5.31	One extracted metallography specimen and the parent part (S10-J2). . . . .	100
5.32	Hardness measurements at crown weld toe location. . . . .	100
5.33	Optical micrographs of the extracted specimen at crown toe etched with 2% Nital. . . . .	101
5.34	S-N curves for K-joints of trusses S10 and S11 compared to trusses previously tested at ICOM. . . . .	102
5.35	S-N curves for cast nodes of trusses S10 and S11. . . . .	103
6.1	Weld pass reduction for 8-pass K-joint weld; Cross section of lumped weld pass 1 is 20% of total weld cross section and cross sections of weld passes 2 and 3 are 40% of total weld cross section each. . . . .	108
6.2	Weld section partitioning at various locations along the weld line. . . . .	110
6.3	Weld torch trajectory for the third weld pass. The triads depict the pass of the weld torch along the weld line. The normal-to-surface vector (colored light green) shows the torch direction. . . . .	111
6.4	Details of FE mesh (fine mesh model). . . . .	112
6.5	Coarse mesh and fine mesh details; Longitudinal cut at the gap region. . . . .	112
6.6	Convergence study results; Stress profiles and temperature history at the weld toe after one lumped welding pass (phase transformation effects not included). . . . .	113
6.7	Effect of time step size on the stability of residual stress results (Rohr, 2013). . . . .	114
6.8	Thermal-metallurgical-mechanical simulation coupling in Morfeo 2012. . . . .	116
6.9	Temperature-dependent specific heat capacity values from Radaj (2003) (originally from Richter (1973)), EN1993 (2005), Mertens and Lecomte-Beckers (2012), Acevedo et al. (2013), Brown and Song (1992), and Wichers (2006). The first peak at around 750 °C corresponds to solid-state $\alpha \rightarrow \gamma$ phase transformation. The second peak at 1500 °C denotes the <i>equivalent</i> specific heat capacity associated with melting/solidification. . . . .	119

6.10 Young's modulus and yield stress of S690QH specimens measured at various temperatures (Krummenacker, 2011), compared with EN 1993:2005 curves and experimental data from Outinen (2007). . . . .	121
6.11 Young's modulus and yield stress of S690QH specimens measured at various temperatures (Rohr, 2013), compared with Eurocode 2005 curves. . . . .	121
6.12 Change of stress-strain curve with temperature; Eurocode 3 (2005) part 1-2 models.	122
6.13 Yield limit of various phases in studied steel material (Rohr, 2013); Data from Börjesson and Lindgren (2001), Krauß (2005), and ESI Group (2009). . . . .	123
6.14 Simulated material model (Ludwik) versus Eurocode curve (room temperature).	124
6.15 Thermal expansion coefficient used in this study (Mertens and Lecomte-Beckers, 2012) and by Acevedo (2011). . . . .	125
6.16 Linear dilatations of various phases; Expansion curve for Ferrite, bainite, and austenite are derived from the experiments reported by Mertens and Lecomte-Beckers (2012). Heating/cooling rate in experiments were $3\text{ }^{\circ}\text{C min}^{-1}$ . Dilatation curve for martensite is based on calculations of lattice parameters. Indices in equations stand for various microstructures: A:austenite, F:ferrite, P:pearlite, B:bainite, M:martensite. . . . .	127
6.17 Free dilatometry curves showing volume change due to phase transformation.	127
6.18 Computed austenite transformation into Ferrite+Pearlite, Bainite, and Martensite at various cooling rates. . . . .	130
6.19 CCT curve for S690QL from Nolde and Meyer (1998); Seyffarth et al. (1992). Peak austenitization temperature: $1395\text{ }^{\circ}\text{C}$ . . . . .	131
6.20 CCT curve for S690QL computed based on Leblond model with parameters shown in Tables D.1 and D.2. . . . .	131
6.21 Combined coefficient for convection and radiation according to Acevedo (2011) and Krauß (2005). . . . .	133
6.22 Double ellipsoid heat source model parameters (MORFEO, 2012); welding direction is considered as z-axis. . . . .	134
6.23 Temperature histories for a point on chord surface 6mm from the weld toe (compare to maximum for TC#7 in graphs of Figure 5.15b). . . . .	138
6.24 Temperature time history for two points P1 and P2 located in fusion zone and heat affected zone, respectively. the time history is shown only for the time that weld torch of pass 2 has reached the crown toe. . . . .	139
6.25 FZ and HAZ size predicted by model Y-333-BLK-N (cylindrical heat source, normal weld torch speed) compared to macrograph of weld. Contours are drawn for $650\text{ }^{\circ}\text{C}$ and $1500\text{ }^{\circ}\text{C}$ . . . . .	139
6.26 FZ and HAZ size predicted by model Y-333-LEB-TP-A-sh (double ellipsoid heat source, augmented weld torch speed) compared to macrograph of weld. Contours are drawn for $650\text{ }^{\circ}\text{C}$ and $1500\text{ }^{\circ}\text{C}$ . . . . .	139
6.27 Comparison of calculated transverse residual stress fields in the gap region between K-Joint and Y-Joint. . . . .	141

## List of Figures

---

6.28	Comparison of calculated stress profiles for K-Joint and Y-Joint, together with measured residual stress profiles and value ranges suggested by BS 7910 (2005).	142
6.29	Transverse residual stress build-up in gap region of K-Joint (Model K244-BLK-N-h2t: heel-to-toe weld trajectory, No phase transformation, 20/40/40% power distribution between passes). Snapshots at the end of cooling stages. . . . .	143
6.30	Transverse residual stress build-up in crown toe of Y-Joint (Model Y244-BLK-N-h2t: heel-to-toe weld trajectory, No phase transformation, 20/40/40% power distribution between passes). Snapshots at the end of cooling stages. . . . .	144
6.31	Comparison of calculated stress profiles for different start/stop locations, power distribution, and torch speed, together with measured residual stress profiles and value range suggested by BS 7910 (2005). . . . .	146
6.32	Comparison of calculated stress profiles with and without transformation plasticity effect, together with measured residual stress profiles and value ranges suggested by BS 7910 (2005). . . . .	148
6.33	Phase fraction distributions of bainite and martensite in the weld zone at crown toe at the end of simulation (CCT-based phase kinetics with augmented speed model. . . . .	149
6.34	Temperature vs. cooling rate diagram derived from CCT curve of Figure 6.19 and estimated cooling curve for point P1 (see Figure 6.24a). $M_s$ and $M_f$ are martensite start and finish temperatures respectively; $B_s$ and $B_f$ are bainite start and finish temperatures respectively (GeonX S.A., 2014). . . . .	149
7.1	Mesh of the K-joint (joint J1 of truss) with tetrahedral elements refined at the crack location. Initial semi-elliptical crack size: $a_i = 0.5$ mm, $2c_i = 2$ mm. . . . .	155
7.2	Crack shape at joint S10-J5; As can be seen, crack shape and direction are not correctly reproduced by model (c.f. Figure 5.29). . . . .	156
7.3	Equivalent stress intensity factors for models with, and without residual stresses.	156
7.4	Contact of crack faces not implemented in Morfeo. . . . .	157
7.5	Illustration of 3D crack closure behind the tip. Schematic diagram shows total intensity factory $K_{tot}$ versus external loading $\sigma_{app}$ for the two cases of compressive and tensile (or none) residual stresses. Note that even if in both cases cracks are open under the same load, stress intensity factors $K_2$ and $K_1$ are not the same.	158
7.6	Suggestion for implementation of crack faces contact in Morfeo/Crack. . . . .	159
B.1	As-built dimensions of test truss S10. . . . .	170
B.2	Locations of strain gages and LVDT transducer for truss S10-690. . . . .	171
B.3	Locations of strain gages and LVDT transducer for truss S11-690. . . . .	172
B.4	Calculated normal force and bending moment range diagrams for truss S10-690 ( $\Delta Q = 300$ kN). . . . .	173
B.5	Calculated normal force and bending moment diagrams due to post-tensioning truss S11-690 ( $T_{PS} = 137$ kN). . . . .	173



# List of Tables

4.1	Specifications of the specimens . . . . .	36
4.2	Chemical composition of steel S355J2H and S690QH. Values are given as % of weight . . . . .	37
4.3	Measurement of Reference lattice spacing ( $d_0$ ) on two different samples . . . . .	42
4.4	Scattering angle and corresponding strain results for location M1 at the depth of 2mm from the tube surface. . . . .	43
5.1	Sizes and geometric parameters of the specimens studied in ICOM, together with those of some tubular bridges (adapted from Acevedo (2011)). . . . .	60
5.2	Measured joint gap sizes and eccentricities for trusses S10 and S11. $e_1$ is back-calculated from equation 5.7 by measuring $g^*$ and $e_2$ is calculated from measured $g_c$ values. . . . .	68
5.3	Mechanical properties of steel tubes in S690QH reported by manufacturer. . . . .	68
5.4	Chemical composition of cast nodes' steel (G10MnMoV6-3, steel number 1.5410) according to EN 10293 (2005). . . . .	69
5.5	Mechanical properties of cast nodes' steel (EN 10293, 2005). . . . .	69
5.6	Welding parameters for CHS–cast node joints. . . . .	71
5.7	Welding parameters for K-joints. . . . .	75
5.8	Load range ( $\Delta Q$ ), Maximum hot spot stress range and corresponding predicted fatigue life for test trusses. . . . .	82
5.9	Nominal stress ranges and DOBs at crown toes for the joints of trusses S10 and S11 from structural analysis. The values in parentheses are deduced from strain gage measurements; Stress values are given in [MPa]. . . . .	92
5.10	Hot-spot stress ranges at the joints on the tension brace side (hs1); Stress values are given in [MPa]. SCF values are interpolated from ICOM 489E publication (Nussbaumer et al., 2004). . . . .	95
5.11	Hot-spot stress ranges at the joints on the compression brace side (hs1c); Stress values are given in [MPa]. SCF values are interpolated from ICOM 489E publication (Nussbaumer et al., 2004). . . . .	95
6.1	Consistent system of units adopted in the simulations. . . . .	109
6.2	Models used in h-convergence study. . . . .	112
6.3	Thermal conductivity $\lambda$ values for S690QH (Mertens and Lecomte-Beckers, 2012). . . . .	119

**List of Tables**

---

6.4 Timing of welding and cooling steps; Right side is the positive side of x-axis (shown on Figures 6.2 and 6.4), and front side is the positive z-axis. Net heat power distribution for this case was 30% for pass 1 and 35% for each of passes 2 and 3. . . . . 136

6.5 List of models and corresponding parameters for each model. . . . . 137

C.1 Summary of fatigue test data for the full-scale truss tests carried out at ICOM; The last column is hot-spot stress with CIDECT thickness correction factor included. 176

C.2 Summary of nominal stresses acting on CHS–Cast joints; No visible cracking was found in these joints. . . . . 176

D.1 Parameters  $p_{j,eq}^{ij}(T)$  and  $\tau^{ij}(T)$  of Leblond and Devaux (1984) model for transformations derived from CCT curve of Figure 6.19 and corresponding to the CCT curve of Figure 6.20 . . . . . 183

D.2 Parameter  $f_{ij}(\dot{T})$  of Leblond and Devaux (1984) model for transformations derived from CCT curve of Figure 6.19 and corresponding to the CCT curve of Figure 6.20 . . . . . 183

# 1 Introduction

## 1.1 Background

Circular hollow sections (CHS) are frequently observed in nature (e.g. bones, bamboos) because of their efficiency in bearing compression, bending, and torsion. The same reason applies to their use in engineering, for example in 3-dimensional truss systems for offshore structures.

In the past 25 years, there has been an increasing interest in use of CHS profiles in construction of road truss bridges, mainly in Europe. Tubular bridges bring together aesthetics with structural efficiency and sustainability (Nussbaumer et al., 2010). The form of the tubes resembles organic shapes and the bridge can be in a better harmony with the surrounding (Figure 1.1).



Figure 1.1: Traunstein (tree buttress) bridge with the detail of a cast node. Design R. J. Dietrich (Nussbaumer et al., 2010).

Composite structural solution of concrete deck supported by planar or 3-dimensional tubular CHS truss is relatively new and several bridges have been made based on this concept; A summary of bridges constructed with this structural system is presented in Table 5.1. One recent example is Lichtenfels 4-lane road bridge (Figure 1.2a) located in Thuringia state which was the first bridge in Germany made completely with welded K-joint connections.

Using high-strength low-alloy steel yields a more transparent and lighter structure with a higher live load to dead load ratio. For example, 38m Kurt-Heartel-Passage footbridge (Figure 1.2b) in Munich was made of S690 which resulted in significant reduction in use of material (Josat, 2010). This also facilitated the construction of the bridge; After fabrication, the whole bridge was carried to the site and installed by cranes.



(a) Lichtenfels road bridge (span: 90.8 m)



(b) Kurt-Heartel-Passage footbridge in Munich

Figure 1.2: Two recent tubular bridges.

## 1.2 Problem statement

Fatigue of welded parts is one of major issues in structural integrity assessment of both new and existing structures under cyclic loading. For the case of steel bridges, fatigue strength is the dominant factor in design and dimensioning of welded connections. Thus, the benefits of high-strength steel (HSS) truss bridges can not be achieved without fulfilling the fatigue strength requirements for the connections, which are the weakest link in fatigue of the structure.

Heterogeneous temperature field – created by highly localized heat of moving weld torch – causes displacement misfits between weld region and its surrounding that leads to welding residual stresses (Withers and Bouchard, 2006). Tensile welding residual stresses adversely affect fatigue life when superposed on cyclic applied stresses by changing the stress ratio in the detail, similarly to the effect of mean stresses<sup>1</sup>.

Estimation of residual stresses in a welded K-joint made of non-alloyed steel S355J2H was carried out by (Acevedo, 2011) and their effect on crack growth behaviour were estimated by an analytical approach implemented in FEM. However, for the case of HSLA steel grade S690QH used in this study, an extra parameter – metallurgical transformations during welding – is present, which was not included in previous study. Solid-state microstructural changes have a favourable effect on residual stresses by reducing the tensile ones and need to be considered in thermo-mechanical analysis of welding. Therefore, reduction of residual stresses due to this effect had to be verified and quantified and their effect on fatigue crack growth re-evaluated

---

<sup>1</sup>The effect of residual stresses on fatigue life is *not identical* to the effect of mean stresses, since the residual stress field changes with crack propagation (c.f. section 7.3.1).

for the case of S690QH.

### 1.3 Objectives

The following objectives fixed for this study:

- Experimental evaluation of residual stress field at the crack-prone part of the detail (gap region) using neutron diffraction method.
- Numerical calculation of thermal residual stresses considering microstructural transformation effects.
- Study possibility of state-of-art weld simulation on a complicated geometry, comprising multipass welds, representative of typical connections in structural engineering.
- Experimental assessment of fatigue life of welded K-joints and CHS–cast connections using large-scale fatigue tests.
- Numerical evaluation of fatigue crack growth within the residual stress field using extended Finite Element Method.

### 1.4 Scope

This study focuses on planar non-overlapping K-joints made of S690QH with dimensions typical to road bridges. For residual stress calculations, residual stresses from manufacturing phases prior to welding were neglected. It was assumed that previous residual stresses within a joint were eliminated by the high temperatures during welding.

Only constant amplitude high-cycle fatigue life of welded joints were investigated in this project. Crack initiation life was not considered in numerical investigation of fatigue life; only stable crack growth stage was considered. Only cracking in locations 1 and 1c (Figure 3.1) was considered. Selection of these hot spots was based on experience from previous fatigue tests on K-joints (ICOM, University of Stuttgart, Delft University of Technology) for which the cracking locations were exclusively at these two locations. Fatigue tests were carried out in normal environmental laboratory conditions. Filler material was assumed to have the same chemical composition and same thermo-mechanical properties as the base material. Effect of microstructural changes on fracture properties of HAZ was not investigated.

### 1.5 Structure of the dissertation

This thesis includes eight chapters:

- **Chapter 2** provides an introduction to forming of welding residual stresses, a review of different aspects of welding simulation, and incorporation of microstructural transformations into calculation model.
- **Chapter 3** briefly reviews fatigue assessment methods and different propositions for determination of fatigue crack path.
- **Chapter 4** presents a brief theory of neutron diffraction technique for residual stress measurements. Then describes experimental method and measurement results attained during two campaigns of measurements.
- **Chapter 5** describes experimental procedure for fabrication, instrumentation and fatigue testing of the two large-scale truss specimens. Fatigue test results are presented and discussed.
- **Chapter 6** presents detailed procedure for development of a numerical model for 3D analysis of thermal residual stresses as well as validation of the model and study of influencing parameters.
- **Chapter 7** details fatigue crack growth analysis within the residual stress field using eXtended Finite Element Method. It identifies the limitations of current implementation and gives propositions to improve it. Crack closure problem is briefly discussed with a distinction between crack closure in the crack tip (Elber) versus closure behind the crack tip.
- **Chapter 8** concludes and synthesises the main findings and proposes future work.

Additional information on the work done, including experimental data and programs written for calculation of microstructural transformations are presented in appendices.

## 2 Background on welding residual stresses and simulation

### 2.1 Introduction

Welding residual stresses are regarded as “flaws” in the quality of the components because they may obstruct reliable operation of the welded structure (Radaj, 2003). Residual stress field in the structural components can be estimated either by calculation or by measurement. Some of the measurement methods for residual stresses are briefly reviewed in Chapter 4 while neutron diffraction method – which was used in this study – is explained in more detail.

Computational welding modeling (CWM) is a tool to evaluate welding residual stresses and distortions by numerically solving the governing equations for thermal, mechanical, and metallurgical fields. The aim is to eventually use this information for optimizing the manufacturing process and improving the quality and service life of the components. Considerable development in this area has been made during the past two decades (Lindgren, 2001a, 2007), which has helped using of computational welding simulation for practical applications. Some advantages of computational weld modelling compared to the experimental methods for determination of welding distortions and residual stresses are, according to Radaj (2003), as follows:

- Simulation of welding process paves the way to more comprehensive understanding of physical phenomena that happen during welding and their relationships.
- Limitations on parameters inherent to experimental models (e.g. limitations on heat input or welding speed) can be waived in numerical model in order to perform sensitivity analyses.
- Computations are less expensive and more rapid than real experiments

- There are quantities that are either hard or impossible to measure (e.g. temperatures inside HAZ) which can be evaluated in the simulations.

Therefore, utilisation of computational welding simulation is increasing as an essential tool for innovative welding processes, welded structures, and materials. For example, when a new welding technique is developed, CWM can prove useful in predicting the residual stress field which in turn can be used in fatigue life assessment of the welded detail. Kranz et al. (2013) examined such an application of simulations for the case of laser-GMA hybrid welding for thick plates. They found that the method is economical compared to conventional experimental techniques and according to the authors, results in better weld profiles, smaller molten pool, and increased fatigue life.

In this chapter, the physical phenomena leading to formation of residual stresses are briefly discussed. Then, various aspects of weld modelling are presented. Lastly, incorporation of microstructure evolution into weld modelling is discussed.

## 2.2 Description of phenomena

### 2.2.1 Residual stresses

Residual stresses are self equilibrating stresses that exist in a structure without any external load acting on the structure. The source of residual stresses is the “mismatch” or inhomogeneous deformations. The inhomogeneous deformation can happen as change of volume (caused by thermal expansion, chemical reaction, or metallurgical transformation), or change in shape (caused by plastic or visco-plastic deformation) (Radaj, 2003). Residual stresses are usually an unwanted outcome from manufacturing processes (rolling, heat treatment, welding, flame-cutting, pressing); But it is also possible to intentionally generate or modify the residual stress field into a desirable state in order to increase the life cycle of the manufactured product. High Frequency Mechanical Impact (HFMI) treatment of welded parts is a noticeable example of these modification methods (Weich et al., 2009). Another technique recently introduced is low transformation temperature welding (LTTW) wires. They exhibit the potential for improving the fatigue life of weldments, specially in the case of high strength steel welds (Ohta et al., 2003; Ooi et al., 2014). The wires have reduced martensitic start temperature and large transformation strains. As a result, final welding residual stresses are compressive which is favourable to the fatigue life of the component.

First kind ( $\sigma^I$ ), or macroscopic, residual stresses extend over macroscopic regions spanning several grains of material. These are the residual stresses that are of particular interest for engineering applications. Their origin and distribution is described using continuum mechanics. Second kind ( $\sigma^{II}$ ), or microscopic residual stresses act between the grains of the metallic structure (sizes between  $1.0mm$  to  $0.01mm$ ). The third kind of residual stresses ( $\sigma^{III}$ ) act between atomic regions in an individual grain in the sizes between  $10^{-2}mm$  to  $10^{-6}mm$ . An



example of the latter kind is the residual stresses formed around a single dislocation in the crystalline structure. Figure 2.1 depicts these three types of residual stresses.

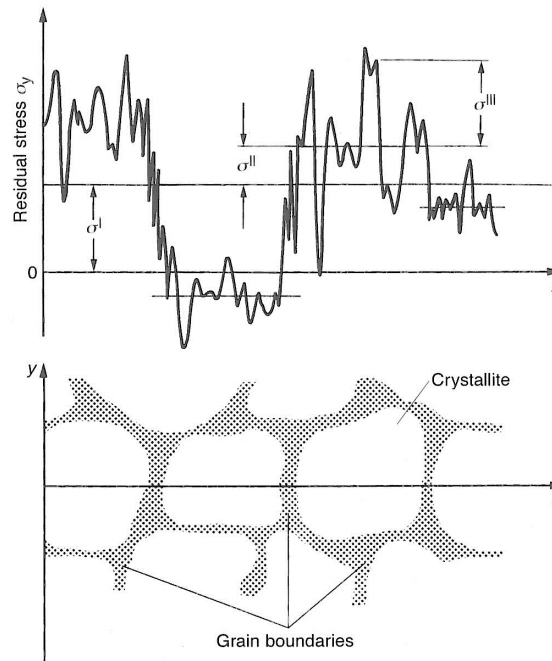


Figure 2.1: Three distinct types of residual stresses ( $\sigma^I$ ,  $\sigma^{II}$ , and  $\sigma^{III}$ ) categorized based on their range of action; after Macherlauch et al. (1973) according to Radaj (2003).

### 2.2.2 Formation of welding residual stresses

There are various definitions for welding. One shared statement between all these definitions is: “Welding serves to create continuity of the previously separate material” (Radaj, 2003). For arc welding, this continuity is reached by melting and solidifying the two parts in a molten pool, with or without adding a filler material. The application of heat and/or pressure is necessary for this process to start. If the melting point of the filler metal is lower than the parent metal, no surface melting happens and the process is called “soldering” or “brazing”. Various heat sources are used for welding, including gas flame, electric arc, laser beam, electron beam, frictional and resistance heating. Figure 2.2 illustrates MAG welding process which was used for the fabrication of test trusses in this project. The temperature field generated by heat source is highly heterogeneous and varies over time.

Localized heating by the welding torch causes melting of the metal at the fusion zone (FZ). The material in FZ expands. This thermal expansion is restricted by the colder regions in the vicinity of the weld pool. The yield stress is reduced at high temperatures existing in the welding region and thermal stresses exceed this reduced yield stress at some points, which leads to plastic deformations. During cooling down, thermal shrinkage of weld region, which is restrained by the neighbouring cold regions, will result in tensile residual stresses in the

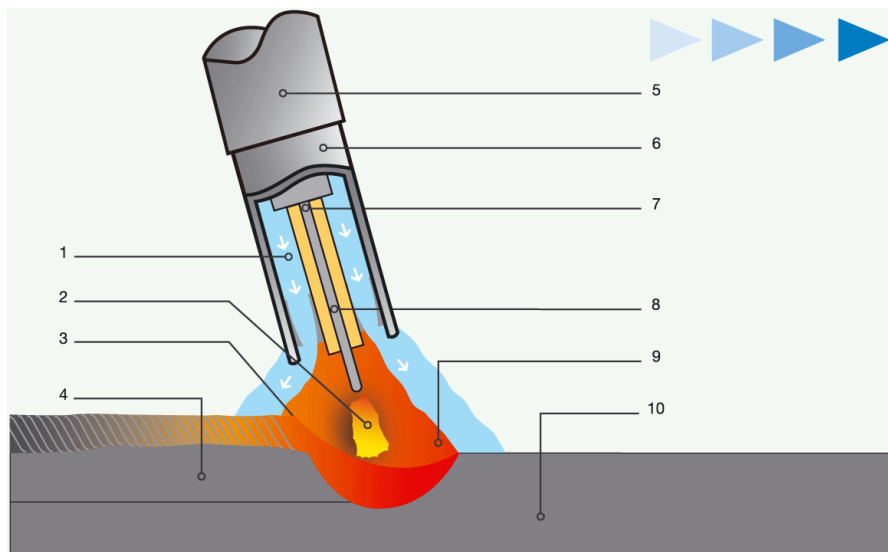


Figure 2.2: MIG/MAG welding (WMB, 2009) : 1.Shielding gas, 2.Electric arc, 3.Weld pool, 4.Solidified weld metal, 5.Welding torch, 6.Gas nozzle, 7.Wire feed, 8.Welding wire(solid or flux-cored), 9.Protective atmosphere, 10.Base material.

weld zone and compressive residual stresses in the surrounding regions (Hensel et al., 2013; Radaj, 2003). Metallurgical transformations during cooling (e.g. for the case of steel material, austenite decomposition into martensite) lead to a volume increase. This can cancel the tensile residual stresses partially or completely to a degree that they even cause compressive residual stresses in the weld and tensile residual stresses in the surrounding areas. Transformation strains are further discussed in section 2.4. To summarize, for the regions which cool down the latest, residual stresses will be tensile if thermal strains are dominant, and they will be compressive if transformation stresses dominate.

Various factors can affect welding residual stresses:

- Pre-existing residual stresses: residual stresses from previous manufacturing stages (e.g. rolling, casting, machining, surface treatments, heat treatments) or by improper assembly.
- Relaxation or creep due to cyclic loading
- Overloads: When the loading stresses superimpose onto the residual stresses and locally surpass the yield limit, this will result in a redistribution of self-equilibrated stresses.

The effect of pre-existing residual stresses is usually not considerable, since the magnitude of rolling and heat treatment residual stresses is small compared to welding residual stresses. Furthermore, high welding temperatures cause annealing at the weld region and majority of the prior residual stresses are “erased” by welding (at least the types II and III).

Relaxation of residual stresses with cyclic loading is of special interest for fatigue-loaded structures. As Farajian (2013) states, to correctly consider the effect of residual stresses on fatigue life, the influence of fatigue loading on the residual stress field should also be investigated. Farajian studied relaxation of welding residual stresses in low-cycle and high-cycle (up to  $2 \times 10^6$  cycles) regimes for various grades of construction steel, including S690QL. The relaxation studies on both small-scale and large-scale specimens revealed that – except for a small decrease at the beginning of cyclic loading – residual stress relaxation in high-cycle loading is negligible.

## 2.3 Computational welding simulation

### 2.3.1 Subdomains

Welding simulation can be carried out in various scales and for different purposes. These simulation types are categorized into three main subdomains:

1. *Process simulation*: Involves analysis of processes ongoing at the fusion zone (weld pool dynamics) and determining characteristics and geometry of the fusion zone (e.g. arc efficiency, weld width, penetration depth, size and shape of the molten pool). Multiphysics models are required to model several phenomena ongoing in the weld pool, including plasma and molten metal flow, surface tension, Marangoni movements, effect of electric and magnetic fields on droplet transfer,
2. *Structure simulation*: Evaluation of residual stresses and distortions and their impact on strength and stiffness of the components (this study).
3. *Material simulation*: Modelling of evolution of microstructural states in fusion zone and heat affected zone with variation in hardness, hydrogen diffusion, and the hot or cold cracking tendency.

Figure 2.3 shows these three subdomains, depicts which information is acquired by these models, and how the information is shared between these subdomains. For example, the result of a weld pool process simulation, is summarised into an equivalent heat source model which will be used as thermal loading in a structure simulation. In this study, the focus is on structure simulation with consideration of microstructural transformations (material simulation). Process simulation is not treated here.

### 2.3.2 Previous work

Joseph Fourier established the basic theory for heat transfer. Rosenthal (Rosenthal, 1946) and Rykalin (Rykalin, 1974) applied this theory to predict the thermal field for moving heat sources starting from late 1930s. With the developments in computational facilities, thermal

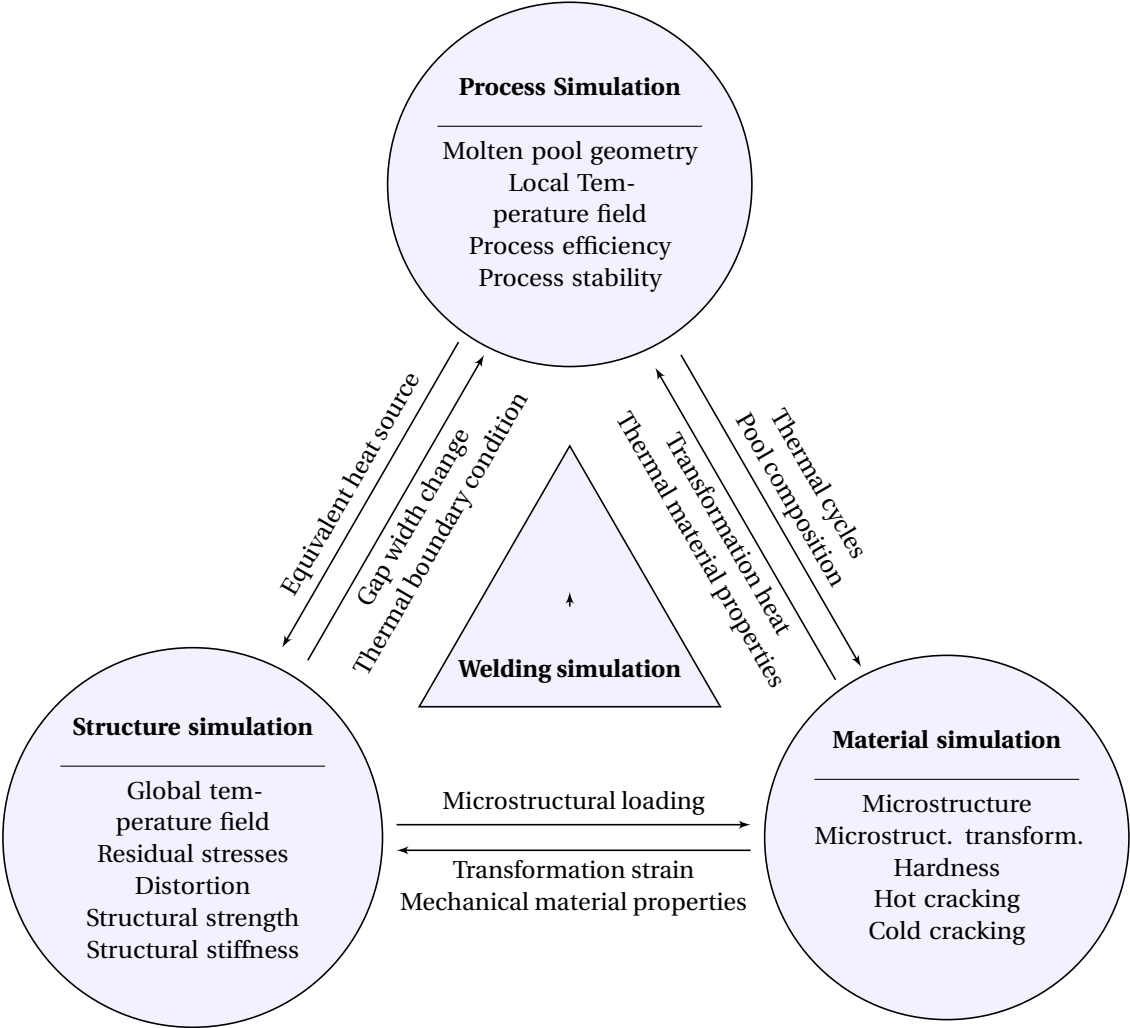


Figure 2.3: Subdomains of welding simulation including objectives of each subdomain and the coupling factors, (Karlsson, 1986; Radaj, 2003)

stress analyses using finite element method began with Ueda in 1972, according to (Goldak and Akhlaghi, 2005). This trend continued in the later decades, with increase in complexity of the models. The increased complexity of the model included improved material models, multi-pass weld modelling, using 3D models instead of 2D models, and incorporation of metallurgical transformations into models. Macherauch and Wohlfahrt (1978) explained the residual stress formation as superposition of three distinct processes: shrinkage of weld seam and HAZ, residual stresses due to rapid cooling of the surface (similar to quenching), and residual stresses due to phase transformations. Later, Nitschke-Pagel and Wohlfahrt (1992) and Voss et al. (1997) emphasized the role of transformation strains in formation of residual stresses in addition of shrinkage stresses. Shrinkage stresses happen because, during cooling, contraction of highly heated areas at the weld seam is hindered by surrounding colder areas. This is superposed by transformation strains. The transformation of austenite (which takes place in the areas heated highly enough) into martensite, bainite or ferrite-pearlite will result in different volume changes which – for the case of martensitic transformation – partly compensate the shrinkage strains and will reduce final residual stresses in the weldment.

There is a large volume of published studies on welding residual stress analyses using FEM, which is reviewed by Lindgren (2001a,b,c) and Mackerle (2002).

Due to the variability of the results reported by different researchers, a round-robin FEM analysis program was organized by International Institute of Welding in order to assess the existing analysis approaches. An earlier summary of the work is reported by Dong and Hong (2002). Recently, Wohlfahrt et al. (2012) compared the old results with the new and improved analyses and made recommendations for the choice of mechanical material model. They recommended using isotropic hardening instead of kinematic hardening for austenitic steel welds.

A German initiative for standardization of FEM welding residual stress analysis has started (Schwenk et al., 2011) and a preliminary specification – DIN SPEC 32534-4 – is published, but is still far from complete.

**Alternative methods:** Inherent strain method is proposed by Japanese researchers, (Mochizuki, 2007; Ueda et al., 2012). The basic assumption of the method is that the inherent strains resulting from a complex welding process can be approximated by the inherent strains of a similar and simpler structure. This method is not considered in the work herein.

### 2.3.3 Governing equations

Several interactions between thermal, mechanical, and metallurgical domains occur during welding. A simplified diagram which shows some more significant interactions is presented in Figure 2.4. Dark arrows show dominating effects and dotted arrows indicate less important effects. Temperature field affects both residual stress field and microstructure field, but the

## Chapter 2. Background on welding residual stresses and simulation

---

inverse effects are generally considered as secondary. This helps de-coupling of the thermo-mechanical analysis into a sequential procedure of solving the heat conduction problem, followed by metallurgical and mechanical analyses. Diagram in Figure 2.5 shows how the governing equations are applied in staggered scheme for calculation of thermal welding stresses, considering only thermal and mechanical fields. Incorporation of metallurgical field into problem, does not change the thermal solution, but material properties are to be calculated by a mixture rule based on phase data, including phase volume fractions and temperature-dependent mechanical properties for each phase.

Definitions of quantities used for thermal analysis in figure 2.5 are as follows:

- $h$  : heat transfer coefficient;
- $T_0$  : gas or liquid temperature of surrounding;
- $T^S(x, y, z, t)$  : prescribed temperature;
- $q_n^S$  : prescribed heat flux density normal to the boundary;
- $\lambda$  : conductivity of material;
- $c_p$  : specific heat capacity of material;
- $T(x, y, z, t)$  : Temperature as a function of location and time;
- $Q$  : Heat input into the system.

And for mechanical analysis, following quantities are defined:

- $\nabla^T \boldsymbol{\sigma}$  : divergence of stress tensor;
- $\mathbf{b}$  : body force vector;
- $\dot{\boldsymbol{\epsilon}}^{el}$  : elastic strain rate;
- $\dot{\boldsymbol{\epsilon}}^{pl}$  : plastic strain rate;
- $\dot{\boldsymbol{\epsilon}}^{thm}$  : thermo-metallurgical strain rate (see section 6.6.1);
- $\mathbf{U}_e$  : displacement field.

## 2.4 Evolution of microstructure

### 2.4.1 Welding effects

The microstructure evolves during the thermal loading cycle caused by welding. During the heating phase, the existing ferrite – with body-centered-cubic (bcc) crystal structure – transforms into austenite – with face-centered cubic (fcc) structure – (see Figure 2.7). The transformation occurs in the temperature range of  $A_{c1}$  to  $A_{c3}$ . The lower transformation temperature  $A_{c1}$  for iron and all steels is approximately 720 °C. The upper transformation temperature  $A_{c3}$  varies for each alloy and can be between 720 °C and 910 °C. For hypoeutectoid steels, the lower the carbon content, the higher the upper transformation temperature will be. At temperatures above  $A_{c3}$ , austenite volume fraction is 100% and the added heat is consumed for austenite grain growth.

Figure 2.6 depicts different metallurgical zones formed in a low-alloy steel weldment. The

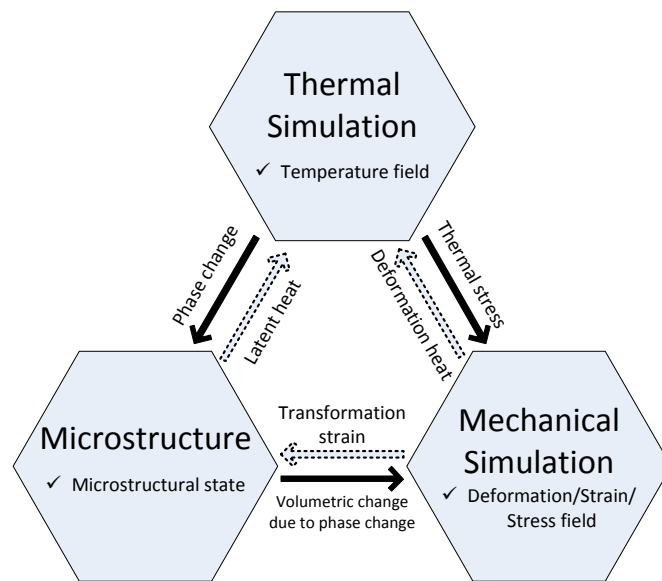


Figure 2.4: Interaction of temperature, mechanical and microstructural fields for the welding simulation, adapted from Radaj (2003)

zones are categorized based on the severity of the thermal cycle they experience. The fusion zone (FZ) fully transforms into austenite during welding and after solidification the material undergoes solid-state transformation based on the cooling rate and CCT curve for that specific alloy. Heat Affected Zone (HAZ) is the region in the vicinity of FZ that is austenitized either partially (ICHAZ) or fully (FGHAZ and CGHAZ). Several subdivisions are observed in HAZ based on the extent of grain growth and austenitization they have experienced in the heating phase. These include coarse-grained zone (CGHAZ), fine grained zone (FGHAZ), inter critical zone (ICHAZ), and over-tempered parent metal. Obviously, phase-transformations do not occur at the last subdivision (over-tempered region) since it is not austenitized during the heating cycle.

During cooling, the regions transformed (fully or partially) to austenite will undergo a reverse transformation in temperature range  $A_{r3}$  to  $A_{r1}$  which are lower than  $A_{c3}$  and  $A_{c1}$ , respectively. The reason why austenite decomposition is more sluggish than its formation being that diffusion speed of carbon atoms within the alloy in  $\alpha \rightarrow \gamma$  transformation and the reverse transformation are different. The kinetics of phase change can be illustrated by using continuous cooling transformation (CCT) diagrams, such as the diagrams shown in Figure 2.8. The diagrams are for steel grade S690QL – which is close to the steel grade S690QH used in this project. S690QH is an HSLA steel (see 3.2) for which no CCT data was found. The difference between the two diagrams is due to the slight change in alloying element contents and also difference in austenitization temperature and hold time (austenite grain size). CCT diagrams should be read by following individual cooling curves and reading their intersection with microstructure lines (thick lines in Figure 2.8l) to evaluate of volume fraction of each phase in the final transformation product. A generally accepted index for representing thermal

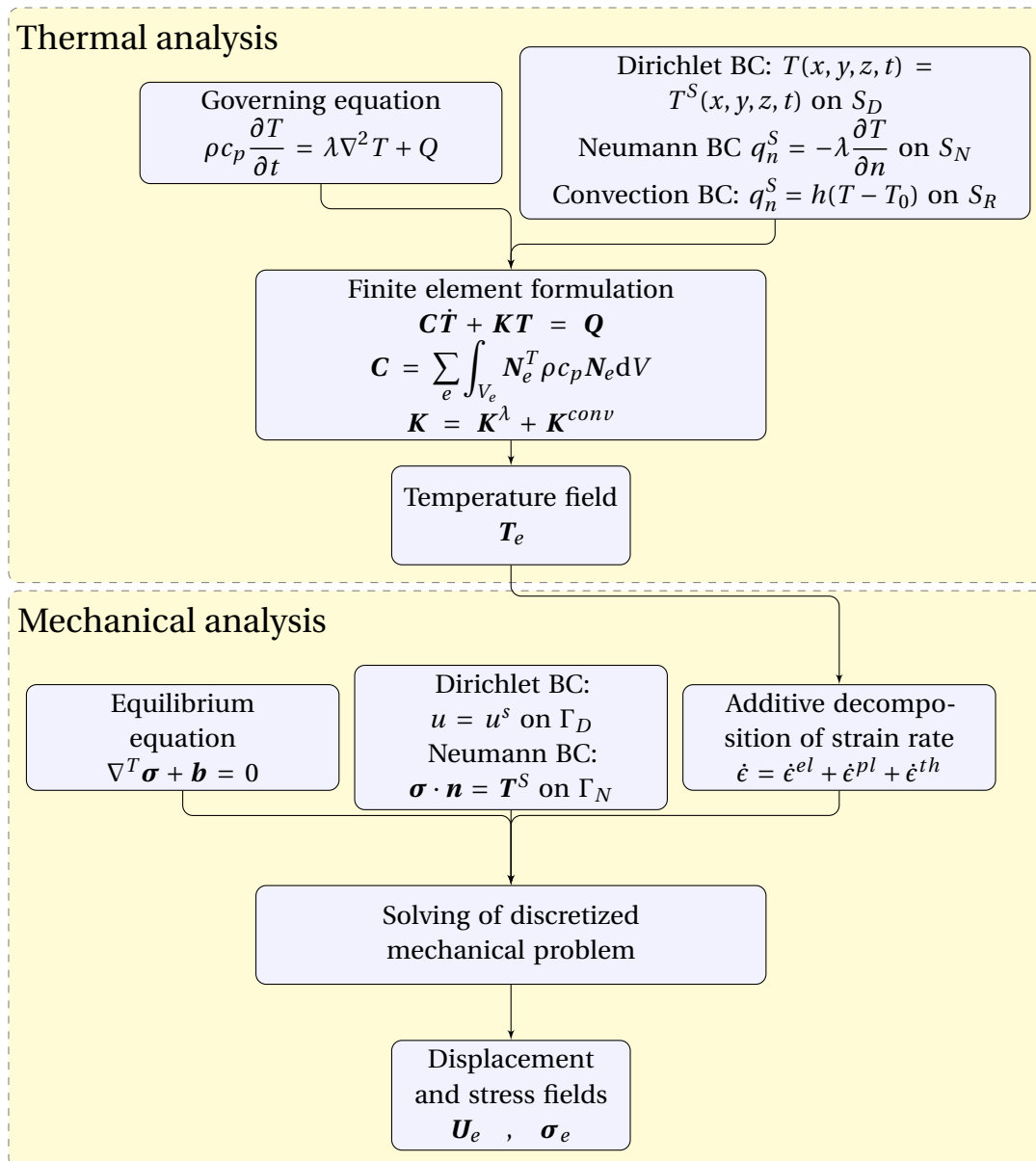


Figure 2.5: Uncoupled sequential analysis procedure for thermo-mechanical analysis



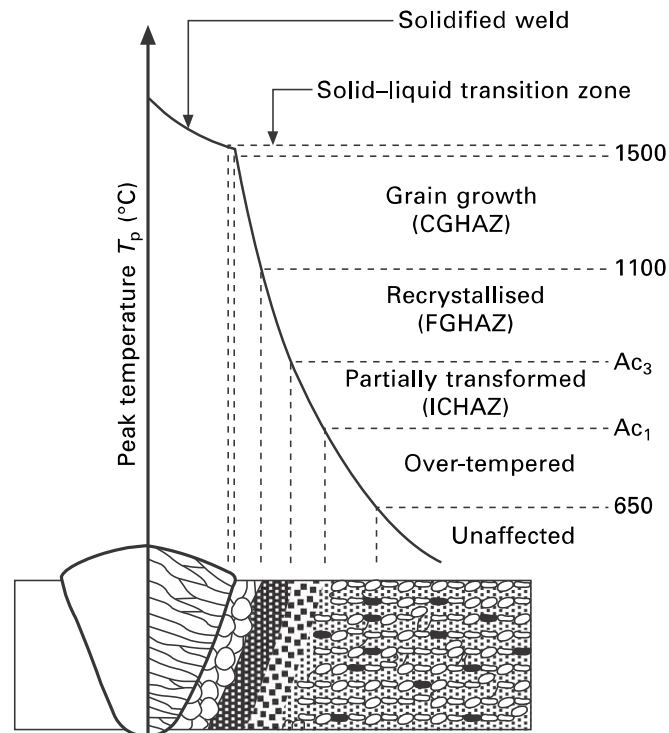


Figure 2.6: Metallurgical zones in a single-pass weld categorized by maximum temperature at each region (Francis and Withers, 2011).

conditions in welding of low alloy steels, is the cooling time from 800 °C to 500 °C ( $t_{8/5}$ ) which is the range that austenite decomposition takes place Grong (1997). As can be seen in CCT diagrams, very short cooling times (i.e. high cooling rates) lead to a microstructure that is exclusively martensitic<sup>1</sup>. This corresponds to welds with low heat input. On the other hand, a high heat input welding will cool down slowly and the result will be a combination of bainite<sup>2</sup> and ferrite/pearlite.

In addition to cooling rate, the phase transformation depends also on the grain size and carbon content of the transformed austenite (Lindgren, 2007). That is why the peak temperature and hold time for the CCT curves should be similar to the welding process (usually between 1350 °C to 1400 °C in order to help grain growth). Heinze et al. (2013) investigated the effect of variation in austenite grain size on welding residual stresses of steel grade S355J2. Surprisingly, they observed no significant effect due to consideration of austenite grain size which can not be explained with the above statement.

Various mathematical models for transformation kinetics are proposed by researchers. Two of the most known models are Leblond model for diffusive transformations (Leblond and

<sup>1</sup>Martensite microstructure: body-centered tetrahedral (bct) microstructure that is a metastable iron phase supersaturated in carbon (Callister, 2005). It possesses very high hardness values

<sup>2</sup>Bainite is not a phase, but an acicular microstructure. It is a fine non-lamellar aggregate of carbides and plate-shaped ferrite.

## Chapter 2. Background on welding residual stresses and simulation

---

Devaux, 1984) and Koistinen-Marburger relation for martensitic transformation Koistinen and Marburger (1959). These two models are further explained in section 6.6.4.

Due to the difference in unit volume of martensite (bct) and ferrite (bcc) structure, martensitic transformation exhibits a positive volume change, which superposes with hindered shrinkage caused by thermal cycle (see section 2.2.2) and leads to lower residual stresses. Another phenomena that occurs during austenite decomposition is that the variation of stress and strains on the length scale of grains contributes to the plastic strains (Goldak and Akhlaghi, 2005). These strains are called transformation-induced plasticity (TRIP) and were first observed by Wassermann in 1937 (Fischer et al., 1996). A mechanism for TRIP was first proposed by Greenwood and Johnson (1965), but other mechanisms exist as well.

Transformation plasticity shows characteristics of superplasticity (Fischer et al., 1996; Radaj, 2003). When a macroscopic (external) stress field exists at the time of solid-state transformation, internal stresses within the residual austenite cause yielding in the austenite, even for low levels of macroscopic stress. The consequence for welding is that part of high compressive residual stresses generated by volume change vanishes, which leads to slightly higher residual stresses when the weld is cooled down. The combined effect of thermal strains, volume change strains, and TRIP strains is investigated by several author, including Börjesson and Lindgren (2001). Figure 2.9 from Francis and Withers (2011) shows the effect of these parameter on the final residual stress state of a multipass weld. The very low calculated residual stresses produced by transformation volume change are moderated by transformation plasticity. Dai et al. (2010) reported the final calculated residual stress value considering the effect of volume change *plus* transformation plasticity (the curve in the middle of the two other curves in Figure 2.9) was in better agreement with residual stress measurements.

Several relations for calculation of strains due to transformation plasticity are suggested by various authors in literature (Fischer et al., 1996; Leblond et al., 1986). The following relation is given originally by Mitter (1987) according to Radaj (2003):

$$\Delta\epsilon_{tp} = \frac{3}{2}K_{tr}(1-p)\sigma^d \Delta p \quad (2.1)$$

Where:

- $\epsilon_{tp}$  : transformation plasticity strain;
- $K_{tr}$  : transformation plasticity coefficient;
- $p$  : volume fraction of newly formed microstructure (e.g. martensite);
- $\sigma^d$  : deviatoric external stress tensor acting in the region.

Limited number of transformation plasticity coefficients exist in literature. In a recent study, Deng and Murakawa (2013) provide a short table of the values they found in literature for various steel grades with all values being in the range  $4.8 \times 10^{-5} \text{ MPa}^{-1}$  to  $10 \times 10^{-5} \text{ MPa}^{-1}$ . Radaj

## IRON-CARBON EQUILIBRIUM DIAGRAM

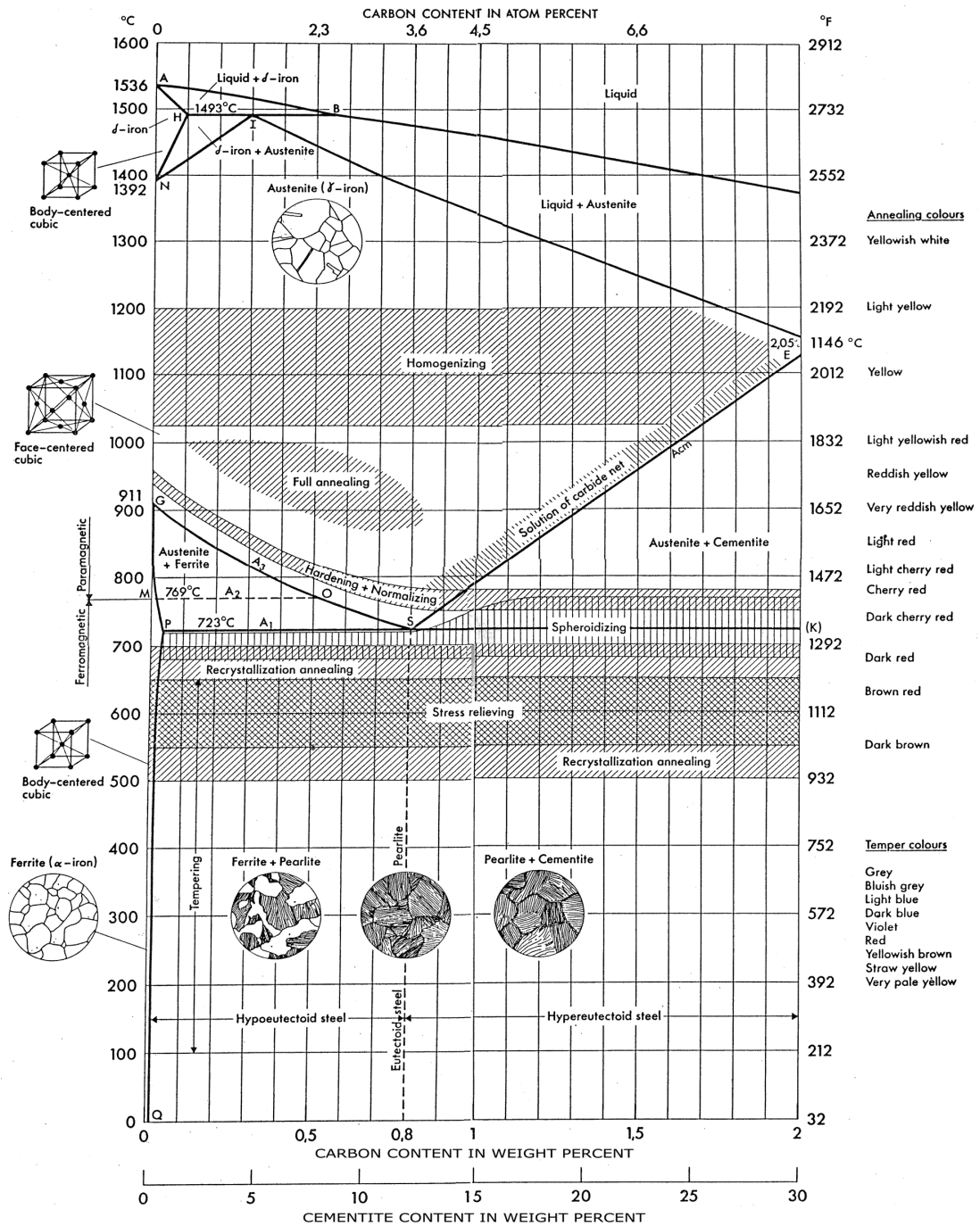
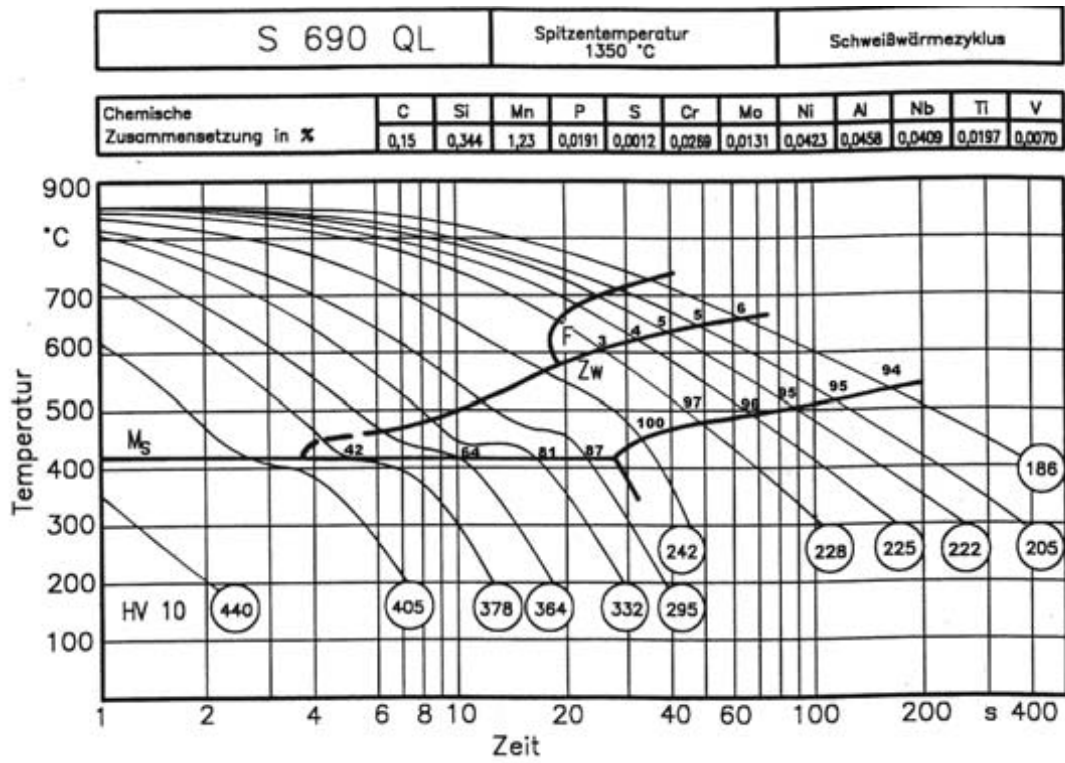
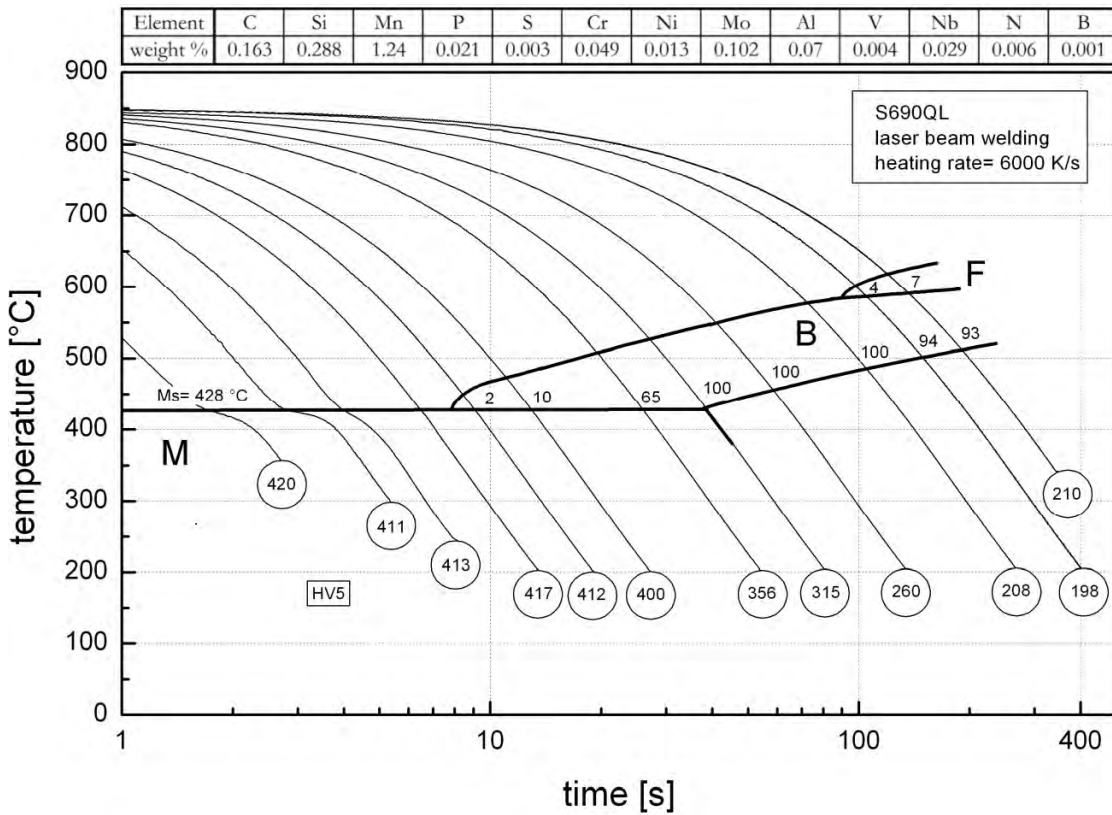


Figure 2.7: Iron–Carbon Phase diagram (Brandt and Warner (2009), Originally from Struers Inc.). Pearlite: two-phase, lamellar structure composed of  $\alpha$ -iron (88 wt%) and cementite (12 wt%).

Chapter 2. Background on welding residual stresses and simulation



(a) Seyffarth et al. (1992)



(b) Scharff (2012)

Figure 2.8: CCT diagrams for S690QL from literature.

(2003) gives the range of  $K_{Tr}$  as  $3 \times 10^{-5} \text{ MPa}^{-1}$  to  $12 \times 10^{-5} \text{ MPa}^{-1}$  and  $K_{Tr} \approx 5 \times 10^{-5} \text{ MPa}^{-1}$ . Experimental procedure for calculation of transformation plasticity coefficient is explained by Taleb et al. (2001),

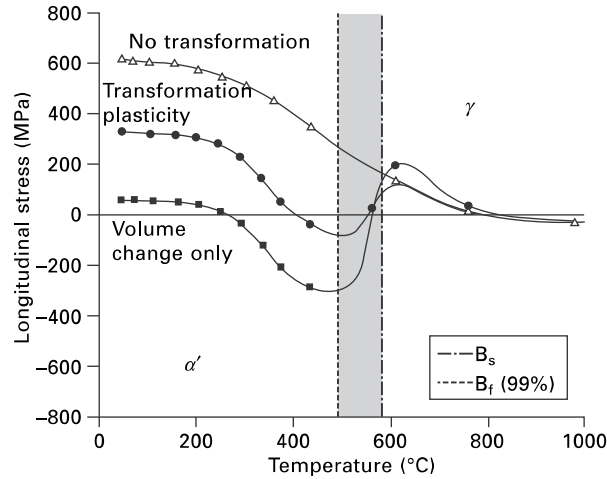


Figure 2.9: Impact of different modelling assumptions on longitudinal stresses of a multipass plate weld (after Francis and Withers (2011)); Shaded area is the temperature range where transformations take place.  $B_s$  and  $B_f$  are bainite start and finish temperatures, respectively.

### 2.4.2 Multipass welds

For the case of multipass welds, the HAZ undergoes multiple thermal cycles. Only a small part of HAZ undergoes the peak welding temperatures twice, as can be inferred from Figure 2.10b. For these parts, the peak in second thermal cycle is larger. But the major part of HAZ (shaded regions in figure), receives relatively mild heat treatments.

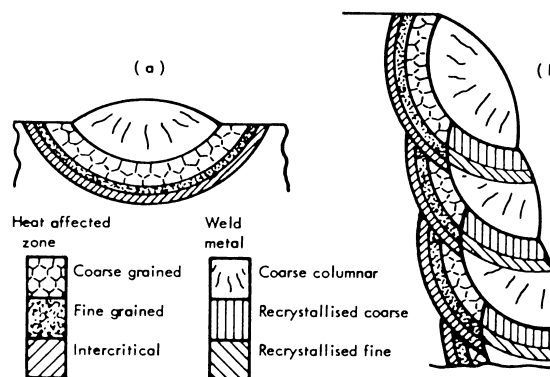


Figure 2.10: Schematic microstructure in a single pass weld (a) versus multipass weld (b) (Easterling, 1992).

Each weld pass alters the stresses produced by previous passes. As Lindgren (2001a) states, analysing multipass welds as a series of single-pass welds is a costly and demanding task. Such

## **Chapter 2. Background on welding residual stresses and simulation**

---

simulations can be found for example in the works of Brickstad and Josefson (1998), Börjesson and Lindgren (2001) and more recently by (Hildebrand, 2008). Lindgren (2001a) mentions lumping of successive passes together as a way to reduce the cost of computation. This will be discussed in more detail in Chapter 6; However, for the analyses in the present study it was not the cost issues, but the complex geometry that stipulated using the weld pass lumping.

## 2.5 Summary

- The major physical phenomena involved in welding are introduced in this chapter. Mathematical modeling of weld phenomena and governing field equations are given. Different subdivisions of welding simulation are discussed and finally the metallurgical transformations taking place during the welding are reviewed. Background knowledge acquired will help establishing the numerical weld model in Chapter 6.
- This study will focus on *structural modelling* and to some degree *material modelling* in calculation of type *I* (macroscopic) residual stresses which are most influential in fatigue crack growth.
- Paucity of data for some material parameters – specifically transformation plasticity coefficient – was observed. Also for CCT diagrams, data for steel grades close to the steel grade S690QH are found in published research; but not for the exact same material.
- Although effect of austenite grain size on martensite transformation in a known fact, some authors did not confirm that – for specific case of S355 steel – this factor have considerable impact on welding residual field.
- Previous research shows that the effect of phase transformations for low alloy bainitic steels need to be considered in calculation of residual stresses. Martensitic transformations that occur at the cooling period of welding in these materials, has considerable impact on the welding residual stresses.





# 3 Fatigue assessment of tubular joints

## 3.1 introduction

In this chapter characteristics of high strength steels and fatigue assessment methods for tubular joints are presented. It is convenient to first present the convention for naming the different locations and hot spot numbering of the K-joint which will be used across the thesis. These conventions are presented in Figure 3.1.

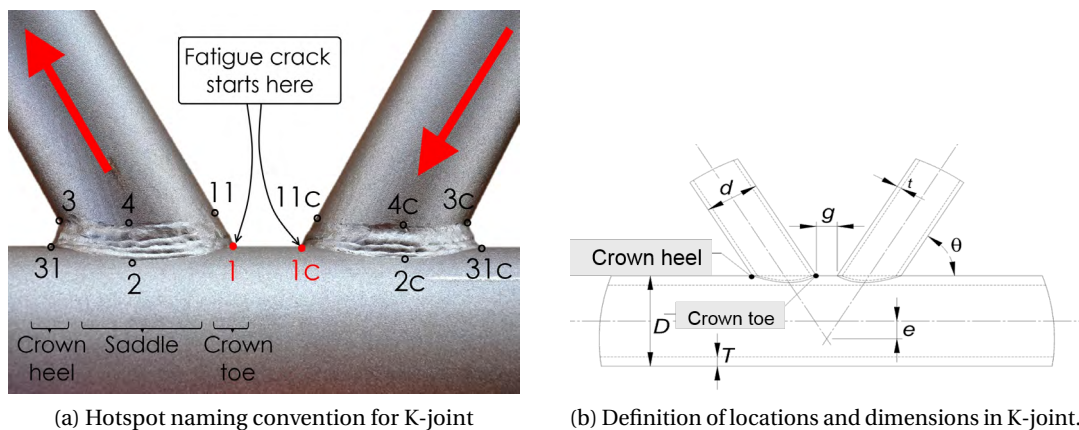


Figure 3.1: Naming convention for locations and hot spots on K-joint.

## 3.2 High strength steel material

Until the 1970's only two constructional steel grades were used: St 37(S235) and St 52 (S355). The "Oil shocks" in that period motivated producers to save raw materials and energy. The research in the steel-making led to development of high strength low alloyed (HSLA) steels (Ponge, 2005). Figure 3.2 shows the time-line for the introduction of the different steel grades.

At first, only plate elements were produced, followed recently by production of hollow sections in high strength steel grades.

## Chapter 3. Fatigue assessment of tubular joints

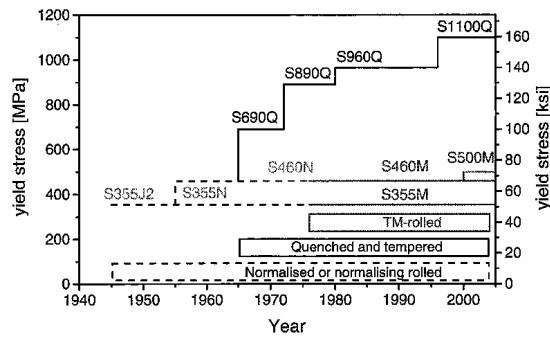


Figure 3.2: Historical development of construction steel products and production processes (Samuelsson and Schröter, 2005)

The increase in the strength is gained through grain refinement, not by increasing carbon content, alloying, or hard-working. The significant advantage of this method is that it increases not only the yield strength, but also improves the toughness of the steel, as shown in Figure 3.3. Fine-grain microstructure is achieved by means of controlled thermal process after rolling. For S690 steel, it consists in water quenching of rolled steel followed by tempering.

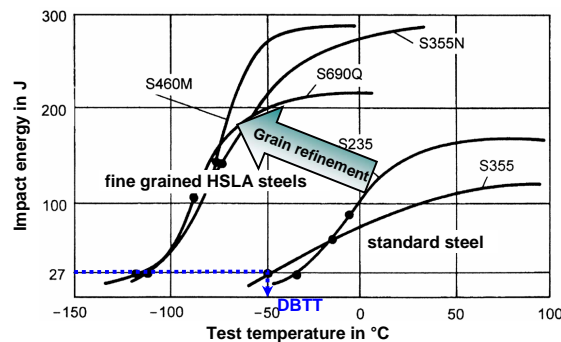


Figure 3.3: Effect of grain refinement on toughness (DBTT: ductile to brittle transition temperature) (Ponge, 2005)

Modern high-strength steels exhibit these features:

- high yield strength;
- high toughness even at low temperatures (low transition temperature);
- good weldability (carbon content below 0.2%).

These steels have been referred to with different technical terms in the literature. Very high strength steel (VHSS) (Pijpers, 2011) for grades higher than S690, High performance steel (Samuelsson and Schröter, 2005) for whole range of steels that are higher than S355, and High-strength steel (Puthli, 2008). The term HSLA (High-strength low-alloy steel) (Ponge, 2005) is used mostly in Materials science for the whole range of fine-grain construction steels.

Technical delivery conditions for the various steel grades of hot-rolled structural hollow sections is published in Eurocode EN 10210-1 (2006). Chemical composition of steel grade S690QH – which was used in this study – is presented in Table 4.2. The microstructure is considered to be similar to the microstructure of S690QL consisting of 84% bainite and 16% martensite, according to Hildebrand (2008).

### 3.3 Overview of fatigue assessment methods

Radaj (1996) and Radaj et al. (2009) divide the methods for service life evaluation of welded components into two main categories: “Global approaches” and “local approaches”.

Global approach implies that the fatigue life evaluation is directly based on the external forces and moments or from the nominal stress ranges in the critical cross-section. This is calculated by using e.g. simple beam theory. The nominal stress ranges then are compared to S-N diagrams corresponding to the studied detail. Strength assessments which are based on local stress and strain parameters are “local approaches”. The local aspects of fatigue damage (i.e. crack initiation, crack propagation and final fracture) can be considered in these approaches. The local approaches can be classified as:

- Structural hot spot stress method: takes into account change in structural stress range ( $\Delta\sigma_{hs}$ ) due to the part geometry. The approach is suitable for welded joints of hollow section members and for plated structures.
- Notch stress, notch stress intensity and notch strain approaches: these methods use the elastic notch stress range ( $\Delta\sigma_k$ ) or stress intensity or elastic-plastic strain range ( $\Delta\epsilon_k$ ) at the weld toe or root to assess the fatigue strength and service life of the weldments.
- Crack propagation approach: based on linear elastic fracture mechanics (LEFM) theory, assumes a crack is already available and uses special parameters such as J-integral or the range of the stress intensity ( $\Delta K$ ) to determine the increase in the crack length per cycle (or: crack propagation rate  $da/dN$ ).

Notch stress method is used for crack initiation phase. For welded structures this phase stands for less than 10% of fatigue life Schijve (2001), because generally some crack-like defects exist at the weld toe (or weld root) region which can be considered as initial crack size.

Structural hot spot stress method and fracture mechanics method are the two methods which are mostly used in the domain of tubular structures (Dover and Holdbrook, 1980; Marshall and Wardenier, 2005).

### 3.3.1 Structural hot-spot stress method

The method was originally developed for welded joints of circular and rectangular hollow sections and has been in use for more than 30 years in offshore industry. Later it was extended for use in plated structures (Radaj, 1996).

The hot-spot stress is calculated using extrapolation of surface stresses at the vicinity of the weld toe (and in the direction perpendicular to the weld line), as shown in Figure 3.4. The location of extrapolation points ( $L_{r,min}$  and  $L_{r,max}$ ) are determined according to the code recommendations (Zhao et al., 2000). The code also stipulates the type of extrapolation, whether it is linear (for circular hollow sections) or quadratic (for rectangular hollow sections). The calculated hot spot stresses then shall be used in a S-N fatigue diagram to estimate the fatigue life (Figure 3.5).

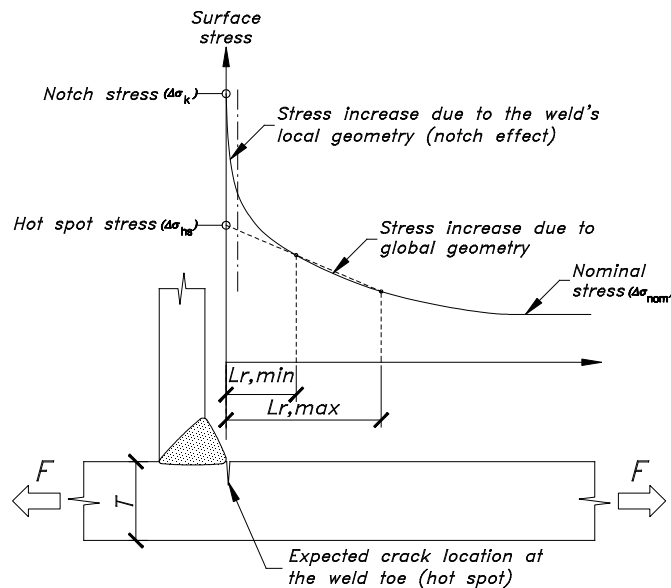


Figure 3.4: evaluation of hot spot stress by extrapolation of surface stress (Zamiri Akhlaghi, 2009).

### 3.3.2 Linear elastic fracture mechanics (LEFM)

Linear elastic fracture mechanics (LEFM) has been accepted as a powerful tool in assessment of the fatigue life of new structures as well as in evaluation of the remaining fatigue life of existing structures. The main assumption is that there is a crack present in the material. Therefore the location of crack and the initial size need to be determined prior to the analysis. van Straalen and Dijkstra (1993) suggest that an initial semicircular crack with a depth of 0.15 mm yields reasonable results for the fatigue life of the structure.

The fatigue life of the detail is then determined by calculating the crack propagation rate during the course of fatigue loading until crack size reaches its critical value which means

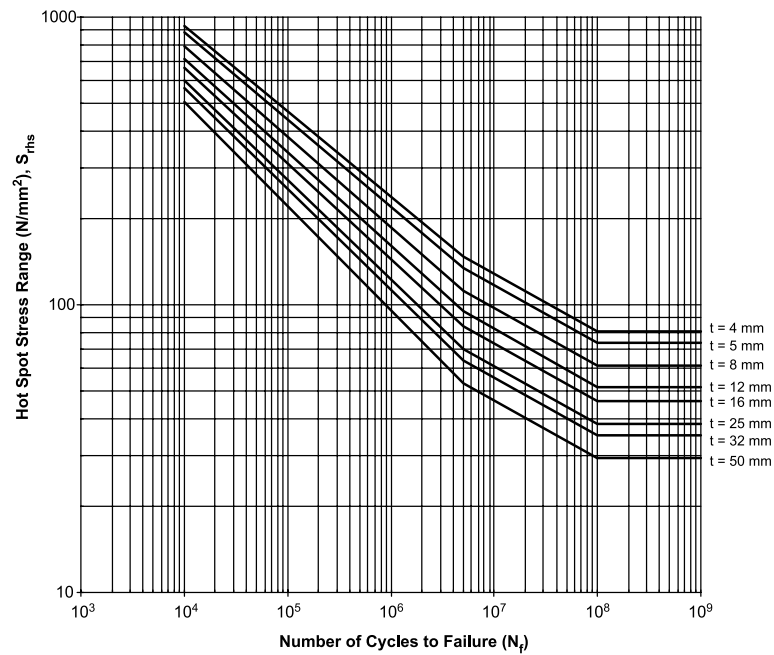


Figure 3.5: CIDECT (Wardenier et al., 2008) fatigue strength curves for CHS joints according to the hot-spot stress method.

failure of the detail. The crack propagation rate is a function of stress intensity factor (SIF) which is a measure of the intensity of the stress field in the vicinity of crack site.

The number of cycles to crack initiation is neglected in this method. Since for welded details, this phase accounts for less than 10% of the total fatigue life of the detail, it is an acceptable assumption for this type of structures. In fact, Nussbaumer and Costa Borges (2008) and Schumacher et al. (2009) showed that the fatigue crack propagation in welded K-joints can start from as early as first load cycles.

### 3.4 Prediction of crack path

Several criteria have been proposed to predict the direction in which an existing crack will grow under a mixed-mode loading. A more detailed review of these criteria can be found in Mohammadi (2008) or Richard et al. (2005). The most relevant of these criteria are presented in the following subsection. The crack kinking angles predicted by these methods are slightly different. It is implied in all these methods that  $K_{II} = 0$  at the crack tip after crack extension (ABAQUS, 2012).

### 3.4.1 Maximum Tangential stress criterion (MTS) (Erdogan and Sih, 1963)

Considering a polar coordinate system  $(r, \varphi)$  with its origin located at the crack tip and in a plane perpendicular to the crack front (as shown on Figure 3.6), the stress field close to the crack tip can be written as:

$$\sigma_{\varphi\varphi} = \frac{1}{\sqrt{2\pi r}} \cos \frac{\varphi}{2} \left( K_I \cos^2 \frac{\varphi}{2} - \frac{3}{2} K_{II} \sin \varphi \right) \tau_{r\varphi} = \frac{1}{2\sqrt{2\pi r}} \cos \frac{\varphi}{2} [K_I \sin \varphi + K_{II} (3 \cos \varphi - 1)] \quad (3.1)$$

With setting either  $\frac{\partial \sigma_{\varphi\varphi}}{\partial \varphi} = 0$  or  $\tau_{r\varphi} = 0$ , the direction of crack propagation (measured with respect to the crack plane) can be calculated:

$$\hat{\varphi} = \arccos \left( \frac{3K_{II}^2 + \sqrt{K_I^4 + 8K_I^2 K_{II}^2}}{K_I^2 + 9K_{II}^2} \right) \quad (3.2)$$

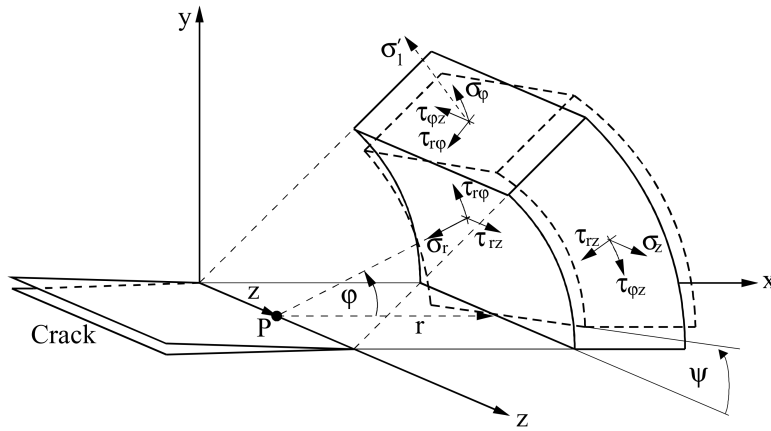


Figure 3.6: Definition of the coordinate system and stress components in the vicinity of the crack (Richard et al., 2005).

### 3.4.2 Maximum energy release rate (Nuismer, 1975)

Nuismer (1975) calculated the energy release rate  $G(\varphi)$  at the zip of a kinked crack as:

$$G(\varphi) = \frac{1 - \nu^2}{E} (K_I^{*2} + K_{II}^{*2}) \quad (3.3)$$

This criterion assumes that the crack propagation occurs in the direction of maximum energy release rate (i.e. at the  $\varphi$  angle that maximizes the G value). The resulted crack deflection angle computed by this method are identical to those of MTS criteria.

### 3.4.3 Minimum strain energy density (Sih, 1974)

According to this criterion, a crack extends in the direction of lowest energy density factor  $s_{min}$ . Strain energy density factor, S, for a homogenous isotropic material has the following form:

$$S = a_{11}K_I^2 + 2a_{12}K_I K_{II} + a_{22}K_{II}^2 + a_{33}K_{III}^2 \quad (3.4)$$

Crack growth direction happens in a direction which S value reaches a relative minimum.

### 3.4.4 Zero $K_{II}$ criterion

In this method, the in-plane stress intensity factor  $K_{II}$  is set to zero for a very small crack extension. The crack extension direction is then found based on this criterion.

## 3.5 Conclusion

This chapter provided a brief introduction to high strength steel material and presented two fatigue assessment methods used in the domain of tubular structures, namely structural hot-spot stress method and linear elastic fracture mechanics (LEFM). Crack extension prediction methods based on LEFM were discussed which will be referred to later in Chapter 7.





## 4 Residual stress measurements

### 4.1 Introduction

In this chapter, various methods of residual stress measurement are briefly reviewed with more focus on the neutron diffraction technique, which was utilized in this study. Later, the details of experiments and the evaluated residual stresses are presented.

Although modern computational and numerical tools allow for convenient estimation of service stresses of a component, this is not always sufficient for the reliable determination of component's service life. In many past cases which involved the unpredicted failure of a component, the cause of the failure has been the presence of residual stresses, which in combination with applied stresses, have diminished the service life (Withers and Bhadeshia, 2001). Thus, reliable measurement methods, such as neutron diffraction, are instrumental for assessing the residual stress state and for validating the numerical models.

Two campaigns of residual stress measurements were carried out during the course of the project: The first series of experiments focused on assessing the full strain and stress tensor in a limited number of points located on the chord's weld toe. This was done to examine whether the transversal and longitudinal stress components (in relation to the weld line) are principal stresses or not. In the second series, the distribution of only three components of residual stress field in the gap region was sought. With the larger set of data gathered in this series, more extensive validation of numerical model became possible.

#### 4.1.1 Residual stress measurement methods

Within the general domain of stress and strain measurement, residual stress measurement is considered as a specific field (Radaj, 2003). There are both destructive and non-destructive

## Chapter 4. Residual stress measurements

methods for residual stress measurement (Withers and Bhadeshia, 2001). The capabilities of some of the available methods are shown in Figure 4.1.

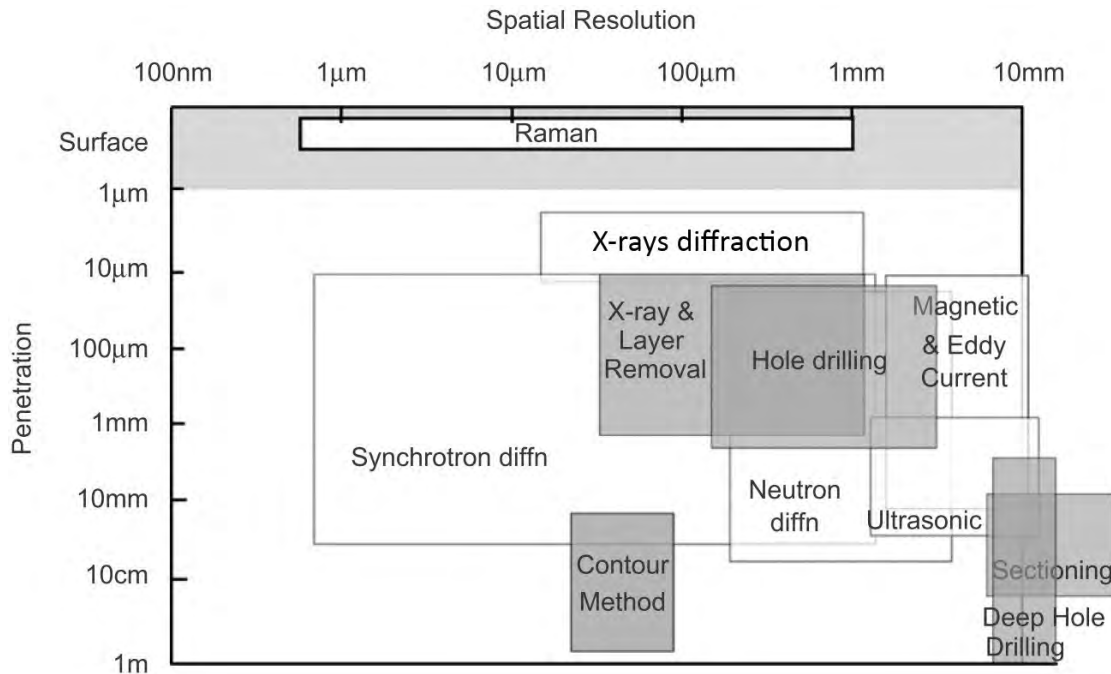


Figure 4.1: Ranges of current capabilities of available techniques of residual stress measurement. The grey shaded areas indicate destructive methods (Withers et al., 2008).

Destructive (mechanical) methods are based on making a section cut (or a hole) in the material and measuring the deformations due to the cut. The residual stress components that have been available prior to the cutting can be back-calculated based on the observed deformations in the vicinity of the cut or hole assuming elastic behavior. Care should be taken to not to change the residual stress state during the cutting by putting plastic strains into material. Another issue which may arise when dealing with residual stresses close to the yield strength, is that the release of residual stresses in one location can cause yielding in another location in the material (Withers et al., 2008). The *Standard Test Method for Determining Residual Stresses by the Hole-Drilling Strain-Gage Method* (E28 Committee, 2009) recommends checking that the measured residual stresses are below 50% of yield strength. A detailed explanation of hole-drilling method can be found in (Acevedo, 2011).

Ultrasonic techniques for stress measurement rely on the difference of ultrasonic wave travel speed in the stressed and un-stressed elastic media. Residual stresses can be deduced from this difference (Lu, 1996). Interaction between magnetization and elastic deformations in ferromagnetic materials is the basis of magnetic methods for residual stress measurement.

Barkhausen noise method, and magnetostriction<sup>1</sup> method belong to this category. Eddy current method is based on the influence of stresses on conductivity of the metallic material. While magnetic and ultrasonic methods are rapid and economic, their sensitivity to changes in the microstructure as well as to the stress state, reduces their potential for being reliably used for residual stress measurement in general application. However, they are specially suitable in manufacturing quality control applications, because of the fast measurement speed and feasibility for automation (Radaj, 2003).

The residual stress measurement using diffraction is based on the fact that the crystalline lattice can be used as a tiny strain gauge. The method works according to Bragg's diffraction principle valid for normal and high energy (synchrotron) X-rays and neutrons. This will be explained in more detail in the following sections.

## 4.2 Theory

### 4.2.1 Principles of residual stress measurement using neutron diffraction

In 1913 W.H. Bragg and his son W.L. Bragg developed Laue's finding that the structure of a crystalline can be found from the diffraction pattern it creates, to a tool for measurement of the crystalline lattice spacing using X-rays (Hutchings et al., 2005). Following the discovery of neutron by Chadwick in 1932, Shull and Brockhouse formulated the neutron scattering techniques in the late 1940s while working in the frame of Manhattan project (Fitzpatrick and Lodini, 2003).

As it can be seen in Figure 4.2, the various incident rays that are diffracted by different layers of the crystalline structure will travel different distances. As a result, the diffracted beam will consist of rays that have a phase difference between them and hence can interact constructively or destructively. The Bragg equation is derived by calculating the extra path that is travelled by the deeper rays ( $2d \sin \theta$ ) and relating it to the wavelength  $\lambda$ :

$$\lambda = 2d_{hkl} \sin \theta \quad (4.1)$$

In this relation between wavelength, lattice spacing  $d_{hkl}$  (for the reflection in the hkl plane, as in the Miller indices definition), and the diffraction angle  $\theta$ , the  $\lambda$  and  $\theta$  can be measured and therefore lattice spacing can be calculated. If one measures the lattice spacing in the

---

<sup>1</sup>Deformation of ferromagnetic materials due to the magnetization; One familiar example of this phenomena is the noise heard from a transformer which is caused by the vibration of its parts due to alternating magnetic field.

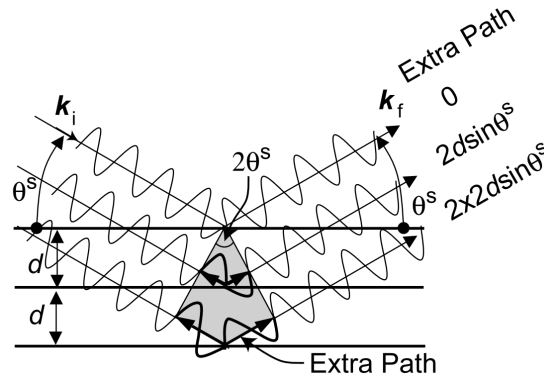


Figure 4.2: Difference in the phase of the various rays of a coherent beam inciding a crystalline structure (Bragg's rule)(Hutchings et al., 2005)

stress-free condition ( $d_{hkl}^0$ ) and compare it to lattice in the stressed condition ( $d_{hkl}$ ), the strain ( $\epsilon_{hkl}$ ) can be deduced from the following equation:

$$\epsilon_{hkl} = \frac{d_{hkl} - d_{hkl}^0}{d_{hkl}^0} = -\cot\theta \cdot (\theta - \theta^0) = -\cot\theta \cdot \Delta\theta \quad (4.2)$$

For polycrystalline materials, the diffraction technique measures the average of strains in the various grains contained within the gauge volume.

Various suggestions for selection of crystalline plane for diffraction exist (Hutchings et al., 2005; Webster, 2001). ISO VAMAS standard (Webster, 2001) recommends using 211 plane for bcc FE (body-centred cubic structure, as observed in ferrite).

Of the three available radiation sources for measuring the lattice spacing, namely electrons, x-ray photons and neutron beams, the neutrons can travel the deepest distances inside the material, before they attenuate. This is because the neutrons have zero electric charge, relatively high mass ( $m = 1.67 \times 10^{-24} \text{ g}$ ) and a small radius ( $r_0 = 6 \times 10^{-16} \text{ m}$ ) which is 5-6 order of magnitude smaller than the average size of an atom ( $10^{-10} \text{ m}$  or  $1 \text{ \AA}$ ) (Fitzpatrick and Lodini, 2003). These properties enable neutrons to penetrate within the dense matter by several millimetres or even centimetres. The wavelength of thermal neutrons<sup>2</sup> is between 1 to 3  $\text{\AA}$ . This wavelength results in a scattering angle of about  $90^\circ$ , which corresponds to a cubical gauge volume. This is in contrast to X-rays which diffract in much wider angle which results in a diamond-shaped gauge volume. Thus, as Pirling et al. (2006) point out, the deeper regions

<sup>2</sup>The kinetic energy of the neutrons is perceived as its *temperature*. Thermal neutrons are slow neutrons in thermodynamical equilibrium with their medium at ambient temperature and have an energy of  $10^{-2} \text{ eV}$  (Fitzpatrick and Lodini, 2003).

in a large or thick specimen are easier accessible when using neutron beam source.

#### 4.2.2 Calculation of stress components

In general, the full stress tensor can be evaluated by evaluating the lattice strains in different directions. Theoretically, this can be done by measuring 6 strain components in various directions. In practice, to attain a satisfactory accuracy, strains should be measured in 8 to 10 carefully selected directions, according to (Hutchings et al., 2005). For an isotropic material the Hooke's law can be written as:

$$\sigma_{ij} = \frac{E}{(1+\nu)} \left[ \epsilon_{ij} + \frac{\nu}{(1-2\nu)} (\epsilon_{11} + \epsilon_{22} + \epsilon_{33}) \right] \quad (4.3)$$

Where  $i, j = 1, 2, 3$  are the axes indices, and  $E, \nu$  are the Young's modulus and Poisson's ratio, respectively. In order to calculate the strain tensor  $\epsilon_{ij}$ , one can measure the strain component  $\epsilon_{lmn}$  (strain in the direction indicated by direction cosines  $l, m$ , and  $n$  in the orthogonal sample coordinate system), thus having:

$$\epsilon_{lmn} = l^2 \cdot \epsilon_{11} + m^2 \cdot \epsilon_{22} + n^2 \cdot \epsilon_{33} + 2lm \cdot \epsilon_{12} + 2mn \cdot \epsilon_{23} + 2nl \cdot \epsilon_{13} \quad (4.4)$$

Therefore, by measuring strain components in 6 different directions, we will have a system of 6 linear equations with 6 unknowns:

$$\begin{bmatrix} \epsilon(l_1, m_1, n_1) \\ \epsilon(l_2, m_2, n_2) \\ \epsilon(l_3, m_3, n_3) \\ \epsilon(l_4, m_4, n_4) \\ \epsilon(l_5, m_5, n_5) \\ \epsilon(l_6, m_6, n_6) \end{bmatrix} = \begin{bmatrix} l_1^2 & m_1^2 & n_1^2 & 2l_1m_1 & 2m_1n_1 & 2n_1l_1 \\ l_2^2 & m_2^2 & n_2^2 & 2l_2m_2 & 2m_2n_2 & 2n_2l_2 \\ l_3^2 & m_3^2 & n_3^2 & 2l_3m_3 & 2m_3n_3 & 2n_3l_3 \\ l_4^2 & m_4^2 & n_4^2 & 2l_4m_4 & 2m_4n_4 & 2n_4l_4 \\ l_5^2 & m_5^2 & n_5^2 & 2l_5m_5 & 2m_5n_5 & 2n_5l_5 \\ l_6^2 & m_6^2 & n_6^2 & 2l_6m_6 & 2m_6n_6 & 2n_6l_6 \end{bmatrix} \times \begin{bmatrix} \epsilon_{11} \\ \epsilon_{22} \\ \epsilon_{33} \\ \epsilon_{12} \\ \epsilon_{23} \\ \epsilon_{13} \end{bmatrix} \quad (4.5)$$

Solving this system of equations yields the strain, and from there stress tensor. Note that if we measure the strain in three mutually perpendicular directions, we still can use Equation 4.3 to calculate the stresses in those directions, but we will not know whether these stresses are principal stresses or not.

In the case of measurement directions being mutually perpendicular, the set of three linear

equations of 4.5 can be separated and easily solved:

$$\sigma_{xx} = \frac{E}{1+\nu} \cdot \left( \epsilon_{xx} + \frac{\nu}{1-2\nu} (\epsilon_{xx} + \epsilon_{yy} + \epsilon_{zz}) \right) \quad (4.6)$$

$$\sigma_{yy} = \frac{E}{1+\nu} \cdot \left( \epsilon_{yy} + \frac{\nu}{1-2\nu} (\epsilon_{xx} + \epsilon_{yy} + \epsilon_{zz}) \right) \quad (4.7)$$

$$\sigma_{zz} = \frac{E}{1+\nu} \cdot \left( \epsilon_{zz} + \frac{\nu}{1-2\nu} (\epsilon_{xx} + \epsilon_{yy} + \epsilon_{zz}) \right) \quad (4.8)$$

## 4.3 Method

### 4.3.1 Specimens

The specimens were taken from fatigue-tested trusses S7-355, S10-690, and S11-690, as will be described in Chapter 5. The characteristics of the specimens are summarized in Table 4.1. Since the specimens were welded during the fabrication of the trusses with the same welding procedure specifications as of the other nodes, their residual stress state can be representative of the residual stress field in any of the cracked joints of the corresponding truss. Having the specimens on the fatigue-tested truss means that the effect of stress relaxation is taken into consideration (but obviously the extracted joints were not loaded on braces and were not cracked, c.f. Section 5.3.1). The material for the first sample was constructional steel S355J2H and the two following samples were made of high strength steel grade S690QH. The chemical compositions of the two steel types are shown in Table 4.2. Figure 4.3 shows the fatigue-tested truss with the extracted specimen. It was known from the fatigue tests that the cracking site is located at the weld toes on the chords in the gap region. Therefore, the residual stress measurements focused on this zone.

Table 4.1: Specifications of the specimens

Specimen	Steel grade	Chord [mm]	Braces [mm]	Gap size [mm]
S7-355	355J2H	168.3 × 30	88.9 × 8	30
S10-690	690QH	193.4 × 20	101.6 × 8	18
S11-690	690QH	193.4 × 20	101.6 × 8	22.5

As mentioned in section 4.1, for the first sample (S7-355), the aim was to determine the residual stress principal directions. This would help to understand firstly the amount of error introduced by the assumption of the transverse stress (stress component perpendicular to the weld line) as principal stress, and secondly, how the direction of maximum principal residual stress affects the crack propagation. For this, capturing the full strain tensor was necessary.

### 4.3. Method

Table 4.2: Chemical composition of steel S355J2H and S690QH. Values are given as % of weight

		Chemical composition of S355J2H		Chemical composition of S690QH	
Element		Nominal max % (EN 10210)	Effective avg. mass % (V&M analysis)	Nominal max % (EN 10210)	Effective avg. mass % (V&M analysis)
Carbon	C	0.180	0.170	0.200	0.150
Silicon	Si	0.550	0.260	0.600	0.290
Manganese	Mn	1.60	1.36	1.70	1.54
Phosphorus	P	0.030	0.010	0.025	0.010
Sulfur	S	0.0300	0.0040	0.0150	0.0010
Aluminum	Al	0.100	0.030	0.060	0.026
Copper	Cu	0.400	0.060	0.500	0.060
Chromium	Cr	0.100	0.050	1.500	0.700
Nickel	Ni	0.300	0.040	1.500	0.100
Molybdenum	Mo	0.080	0.005	0.700	0.210
Vanadium	V	—	0.043	0.140	0.070
Tin	Sn	—	—	—	0.0040
Titanium	Ti	0.050	0.001	0.050	0.005
Niobium/ Columbium	Nb/Cb	—	0.002	0.050	0.032
Nitrogen	N	—	0.0070	0.0200	0.0063
Boron	B	0.0008	0.0002	N/A	N/A

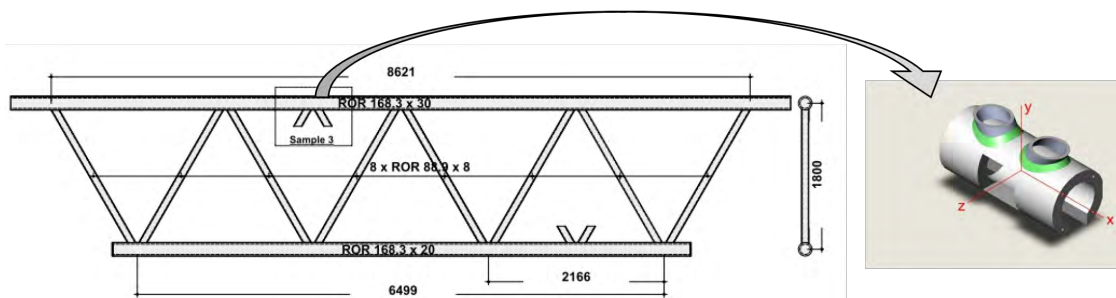


Figure 4.3: The fatigue tested truss and the extracted specimen.

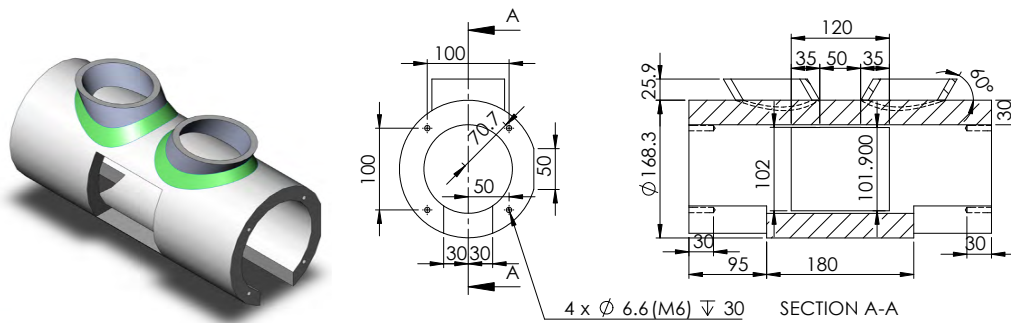


Figure 4.4: Geometry of specimen used for the ND measurement (S7-355). The weld lines are only shown in the 3D rendering.

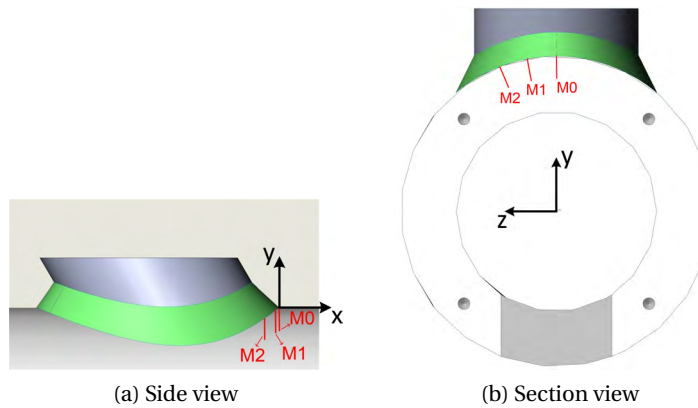


Figure 4.5: Measurement locations on the chord's weld toe (Specimen S7-355).

Specimen dimensions are shown in Figure 4.4. Figure 4.7 shows the dimensions of specimens used for second campaign of measurements (strain scanning) which will be discussed in section 4.4.3. Three locations M0, M1, and M2 on specimen S7-355 were selected, as shown in Figure 4.5. M0 is located on the symmetry (xy) plane of the connection. M1 and M2 are on planes rotated 12.5° and 25° around the y-axis, respectively. This allows the study of evolution of residual stresses along the weld line at the vicinity of the cracking site. The measurements were carried out at 6 different depths from the outer surface of the tube, namely 2, 2.5, 3, 6, 10, and 12mm (center of gauge volume). The neutron beam had to pass the tube wall at the locations opposite to the studied points. But its travel distance inside the steel material must be limited and the longer, the more background noise in the reflected beam. To bypass this limitation, two openings were created in the tube wall to let through the neutron beam. This is shown in Figure 4.6.





### 4.3.2 Apparatus

#### Neutron source

Two laboratory sources for neutrons are available: one is the continuous neutron flux from the fission in a nuclear reactor, and the other source is the pulses of high energy neutrons produced by spallation (Hughes et al., 2002). Figure 4.8 illustrates the experimental setup for the case of continuous neutron flux (reactor source). In this case, the diffraction angle  $\theta$  of a monochromatic neutron beam is measured in the detector and  $d_{hkl}$ , corresponding to the strains in the direction of vector  $Q$ , is evaluated, as stated before.

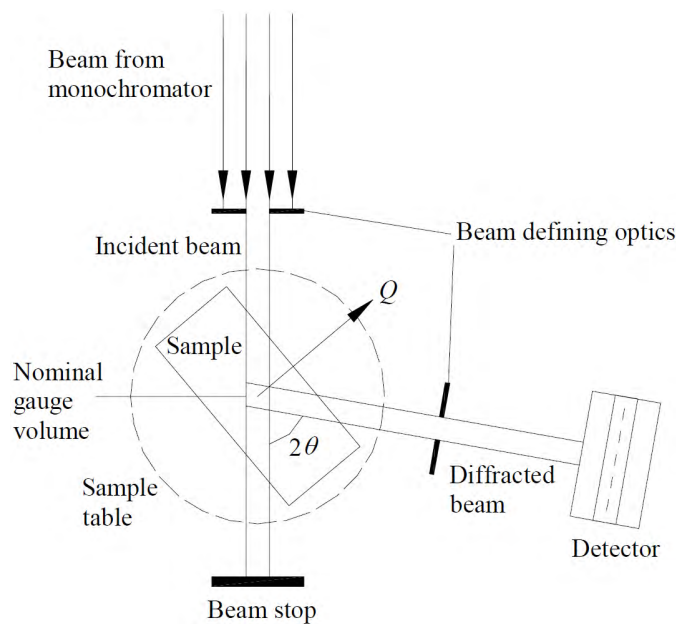


Figure 4.8: Experiment setup for continuous neutron beam instrument (Webster, 2001)

The experiments were conducted using SALSA facility (Hughes et al., 2006) in ILL (Institut Laue Langevin) located in Grenoble and which, with its 58.3MW fission reactor, produces the world's most intense continuous neutron flux of  $1.5 \times 10^{15} \text{ Neutrons/s/cm}^2$ . The produced neutron beam is then moderated to get the neutrons with energy and wavelength in the desired range. The beam wavelength was  $\lambda = 1.642 \times 10^{-10} \text{ m}$  and Fe 211 reflection was selected as it was used in similar studies (Acevedo et al., 2012). To cut the long measurement times and to attain a satisfactory spatial resolution, a cubic gauge volume of  $2 \times 2 \times 2 \text{ mm}^3$  was selected for measurements.

#### Specimen manipulator

The specimen manipulation was done by Hexapod (Pirling et al., 2006), which is a Gough-Stewart platform, able to perform translations and rotations in all three directions (See Figure 4.9). This robotic platform was an essential part of the measurement because of its flexibility

to position the tubular sample in non-orthogonal orientations, as for the two positions shown in Figure 4.9a and b.

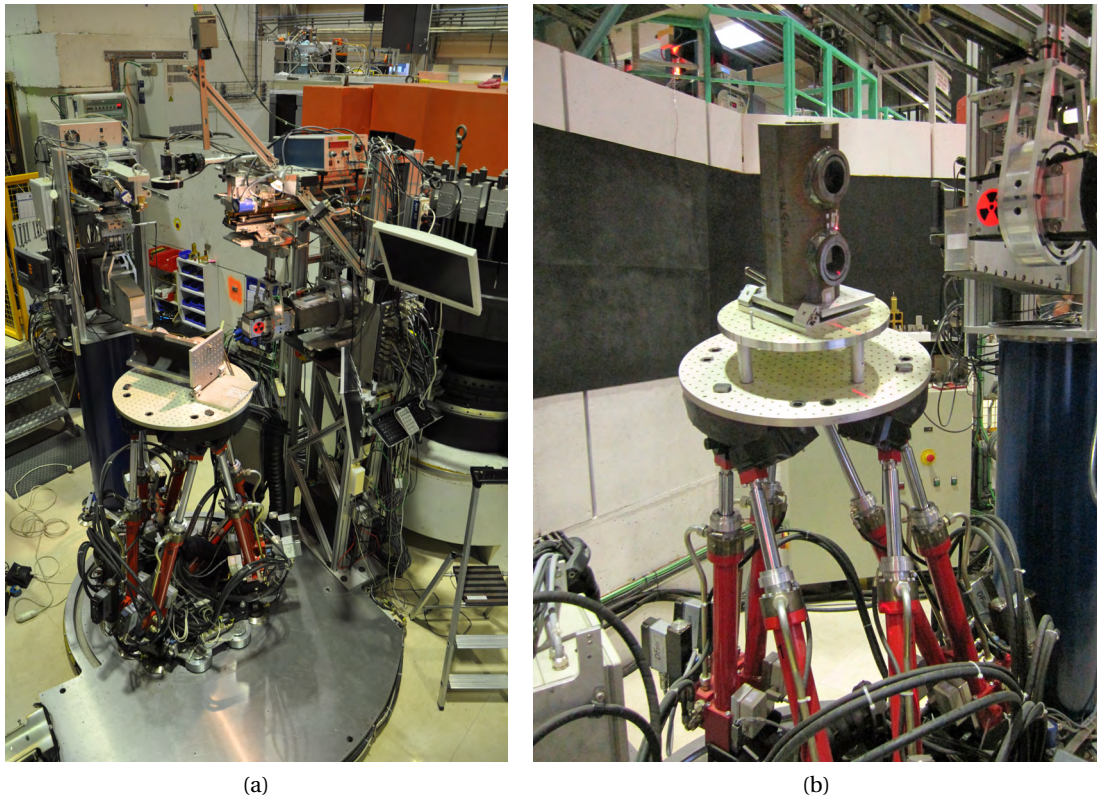


Figure 4.9: Hexapod platform with the specimen mounted on it.

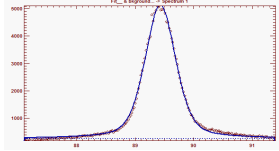
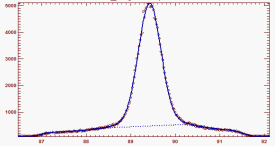
## 4.4 Results

### 4.4.1 Reference lattice spacing

Measurement of either lattice spacing ( $d_0$ ) or diffraction angle ( $\theta_0$ ) in the stress-free condition was needed for calculation of strains (c.f. Equation 4.2). Two types of stress-free specimens were selected, according to ISO VAMAS (Webster, 2001) recommendations: a cube made by gluing together smaller cubes of  $1\text{ mm}$  dimension which were cut by electro-discharge method (Figure 4.10a), and a comb specimen produced by making cuts on a slice cut out of the tubular joint at the crown toe location (Figure 4.10b) with a thickness of  $8\text{ mm}$ . Although the  $\theta_0$ -values resulted from the two were close, the values from the cubic specimen were selected for subsequent calculations, because it better satisfies the stress-free conditions. Table 4.3 summarizes the reference lattice spacing measurement for the two samples, as well as the case of considering pooled measurement data of the two samples (i.e. results obtained by combining the datasets from the two measurements). The background noise reduction will be addressed later in section 4.4.3.

## Chapter 4. Residual stress measurements

Table 4.3: Measurement of Reference lattice spacing ( $d_0$ ) on two different samples

Background correction		Comb	Cube	Pooled data <sup>†</sup>	Intensity graph
Flat background	$\mu_{\theta_0}$ <sup>††</sup>	89.42920	89.43914	89.43059	
	$SD_{\theta_0}$ <sup>††</sup>	0.00119	0.00195	0.00118	
Nonlinear background	$\mu_{\theta_0}$	89.42577	<b>89.43629</b>	89.42722	
	$SD_{\theta_0}$	0.00075	0.00153	0.00072	

<sup>†</sup> Pooled data consists of datasets from the two (comb and cube) measurements.

<sup>††</sup>  $\mu_{\theta_0}$  and  $SD_{\theta_0}$  are mean and standard deviation of  $\theta_0$  measurements, respectively.

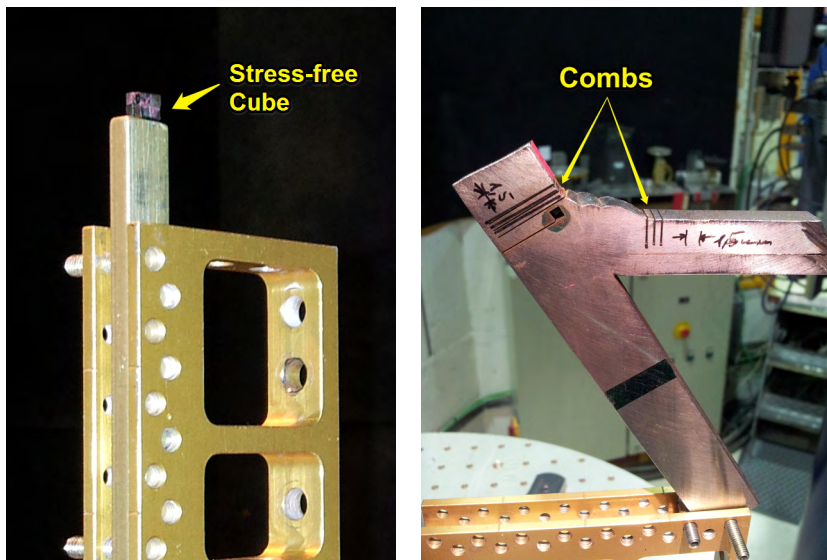


Figure 4.10: Cube and Comb stress-free samples to measure  $d_0$ .

#### 4.4.2 Estimation of full strain tensor (S7-355 specimen)

Residual strains were measured in 5 to 8 different directions at each of 18 measurement locations. As an example, table 4.4 summarizes the data gathered during the strain measurements for a point at location M1 and at the depth of  $2\text{mm}$  from the chord surface. Pseudo-Voigt profiles were fitted to the diffraction data to find the diffraction peaks.

Table 4.4: Scattering angle and corresponding strain results for location M1 at the depth of  $2\text{mm}$  from the tube surface.

$\alpha$	$\beta$	$\gamma$	$\theta$	$\delta(2\theta)$	$\mu\epsilon$	$\delta\epsilon$
0	90	90	$89.52251^\circ$	$0.00296^\circ$	-284	24
90	90	0	$89.45187^\circ$	$0.00935^\circ$	336	76
10.8	90	79.2	$89.52227^\circ$	$0.00266^\circ$	-276	22
90	0	90	$89.34052^\circ$	$0.00813^\circ$	1325	68
100.8	90	10.8	$89.44777^\circ$	$0.00576^\circ$	373	55
99.3	101.7	15	$89.38370^\circ$	$0.01880^\circ$	907	182
16.9	78	78.3	$89.52325^\circ$	$0.00238^\circ$	-293	21
75.8	18.6	101.7	$88.93322^\circ$	$0.04269^\circ$	4956	414

$\alpha$ ,  $\beta$ , and  $\gamma$  are the angles of the scattering vector with the x, y, and z axes, respectively, in the specimen global coordinate system (see Figure 4.5).

These measurements were used in a least-squares procedure using Moore-Penrose matrix inversion algorithm implemented in MATLAB to find the residual stress tensors. Having the residual stress tensors, the principal stresses and the principal directions could be calculated. The propagation of the peak-fitting errors for the diffraction angles into the calculated principal residual stresses can not be estimated by a simple analytic formula. Hence, the propagation of the error was assessed by means of Monte-Carlo simulation. For the directions of principal stresses, only the mean values of the estimated stress tensors were considered. Figures 4.11 to 4.13 show the profiles of the deduced principal residual stresses in the three investigated locations. The principal residual stress values close to the surface were slightly higher than the nominal yield strength ( $f_y = 355\text{ MPa}$ ). As it can be seen, the accuracy of the measurements in some points (e.g. M2 location) were not satisfactory. The improvement of the results in these points can be achieved by increasing the number of the directions in which the strains are measured (between 8 to 10 directions per point).

Measured strain tensors are visualized by ellipsoid glyphs in Figure 4.14, as described by (Yaman et al., 2007). Direction and size of the axes of the stress ellipsoids show direction and magnitude of principal residual stresses, respectively. As can be seen, the direction of two largest principal stresses at each point are generally perpendicular to the weld line and transversal to it. For the point M0 at crown toe, longitudinal principal stress is slightly larger than the transversal component. Longitudinal principal stress component at this point coincides the tangent to the weld with a good accuracy, while the transverse component is

**Chapter 4. Residual stress measurements**

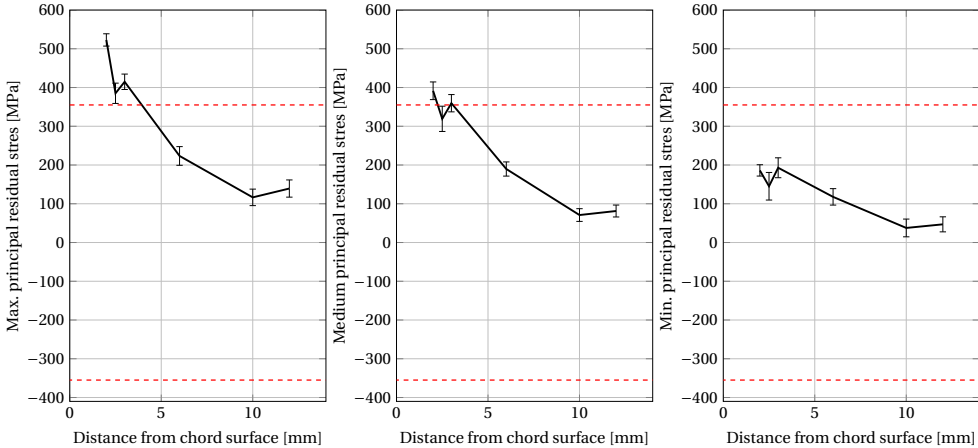


Figure 4.11: Through-thickness profiles of the principal residual stresses at point M0; horizontal dashed lines indicate nominal yield stress value of S355.

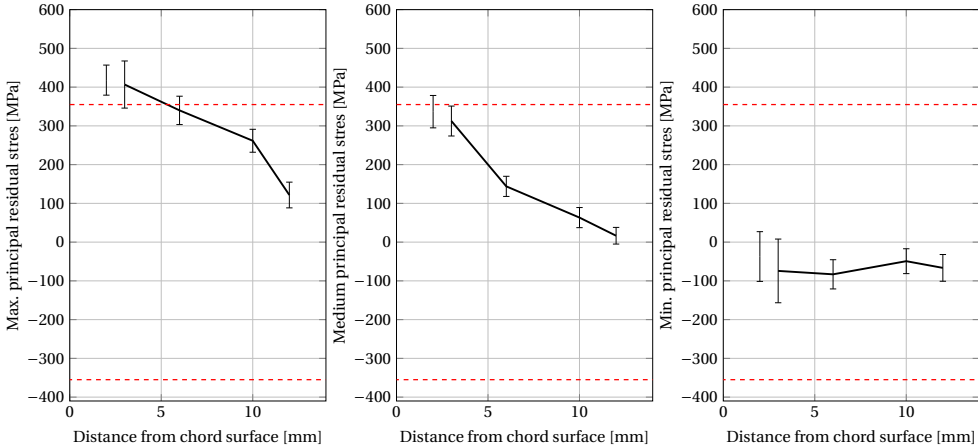


Figure 4.12: Through-thickness profiles of the principal residual stresses at point M1; horizontal dashed lines indicate nominal yield stress value of S355. Measurements in 2.5mm depth were removed from dataset due to high measurement error at that location.



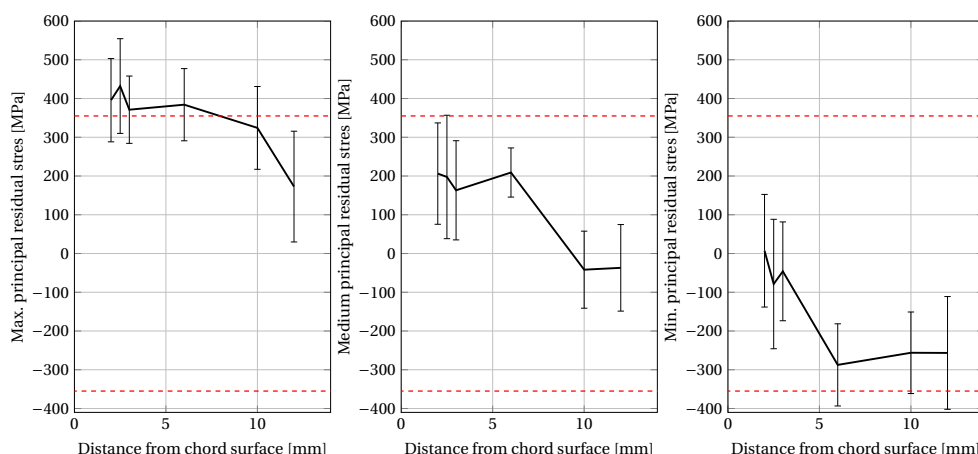


Figure 4.13: Through-thickness profiles of the principal residual stresses at point M2; horizontal dashed lines indicate nominal yield stress value of S355.

off by a range of  $0^\circ$  to  $25^\circ$ . This verifies that in general the assumption that principal stress directions at the crown toe are the same as longitudinal, tangential, and radial directions is a valid assumption. Numeric values of principal residual stresses and principal residual stress axes for all measurement points are presented in Appendix E.

#### 4.4.3 Strain scanning measurements (S10-690 and S11-690 samples)

For the second campaign of measurement, the scanning of three eigenstrain (residual strain) components in the gap region was of more interest. This was selected mainly because the strain values were required for the validation of the numerical model. Limited data is available in the literature for the residual stress measurement of welded tubular K-joints, such as work of Acevedo et al. (2012). Measurements of residual strains were made in three mutually perpendicular sample directions X(transverse - across the welding direction), Y (radial - normal to the surface of the chord), and Z (longitudinal - along the direction of welding) for two specimens extracted from S10 and S11, similar to the procedure described earlier in previous section. With the experience acquired from measurements described in the previous section, it was known that – with an acceptable tolerance – the selected measurement directions were the same as principal residual stresses at crown toe. The geometry of the specimens is shown in Figure 4.7. The locations of measurement points in the gap region for S10 specimen are shown in Figure 4.15. The measurements were carried out at depths 2, 2.5, 3.0, 3.5, 4.0, 4.5, 5.0, 5.5, 6.0, 7.0, 8.0, 9.0, 11.0, 13.0, 15.0, and 17.0mm for specimen S10, and 2, 2.5, 3, 3.5, 4, 5, 6, and 10mm for sample S11. As can be seen in the Figure, we also measured the residual stresses in the weld root region for specimen S10. The gap distances for the two specimens were slightly different (18.0mm for S10 and 22.50mm for S11) and the measurement grid was modified accordingly to accommodate this change.

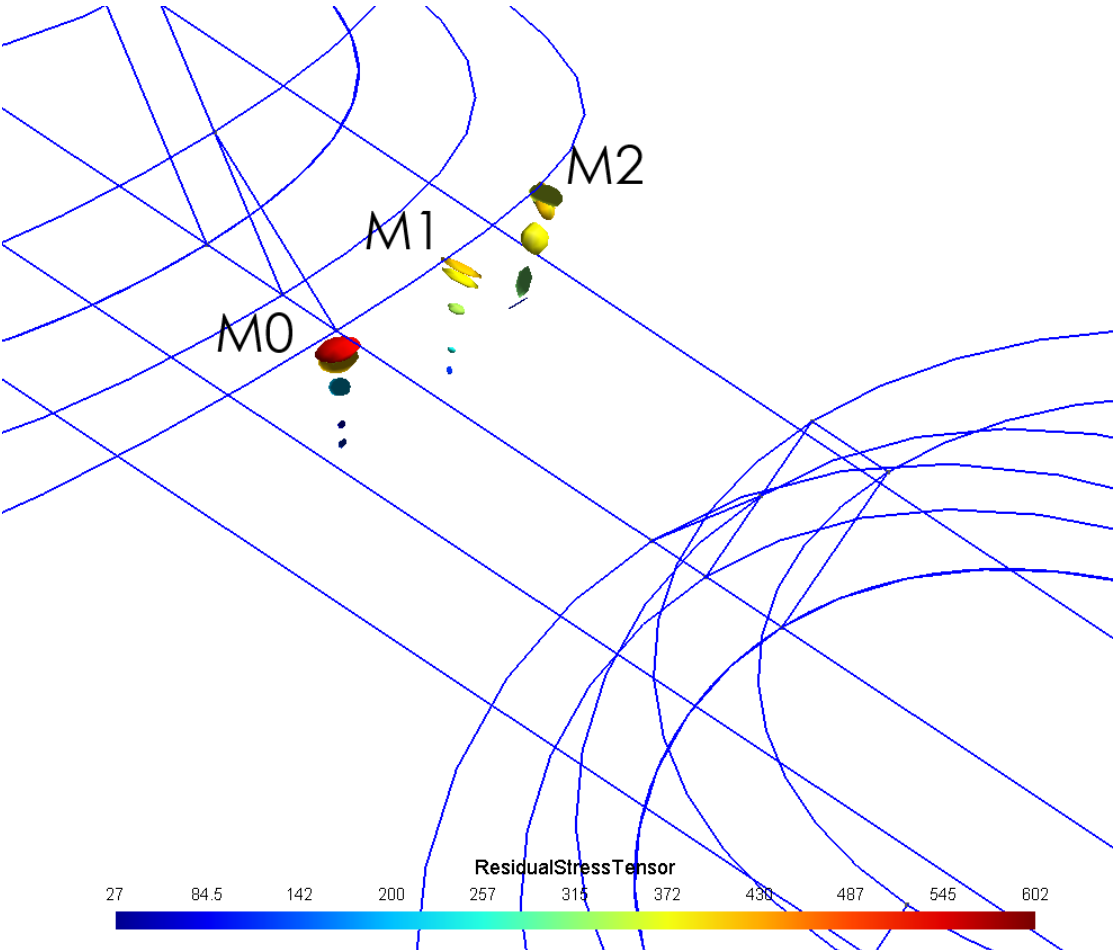


Figure 4.14: Measured residual stress ellipsoids on specimen S7-355 superposed on a wire-frame model of the joint.



To improve the peak-fitting of the diffraction data, non-linearity of the background noise, which is a characteristic of the test apparatus, was taken into consideration. The nonlinear background function generated for this set of measurements can be seen in Figure 4.16. The impact of selection of nonlinear background function can be compared to that of the flat background function in Figure 4.17. The difference in measurement of diffraction angle  $\theta$  is very small ( $0.0033^\circ$ ) but can lead to a change of  $50\text{MPa}$  in the measured stress values.

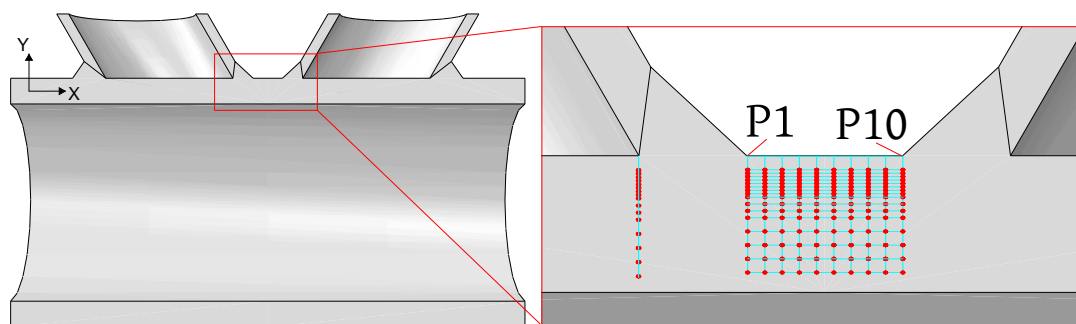


Figure 4.15: Locations of measurements for the specimen S10-690 (Weld backing ring not shown in the drawing).

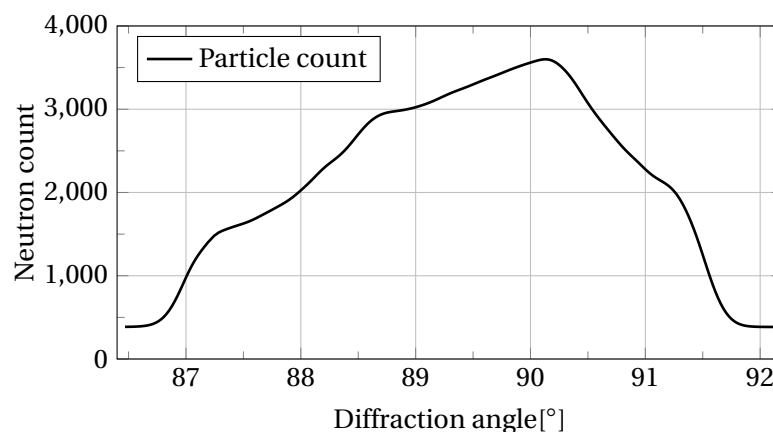
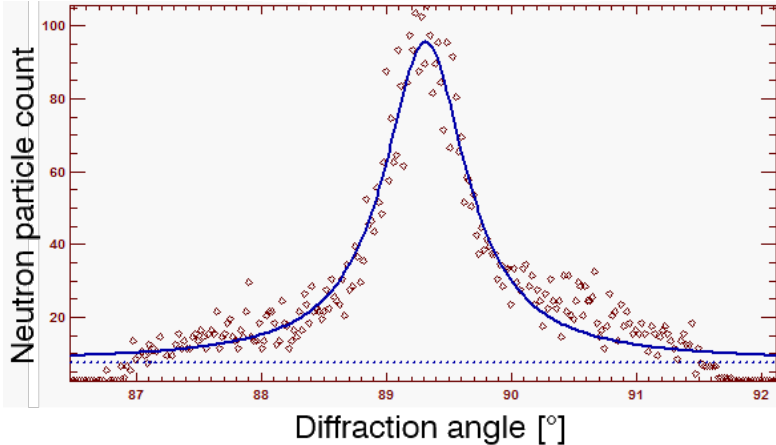
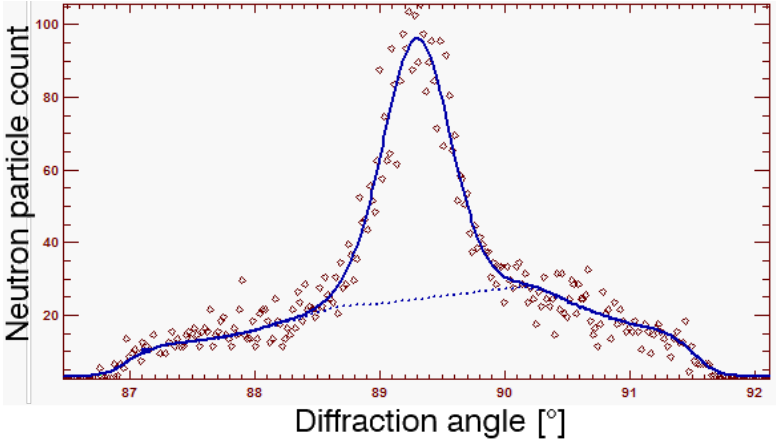


Figure 4.16: Nonlinear background function used for the peak-fitting.

Figures 4.18 and 4.19 show the measured residual stress fields at the gap region for the two specimens S10 and S11, respectively. Three residual stress components, namely transverse (perpendicular to the weld), longitudinal (parallel to the weld line), and radial (along the radial direction of the tube) components are shown in the figures. The von Mises stress calculated from these three components is also computed and shown as a measure for closeness of the residual stress state to the yield surface. The ratio of maximum von Mises residual stress to nominal yield stress ( $f_y = 690\text{ MPa}$ )  $\frac{\sigma_{vM,max}}{f_y}$  is low (approximately 50%) for both specimens which means the yielding is unlikely to happen for small external loading due to superposition of residual and applied stresses. Largest transversal and longitudinal stress values in the gap region occur at the vicinity of the weld toes, and their values are  $468\text{ MPa}$  and  $409\text{ MPa}$ ,



(a) Flat background ( $\theta = 89.4292$ ).



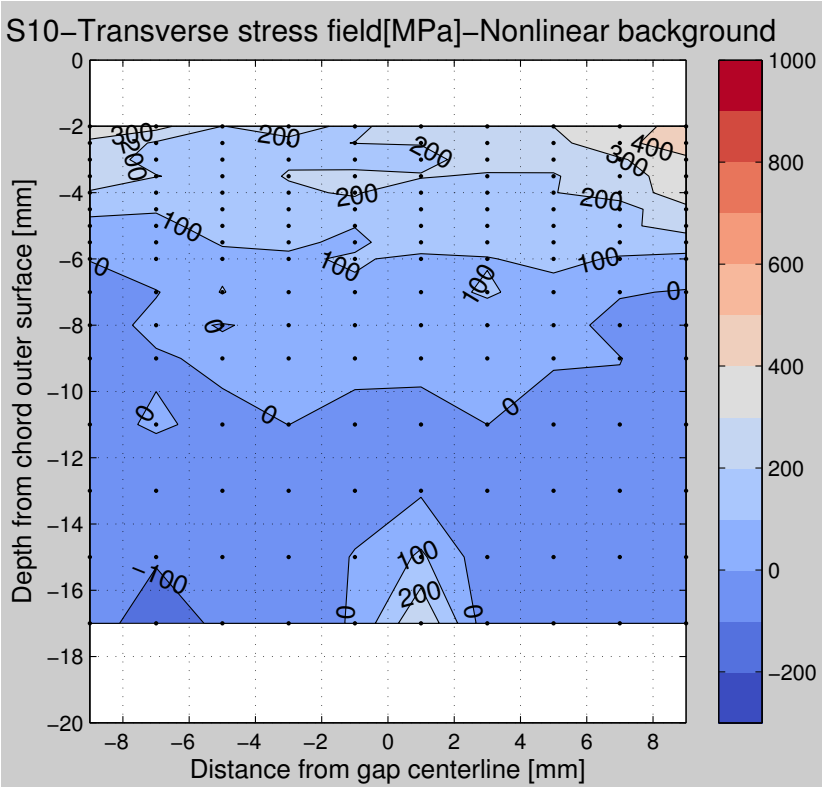
(b) Nonlinear background ( $\theta = 89.4258$ ).

Figure 4.17: Effect of selected background function on the result of peak-fitting.

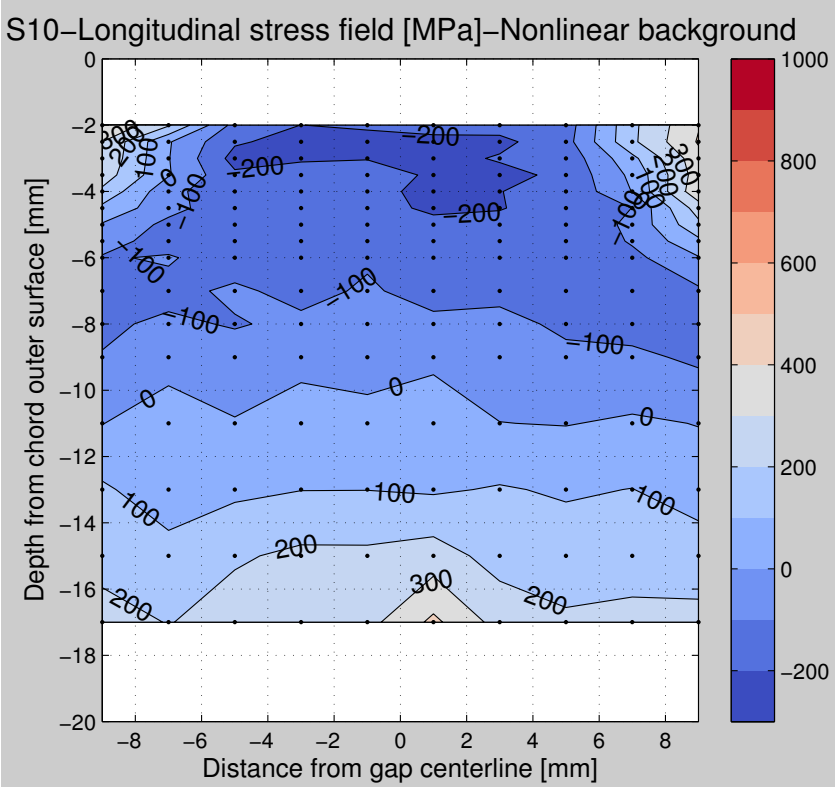
respectively.

The through-thickness residual stress profiles in points S10-P1 (left weld toe) and S10-P10 (right weld toe) are presented in Figure 4.20(a). The magnitude of longitudinal stress in these points is comparable with the magnitude of the transversal stress. The largest transverse stress values registered are about 60% of nominal  $f_y$ . The difference in the stress values between left and right weld toes is marginal. Figure 4.20(b) shows the estimated residual stress profile in the weld root close to the left weld toe (close to Point P1). According to numerical welding simulations (see Chapter 6), we would expect compressive stresses, or small tensile stresses in this region. But the profile shows peculiar high tensile stresses at this region. The error can be traced back to the high background noise in diffraction pattern (Figure 4.21) because of excessive travel distance of the neutron beam inside the steel media. The poor accuracy of the peak-fitting renders the results in this location unusable. The minimum acceptable peak-to-noise ratio of 4 was not attained at this location.

Finally, through-thickness profiles for three components (transversal, longitudinal, and radial components) of residual stresses are presented in Figure 4.22. These profiles are compared with previous measurements on S355J2H carried out by Acevedo (2011) and with scatter range given by BS 7910 (2005) standard. While they measured profiles still fit within the scatter band given by BS7910, it can be noticed that – specially for the case of transverse residual stresses – the measured values for S690QH and S355J2H tubular joints are comparable. In other words, the residual stress values are not proportional to the nominal yield stress for the studied cases here.

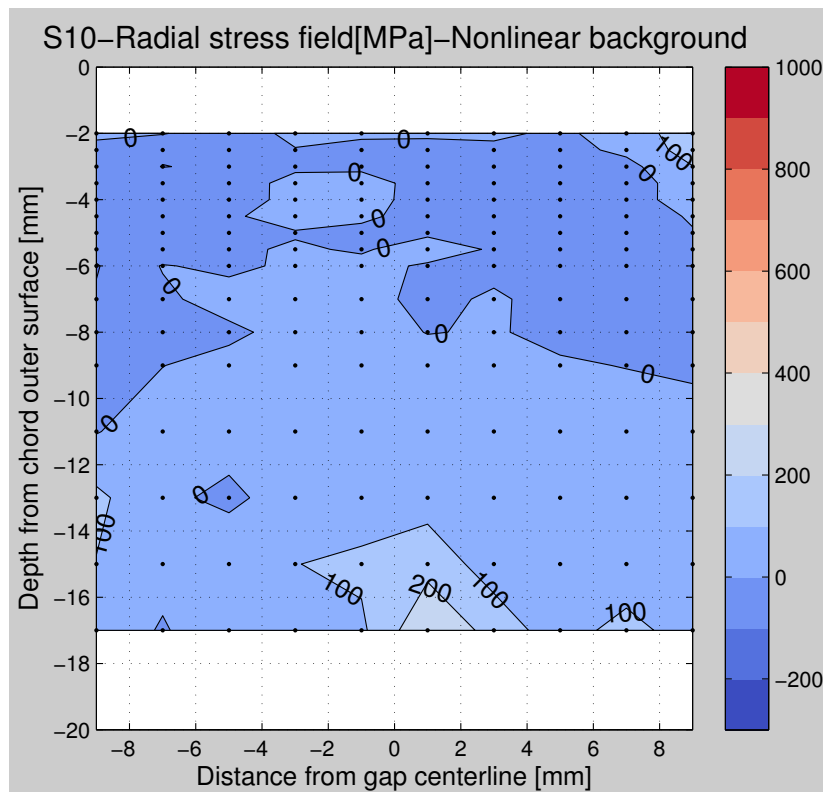


(a) Transverse component.

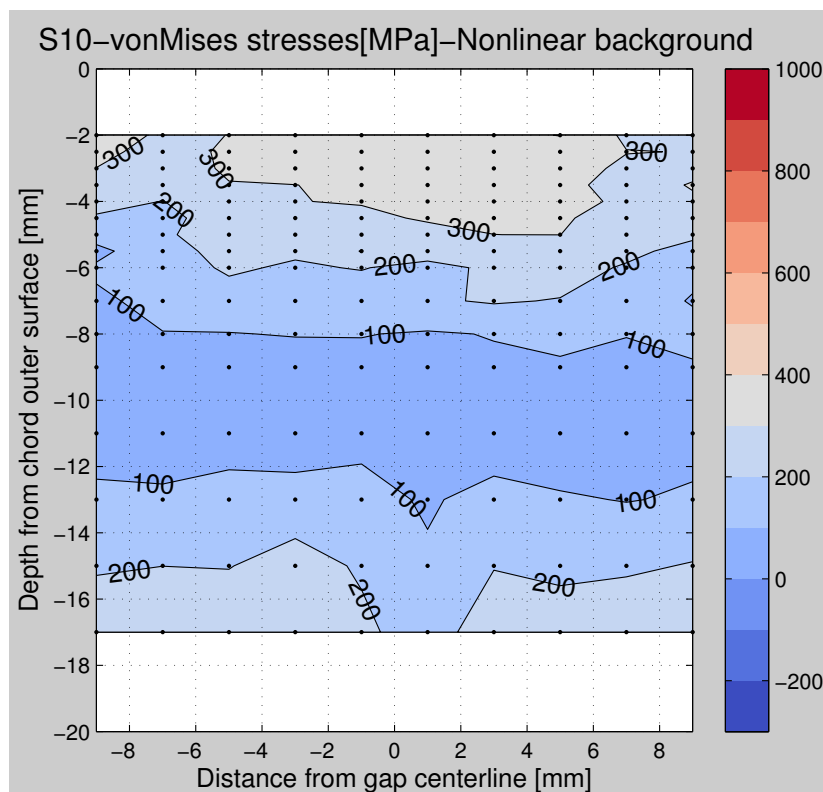


(b) Longitudinal component.

Figure 4.18: Evaluated residual stress field components for specimen S10.

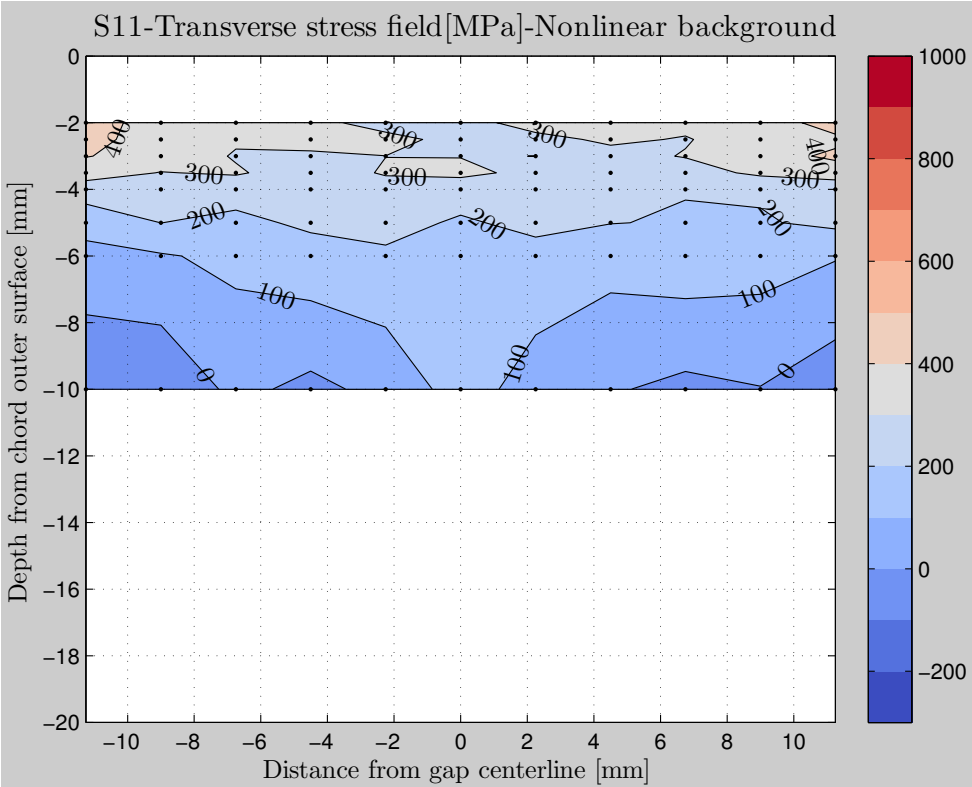


(c) Radial component.

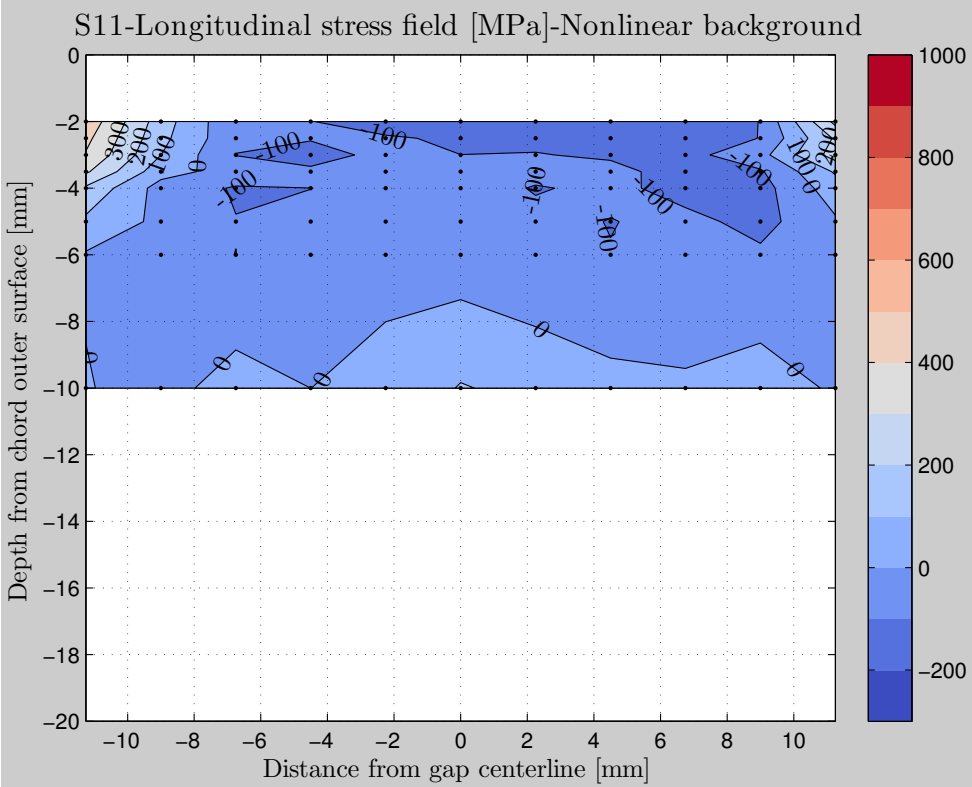


(d) Equivalent von Mises stress.

Figure 4.18: (Continued) Evaluated residual stress field components for specimen S10. 51

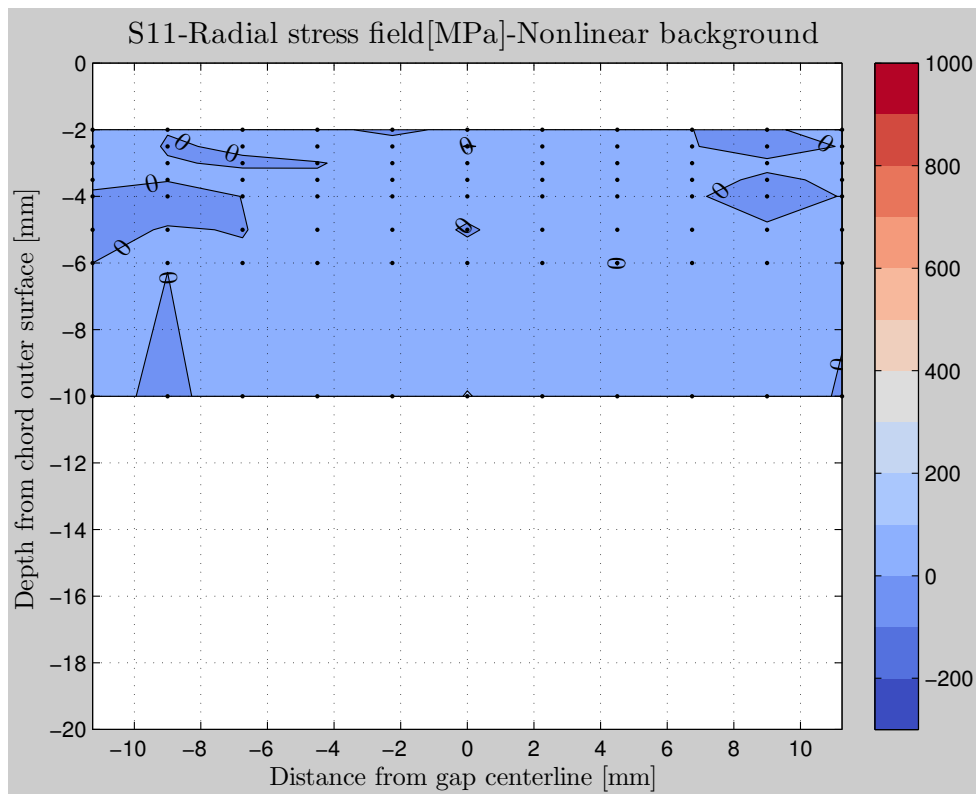


(a) Transverse component.

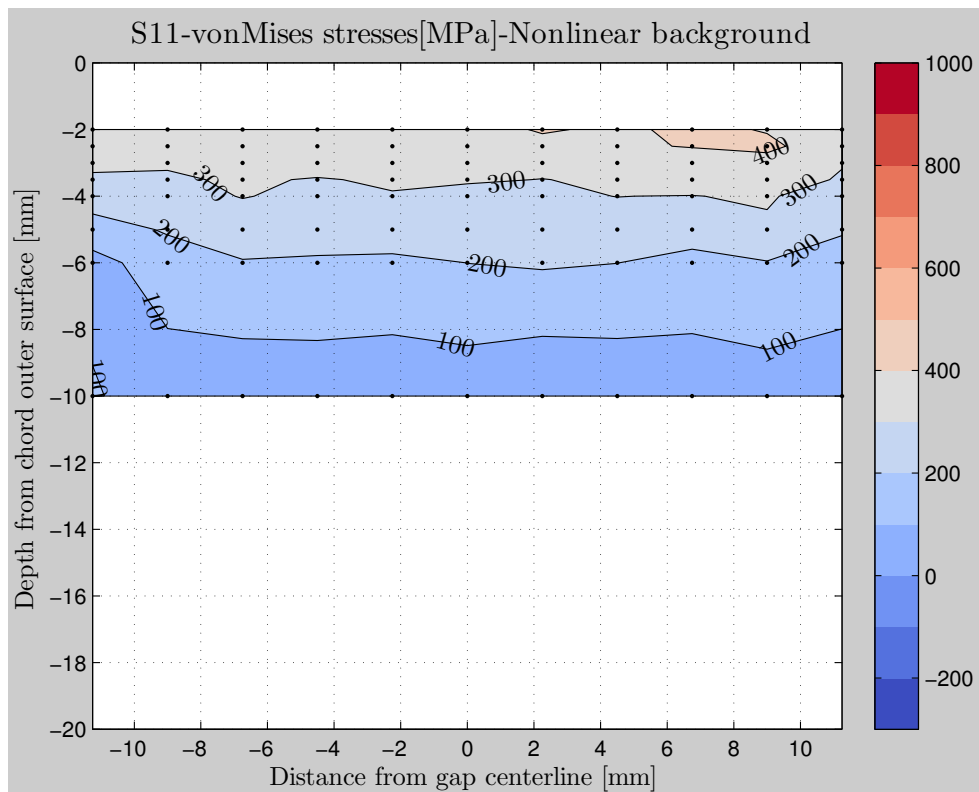


(b) Longitudinal component.

Figure 4.19: Evaluated residual stress field components for specimen S11.



(c) Radial component.



(d) Equivalent von Mises stress.

Figure 4.19: (Continued) Evaluated residual stress field components for specimen S11. 53

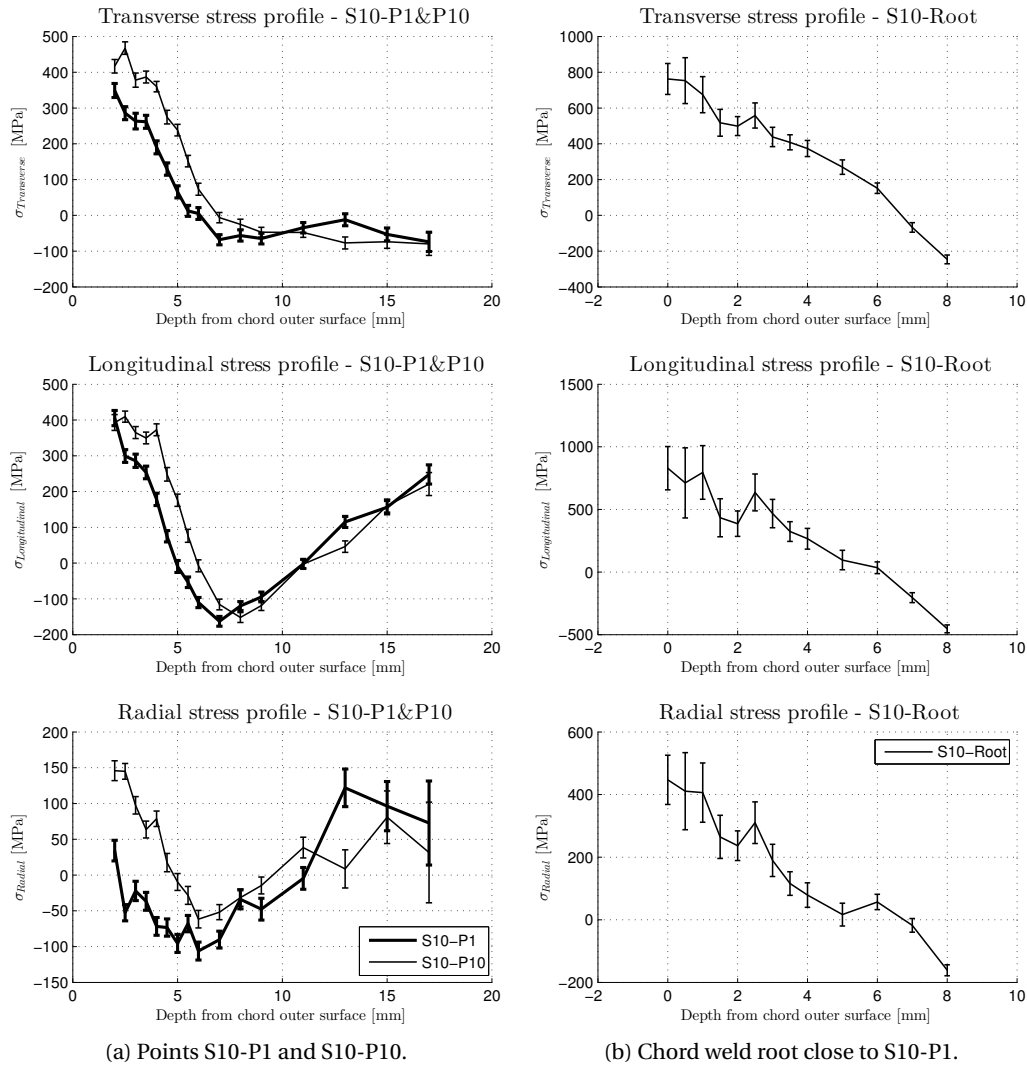


Figure 4.20: Residual stress profiles for selected points on S10. Note that for the weld root measurements, the high background noise prevented getting reliable measurements.

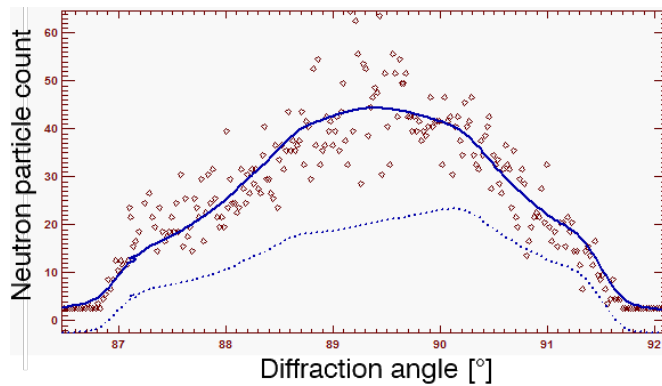


Figure 4.21: High signal-to-noise ratio resulting in a poor peak fit for the left weld root.



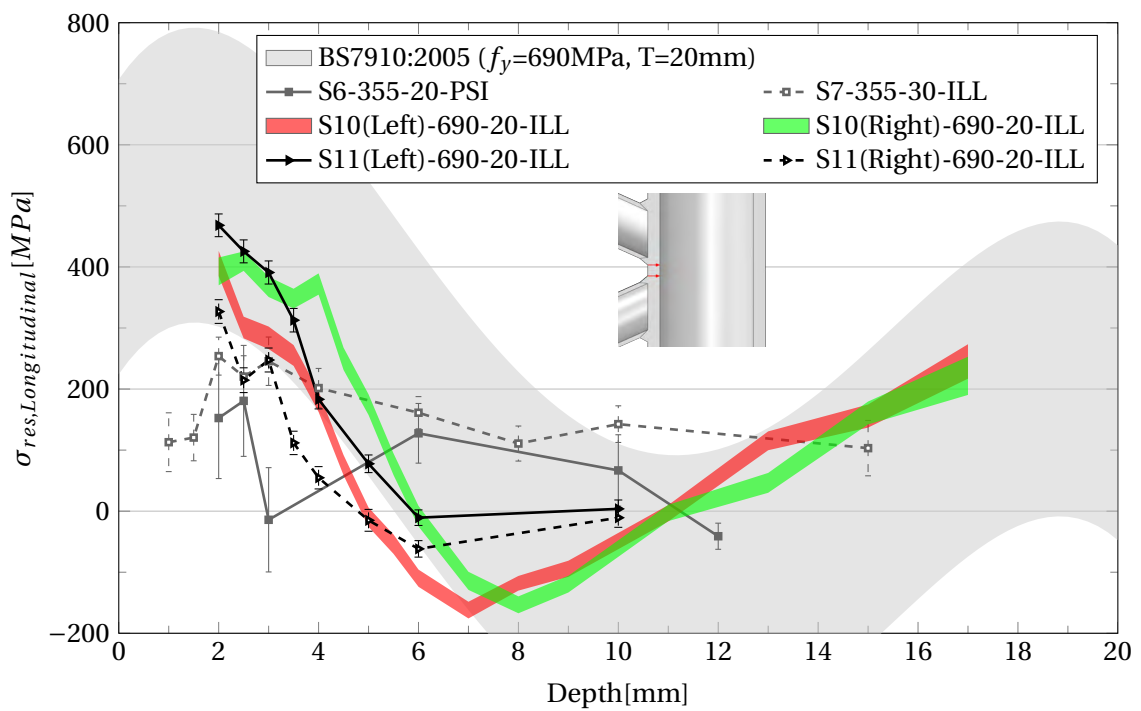
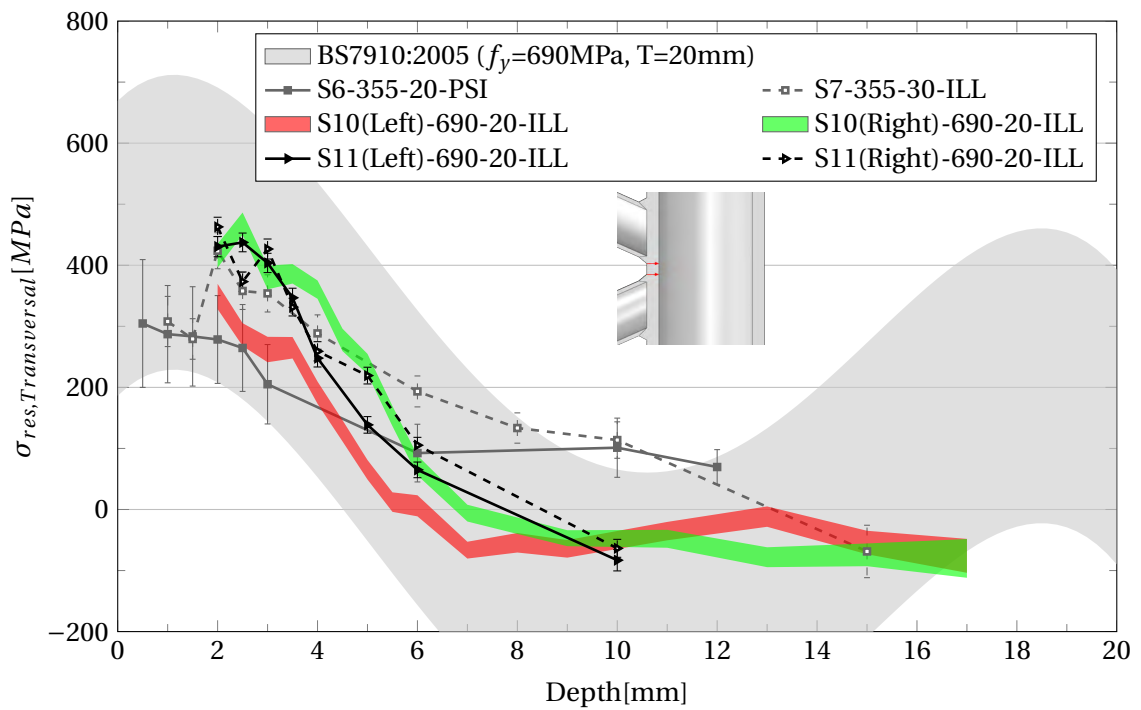
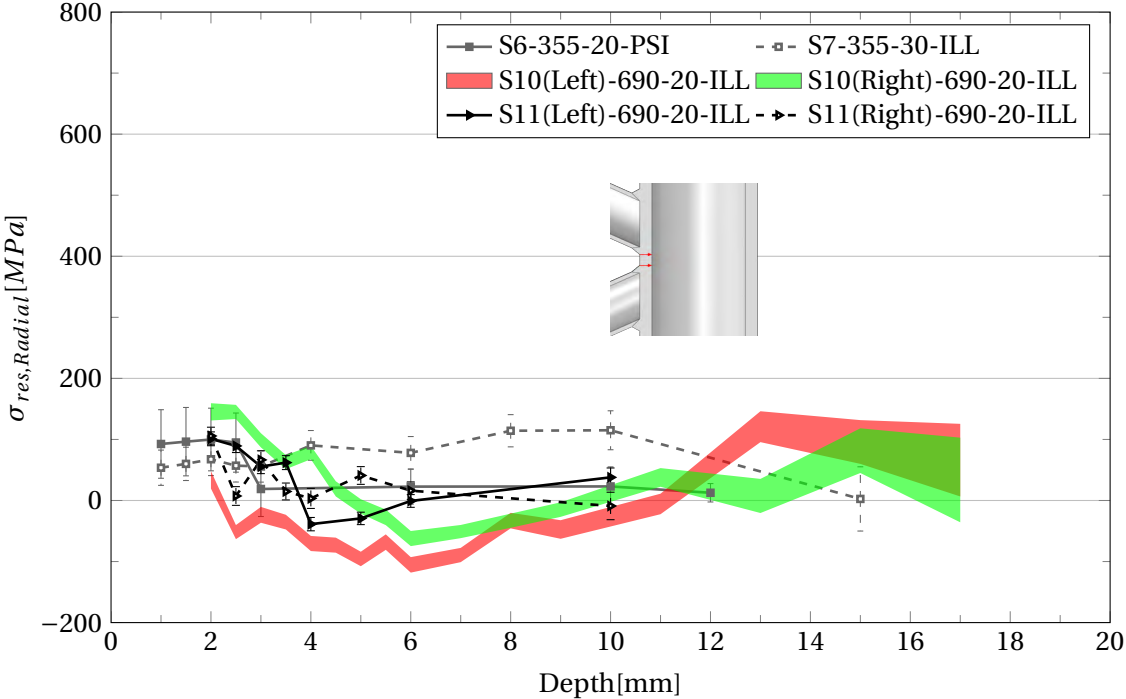


Figure 4.22: Residual stress profiles obtained from several neutron diffraction measurements. Shaded area shows the range of stresses proposed by the code (BS 7910, 2005).



(c) Radial component

Figure 4.22: (Continued) Residual stress profiles obtained from several neutron diffraction measurements.

### 4.5 Conclusion

The results of residual stress measurements using neutron diffraction were presented in this chapter. The measurements show that the residual stresses in the high strength steel are approximately  $0.6f_y$  (nominal) of steel (however, this can not be verified for the close-to-surface locations by the current data). This observation does not match well to previous results for S355 steel Acevedo et al. (2012) and BS 7910 code recommendations for tubular T-butt and fillet welds (BS 7910, 2005). One possible explanation is the tensile residual stresses due to hindered shrinkage are reduced due to superposition of compressive stresses from volumetric change as a result of martensitic transformation in HAZ.

Measurements on S355J2H tubular joint specimen showed that the principal residual stresses are – with an acceptable tolerance – in longitudinal (tangential to the weld) and transversal (perpendicular to the weld) directions.

The residual stress field is found not to be a function of the yield stress, which is in opposition with BS 7910; however the measurements, for the most part, fall within the band from BS 7910 and also follow its trend in function of depth.

The beam travel length limitation was solved partially for the gap region by cutting the tube. Previously, it was done using windows in the sides of the tube. Still, the weld root is unreachable for the neutron diffraction technique (i.e. high background noise at this location).



# 5 Fatigue experiments

## 5.1 Introduction

Two full-scale trusses were tested under constant amplitude cyclic loading. The main objective was confirmation of fatigue strength of these high strength steel welded structures. Major codes do not differentiate between the fatigue categories of welded steel structures with different yield stresses. IIW (Hobbacher, 2013) considers the same fatigue strength for welded structures made of steel grades up to S900<sup>1</sup>. This is because of the fact that the majority of the fatigue life of the welded details is consumed in the propagation phase, which is not directly related to the yield stress (Maddox, 1991; Schijve, 2001). However, the secondary effects due to change in residual stress distribution at the cracking region might influence the crack growth behavior. IIW 2013 states that a higher fatigue class for a high strength steel can be considered given that it is validated by tests.

Furthermore, despite the development of new high strength steel profiles, and particularly CHS profiles, their usage in the bridge structures is still limited, partly because of the lack of the experimental data. The large-scale tests carried out in this study, are considered a necessary step towards promotion of application of these profiles (both hot-rolled and cast) in new bridge structures.

The results of the fatigue tests were compared to previous tests carried out at ICOM on similar trusses and joints made of steel grades S355J2H, plus the database of fatigue tests on tubular joints. A summary of geometric parameters of trusses tested during this study and the previous full-scale fatigue tested trusses at ICOM in the past is presented in Table 5.1, together with dimensions of some road bridge trusses as examples.

---

<sup>1</sup>For Eurocode 3 part 1-12[2007] this limit is up to grade S700

Test beams /bridges	Ref. <sup>†</sup>	pcs.	Nominal dimensions [mm]					Geometrical parameters						
			Eccentricity e [mm]	Gap g [mm]	Chord $D_{sup} \times T_{sup}$	Chord $D_{inf} \times T_{inf}$	Brace $d \times t$	$\alpha$ ( $2L_{ch}/D$ )	$\beta$ ( $d/D$ )	$\gamma_{sup}, \gamma_{inf}$ ( $D/2T$ )	$\tau_{sup}, \tau_{inf}$ ( $t/T$ )	$\zeta$ ( $g/D$ )	$e/D$	$\theta$ (°)
S1	AS	4	20-28	20-29	I-beam	273×20	139.7×12.5	15.4	0.51	–, 6.83	–, 0.63	0.1	0.1	60
S2 <sup>1</sup>	AS	4	50-55	54-60	I-beam	273×20	139.7×12.5	15.4	0.51	–, 6.83	–, 0.63	0.2	0.2	60
S3	AS	4	28-39	31-44	I-beam	168.3×12.5	88.9×8	25	0.53	–, 6.73	–, 0.64	0.2-0.3	0.2	60
S4-1 <sup>2</sup>	AS	2	20-28	20-29	I-beam	273×20	139.7×12.5	15.4	0.51	–, 6.83	–, 0.63	0.1	0.1	60
S4-2 <sup>2</sup>	AS	2	50-55	54-60	I-beam	273×20	139.7×12.5	15.4	0.51	–, 6.83	–, 0.63	0.2	0.2	60
S5	LB	2	22	19.9	168.3×20	168.3×20	88.9×8	25	0.53	4.21, 4.21	0.4, 0.4	0.12	0.13	60
S6	CA	1	44-47	45-49	168.3×20	168.3×30	88.9×8	25	0.53	4.21, 2.81	0.4, 0.27	0.28	0.27	60
S7	CA	1	42-47	43-49	168.3×30	168.3×20	88.9×8	25	0.53	2.81, 4.21	0.27, 0.4	0.27	0.26	60
S8 <sup>3</sup>		1	38	32	168.3×20	168.3×30	88.9×8	25	0.53	4.21, 2.81	0.4, 0.27	0.23	0.23	60
S9 <sup>3</sup>		1	38	32	168.3×30	168.3×20	88.9×8	25	0.53	2.81, 4.21	0.27, 0.4	0.23	0.23	60
S10 (S690QH) <sup>4</sup>	FZ	1	32-41	42-48	193.4×20	193.4×20	101.6×8	22.4	0.53	4.84, 4.84	0.4, 0.4	0.22	0.18	60
S11 (S690QH) <sup>4</sup>	FZ	1	29-36	36-45	193.4×20	193.4×20	101.6×8	22.4	0.53	4.84, 4.84	0.4, 0.4	0.22	0.18	60
Antrenas FR-1994						Arch 1200×32	508×16		0.42	–, 18.75	–, 0.5			
Aarwangen CH-1997 (Steel grade S355)					406×36–50	406×36–50	194×20–28	12.4	0.48	4.1–5.6	0.4–0.78			45
Lully CH-1997					508×25–50	508×25–50	267×11–25	14.0	0.53	5.1–10.2	0.22–1			60
Nesenbachtal DE-1999					324×16–80	324×16–80	194×10–60	19.5	0.6	2–10.1	0.63–0.75			46
Dättwil CH-2001					508×50	508×50	267×11–25	14.4–14.8	0.53	5.1	0.22–0.5			60
Korntal-M. DE-2002					457×45–65	457×45–65	267×28–45	16	0.58	3.5–5.1	0.62–0.69			60
St-Kilian DE-2006					I-beam	610×50–60	298.5×55–60	~12.5	0.49	–, 5.1–6.1	1–1.1			~60
Lichtenfels DE-2008					800–?×?–50	?×?	?×?	~?	~?	?–?, ?–?	?–?, ?–?			?~
Typical values for truss bridges					300–700 ×10–80	300–700 ×10–80	100–300 ×10–60	10 –20	0.4 –0.6	3 –12	0.2 –1.1		0.2	40 –60

<sup>1</sup> Without backing ring; All other trusses were welded with backing ring.

<sup>2</sup> All joints were post-weld treated with needle peening.

<sup>3</sup> All joints were post-weld treated with High Frequency Mechanical Impact (HFMI) method.

<sup>4</sup> Made of high-strength S690QH steel. The test beams S1 to S9 were made of S355 steel

<sup>†</sup> **References:**

AS: Schumacher (2003)

LB: Costa Borges (2008)

CA: Acevedo (2011)

FZ: This study

Table 5.1: Sizes and geometric parameters of the specimens studied in ICOM, together with those of some tubular bridges (adapted from Acevedo (2011)).

## 5.2 Theory

In this section, theoretical background for Alternative Current Potential Drop (ACPD) for crack initiation and crack depth measurement is presented.

### 5.2.1 Alternative current potential drop (ACPD)

The ACPD method for monitoring crack growth has been in use since several years. The method is relying on skin effect which is the tendency of alternative currents in a conductor to distribute in the cross section such that the majority of the current density is in a distance  $\delta$  (skin depth) from the conductor's surface (Marsh et al., 1991). Skin depth  $\delta$  is calculated from following formula:

$$\delta = (\pi\mu\sigma f)^{-1/2} \quad (5.1)$$

where  $\mu$  is magnetic permeability of conductive material,  $\sigma$  is the electrical conductivity, and  $f$  is the electrical current frequency. The higher the frequency, the smaller skin depth will be. Finding crack depth using thin skin theory – in which the skin depth is small compared to the surface crack – is straightforward. Potential drop  $V_R$  picked up by the two probes on uncracked surface of the plate in Figure 5.1 will be different from the potential drop  $V_C$  registered by the probes having the same distance  $\Delta$ , but on the sides of a surface-breaking crack. The crack depth  $d$  is calculated from the change in potential drop from  $V_R$  to  $V_C$  by the following relation (Dover and Monahan, 1994; Marsh et al., 1991):

$$d = \frac{\Delta}{2} \left[ \frac{V_C}{V_R} - 1 \right] \quad (5.2)$$

Saguy and Rittel (2005) mention the three following conditions for the thin skin assumption to hold:

$$\frac{t}{\delta} > 10, \quad \frac{d}{\delta} > 10, \quad \frac{w}{\delta} > 10 \quad (5.3)$$

Where  $t$  is the plate thickness,  $d$  is the crack depth, and  $w$  is the crack length. If the conditions given in 5.3 are met, Equation 5.2 (referred to as one-dimensional approximation of crack depth) gives satisfactory results. In order to take into consideration elliptical shape of the crack, Dover and Monahan (1994) propose a factor between 1.05 to 1.1 being applied to the right side of equation 5.2. If any of conditions given in 5.3 is not true, the thin skin effect

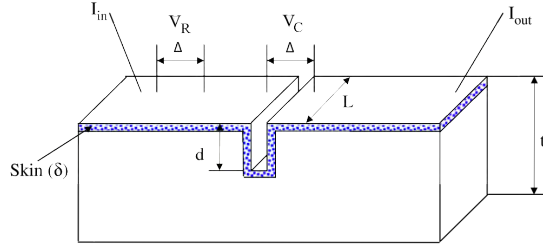


Figure 5.1: Principle of crack depth measurement using ACPD (Saguy and Rittel, 2005).

does not hold. In this case, the thick skin theory ( $\frac{\delta}{d} = \infty$ ) gives a lower bound approximation (Mirshekar-Syahkal et al., 1982):

$$d = \frac{\Delta}{2} \left( \frac{V_R}{V_C} \right)^{\frac{1}{2}} \left[ \frac{V_C}{V_R} - 1 \right] \quad (5.4)$$

ACPD instruments generally work in the frequency range of 1 kHz to 10 kHz. Given the magnetic permeability of  $\mu = 6.28 \times 10^{-4} \text{ H m}^{-1}$  and conductivity of  $\sigma = 5.75 \times 10^6 \text{ S m}^{-1}$  for ferrous material, and working frequency of 5 kHz for the instrument, the skin depth will be  $\delta = 0.13 \text{ mm}$ . This skin depth gives satisfactory accuracy for practical crack depth measurement applications. However, the custom-built ACPD instrument used in this study worked in a much lower frequency<sup>2</sup>(5 Hz). The skin depth in this case is  $\delta = 4 \text{ mm}$  and apparently thin skin assumption is not valid. Saguy and Rittel (2005) proposed an intermediate (thin-to-thick) solution as follows:

$$\left\{ \begin{array}{l} d = \frac{\Delta}{2} \left( \frac{V_C}{V_R} - 1 \right) + \frac{f_1(\Delta, \delta) + f_2(d, \delta)}{2} \\ f_1(\Delta, \delta) = \Delta \cdot \exp\left(-\frac{\frac{\Delta}{2} + \delta}{\delta}\right) \\ f_2(d, \delta) = 2 \cdot d \cdot \exp\left(-\frac{d + \delta}{\delta}\right) \end{array} \right. \quad (5.5)$$

However, this solution gives non-zero values for  $d$  when  $V_C = V_R$  (the term  $f_1(\Delta, \delta)$  is always larger than zero) which is unrealistic. Therefore, instead of using this solution, it was preferred to use thin skin solution given by equation 5.2 with a calibration factor which was estimated by measuring the final crack depth using calipers after the fatigue tests.

Lugg et al. (1988) describe a method to measure the crack inclination using ACPD, but their

<sup>2</sup>This technical limitation was due to high output current intensity of the instrument(75 A to 300 A) which could not be found among other instruments available in the market.



method requires four probes (two on each side of the plate at the crack region) which is not feasible for the tubular structures.

## 5.3 Experimental method

This section deals with geometry and material selection, fabrication, fatigue testing, and repair of truss specimens. Two planar Warren trusses were tested for in plane bending (IPB) in this study. Tube sizes of grade S90QH used in the fabrication of specimens were not in production at an industrial scale at that time. Special production batches were requested from *Vallourec & Mannesmann Tubes* (manufacturer).

### 5.3.1 Fabrication of test trusses

#### Geometry

Member and section sizes were decided to be as close as possible to mid-span road bridge trusses (typical sizes for these structures are presented in Table 5.1). Given the limitations of experimental equipment, the overall height of the truss was selected about  $\frac{2}{3}$  of a typical bridge truss and the chord diameter was reduced accordingly ( $\beta$  was greater and  $\gamma$  was smaller than the corresponding values in an exemplary road bridge). The overall Warren truss dimensions were 9285 mm long and 1993 mm high.

Compared to testing of an individual joint, the large-scale truss allows for joints to be tested simultaneously while each joint experiences a different loading combination. In addition, the welding conditions and positions will be better representative of the real-world applications in terms of welding imperfections and welding residual stresses.

The members of the two trusses S10 and S11 were identical in size: upper and lower chords were  $193.4 \times 20$  circular hollow sections and braces were  $101.6 \times 8$ . Selection of similar tube sizes was meant to reduce manufacturing complexities raised by several one-off production sizes. Similarity of dimensions with previous trusses tested at ICOM provides a more convenient comparison between the specimens. In particular, the eccentricity ratio was kept close to the values used in specimens S5 to S7. Dimensions of the test trusses are shown in Figure 5.2

Fatigue resistance of cast joints was also planned to be examined during the tests. Cast joints have shown superior fatigue performance compared to the welded K-joints, as documented by Haldimann-Sturm and Nussbaumer (2008) for the case of S355 steel, Nussbaumer et al. (2010) for S460 steel, and Pijpers (2011) for very high strength steel up to S1100 (with matching cast steel joints). The main reason is that these type of joints allow for a more smooth transition of forces when several members meet at the joint location. The weld location is moved from the K-joint area, where high stress concentrations exist, to some place on the chord or brace length with considerably less stress concentration factors. Moreover, the complex geometry of weld at K-joint (and corresponding beveling of brace edges) are replaced by a simpler girth weld.

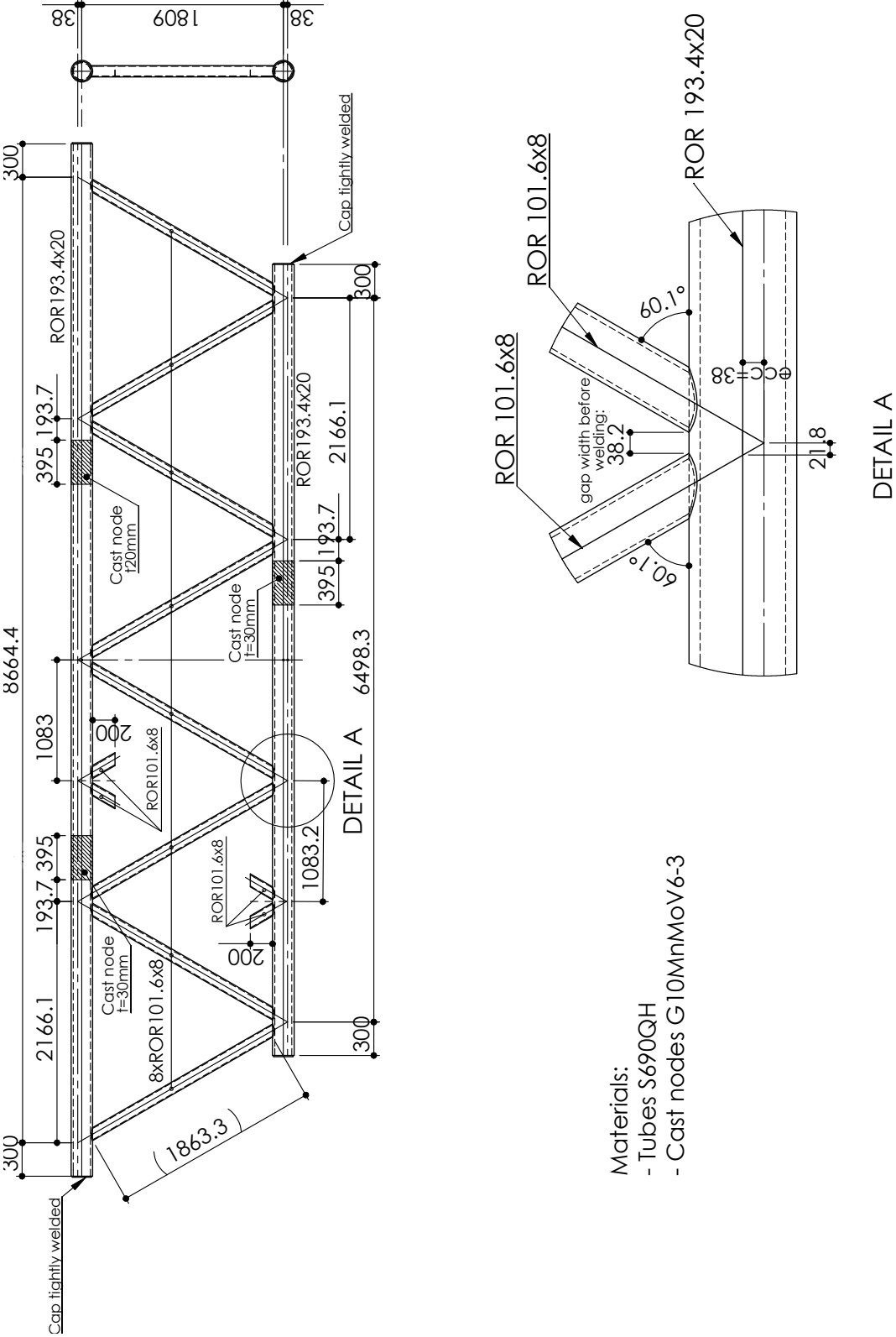


Figure 5.2: Nominal dimensions of test trusses S10 and S11.

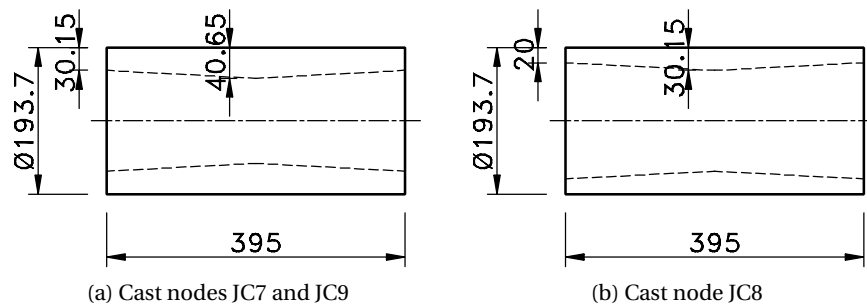


Figure 5.3: Dimensions of cast nodes used in fabrication of trusses S10 and S11; End preparation (bevels) is not shown (see figure 5.7).

Haldimann-Sturm and Nussbaumer (2008) have shown that the cast nodes, if dimensioned properly, are more tolerable to internal casting defects than welds. Cast nodes can withstand large internal defects, up to 28 % of wall thickness, before showing a decrease in the fatigue life. Hence, they identified the girth butt weld between cast joint and tube as the weak point of the connection, given that the internal imperfection sizes are within the allowable range mentioned above.

Having this conclusion in mind, it was decided to keep the cast-to-tube girth weld location intact, but swap the sides of the tube and the cast node. This resulted in cast nodes being easier and cheaper to produce. For example, the cast joint *JC9* in Figure B.2 is moved to the left side of the girth weld. The girth weld was located at a distance of  $a = D = 193.7\text{ mm}$  from the center line of the connection, where it should be in a typical cast node connection. This way, it was possible to simultaneously test both K-Joint *J2* and cast node *JC9*. In each truss, cast nodes with two different edge thicknesses ( $T = 20\text{ mm}$  and  $30\text{ mm}$ ) were used. Figure B.2 shows truss dimensions and locations of cast nodes. Cast nodes are labeled S10-JC7,8,9 and S11-JC7,8,9. Cast nodes dimensions are shown in Figure 5.3.

Two unloaded K-joints were also implemented in the middle of the chords for each truss. The aim was to have the joints experience the fatigue loading cycles for reaching the stress relaxation (if any) at the weld toes, without occurrence of fatigue damage at those locations, since the braces were not loaded. Welding procedure specification were similar to the other K-joints to ensure a similar residual stress field is obtained. These parts were cut out after the tests were finished. They were used for semi-non destructive residual stress measurements, as described in Chapter 4.

### Noding eccentricities

Although K-joints with fully or partially overlapping braces show higher static strength, gap joints are preferred in the construction of tubular trusses for practical reasons including: easier edge preparation and fabrication, construction tolerance, and more convenience for NDT

inspections (Nussbaumer et al., 2004; Wardenier et al., 2008). Gap size and the corresponding nodding eccentricity  $e$  (distance between the braces centerlines and chord axis) affect the fatigue life of the joint by their influence on stress concentration factors. Gap size for unwelded joint (distance between the outer walls of braces at crown toe, denoted by  $g$  in Figure 5.4a) is given by (Schumacher, 2003)

$$g = \frac{(D + 2e) \cos \theta - d}{\sin \theta} \quad (5.6)$$

In order to prevent overlapping of the brace welds in the gap region, CIDECT guide for static design of tubular joints (Wardenier et al., 2008) recommends this distance not being smaller than  $2t^3$ , which for the studied trusses it would give  $g_{min} = 16$  mm. The new IIW (2008) and CIDECT (2008) guides set the limit for the nodding eccentricity to  $\frac{e}{D} \leq 0.25$  (positive  $e$  corresponds to non-overlapping joints). If the eccentricity exceeds this value, the designer should take into account the effect of bending moments on static capacity of the joint. Following these limitations and considering the geometry of the previous tested trusses at ICOM (shown in Table 5.1), the values of  $e = 38$  mm and  $g = 38.2$  mm were selected for S10 and S11 trusses.

We can modify Equation 5.6 for calculation of gap size after welding ( $g^*$ ), according to the weld geometry given by Costa Borges (2008):

$$\begin{cases} g^* = \frac{(D + 2e) \cos \theta - d^*}{\sin \theta} + 2W_3 \\ d^* = d + 2W_2 \end{cases} \quad (5.7)$$

$d^*$  is the diameter of a hypothetical tube parallel to the brace whose intersection with the chord defines the weld toe line on the chord (See Costa Borges (2008)).  $W_2$  and  $W_3$  are weld geometry parameters – as shown in Figure 5.4b – with values estimated as:

$$\begin{cases} W_2 = 1.25 t \\ W_3 = 0.627 t \end{cases} \quad (5.8)$$

$g^*$  and  $g_c$  values (see Figure 5.4a) in the joints of fabricated trusses were measured and the eccentricity for each joint was estimated once from  $g^*$  measurement ( $e_1$ ) and once from  $g_c$  value ( $e_2$ ). The measurements are reported in Table 5.2. The agreement between the two estimated eccentricities  $e_1$  and  $e_2$  is generally acceptable. Direct measurement of  $g_c$  was not

---

<sup>3</sup>This distance does not seem to be sufficient for smaller brace angles ( $\theta < 50^\circ$ ). A better approximation for minimum gap distance can be derived based on work of Costa Borges (2008) as:  $g_{min} = \left( \frac{2.5}{\sin \theta} - 1.254 \right) t$

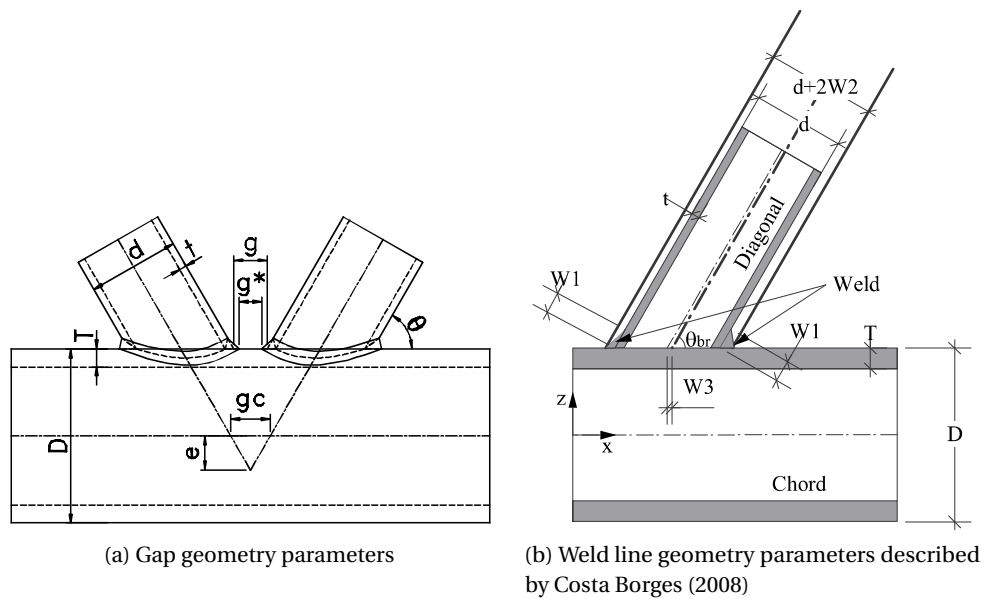


Figure 5.4: Various parameters defining the gap and the weld geometry in K-Joints.

possible on the fabricated joints. Instead, the projection of  $g_c$  on curved outer surface of the chord was measured by marking the extensions of brace centerlines and chord centerline. Therefore, more measurement error is expected from these measurements.

### Materials

As mentioned before, tubes were made of construction steel grade S690QH. This grade is not introduced in the European norm for the technical delivery specifications of hot-rolled hollow sections (EN 10210-1) yet, but S690Q (alloy number 1.8931 according to EN 10027-2) does exist in the European code for the flat rolled high-strength steel sections EN 10025-6 (2004). The manufacturer of the tubes has reproduced the composition and microstructure of S690Q according to EN 10025-6 (2004) and the other delivery specifications, such as surface quality and dimensional controls, in accordance with EN 10210-1 (2006). The name S690QH (H stands for *Hollow*) conforms to the convention for compatible naming and grading between the two codes.

Chemical composition of steel is presented in Table 4.2. The estimated carbon equivalent is 0.61% while maximum allowable CEV is 0.65%. Mechanical properties including impact energy are shown in Table 5.3.

Cast nodes were made of G10MnMoV6-3 alloy (steel number 1.5410), conforming to EN 10293 (2005). The same material was used in an earlier study by Nussbaumer et al. (2010) in combination with tube profiles of grade S460NH. The cast parts were controlled by Ultrasonic tests (UT), dye penetrant (PT), and wet fluorescent magnetic particle (MT) inspection for manufac-

## Chapter 5. Fatigue experiments

Table 5.2: Measured joint gap sizes and eccentricities for trusses S10 and S11.  $e_1$  is back-calculated from equation 5.7 by measuring  $g^*$  and  $e_2$  is calculated from measured  $g_c$  values.

Node	$g^*$ (mm)	$g_c$ (mm)	$e_1$	$e_2$	$e_1/D$
S10-J1	18.3	41.9	32.1	36.3	0.17
S10-J3N	20.5	44.1	34.0	38.2	0.18
S10-J5N	19.7	43.2	33.3	37.4	0.17
S10-J6	23.0	47.6	36.2	41.2	0.19
S10-J2	25.8	46.8	38.5	40.5	0.20
S10-J3S	19.9	44.0	33.5	38.1	0.17
S10-J5S	28.9	43.0	41.2	37.3	0.21
S11-J1	20.4	39.4	33.9	34.2	0.18
S11-J3N	20.7	42.1	34.2	36.5	0.18
S11-J5N	18.2	40.5	32.0	35.0	0.17
S11-J6	14.6	36.4	28.9	31.6	0.15
S11-J2	18.4	41.4	32.1	35.8	0.17
S11-J3S	22.8	41.1	36.0	35.6	0.19
S11-J5S	21.4	45.0	34.8	39.0	0.18
Mean	20.9	42.6	34.3	36.9	0.18
Standard deviation	3.4	2.8	2.9	2.4	0.015
Specified	25.1	43.9	38	38	0.2

Table 5.3: Mechanical properties of steel tubes in S690QH reported by manufacturer.

	Yield stress $f_y$ [MPa]	Tensile strength $f_u$ [MPa]	Elongation $A_5$ [%]	CVN $A_V^a$ [J]
Minimum	650	700	14	40 <sup>b</sup>
Maximum	—	960	—	—
Test	769	809	19.5	227(L)/196(T) <sup>c</sup>

<sup>a</sup> Test temperature  $-20^\circ\text{C}$ .

<sup>b</sup> This corresponds to 27 J at  $-30^\circ\text{C}$  regulation in EN 1993-1-1.

<sup>c</sup> L: specimens from longitudinal direction, T: specimens from transverse direction.

turing defects and were graded as quality category 3. The edges were machined according to the welding procedure specifications. Tables 5.4 and 5.5 show chemical composition of cast parts and their mechanical properties (according to EN 10293), respectively.

Table 5.4: Chemical composition of cast nodes' steel (G10MnMoV6-3, steel number 1.5410) according to EN 10293 (2005).

C(max) %	Si (max) %	Mn %	P (max) %	S (max) %	Cr %	Mo %	Ni %	V %	W %
0.12	0.60	1.2–1.8	0.025	0.020	—	0.2–0.4	—	0.05–0.1	—

Table 5.5: Mechanical properties of cast nodes' steel (EN 10293, 2005).

Min. yield stress $f_y$ [MPa]	Tensile strength $f_u$ [MPa]	Min. elongation $A_5$ [%]	Min. CVN at 20 °C [J]	Min. CVN at –20 °C [J]
500	600–750	18	60	27

For the welding wires, rutile flux-cored ESAB OK Tubrod 15.09 (1.2 mm diameter) was used. Hollow-core electrodes provide a higher deposition rate compared to solid wires for the same wire diameter and at the same current intensity (Weman and Lindén, 2006). These wires facilitate control of the welding process and arc stability for the welder. For hollow-core wires, electrical arc is wider with smaller droplets compared to solid wires, which results in a wider weld pool and this is beneficial for the sidewall penetration.

#### Welding procedure specifications (WPS)

Fabrication of trusses started with assembling and welding the tube  $\varnothing 193.4$  parts and cast nodes together to form the chords. The tack-welding and the root pass were done on a straight fixture. The tubes then were put on a rolling jig to finish welding in PA position according to ISO 6947 (2011) (see figure 5.5). After fabrication of chord members, the whole truss was fit-up and tack-welded<sup>4</sup>. The welding of K-joints was done on a one-by-one basis while the truss was kept vertical maintaining the welding position PA/PC<sup>5</sup> for K-joints.

Nussbaumer et al. (2010) assessed fatigue performance of various cast node girth weld details. Figure 5.6 shows summary of their test results for the six tested details. Although detail type *e* had satisfactory fatigue strength and was more economical because of lower weld volume and less effort for edge preparation, the fabricator opted for the details *b* and *c* to ensure full penetration at the root. The more open double V weld gap provides more working space for the welder and reduces the risk of defects. The downside is that the welding takes more time and the volume of the weld (and the corresponding shrinkage) increases. Dimensions of

<sup>4</sup>In order to secure the integrity of fitted-up truss, part of the root weld at crown hill location was done before lifting the truss and putting it in vertical position.

<sup>5</sup>Flat welding position is called PA; and pipe welding when pipe axis is vertical is denoted by PC (ISO 6947, 2011).



(a) Tack-welding of cast joints on a straight platform.



(b) Cast joint and tubes fitted-up.



(c) Chord on the rolling jig for complete welding.



(d) Close-up of weld gap before tack welds being ground.

Figure 5.5: Stages for assembling and welding of the CHS profiles and cast nodes to fabricate truss chords.

girth weld gaps for the cast nodes in this study are shown in Figure 5.7. As mentioned before, welding was done on a rolling jig. Fabricator's WPS is presented in Appendix A. Table 5.6 summarizes welding parameters for CHS – cast joints.

For fabrication of K-joints, brace member edges were bevelled with a minimum angle of  $30^\circ$  (Figure 5.8a). Steel backing rings were used as requested by Schumacher (2003) and (Nussbaumer et al., 2004) to ensure full penetration. The inclusion of backing rings for K-joint had been the case for previous tubular truss tests at ICOM. Figure 5.8 shows the trusses' fabrication process. As recommended by CIDECT design guide (2000) and IIW code, the welding start-stop points were kept off the crown toe, crown heel, and saddle locations, i.e. locations of high stress concentration (Figure 5.8d). Detailed dimensions of the weld gap are given in Figure 5.9. It should be noted that fabricator's WPS given in Appendix A is not coherent with the Figure (WPS mentions only 4 passes). While all other welding parameters were kept the same as WPS, the filling of weld bead with only 4 passes was not realistic, therefore the numbers of welding passes were increased, which are mentioned in Tables 5.6 and 5.7.

Figure 5.11 shows the sequence for the welding of the two braces to form the K-joint. The



Table 5.6: Welding parameters for CHS–cast node joints.

Welding process	MAG 136
Number of welding passes	10
Consumable	OK Tubrod 15.09
Shielding gas	18% $CO_2$ / 82% $Ar$
Polarity	DC+
Preheating	120 °C
Maximum interpass temperature	250 °C
Arc power	4.3 kW to 4.8 kW
Average welding speed	5 mm s <sup>-1</sup>
Gross heat input energy	0.9 kJ mm <sup>-1</sup> to 1.0 kJ mm <sup>-1</sup>

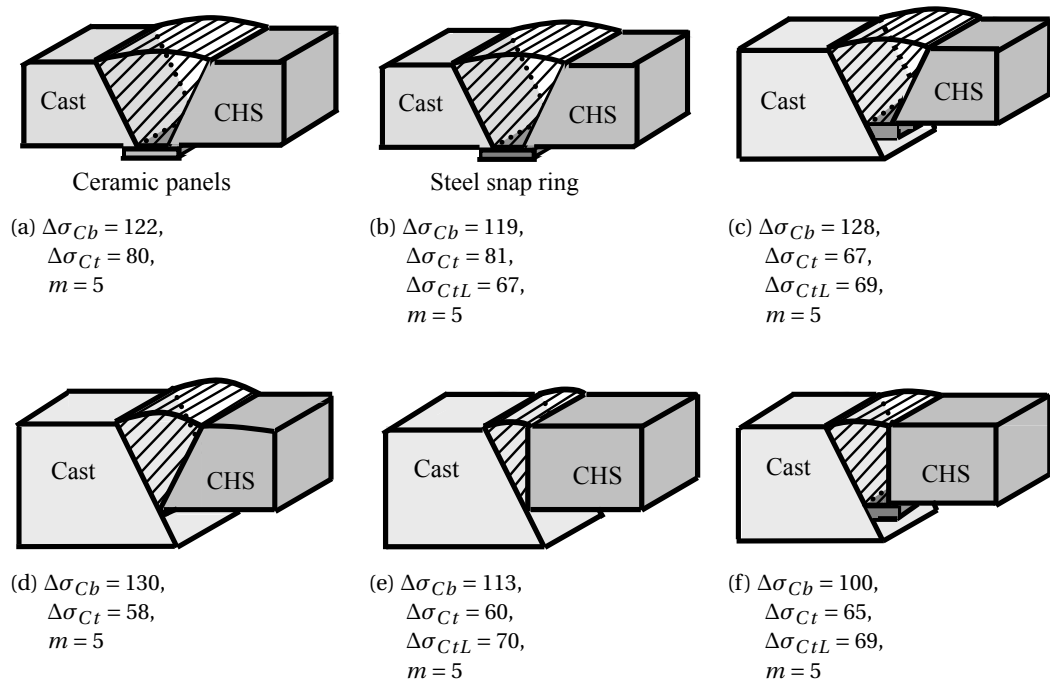


Figure 5.6: Various cast joint details and their suggested detail categories, tested by Nussbaumer et al. (2010).  $\Delta\sigma_{Cb}$ :detail category for bending,  $\Delta\sigma_{Ct}$ :detail category for axial loading(strip specimens cut out of tubes),  $\Delta\sigma_{CtL}$ :detail category for axial loading(tube specimens),  $m$ : slope of S-N curve.

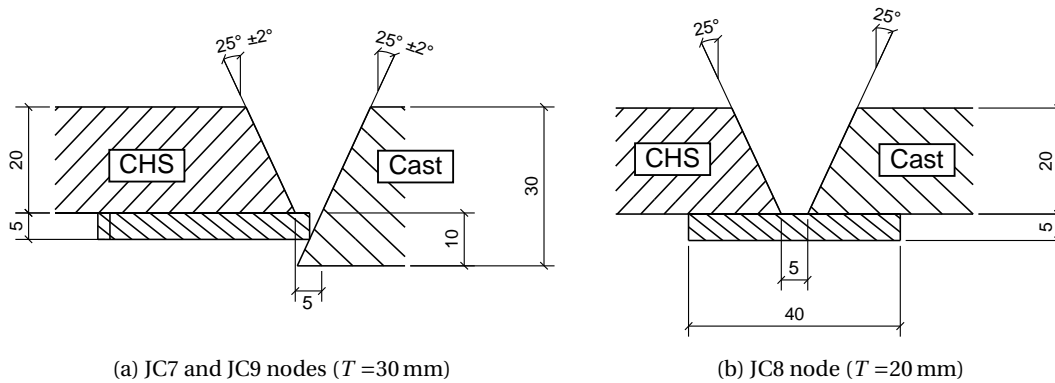


Figure 5.7: Weld gap details for cast node connections in trusses S10 and S11, conforming to details *b* and *c* in Figure 5.6. Tack welds ( $a=3$  mm) not shown.

welding for each brace started at a location between the saddle and the crown heel and finished at a diametrically opposite point close to crown toe. Each weld pass covered half of the corresponding brace perimeter. The welding direction was always from the crown heel towards the crown toe. Once one pass of all 4 weld parts were done, the next pass would start and so forth.

The welding process was registered by a video camera to estimate the welding sequence, timing, and torch speed. Table 5.7 shows welding parameters for K-Joints summarized from those measurements. Arc efficiency value is taken within the range given by Grong (1997). A difference is observed between the original WPS (see Appendix A) and the observations: welding was carried out in a larger number of passes with smaller cross section of weld per pass (which also means higher torch speed), compared to what was suggested by WPS. It is worth mentioning that since the cross section of the weld gap was not constant along the perimeter of the tubular joint, the welder had to either change the torch speed or add partial passes to compensate for the differences in cross sections.

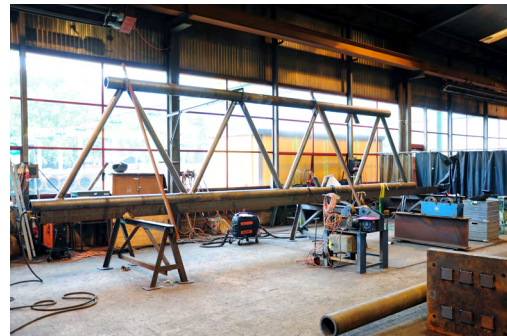
Weld inspection carried out as recommended by SIA (2013) (Weld quality B, 100% VT + 50% UT). No surface finishing (e.g. sandblasting) was applied on the specimens. Three joints were post-weld treated with needle-peening: the K-joint *J6* at mid-span, and the Y-joints *J4N* and *J4S* at the supports. Needle-peening was necessary to prevent premature stop of the tests due to fatigue cracking at these joints.

### 5.3.2 Temperature measurements

Welding temperature history, and particularly cooling rate, is a crucial factor that affects HAZ microstructure. To ensure accuracy of the temperature field predicted by numerical welding simulation, validation against temperature measurements is needed. The main objective to register the weld-induced temperatures during fabrication was to acquire the data needed for



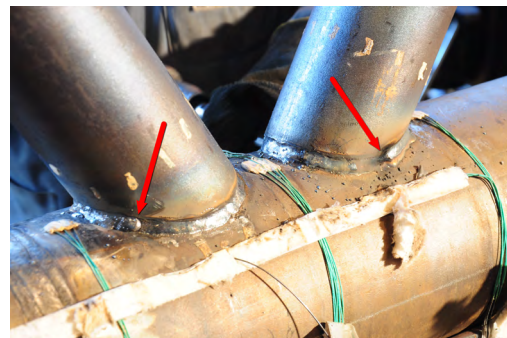
(a) Beveled brace ends with backing rings.



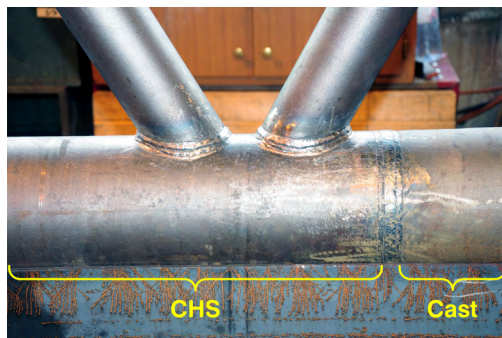
(b) fitted-up truss held vertical to finish the welding.



(c) K-joint before welding.



(d) Welding start-stop points.



(e) Finished K-joint with the neighboring cast node.



(f) Close-up of the gap at a finished joint.  
 $g^* = 23 \text{ mm}$

Figure 5.8: Fabrication of trusses S10 and S11.

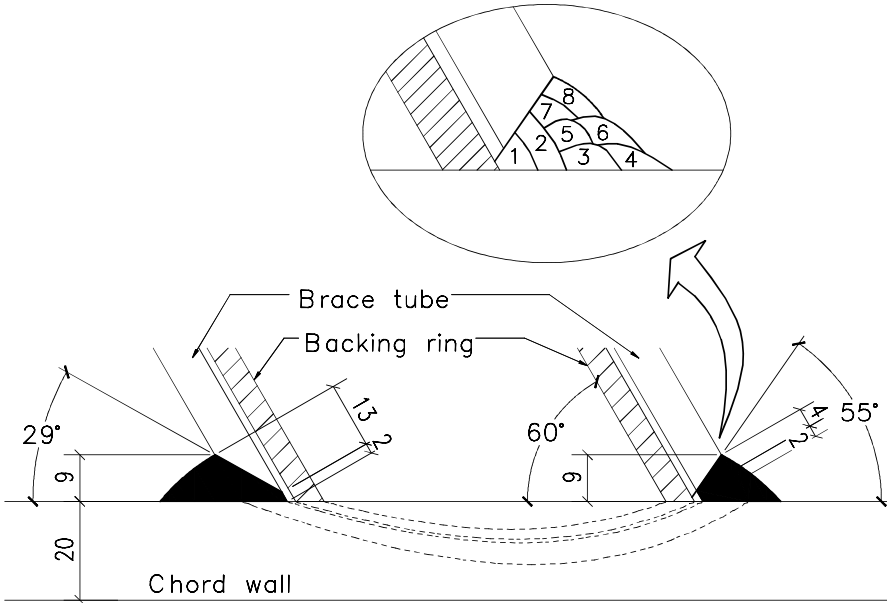


Figure 5.9: Geometry of weld gap for brace-to-chord connections in S10 and S11. The detail shows welding passes according to the welding procedure specifications.

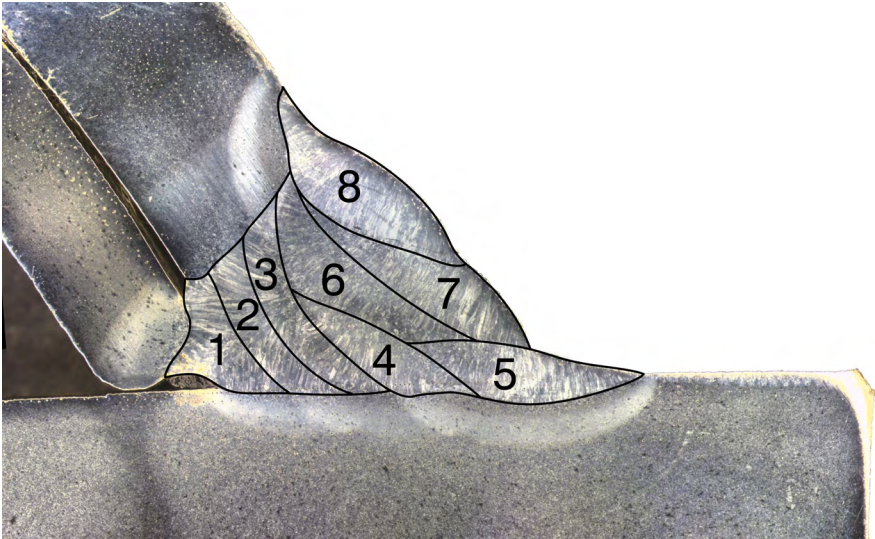


Figure 5.10: Weld passes at crown toe identified from etched sample taken from trusses after testing.

Table 5.7: Welding parameters for K-joints.

Welding process	MAG 136
Number of welding passes	8
Consumable	OK Tubrod 15.09
Shielding gas	18% $CO_2$ / 82% $Ar$
Polarity	DC+
Preheating	100 °C
Maximum interpass temperature	250 °C
Arc power	6.0 kW to 6.4 kW
Average welding speed	7.4 mm s <sup>-1</sup>
Gross heat input energy	0.81 kJ mm <sup>-1</sup> to 0.86 kJ mm <sup>-1</sup>
Arc efficiency <sup>†</sup>	78%

<sup>†</sup> Based on values given by Grong (1997)

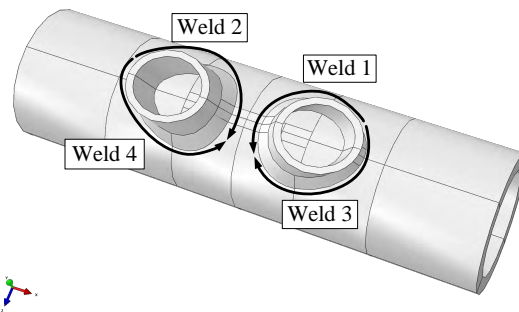


Figure 5.11: Sequence of welding passes. Welding start and stop locations were off the crown toe and crown heel regions.

validation of finite element models.

Two series of temperature acquisitions were carried out on two types of joints: CHS – cast joint (first series), and K-joint (second series). For CHS – cast welding, two surface temperature profiles along the chord axis in two different locations on the perimeter of girth weld were acquired. Figure 5.12a shows acquisition points on one of these locations. 12 points (6 points on each side of the girth weld), located at a distance ranging from 2.5 mm to 50 mm from the edge of the weld gap were registered. The angular distance between the two locations was 90°. The locations of thermocouples on the chord for K-joint welding are shown in Figures 5.12c and 5.13. The weld toe line on the chord was not evident at the beginning of welding. To predict the final weld geometry, the method described by Costa Borges (2008) was used. The model showed satisfactory agreement with the finished weld geometry at the crown toe and crown heel locations, but it was not accurate for the weld line at the saddle region.

Type K (chromel-alumel) thermocouple wires (diameter  $2 \times \varnothing 0.2$ ) were attached<sup>6</sup> to the specimens. Temperatures were registered by two HBM QuantumX MX1609 instruments connected to a computer. In order to protect the wires from direct flame of preheating torch, different protections were used: threading wires through ceramic sheaths (Figure 5.12a), wrapping a part of specimen in fiberglass fabric (for cast nodes, as seen in Figure 5.12b), and using fireproof band tapes<sup>7</sup> (for K-joints, see Figure 5.12d). The latter solution showed to be the preferable protection method due to ease and versatility of usage, adequate protection, and small effect on heat transfer conditions.

Sampling rate was 50 Hz and the measurements lasted up to 1500 s and 4000 s (for CHS – cast and K-joint, respectively) after the last welding pass was finished. It is recalled that the root pass for the CHS – cast girth weld was done before placing the chord member on the rolling jig. Therefore, the temperature history for this welding pass was not registered.

Measured temperature histories for both CHS – cast and K-joints are presented in Figures 5.14 and 5.15, respectively. As can be seen, the interpass delay time was not always the same. Some longer interpass delays were inevitable to fix the malfunctioning rolling jig, or to re-attach some of the thermocouples.

In Figures 5.14 a gradual increase of maximum registered temperature with progression of welding is observed. With weld passes filling up the weld gap, the later weld passes were deposited closer to the thermocouples and thus higher temperatures were registered. The CHS – cast welding temperatures reported here, were not further processed. They can be used for future welding simulations of this dissimilar tube joint.

The prescribed welding sequence for K-joint could not be exactly followed, since the weld cross section was variable along the weld gap and some partial weld passes were done to compensate for the varying weld cross section. Therefore, peaks sequences observed in Figure

---

<sup>6</sup>Attachment was done using percussive welding

<sup>7</sup>The protective material is fibers of alumina-silica ceramic



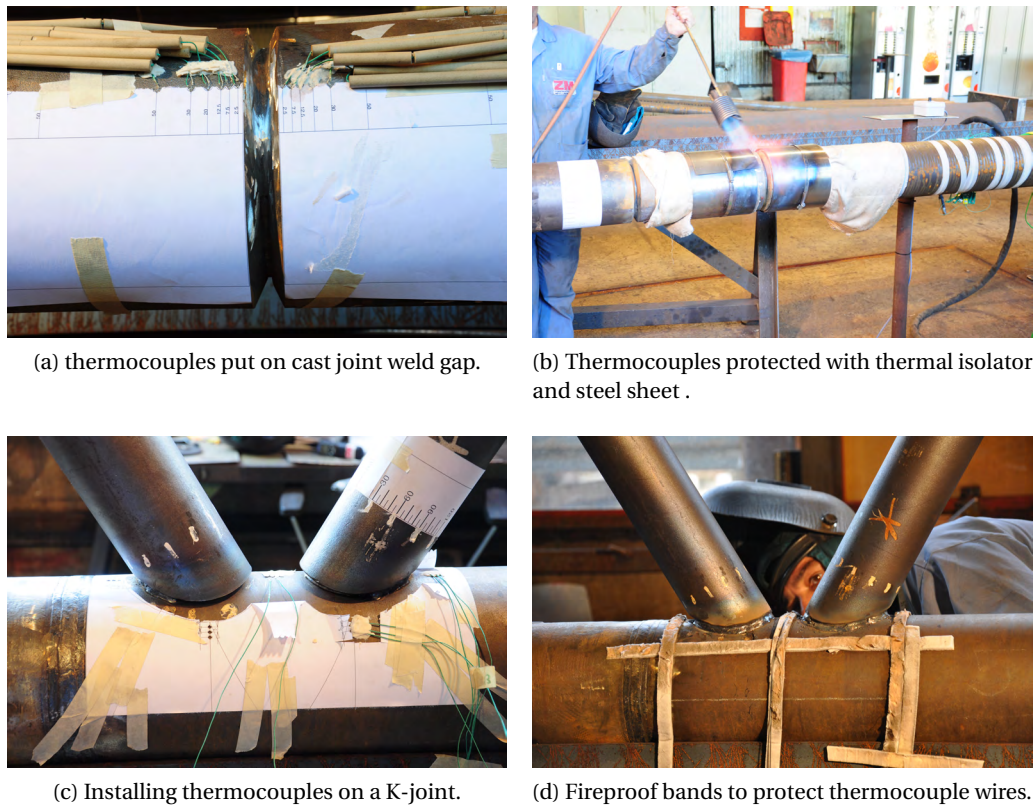


Figure 5.12: Installation of thermocouples on specimens and protecting them against preheating flame.

5.15 are not regular. The peak temperature registered in gap region (Figure 5.15b) was 356 °C which is not high enough for evaluation of  $t_{8/5}$ ; But the peak temperature itself could still be used for calibration of heat source model (See Chapter 6).

#### 5.3.3 Test setup

A three-point load-controlled bending test setup similar to experiments previously done at ICOM (Acevedo, 2011; Costa Borges, 2008; Haldimann-Sturm, 2005) was employed, as shown on Figure 5.16. Loading and support points were all located on the upper chord. Force was applied by a servo-hydraulic Hydrel actuator with a maximum load of  $\pm 1200$  kN and a maximum stroke of 250 mm. Two steel blocks were milled to fit the curved surface of the upper chord and were fixed on the actuator loading pad to apply the load on the truss. Two blocks with similar shape were put at the support locations for the same reason.

In order to secure the specimen and actuator during the test, slings were used to prevent lateral movements, as shown in figure 5.16c. To prevent rolling the specimen around the axis passing through the two supports, a restrainer block – covered with Teflon plates – was

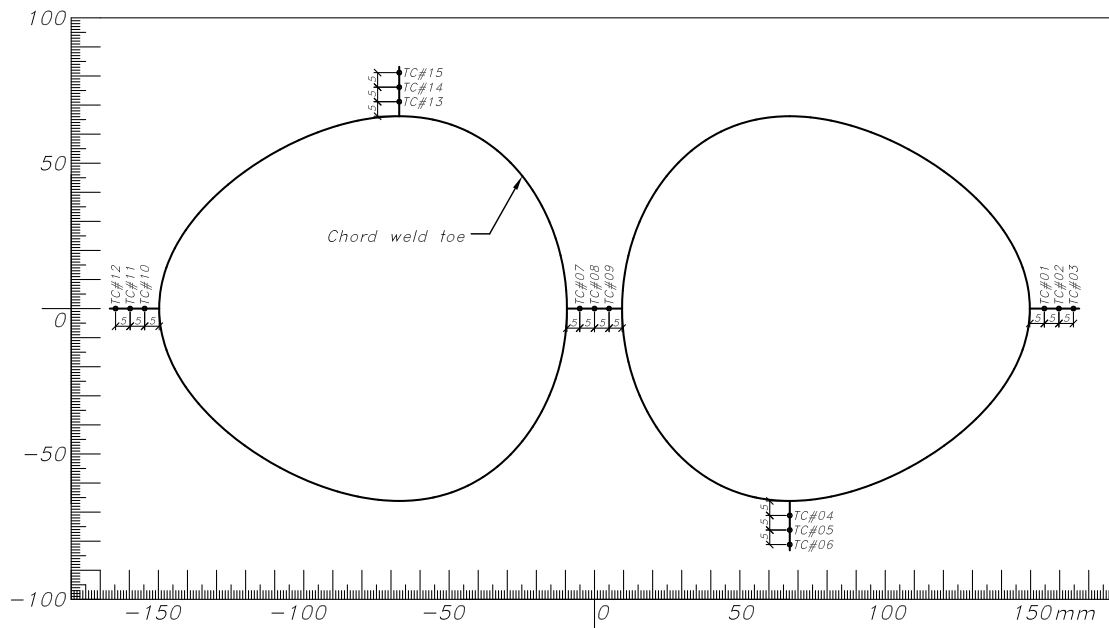


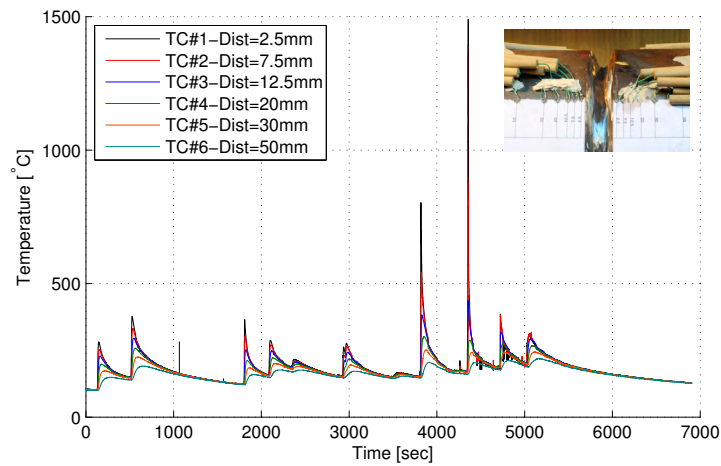
Figure 5.13: Position of thermocouples installed on the chord of the K-Joint to register welding temperatures. The weld toe lines on the chord are shown on the unrolled top view of K-joint.

installed to prevent out-of-plane movement of the lower chord.

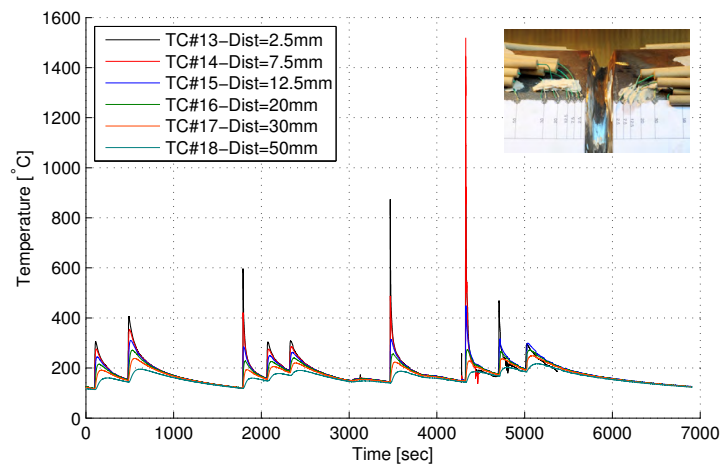
A function generator computer was used to define the sinusoidal actuator loading. Security limit on the stroke was put to stop the loading in case excessive displacements (i.e. excessive cracking) would occur. The security limit was set to trigger if a surplus displacement larger than 0.5 mm (equivalent to approximately 10% extra displacement) happened. This limit was relaxed to a higher value after repairing of the trusses (see section 5.3.6), because of the increased flexibility of the structure.

Fatigue loads for trusses S10 and S11 are given in Table 5.8. The load ranges for the two trusses were chosen by balancing two conflicting considerations: first, lowering the applied stress range such that the fatigue life is comparable to the fatigue life of in-service road bridges; And second, limited time frame for the tests required the fatigue life being within a feasible range. Table 5.8 gives design fatigue life for the most stressed joints (J1 and J2). In the last column, fatigue life range estimation based on survival probability of 50% to 84% assuming standard deviation equal to 0.2 for  $\log(N)$  (Hirt, 1985) is presented. For the load ratio  $R$ , since attaining a zero-load condition ( $R = 0$ ) raises practical difficulties (getting a zero-load on structure is difficult, some undesired movements in supports can occur), a small value  $R = 0.1$  was chosen, as was the case for the two earlier studies at ICOM (Acevedo, 2011; Costa Borges, 2008). The loading frequency, was selected as 1.8 Hz and 1.3 Hz for S10 and S11, respectively. According to Schijve (2001), for the fatigue cracking in non-corrosive environment, this frequency range does not influence fatigue crack growth behaviour.

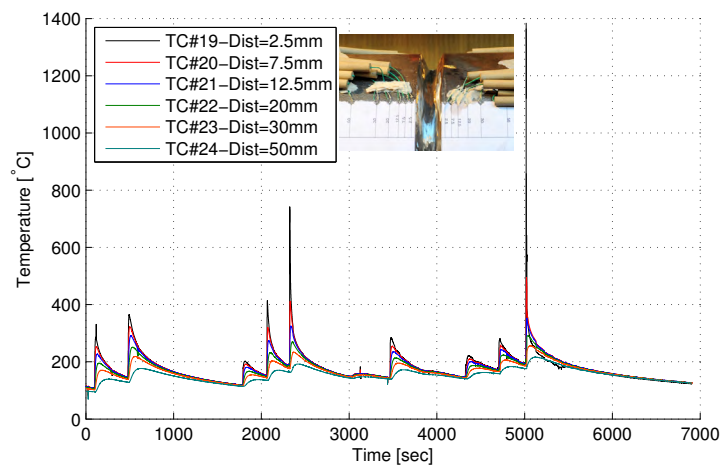




(a) Thermocouples on CHS, first location.

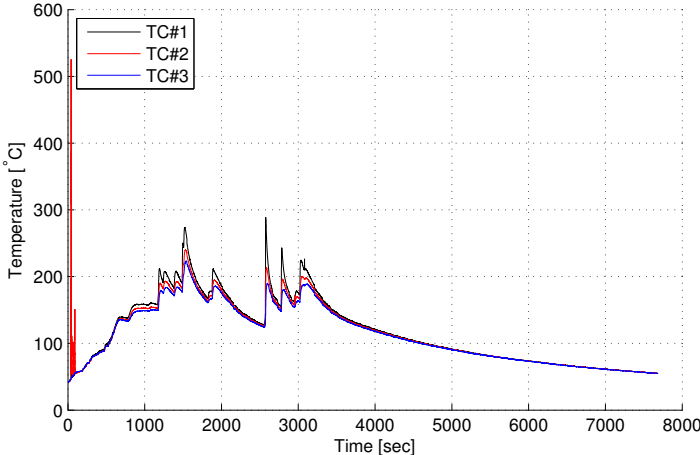


(b) Thermocouples on CHS, second location.

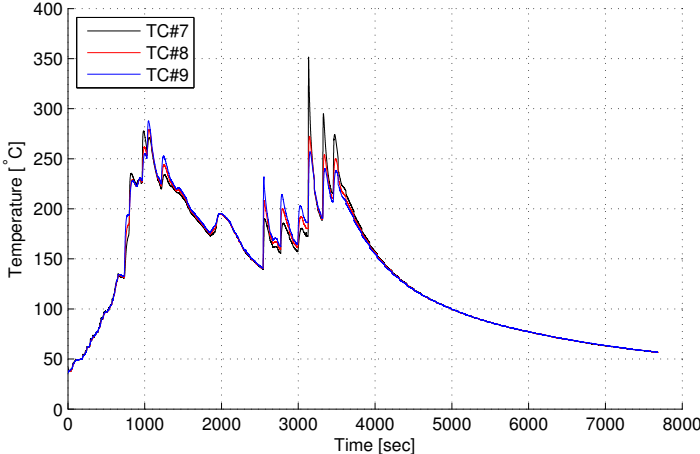


(c) Thermocouples on Cast node, second location.

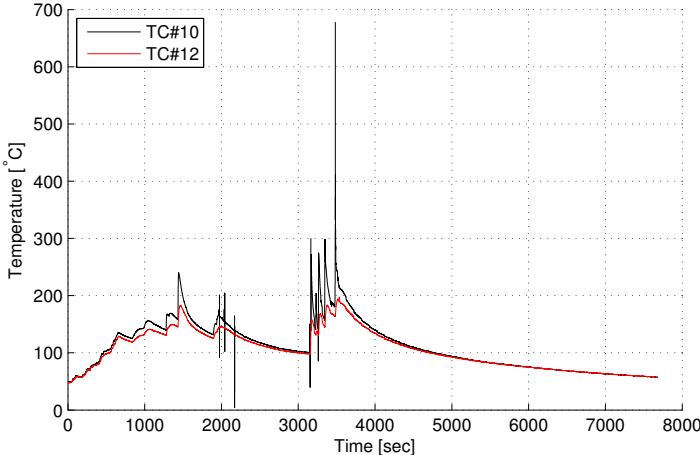
Figure 5.14: Registered welding temperature histories for CHS – cast joint. Distance of each thermocouple from the edge of the weld gap is mentioned on the corresponding legend entry in each graph. First and second locations have a 90° angular distance.



(a) Thermocouples on right-side crown heel.

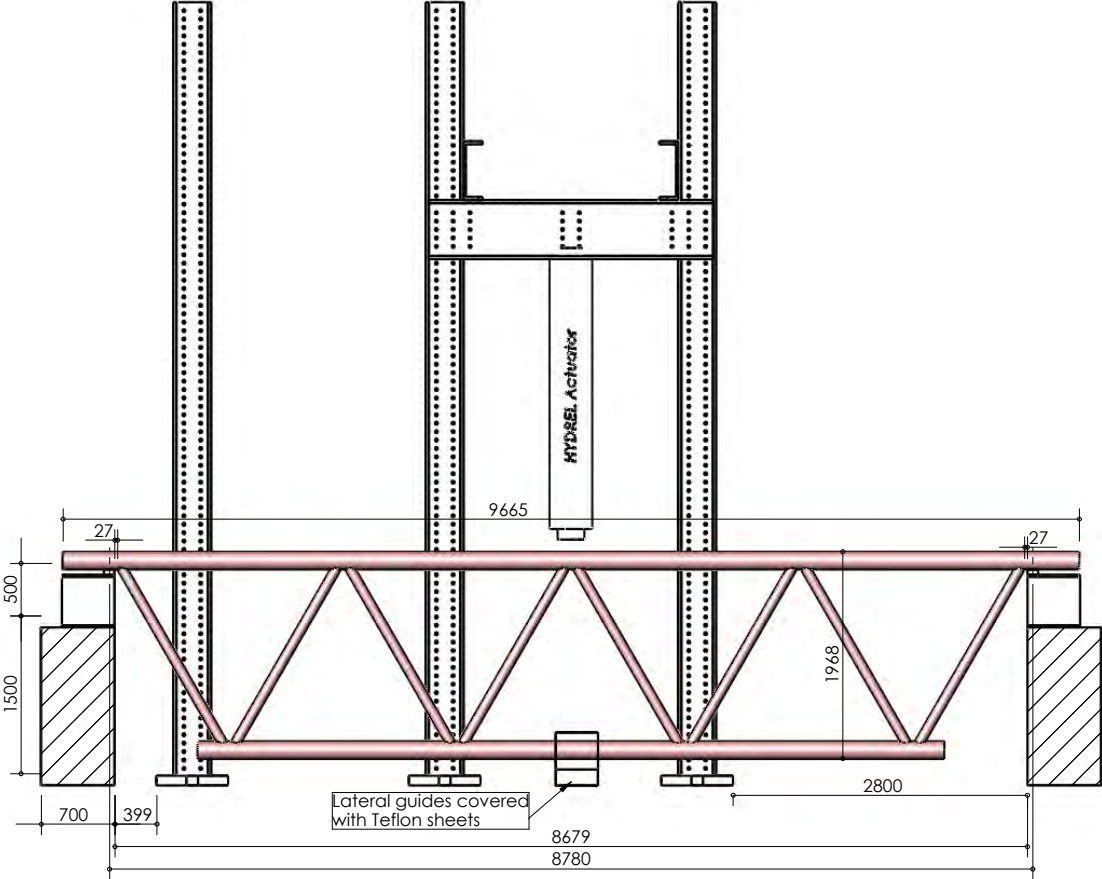


(b) Thermocouples on crown toe.

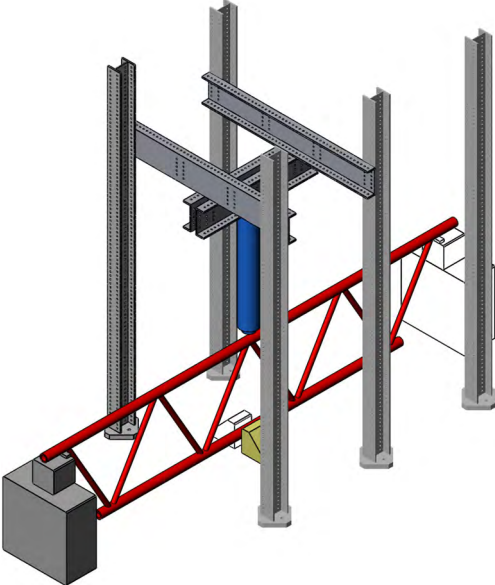


(c) Thermocouples on left-side crown heel.

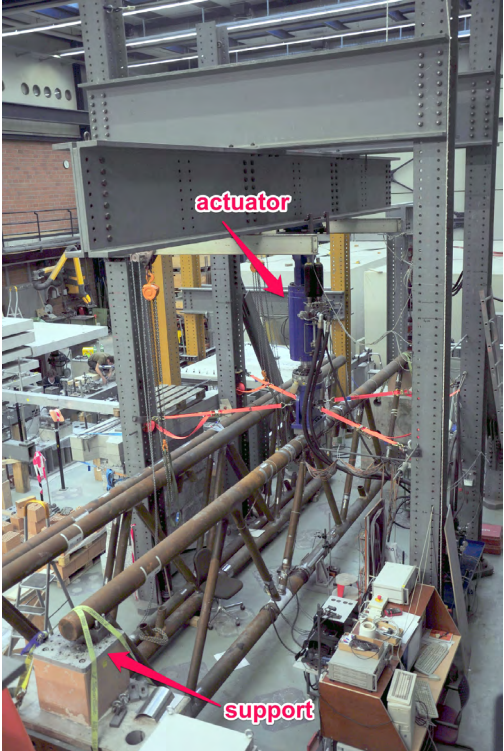
Figure 5.15: Registered welding temperature histories for K-joint. Thermocouple numbering for the K-joint is given in Figure 5.13



(a)



(b)



(c)

Figure 5.16: Test setup.

## Chapter 5. Fatigue experiments

Table 5.8: Load range ( $\Delta Q$ ), Maximum hot spot stress range and corresponding predicted fatigue life for test trusses.

Truss	$Q_{min}$	$Q_{max}$	$\Delta Q$	R	Max. hot spot stress	Design $N_4$	Predicted $N_4$
S10	30 kN	330 kN	300 kN	0.1	113 MPa	717 000	1 140 000-2 850 000
S11	50 kN	550 kN	500 kN	0.1	170 MPa	212 000	337 000-846 000

### 5.3.4 Test procedure

For each truss, the test started with static loading. The load was increased gradually in steps of 50kN or smaller and the deflection and strains were registered. The strain gage and LVDT values were checked to control out-of-plane bending (OPB) and symmetry of the stresses. The static test was repeated after a few cyclic loads (1000 cycles) to shake down. The static tests after the shake down did not show significant difference compared to the static tests at the beginning of the tests. Constant amplitude fatigue loading started after these preliminary tests. Cyclic loading was stopped at regular intervals to repeat the static tests and crack detection. After the failure of the first joint in each truss (J3S for truss S10 and J3N for truss S11), the tests were stopped temporarily to carry out the repair operation (see section 5.3.6) and then the cyclic loading continued. Truss S11 was tested first; The test lasted 516 000 cycles. Afterwards, truss S10 was tested with a lower load range up to 1 949 000 cycles.

### 5.3.5 Measurement methods

The following methods and equipment were utilized during the static and fatigue tests of S10 and S11 trusses:

#### Measurements during static tests

Strain gages of type HBM 1-LY11-10/120 (10mm grid length) were attached in pairs (one each at the extreme fibers for in-plane bending) to truss members at the locations shown in figures B.2 and B.3 for trusses S10 and S11, respectively. As can be seen in the Figures, half of each truss was instrumented more completely, while there were a few strain gages to control the symmetry on the other half. Two strain gage pairs (one for the top chord and one for the bottom chord) were attached to the chords' extreme fibers for out-of-plane bending at the mid-span location. Based on Schumacher's 2003 recommendation, the strain gages were located at a distance of  $1.9D$  from the joint center (for gages attached to the chords), and  $2.2d$  from the chord surface (for gages attached to the braces). A LVDT displacement transducer was installed at the mid-span on the lower chord to register maximum deflection during the fatigue tests. A HBM UPM 100 multipoint measurement device registered the strain gage data.

#### **Dye penetrant tests (PT)**

To detect the cracks during the fatigue tests, PT tests were performed on a regular basis. After applying the dye penetrant, a few fatigue cycles were applied to help the penetration of liquid into cracks; then the surface was thoroughly cleaned and the developer was applied.

#### **Ink and beach marking**

One way to have a *snapshot* of the crack at the time crack is growing, is to paint the crack face. Once the cracks were detected using other methods (PT test), an alcoholic ink (such as red Rotring drawing ink) was applied to the crack and was let to dry out. Since a second ink marking could wash out the first marking, this method was done only once on each crack.

In order to mark the crack shape in the subsequent stages of its growth, the beach marking method as described by Husset et al. (1985) was used. Change of load characteristics (e.g. load range, mean stress, or frequency) leads to change in crack features and can be seen on the crack face as *beachmarks*. The cyclic load range for the beach marking was reduced to half, while keeping the maximum load value. This special cyclic loading block was applied for 10000 cycles at regular intervals. Change of crack propagation rate during this reduced loading would show up as a thin line on the final crack face.

#### **Alternating Current Potential Drop (ACPD)**

The principle of operation for AC potential drop is given in section 5.2.1. One drawback of the method is that prior knowledge of crack location is needed in order to put the voltage probes on the two sides of the possible crack. However, this was not a problem for the studied welded joints whose cracking locations were known to be at the crown toe location.

A custom built ACPD instrument with working frequency of 5 Hz was used. Complete description of the instrument and its operation can be found in Costa Borges (2008) and Acevedo (2011). A HBM UPM 100 data logger acquired the ACPD data and transmitted them to a computer.

Voltage measurement showed that little electrical discharge through metallic supports and the actuator happens. Therefore, electrical insulation of the truss at the supports and at the load application pads which was suggested by Costa Borges (2008) deemed unnecessary.

On each truss, one joint was selected to be monitored by ACPD. All the 7 voltage probes were attached to the joint at the crown toe. Figure 5.17 shows the ACPD probe locations on the two monitored joints: S10-J5N and S11-J2. The arrangement of probes for the compression brace side and tension brace side for these joints is not symmetric. Fatigue cracking was expected to advance more profoundly in the compression brace for S10-J5N, and in tension brace for S11-J2. Therefore, larger number of probes (5 channels) were put on those brace connections,

## Chapter 5. Fatigue experiments

and two other probes on the other side. Attachment of electrical current connections at the vicinity of the joint is shown in Figure 5.18a. Figure 5.18b shows a close-up of the voltage probes at the joint's crown toe. The voltage probes were made of twisted pairs of steel wires attached to the chord surface by percussive arc welding. The distance between the probes was kept minimal to get satisfactory results.

Machine malfunctioning caused some problems in measurements. Despite sending the machine for the repair, the problems persisted. More noise was observed than what was registered in the previous measurements. Several time it happened that the electrical current was cut by the control unit during the fatigue test. This can be seen in the interruptions in the curves. The noise level was more than what was seen before.

The output signal from ACPD was first filtered to remove the invalid data generated by malfunctioning, and then filtered using a moving average function with a window size of 300 to smooth the output curve. The reference voltage  $V_R$  for each channel was calculated by averaging first measurements on the uncracked joint (flat part at the start of the curves in Figure 5.24).

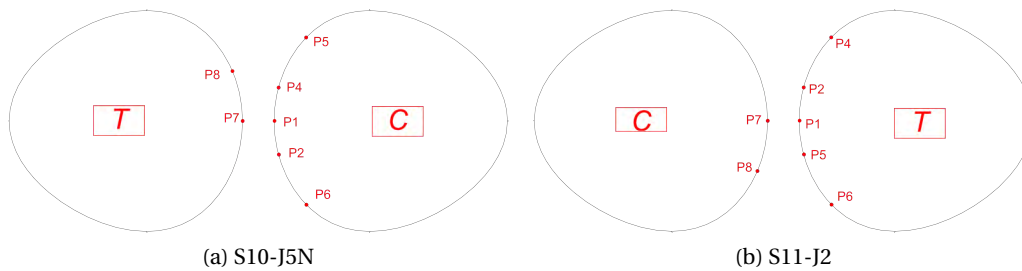
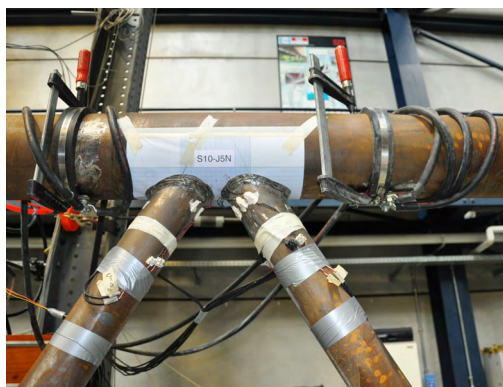


Figure 5.17: ACPD probes locations on joints S10-J5N and S11-J2.



(a) Voltage contacts attached with round-the-tube grips.



(b) Twisted wire probes attached to the cracking sites.

Figure 5.18: Setup on the truss joint for ACPD measurements.

### Eddy current sensors

Three joints S10-J1, S10-J3N, and S10-J5 were instrumented with Eddy current <sup>8</sup> sensors adapted to the shape of the weld profile

### 5.3.6 Repairs

The first failed joints due to excessive cracking in S10 and S11 trusses were S10-J3S (first failure at 1 292 000 cycles), and S11-J3N (first failure at 422 000 cycles), respectively. During each test and in order to continue cyclic loading to observe the failure of subsequent joints, the test was stopped, the repair operation was carried out, and then the test was resumed. A rapid repair method using post-tensioning – which did not require dismantling the truss from the test platform – was applied.

Post-tensioning has been used for strengthening of existing steel bridges to increase their load-bearing capacity or their service life since 1950's. Troitsky (1990) mentions several cases for both beam and truss bridges. One of the simplest solutions for rehabilitation of an existing structure using post-tensioning is to strengthen member(s) at risk with tendons concentric with the member (Albrecht and Lenwari, 2008). This method was chosen for the repair of the outermost brace connection in trusses S10 and S11.

Prestressing assembly consisted of two  $\varnothing 36$  threadbar tendons concentric with the brace and on the two sides of it (Figure 5.19d). The two tendons were connected to the truss by means of two support pieces that provided mechanical anchorage, as shown on Figure 5.19c. The two support pieces were made of tubes  $\varnothing 168.3 \times 30$  (steel grade S355J2H). Their geometry is shown in Figure 5.20. These pieces provided a mechanical anchorage system that fitted to the round shape of the chord.

The prestressing assembly was designed to completely dismantle after the test and to be reused for the subsequent test. Therefore, minimal welding on the truss was used. This had the extra benefit of reducing the number of fatigue hotspots added by repair. As it is usually the case in fatigue of welded structures, the fatigue resistance could actually decrease by *adding* material to the structure. Once the material was available, the mounting was rapid and took only one day. Figure 5.19 shows various steps to mount the assembly on the truss.

As can be seen in Figure 5.19a and c, the welding work on the truss consisted of:

- Two steel stopper pieces (120 mm L  $\times$  50 mm W  $\times$  30 mm T) at the location of extreme fibers of upper and lower chords. These pieces provided horizontal reaction to prevent slipping of mechanical anchorage system.
- Two small steel pieces on each chord to prevent revolving of support piece around chord axis due to unbalanced loading of the two tendons.

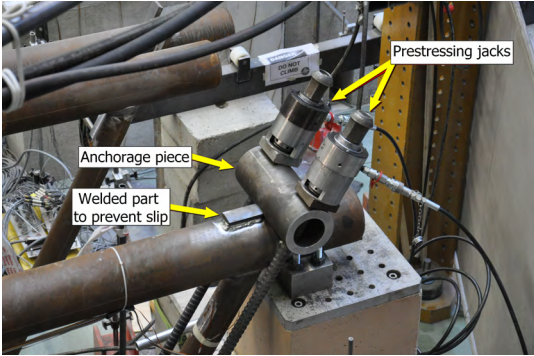
---

<sup>8</sup>Also called *Foucault currents*.





(a) Preheating the chord before welding of stopper piece.



(b) Prestressing using hydraulic jacks.



(c) Close-up of cracked joint after prestressing; crack fully closed.



(d) Repair assembly fully mounted on truss.

Figure 5.19: Repair of truss by prestressing the cracked joint.

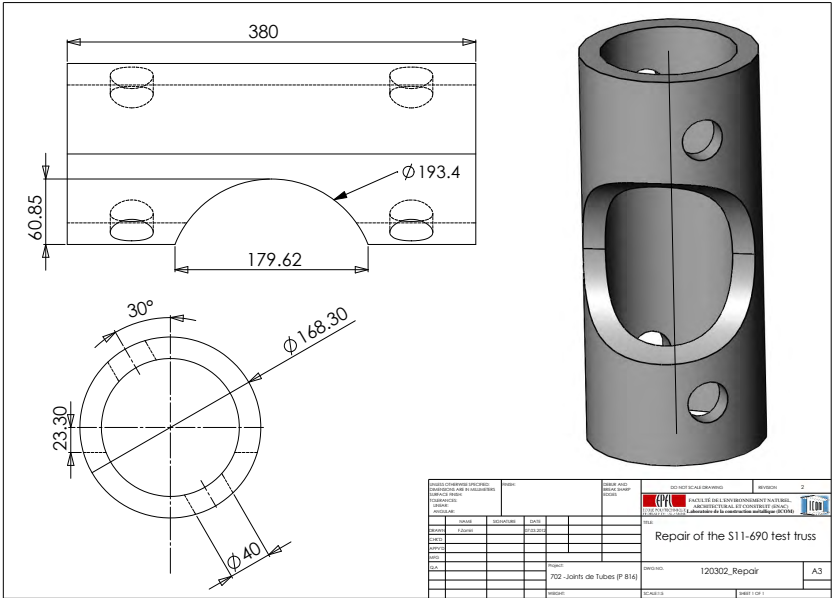


Figure 5.20: Designed piece for mechanical anchorage of tendons.



The actions in truss member and tendons due to external loading was calculated using following equation according to Albrecht and Lenwari (2008):

$$P_{br} + T_{tendon} - N = 0 \quad (5.9)$$

Where  $N$  is the effect of external loading and  $P_{br}$  and  $T_{tendon}$  are actions due to external loading in brace member and tendon, respectively. The small moments in the brace were neglected for the design of post-tensioning. Using equilibrium equation 5.9 and considering compatibility of deformations in tendon and brace members, gives<sup>9</sup>:

$$\begin{cases} T_{tendon} = \frac{A_{tendon}}{A_{tendon} + A_{br}} \cdot N \\ P_{br} = \frac{A_{br}}{A_{tendon} + A_{br}} \cdot N \end{cases} \quad (5.10)$$

Where  $A_{tendon}$  and  $A_{br}$  are cross section of tendons and brace member, respectively. Maximum total force in tendon and in brace then could be calculated:

$$\begin{cases} T_{total,tendon} = T_{tendon} + T_{PS} \\ P_{total,br} = P_{br} - T_{PS} \end{cases} \quad (5.11)$$

Where  $T_{PS}$  is post-tensioning force in unloaded structure. To have the brace always under compression (i.e. keeping the crack closed under maximum load), the  $T_{PS}$  should be equal to, or larger than  $P_{br}$ ; we chose:

$$T_{PS} = 1.2P_{brace} \quad (5.12)$$

Using the above equations for S11 specimen ( $Q_{max} = 500$  kN and  $Q_{min} = 50$  kN), maximum stress in tendons was calculated as  $\sigma_{max} = 116$  MPa and cyclic stress range as  $\Delta\sigma = 44$  MPa.

Prestressing threadbars DYWIDAG  $\varnothing 36$  made of steel grade 950 were used (DYWIDAG, 2009). Fatigue category of threadbars according to DYWIDAG catalog is 630; But SIA 262 [2003] prescribes a much lower fatigue category of 71 MPa with slope  $m = 4$  for the mechanical anchorage system. The stress range in tendons were well below this latter value. Post-tensioning

<sup>9</sup>The equations 5.10 hold if the material modulus of elasticity is the same for tendon and brace:  $E_{tendon} = E_{br}$ .

took place using manual hydraulic prestressing jacks (Figure 5.19b) with  $T_{PS} = 137$  kN. During the first static test after the repair, stresses in tendons were controlled by means of linear strain gages attached to them.

The effect of post-tensioning on the actions in other joints was controlled by strain gage measurements before and after the repair as well as by structural analysis of a beam element model of the truss. Except for the two neighboring joints to the repaired joints, the change of axial forces and moments in other joints were negligible (strain gage values changed less than 6%).

## 5.4 Results

### 5.4.1 Static tests

Deflection measurements during the tests prior to doing the repairs showed that the overall flexibility of the truss did not change with the first cracking in one of the joints. Right after the repairs a small increase in deflection (8% for S10 and 1% for S11) was observed. With progression of the tests after repair that led to cracking on the other joints, the deflections increased. Maximum deflections at the end of the tests for trusses S10 and S11 increased by 28% and 40%, respectively, compared to initial deflections.

The linearity and elasticity of response was controlled by deflection and strain gage measurement. As was stated in section 5.3.5, the strain gage data were used to verify the symmetry conditions, and to control that OPB was negligible. Figure 5.21 shows the registered strain gage data for truss S10. With careful adjustment of the supports, actuator, truss and the restraining slings, the symmetry conditions were mostly satisfied; however, some discrepancies between the symmetric strain gages attached to the upper chord was observed, as was the case in a previous study (Acevedo, 2011). This could be mainly due to the contribution from restraining effect of slings put on the supports to secure the truss in its place which resulted in a small negative moment at the support.

Nominal stresses in truss joints were numerically evaluated using a beam element structural model. Walbridge (2005) has compared various modeling options and concludes the following modeling procedure gives most accurate results:

- Nodal eccentricities are simulated by rigid links
- For brace elements' section properties in the connection region, the real section is used instead of rigid section properties.
- Brace moments are evaluated at brace-to-chord surface intersection.

This model – called model 'C' and originally introduced by Romeijn et al. (1997) – was used in current study. Euler-Bernoulli beam elements were used and the eccentricities in the

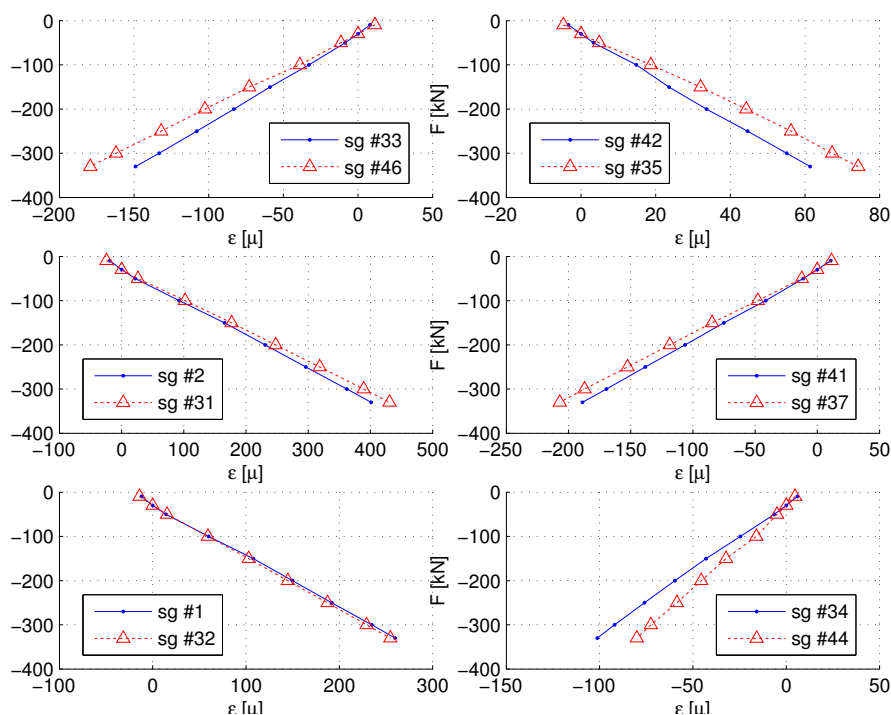


Figure 5.21: Strain gage data for control of the symmetry in truss S10. Locations of strain gages are indicated in Figure B.2.

supports were included in the model. The internal actions diagrams are shown in Figure B.4. based on the analysis results, nominal stresses in truss joints and their decomposition into bending and axial stresses were calculated and are shown in Figure 5.22. Figure 5.23 presents evaluated nominal stresses for cast nodes. Experimental evaluation of nominal stresses was possible for some of joint members; Measured chord and brace strain gage values were linearly extrapolated to the proper locations on joints<sup>10</sup> as described by Schumacher (2003) to evaluate the nominal strain ranges ( $\Delta\epsilon_{nom}$ ).

Nominal stress ranges ( $\Delta\sigma_{nom}$ ) are calculated from nominal strain ranges using Hooke's law. Stress state in the tubular member can be considered as plane-stress. Thus, axial stresses are calculated from following relation<sup>11</sup>:

$$\sigma_{xx} = \frac{E}{(1-\nu^2)} (\epsilon_{xx} + \nu\epsilon_{yy}) \quad (5.13)$$

Where  $x$  is the axis parallel to the member axis and  $y$  is the axis tangent to the member surface and perpendicular to  $x$ . axis  $z$  is perpendicular to the  $x$ - $y$  plane. Two distinct stress conditions

<sup>10</sup>The extrapolation point for the chords is the joint center; For the brace, it was the point where brace intersects chord surface.

<sup>11</sup>In uniaxial stress state,  $\sigma_{yy} = 0$  and  $\epsilon_{yy} = -\nu\epsilon_{xx}$ ; Therefore, equation 5.13 reduces to  $\sigma_{uniaxial} = E\epsilon_{uniaxial}$ .

can be identified along the member: (a) uniaxial stress conditions outside the perturbation zone of the joint; and (b) plane stress state in the joint region where  $\sigma_{yy} \neq 0$  due to restraint conditions. For the plane stress state in the joint zone, we can define the stress ratio  $R_{PS}$  as:

$$R_{PS} = \frac{\epsilon_{yy}}{\epsilon_{xx}} \quad (5.14)$$

Equation 5.13 can be rewritten as:

$$\sigma_{xx} = \underbrace{\frac{1 + \nu R_{PS}}{(1 - \nu^2)}}_{\text{Ratio K}} \underbrace{E \epsilon_{xx}}_{\text{uniax. stress}} \quad (5.15)$$

The ratio  $K$  mentioned above is equal to 1.10 for the case  $\epsilon_{yy} = 0$ . The range of 0.8 to 1.4 for  $K$  has been observed in previous studies (Romeijn, 1994). (Schumacher, 2003) found a range of 1.11 to 1.30 in her experiments with an average value of 1.17. In practice, it is usual to measure only  $\epsilon_{xx}$  using uniaxial strain gages, and then convert the strain values into stresses, using uniaxial Hooke's equation with an additional ratio  $K$  having a value between 1.1 to 1.2:

$$\sigma_{xx} = K \sigma_{uniaxial} = K E \epsilon_{xx} \quad (5.16)$$

Ambiguity has been observed in some publications on distinguishing between uniaxial and plane stress states for the case of hotspot stress evaluation. The following discussion is meant to clarify the subject:

- strain concentration factor (*SNCF*) definition in CIDECT guidelines (2000) is the ratio of hot-spot strain – evaluated by extrapolation of measured strains in the joint region (3D state) – to the nominal stress in the joint (uniaxial state).
- Similarly, stress concentration factor (*SCF*) is the ratio of hot-spot stress (plane stress state) to the member stresses away from joint (uniaxial).

Therefore, to convert *SNCF* values to *SCFs* in the experimental measurements,  $K_{SCF} = K$  ratio should be applied, as stated before:

$$SCF = \underbrace{\frac{1 + \nu R_{PS}}{(1 - \nu^2)}}_{K_{SCF}} \cdot SNCF \quad (5.17)$$

Equation 5.17 is the same as the one given by Lassen and Recho (2006). It should be noted that when doing 3D finite element analysis of the structure using shell or solid elements to calculate  $SCF$ , applying the ratio is apparently irrelevant, provided that the nominal stresses are calculated from axial and bending loads. This is also the case for the finite element analysis using beam elements, for which the purpose is to evaluate  $\sigma_{hs}$  using *nominal* stresses from FEM and  $SCFs$  from the existing tables and graphs.

The value of  $K_{SCF} = 1.1$  is used in this study for evaluation of stresses from measured strains. Table 5.9 summarizes nominal stress ranges in both S10 and S11, together with degree of bending (DOB, see following paragraph) for each member. Numbers in parentheses are experimentally determined and are generally in agreement with the numerical values. An exception is the measured chord stresses for joints J5N and J5S in Both S10 and S11 trusses, which show a large discrepancy compared to calculated stresses. Checking the strain gage values at the location close to joint J6 showed that the strain gages located at the top fiber of the chord were inside the zone perturbed by the loading pads (See section 5.3.3); So, they were not suitable for the calculation of nominal stresses. Thus, Schumacher's 2003 recommendation for placing of strain gages is valid for non-loaded joints and for joints in supports or under concentrated loads, larger distances – such as  $3 \times D$  value recommended by Van Wingerde (1992) – should be considered.

Degree of bendings (DOBs) shown in Table 5.9 indicate the ratio of nominal stresses to axial stresses and are calculated as (Schumacher, 2003):

$$DOB = \frac{\Delta\sigma_{nom}}{\Delta\sigma_{ax}} = \frac{\Delta\sigma_{ax} + \Delta\sigma_{ipb}}{\Delta\sigma_{ax}} \quad (5.18)$$

Where:

$\Delta\sigma_{nom}$  : Nominal stress range;

$\Delta\sigma_{ax}$  : Axial stress range;

$\Delta\sigma_{ipb}$  : In-plane bending stress range.

Degree of bending shows whether the bending stress adds up to axial stress at the studied location ( $DOB > 1$ ) or (partially) cancels it ( $DOB < 1$ ). For S10 and S11, DOB for the chords was smaller than 1, while calculated DOB for the braces was in the range 1.10 to 1.31. A similar trend was observed in previous fatigue tests of S3, S6, and S7. The value of measured DOB equal to 1.54 on S10-J3S can be associated with the negative moment at the support exerted by security slings.

Hot-spot stresses at the joints were calculated by multiplying axial and bending stresses in the joint by relevant stress concentration factors (SCF). according to CIDECT recommendations (Zhao et al., 2000), hot-spot stress at location  $i$  is calculated by superposition of individual

## Chapter 5. Fatigue experiments

Table 5.9: Nominal stress ranges and DOBs at crown toes for the joints of trusses S10 and S11 from structural analysis. The values in parentheses are deduced from strain gage measurements; Stress values are given in [MPa].

Joint	Chord at Tension-brace side				Chord at Compression-brace side			
	$\Delta\sigma_{ax-ch}$	$\Delta\sigma_{ipb-ch}$	$\Delta\sigma_{nom-ch}$	$\frac{\Delta\sigma_{nom-ch}}{\Delta\sigma_{ax-ch}}$	$\Delta\sigma_{ax-ch}$	$\Delta\sigma_{ipb-ch}$	$\Delta\sigma_{nom-ch}$	$\frac{\Delta\sigma_{nom-ch}}{\Delta\sigma_{ax-ch}}$
S10-J3N	0.0	0.0	0.0	0.00	16.6	-9.8	6.8	0.41
S10-J3S	0.0	0.0	0.0	0.00	16.6	-9.8	6.8	0.41
S10-J1	16.6	-3.4	13.2	0.79	32.1 (39.9)	-15.5 (-15.8)	16.7 (24.1)	0.52 (0.6)
S10-J2	16.6	-3.4	13.2	0.79	32.1 (35.6)	-15.5 (-18.1)	16.7 (17.4)	0.52 (0.49)
S10-J5N	-24.4 (-40.7)	0.5 (-3.9)	-23.9 (-44.6)	0.98 (1.10)	-8.3	10.2	2.0	-0.24
S10-J5S	-24.4 (-39.3)	0.5 (-11.6)	-23.9 (-50.9)	0.98 (1.30)	-8.3	10.2	2.0	-0.24
S11-J3N	0.0	0.0	0.0	0.00	24.9	-14.6	10.3	0.41
S11-J3S	0.0	0.0	0.0	0.00	24.9	-14.6	10.3	0.41
S11-J1	24.9	-5.1	19.8	0.79	48.2 (60.0)	-23.2 (-24.8)	25.0 (35.3)	0.52 (0.59)
S11-J2	24.9	-5.1	19.8	0.79	48.2 (51.6)	-23.2 (-24.6)	25.0 (27.1)	0.52 (0.52)
S11-J5N	-36.6 (-60.5)	0.7 (21.6)	-35.9 (-38.9)	0.98 (0.64)	-12.4	15.3	2.9	-0.24
S11-J5S	-36.6 (-60.8)	0.7 (3.9)	-35.9 (-56.8)	0.98 (0.94)	-12.4	15.3	2.9	-0.24

Joint	Tension-Brace				Compression-brace			
	$\Delta\sigma_{ax-br}$	$\Delta\sigma_{ipb-br}$	$\Delta\sigma_{nom-br}$	$\frac{\Delta\sigma_{nom-ch}}{\Delta\sigma_{ax-ch}}$	$\Delta\sigma_{ax-br}$	$\Delta\sigma_{ipb-br}$	$\Delta\sigma_{nom-br}$	$\frac{\Delta\sigma_{nom-ch}}{\Delta\sigma_{ax-ch}}$
S10-J3N	75.7	21.7	97.4	1.29	-76.5	-23.5	-100.0	1.31
S10-J3S	75.7 (86.8)	21.7 (46.9)	97.4 (133.7)	1.29 (1.54)	-76.5	-23.5	-100.0	1.31
S10-J1	71.8	14.0	85.8	1.19	-71.0	-7.0	-78.0	1.10
S10-J2	71.8 (76.3)	14.0 (22.2)	85.8 (98.5)	1.19 (1.29)	-71.0	-7.0	-78.0	1.10
S10-J5N	71.8	20.0	91.8	1.28	-76.5	-22.5	-99.0	1.29
S10-J5S	71.8 (76.9)	20.0 (27.6)	91.8 (104.4)	1.28 (1.36)	-76.5	-22.5	-99.0	1.29
S11-J3N	113.5	32.6	146.1	1.29	-114.8	-35.2	-150.0	1.31
S11-J3S	113.5	32.6	146.1	1.29	-114.8	-35.2	-150.0	1.31
S11-J1	107.8 (114.8)	21.0 (34.9)	128.7 (149.8)	1.19 (1.30)	-106.5	-10.6	-117.1	1.10
S11-J2	107.8	21.0	128.7	1.19	-106.5	-10.6	-117.1	1.10
S11-J5N	107.8 (115.2)	30.0 (40.4)	137.7 (155.6)	1.28 (1.35)	-114.8	-33.8	-148.5	1.29
S11-J5S	107.8	30.0	137.7	1.28	-114.8	-33.8	-148.5	1.29

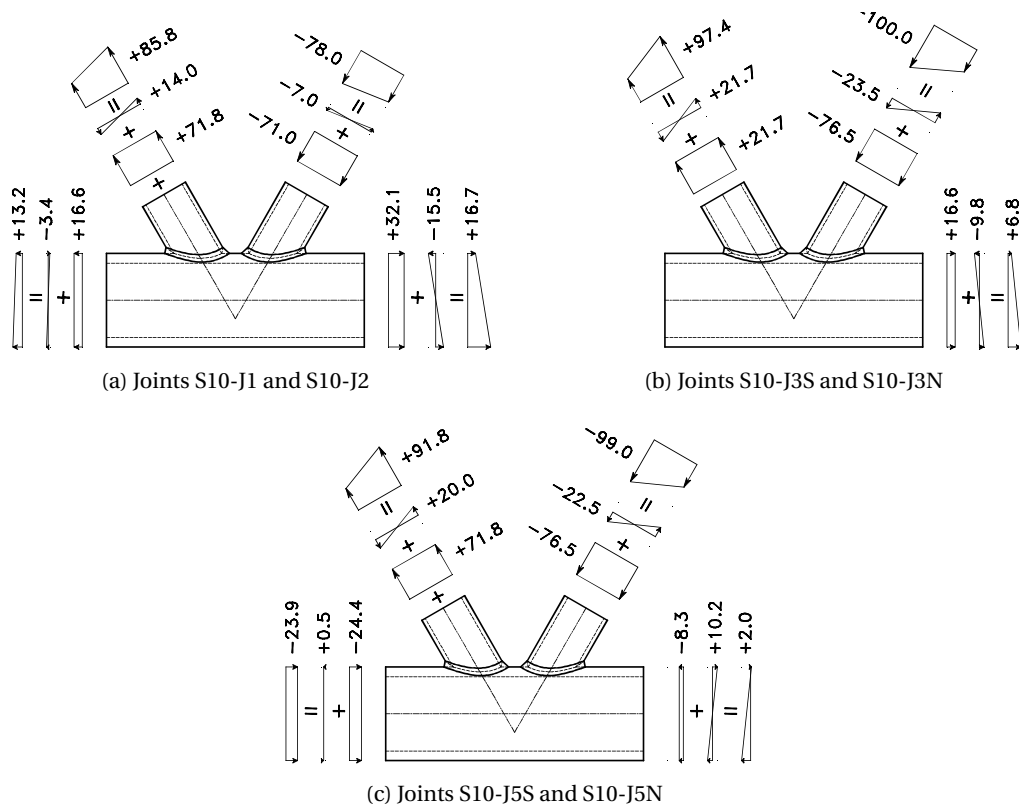


Figure 5.22: Nominal stress diagrams for K-joint in truss S10 (Units in MPa).

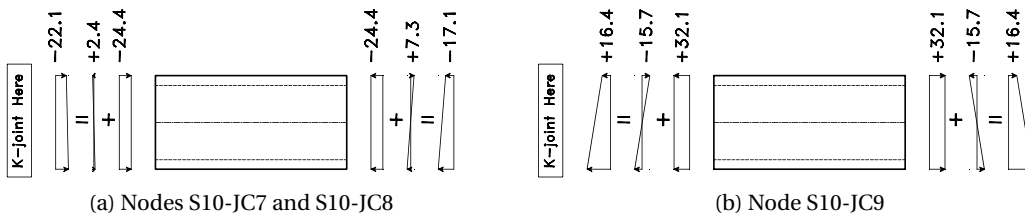


Figure 5.23: Nominal stress diagrams for cast nodes in truss S10 (Units in MPa).

load cases:

$$\Delta\sigma_{hs,i} = \sigma_{ax-br} \cdot SCF_{i,ax-br} + \sigma_{ipb-br} \cdot SCF_{i,ipb-br} + \sigma_{ax-ch} \cdot SCF_{i,ax-ch} + \sigma_{ipb-ch} \cdot SCF_{i,ipb-ch} \quad (5.19)$$

Where:

- $\Delta\sigma_{ax-br}$  : Stress range due to axial loading of brace member at location i;
- $\Delta\sigma_{ipb-br}$  : Stress range due to (balanced or unbalanced) in-plane bending of brace member;
- $\Delta\sigma_{ax-ch}$  : Stress range due to axial loading of chord member;
- $\Delta\sigma_{ipb-ch}$  : Stress range due to in-plane bending of chord member.

If we define a total nominal stress range ( $\Delta\sigma_{tot-nom}$ ) as:

$$\Delta\sigma_{tot-nom} = \Delta\sigma_{nom-br} + \Delta\sigma_{nom-ch} \quad (5.20)$$

Then a total SCF ( $SCF_{tot}$ ) can be defined as (Schumacher, 2003):

$$SCF_{tot,i} = \frac{\Delta\sigma_{ax-br}}{\Delta\sigma_{tot-nom}} \cdot SCF_{i,ax-br} + \frac{\Delta\sigma_{ipb-br}}{\Delta\sigma_{tot-nom}} \cdot SCF_{i,ipb-br} + \frac{\Delta\sigma_{ax-ch}}{\Delta\sigma_{tot-nom}} \cdot SCF_{i,ax-ch} + \frac{\Delta\sigma_{ipb-ch}}{\Delta\sigma_{tot-nom}} \cdot SCF_{i,ipb-ch} \quad (5.21)$$

Finally, the hot-spot stress at location i will be calculated simply using following equation:

$$\Delta\sigma_{hs,i} = \Delta\sigma_{nom-tot} \cdot SCF_{tot,i} \quad (5.22)$$

Geometric parameters of test trusses were not within the application range for SCF tables given by Zhao et al. (2000)<sup>12</sup>. Therefore, SCF tables provided by ICOM 489E publication (Nussbaumer et al., 2004) were used for calculation of stress intensity factors. These tables were the result of an extensive parametric study at a parameter range more suitable for bridge structures ( $0.5 \leq \beta \leq 0.7$ ,  $4 \leq \gamma \leq 30$ , and  $0.3 \leq \tau \leq 0.7$ , with realistic consideration of nodal eccentricities in FE models). Tables 5.10 and 5.11 summarize the hot-spot stress evaluation for the joints of the two trusses in two locations *hs1* (crown toe, tension brace side) and *hs1c*

---

<sup>12</sup> $\gamma = \frac{D}{2T} = 4.8$  and  $e = 38$  mm are outside application range of CIDECT tables ( $12 \leq \gamma \leq 30$  and  $e = 0$ )



(crown toe, compression brace side), respectively.

Table 5.10: Hot-spot stress ranges at the joints on the tension brace side (hs1); Stress values are given in [MPa]. SCF values are interpolated from ICOM 489E publication (Nussbaumer et al., 2004).

Joint	$\Delta\sigma_{ax-br}$	$SCF_{ax-br}$	$\Delta\sigma_{ipb-br}$	$SCF_{ipb-br}$	$\Delta\sigma_{ax-ch}$	$SCF_{ax-ch}$	$\Delta\sigma_{ipb-ch}$	$SCF_{ipb-ch}$	$\Delta\sigma_{tot-nom}$	$SCF_{tot}$	$\Delta\sigma_{hs1}$
S10-3S,3N	75.7	1.18	21.7	0.8	0.0	1.28	0.0	1.35	97.4	1.10	106.7
S10-1,2	71.8	1.18	14.0	0.8	16.6	1.28	-3.4	1.35	99.0	1.14	112.6
S10-5N,5S	71.8	1.18	20.0	0.8	-24.4	1.28	0.5	1.35	67.9	1.03	70.1
S11-3S,3N	113.5	1.18	32.6	0.8	0.0	1.28	0.0	1.35	146.1	1.10	160.0
S11-1,2	107.8	1.18	21.0	0.8	24.9	1.28	-5.1	1.35	148.5	1.14	168.9
S11-5N,5S	107.8	1.18	30.0	0.8	-36.6	1.28	0.7	1.35	101.8	1.03	105.2

Table 5.11: Hot-spot stress ranges at the joints on the compression brace side (hs1c); Stress values are given in [MPa]. SCF values are interpolated from ICOM 489E publication (Nussbaumer et al., 2004).

Joint	$\Delta\sigma_{ax-br}$	$SCF_{ax-br}$	$\Delta\sigma_{ipb-br}$	$SCF_{ipb-br}$	$\Delta\sigma_{ax-ch}$	$SCF_{ax-ch}$	$\Delta\sigma_{ipb-ch}$	$SCF_{ipb-ch}$	$\Delta\sigma_{tot-nom}$	$SCF_{tot}$	$\Delta\sigma_{hs1c}$
S10-3S,3N	-76.5	1.18	-23.5	0.8	16.6	1.28	-9.8	1.35	-93.2	1.08	-101.0
S10-1,2	-71.0	1.18	-7.0	0.8	32.1	1.28	-15.5	1.35	-61.4	1.13	-69.2
S10-5N,5S	-76.5	1.18	-22.5	0.8	-8.3	1.28	10.2	1.35	-97.1	1.08	-105.1
S11-3S,3N	-114.8	1.18	-35.2	0.8	24.9	1.28	-14.6	1.35	-139.7	1.08	-151.5
S11-1,2	-106.5	1.18	-10.6	0.8	48.2	1.28	-23.2	1.35	-92.1	1.13	-103.8
S11-5N,5S	-114.8	1.18	-33.8	0.8	-12.4	1.28	15.3	1.35	-145.6	1.08	-157.6

## 5.4.2 Crack propagation results

Figure 5.24 presents the low-pass filtered data of ACPD (probe voltages). Location of probes is given in Figure 5.17. These values were processed according to the procedure explained earlier to get the crack depth data. After opening up the cracks, the crack depth was measured and based on the measurement a correction factor was applied to the curves. Figure 5.25 shows these corrected values. Crack growth rates were derived from these corrected depth measurements and are shown in Figure 5.26. For the case of joint S11-J2 – which eventually failed under fatigue loading – majority of the fatigue life is spent in the propagation phase.

Figure 5.27 shows the change of deduced total stress intensity factors from the measurements with the crack depth. The considerable noise in the measurements is mainly due to the malfunction of the ACPD instrument. Nevertheless, the results can be used to qualitatively control the results of fatigue crack propagation analyses.

Chapter 5. Fatigue experiments

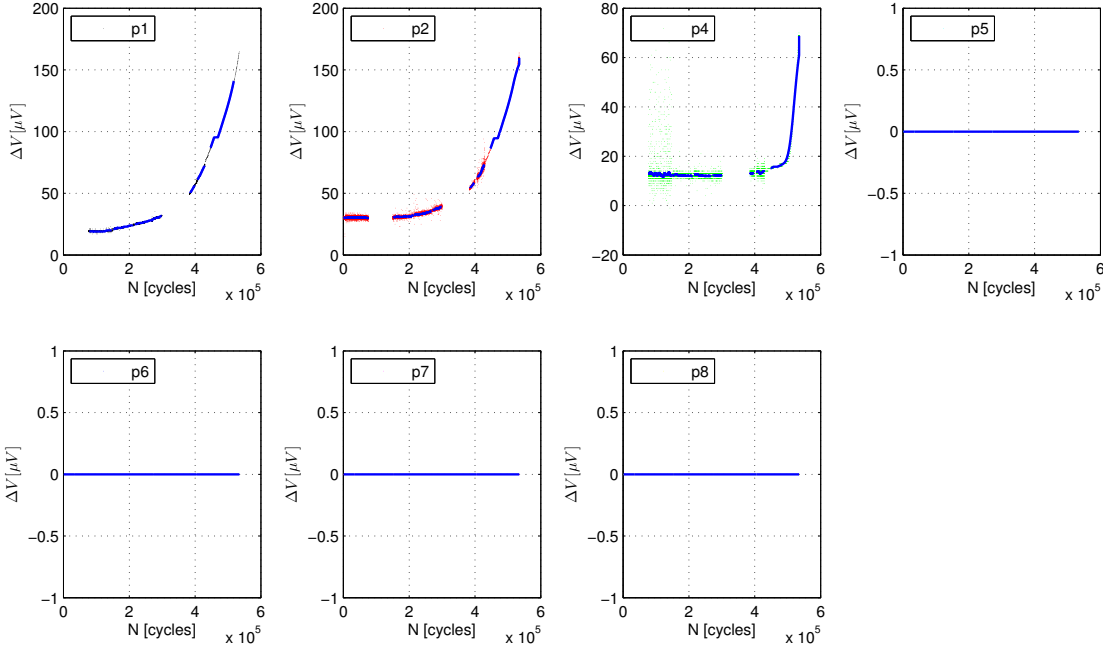
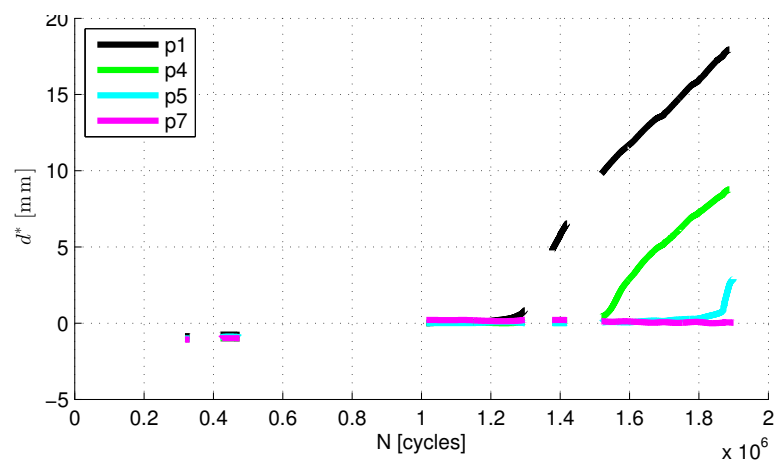
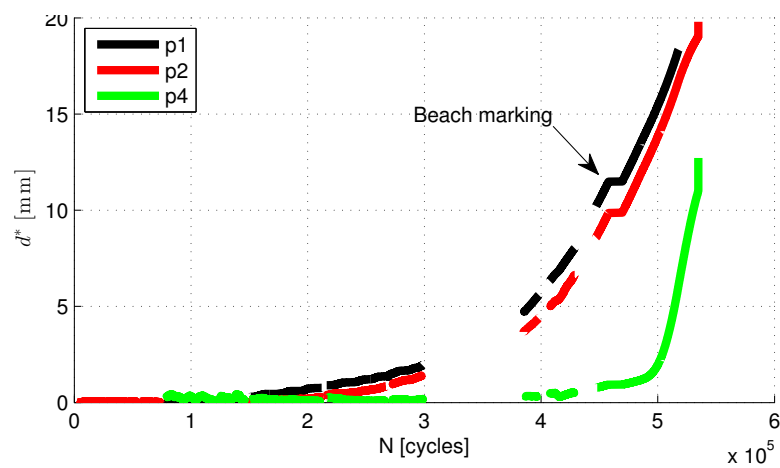


Figure 5.24: S11-J2+ ACPD data, low-pass filtered with a moving average function.

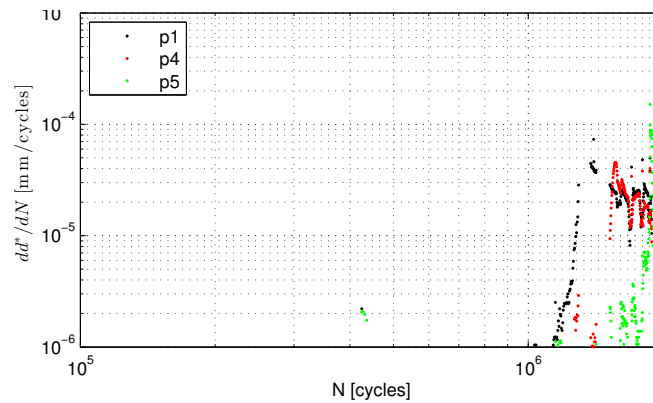


(a) S10-J5N-

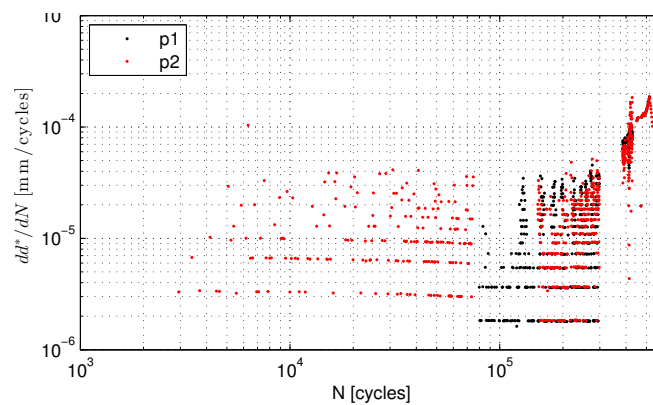


(b) S11-J2+

Figure 5.25: Crack depth corrected to the final crack dimensions ( $d^*$ ), measured by opening the crack after the test.



(a) S10-J5N-



(b) S11-J2+

Figure 5.26: Crack growth rates for joints S11-J2+ and S10-J5N-.

### 5.4.3 Post-mortem examinations

The cracked joints of the trusses were cut out, cooled down in liquid Nitrogen and broken to reveal the crack faces, according to procedure described by Acevedo (2011). Figure 5.28 shows the crack shape for a hotspot hs1 in joint S10-J3N after  $2 \times 10^6$  cycles of loading. The crack propagation in hot spot hs1c in joint S11-J5S and advanced cracking for hot spot hs1 in joint S10-J2 are shown in Figure 5.29. A close up of hs1c in joint S11-J5S is shown in Figure 5.30 which shows the cracking starts from several locations and continues by coalescence of those small cracks towards the forming of a single large crack.

Metallography specimens were also extracted from the crown toe location of the uncracked connections. One extracted metallography specimen and its parent part are shown in Figure 5.31. Hardness measurement results are presented in Figure 5.32. High hardness values up to Hv 417 were measured blow the rightmost weld pass, presumably because of martensite formation due to the high cooling rates. Optical micrographs of the HAZ and parent metal (etched with 2% Nital) are shown in Figure 5.33.

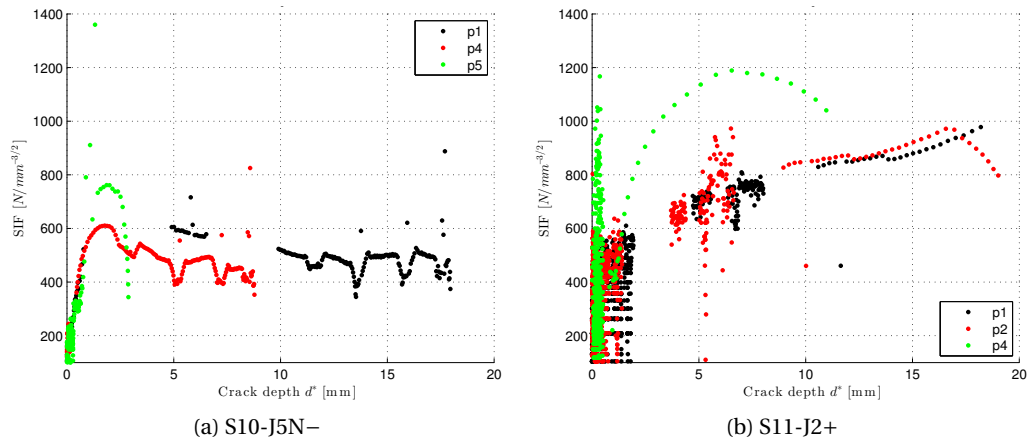


Figure 5.27: Evolution of Stress Intensity Factors with crack depth.



Figure 5.28: Cracking of joint S10-J3N (tensioned brace side).

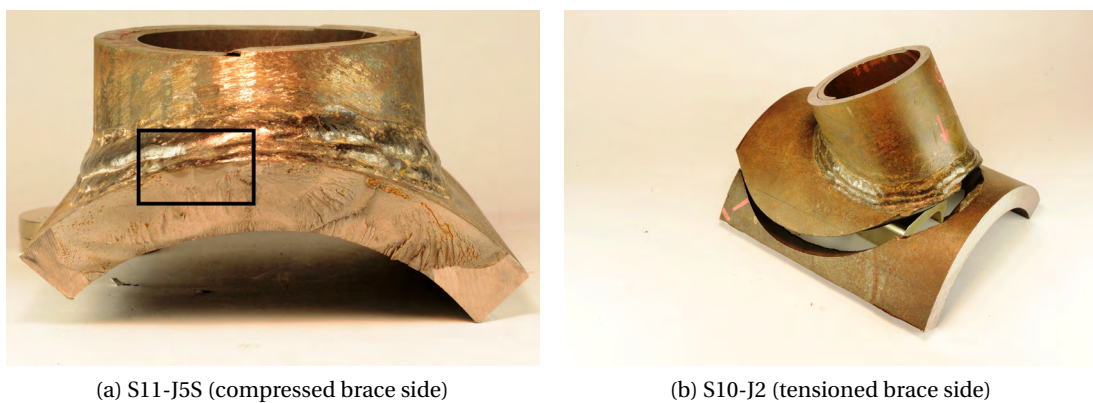


Figure 5.29: Partially cracked (a) and fully cracked (b) joints. See Figure 5.30 for a close-up of partially cracked (marked) region of joint S11-J5S.

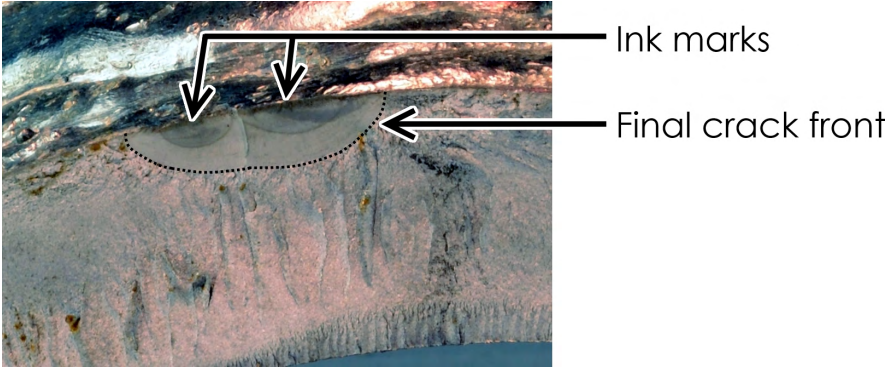


Figure 5.30: Close-up of cracking in S11-J5S.



Figure 5.31: One extracted metallography specimen and the parent part (S10-J2).

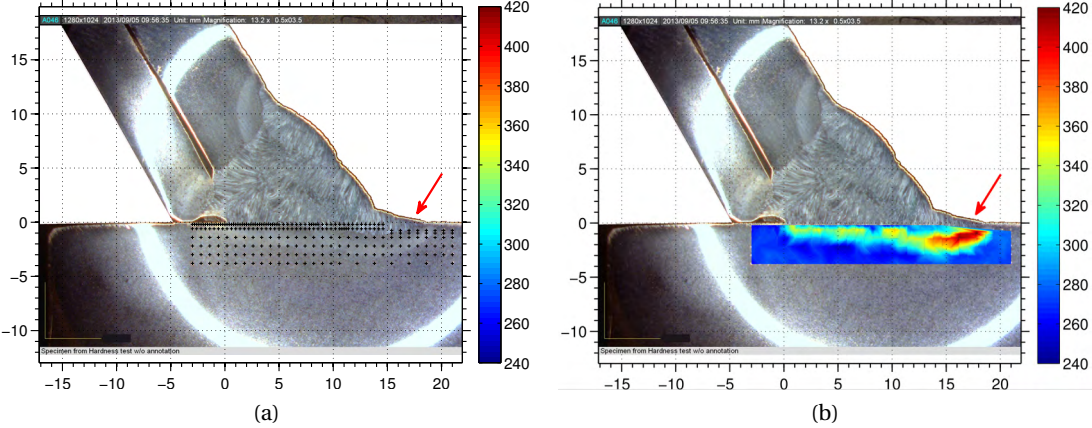


Figure 5.32: Hardness measurements at crown weld toe location.



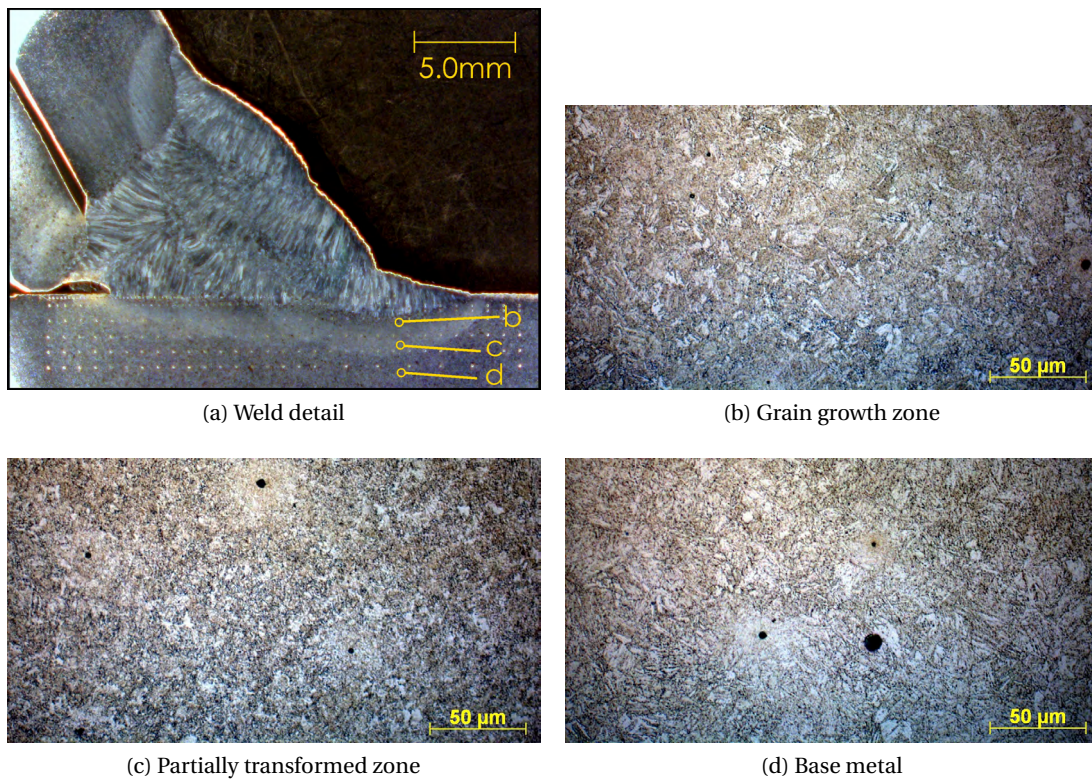


Figure 5.33: Optical micrographs of the extracted specimen at crown toe etched with 2% Nital.

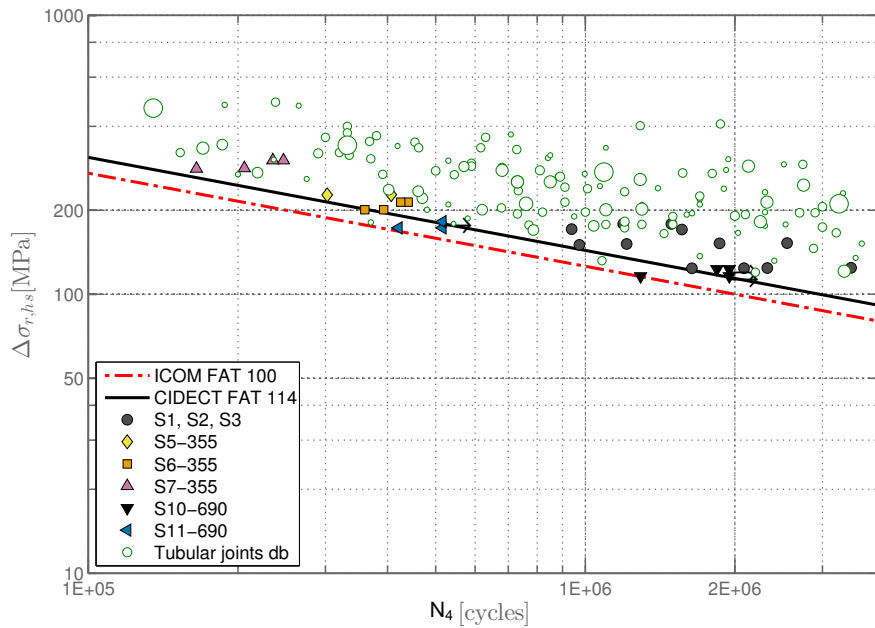


Figure 5.34: S-N curves for K-joints of trusses S10 and S11 compared to trusses previously tested at ICOM.

## 5.5 Discussion

### 5.5.1 $S_{r,hs}-N$ Curves

S-N curves for the K-joints and for CHS–cast node connections are presented in Figures 5.34 and 5.35, respectively. Size effect is included in the calculation of hot spot stresses for K-joints. The results of previous tests and a database of fatigue tests from IIW are included in the S-N curves for K-joints. Fatigue strength curve of category 100 used together with SCF values by Schumacher can be applied for fatigue strength determination of S690Q K-joints. Detailed results of all ICOM fatigue tests – including the results of present study – can be found in Table C.1 for K-joints and Table C.2 for CHS–Cast joints in the Appendix.



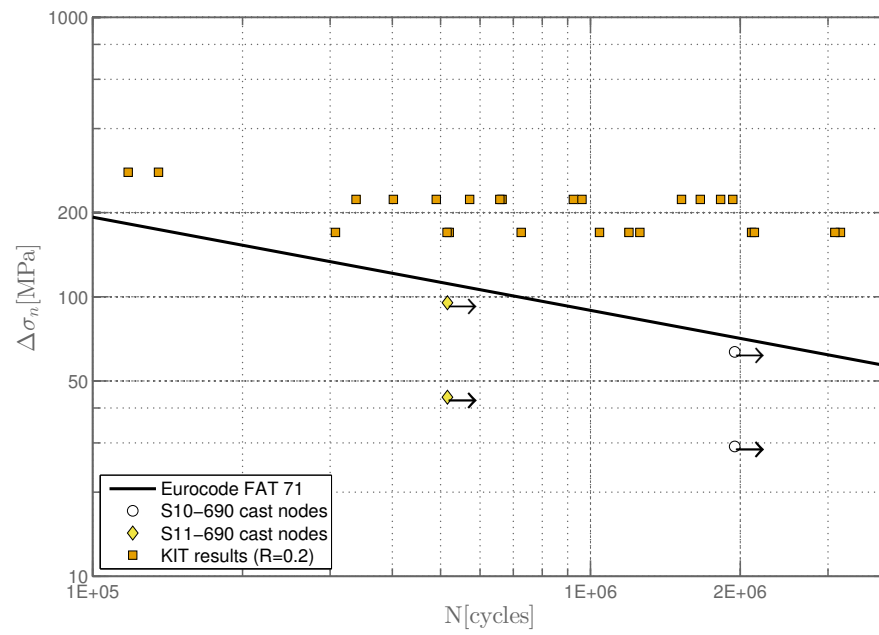


Figure 5.35: S-N curves for cast nodes of trusses S10 and S11.

### 5.6 Conclusion

- Fatigue strength of the tested S690 K-joints is in agreement with CIDECT's strength curves. The hotspot S-N curve could be classified in the same category as S355 K-joints.
- No cracking in the cast nodes and in the joints between cast nodes and tubes was observed.
- Cracking occurred exclusively in locations 1 and 1c (c.f. Figure 3.1), as was the case for previous fatigue tests carried out on S355J2H steel at ICOM.
- No root cracking was observed in the fatigue tests of S690 trusses, as it was the case for the former tests on S355 specimens.
- A fast repair method using post-tensioning – which did not require dismounting the truss from the test platform – was successfully used.
- Recommended hot spot design S-N curve for the K-joints is FAT 100, to be used with SCF values given by Schumacher.

# 6 Modelling of welding

## 6.1 Introduction

This chapter presents the procedure for numerical simulation of welding temperature field and corresponding weld-induced residual stresses. Various simulation approaches are investigated and validation of models is discussed. Finally, the computed residual stresses are compared to values from neutron diffraction measurements. Physical model and fundamental equations governing the coupled thermal-mechanical fields were discussed in Chapter 2.

Computational welding simulation is considered as a relatively difficult analysis because of complexities in geometry and boundary conditions, and nonlinearities due to temperature dependency of thermo-physical material properties. This also makes the analyses time consuming, added the requirement of a relatively fine mesh in the region of interest in order to capture the local effects of heating. For the case of tubular K-joint studied here, modelling and analysis would become even more lengthy as a result of complex geometry of weld line and numerous weld passes on the two weld beads. Therefore, selecting proper simplifying assumptions is an inevitable step. One objective of analyses is to determine modelling simplifications that would yield acceptable results with reasonable computation effort.

Morfeo/Welding<sup>1</sup> software (MORFEO, 2012) from Cenaero research centre was used for the welding simulations in this study. Morfeo is developed for manufacturing simulation tasks and features transient thermal-metallurgical-mechanical transient analyses. It features a variety of heat source models (double ellipsoid with Gaussian distribution, cylindrical, double elliptic cone) and modelling options (such as time-based and temperature-based element activation), and can be used in modelling of a range of welding processes, such as electric arc welding, Electron Beam Welding (EBW), and Friction Stir Welding (FSW).

---

<sup>1</sup>Manufacturing Oriented Finite Element tOol

### 6.2 Modelling simplifications and assumptions

As pointed out in Chapter 2, simulation of welding process comprises analysis of thermal, mechanical and metallurgical fields. Taking into account the dominant interaction effects and neglecting the weak couplings between those three fields, the analysis procedure is done in a sequential manner starting with thermal analysis, followed by metallurgical and mechanical analyses.

Nonetheless, for a modelling that is both sufficiently accurate and computationally cost effective, the complex phenomena involved in welding need to be simplified using proper assumptions. Those assumptions are discussed in this section.

#### 6.2.1 Weld pool modelling

Analysis of several multiphysical phenomena going on in the molten weld pool is the subject of so called “welding process simulation”, as pointed out in section 2.3.1. The result of such a simulation would be the weld width, penetration depth, and shape of the molten pool. In order to avoid this analysis, all the processes in the weld pool are encapsulated in a moving heat source model with a relatively simple geometry (Alberg, 2005; Goldak and Akhlaghi, 2005; Radaj, 2003). In this study, the shape of the heat source geometry was considered as either cylindrical or double ellipsoidal (Goldak et al., 1984).

#### 6.2.2 Modelling of weld metal deposition

When modelling a multipass welding process, additional issues arise, in comparison with single-pass welds. One issue is modelling the addition of weld metal. For the analysis, the mesh for the completed part is created; but the elements belonging to *'not laid'* welds are removed at the start of analysis. They are then added gradually to the model with the progress of welding heat source. Two approaches for simulating addition of filler material exist in literature (Lindgren, 2007; Radaj, 2003):

- Quiet elements: All the elements are available from the beginning of the analysis, but *zero* material properties (e.g. low values for young modulus and yield stress) are assigned to the elements which belong to the unlaidd weld parts. Once the heat source reaches these elements, real material properties are assigned to them.
- Inactive elements: The elements are added to the computational model at the time corresponding to the time of addition of weld metal.

According to (Lindgren, 2007) both methods work well and differ only in computation cost and stability of the finite element analysis (very low material properties can lead to an ill-conditioned global stiffness matrix).

Another assumption would be to totally neglect metal deposition and to consider the final geometry (Base metal+Weld) from the beginning of analysis. For the case of single-pass weld, this gives residual stress results that are similar to the results from a model with element activation applied, as shown in a previous publication (Zamiri et al., 2012); However, this does not apply to the case of multipass welds.

Morfeo provides quiet element approach. Furthermore assignment of real properties can be done based on time or based on temperature. In this study, the first option – activation by time – is used because the other method could produce analysis instabilities. In the temperature activation method, the elements are activated once the temperature reaches a threshold value (melting point). A small numerical error could lead to activation of some isolated elements and corresponding convergence problems. In the time-based element activation, a moving box passes along the weld trajectory with a user-defined speed, which is the same as the speed of the weld torch. When the moving box passes an element, that element is activated and will remain active for the rest of analysis. The effect of filler metal addition on the thermal solution is neglected, since the boundary conditions and the global stiffness matrix do not change considerably. However, the element activation is applied for the solution of the mechanical domain.

### 6.2.3 Weld pass reduction

In order to reduce the computation effort for simulation of multipass weld, some simplifications are suggested in literature regarding laying the welds (Lindgren, 2001c). One approach is to lay each weld pass at once (i.e. infinite welding speed). The other possibility is to lump several weld passes into one equivalent pass which will be laid gradually (Lindgren, 2007; Radaj, 2003). The equivalent heat flux and operating time can then be calculated, according to Radaj (2003):

$$\begin{aligned} q_{eq} &= \frac{1}{t_{eq}} \sum_{i=1}^n q_i t_i \\ t_{eq} &= \frac{1}{n} \sum_{i=1}^n t_i \end{aligned} \tag{6.1}$$

Where:

- $q_{eq}$  : Equivalent heat flux [W];
- $t_{eq}$  : Equivalent operating time [s].

This modelling simplification is comparable to the case where a large heat input and more weld metal are deposited in fewer weld passes. For the studied case of tubular bridge, this simplification was applied. The selection of lumped weld passes was not only due to reduction in computation time, but also because the complex weld geometry was too difficult to model

in a pass-by-pass basis for 8 passes. The weld passes on each weld bead were lumped into three weld passes as will be explained in section 6.3. Selection of three passes was based on the investigation of Dong and Hong (2002) and satisfactory results of a previous research at ICOM (Acevedo et al., 2013). Figure 6.1 shows how the lumped weld passes compare to the real welding sequence; The sequence of laying real weld passes is preserved in the model.

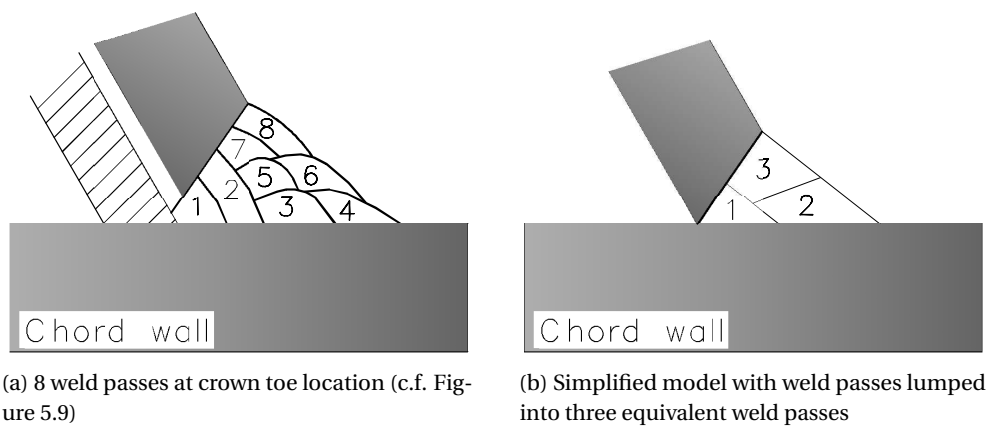


Figure 6.1: Weld pass reduction for 8-pass K-joint weld; Cross section of lumped weld pass 1 is 20% of total weld cross section and cross sections of weld passes 2 and 3 are 40% of total weld cross section each.

Further reduction of weld passes down to one equivalent single pass has also been investigated by author (Zamiri et al., 2012) and by others (Acevedo et al., 2012). Comparing the results from equivalent single pass and three-pass models showed a slight change in the residual stress field in the region of interest (i.e. gap region). For the transversal residual stresses, the position of peak was predicted closer to the surface and decrease of tensile residual stresses with depth was faster in the case of three-pass weld model, because of more gradual heat input. Another reason for modelling in 3 lumped passes (and not in 2 or 4) is the fact that a pass is deposited (in the proper order) at each of the three weld transition to base metal (the weld root and the 2 weld toes). All the models presented in this chapter, were modelled with three lumped weld passes. However, for large models used in convergence study, the equivalent single-pass model was utilized.

### 6.2.4 Symmetry in model

There are two symmetry planes for the geometry of K-joint; However, the thermal loading is not symmetric and hence full symmetry conditions do not hold. In this study, a *semi-symmetry* assumption for the symmetry plane passing through the middle of the gap and being perpendicular to the chord axis was investigated. For the semi-symmetric model, only welding of one brace – i.e. Y-joint – was modelled and the residual stress field was compared to the K-joint to see whether the so called “restraining effect” in transversal residual stresses (Acevedo et al., 2013) is due to structural interaction of the two braces or is simply superposition of the

two residual stress fields.

### 6.2.5 Utilized units system

Table 6.1 presents the metric units of various quantities and a consistent set of units used in modelling.

Table 6.1: Consistent system of units adopted in the simulations.

Physical quantity	Symbol	Regular unit	Conversion factor	Used unit
Mass	$m$	kg	–	kg
Length	$L$	m	$10^3$	mm
Time	$t$	s	–	s
Temperature	$T$	°C	–	°C
Density	$\rho$	$\text{kg m}^{-3}$	$10^{-6}$	$\text{kg mm}^{-3}$
Force	$F$	N	$10^3$	mN
Stress	$\sigma$	MPa	$10^3$	kPa
Thermal Conductivity	$\lambda$	$\text{W m}^{-1} \text{K}^{-1}$	$10^3$	$\mu\text{W mm}^{-1} \text{K}^{-1}$
Mass Specific heat capacity	$c_p$	$\text{J kg}^{-1} \text{K}^{-1}$	$10^6$	$\mu\text{J kg}^{-1} \text{K}^{-1}$
Heat energy	$E$	J	$10^6$	$\mu\text{J}$
Heat power	$Q$	W	$10^6$	$\mu\text{W}$
Volumetric Heat flux	$q$	$\text{W m}^{-3}$	$10^3$	$\mu\text{W mm}^{-3}$

## 6.3 Geometry of the model

The geometry was created with the method explained by Costa Borges (2008) (see also Figure 5.4b) and with dimensions mentioned in 5.3.1. Since the method is lengthy and includes several operations on volumes with intricate geometry (adding, intersecting, merging), Abaqus/-CAE (ABAQUS, 2012) was selected for pre-processing the model geometry, as it provides versatile modelling options for such geometries. A Python script was written to automate the generation of the geometry through Abaqus scripting interface.

Weld bead was divided into three passes by selecting sections on the saddle points and on the crown points and partitioning them to three parts as shown in Figure 6.2. Section area of weld pass number 1 was 20% of the total weld area, and the section area of weld passes 2 and 3 were 40% of the total cross section each. The face of weld line number 1 was assumed to be parallel to the final weld face.

The length of the chord and braces in the joint were taken large enough to allow for reproducing the cooling times of the welded parts similar to the real joints. Obviously, the mass of the material and surface area of the modelled joint were in any case smaller than the real truss. Increasing the length could slightly increase the accuracy, but the computation times would increase. The selection of member lengths in the model was carried out such that the majority

of the heat loss through conduction and convection was captured by the model, without the cost of very long computation times.

### 6.3.1 Weld torch trajectory

Weld torch trajectory for each weld pass was defined at the (curved) center line of the weld face. The position of the weld torch was perpendicular to the weld face, as shown in Figure 6.3. Stockie (1998) assumed a welding trajectory to be as bisector of the dihedral angle<sup>2</sup>. Since the weld shape is approximately an isosceles triangle, the direction of weld torch taken here agrees well with the recommendations given by Stockie.

For the start/stop points, two variants were considered. In the first variant, the heat source moved from crown toe towards crown heel; In the second variant, the start points were located between crown points and saddle points, which corresponded better with the real welding sequence (See figure 5.11). The reason for having two variants was to assess the effect of start/stop points on residual stress distributions.

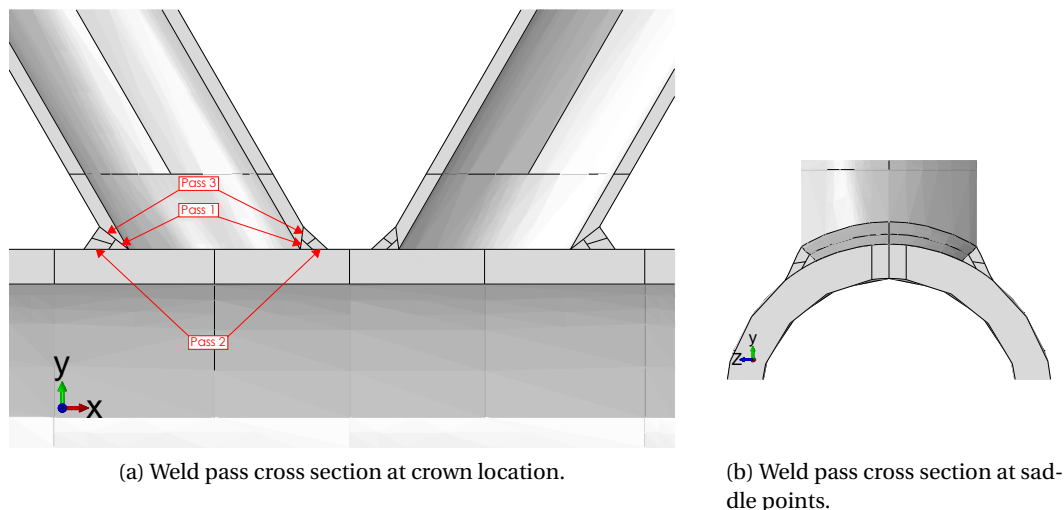


Figure 6.2: Weld section partitioning at various locations along the weld line.

## 6.4 Finite element meshes

The geometry was meshed with first order (linear) tetrahedral solid elements. The reason was that these elements give satisfactory accuracy within a reasonable computation time. Although hexahedral elements exhibit better convergence Lindgren (2001a), but the complicated geometry makes the meshing difficult and resulted ill-shaped hexahedral elements reduce the accuracy.

The generated mesh for the K-joint is shown in Figure 6.4. The Global element size was 16 mm

<sup>2</sup>The angle between chord and brace surfaces at selected point.



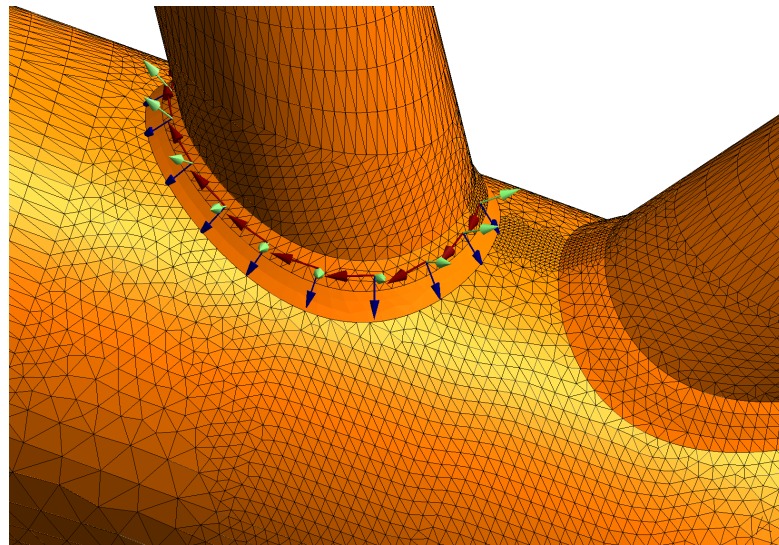


Figure 6.3: Weld torch trajectory for the third weld pass. The triads depict the pass of the weld torch along the weld line. The normal-to-surface vector (colored light green) shows the torch direction.

which was refined in the vicinity of weld region to 5 mm. For the region of interest (ROI, i.e. gap region), element size was refined more – up to 2 mm – to capture the residual stress profile in this region with sufficient resolution. Information on the mesh size is given in Table 6.2 (Fine mesh model).

#### 6.4.1 Convergence study

For mesh h-convergence study, three mesh sizes were selected, as shown in Table 6.2. Figure 6.4 shows the details of “fine” mesh while Figure 6.5 depicts mesh details at the gap region – denoted as Region Of Interest (ROI) in Table 6.2 – for the two other models; one being one step coarser and the other being one step finer than the mesh shown in Figure 6.4. Mesh size in the far field was kept the same for all three models (16 mm edge size) as it would not affect the results, nor the computation time considerably; instead, the mesh size in the weld line region and in the gap region were modified. All meshes had acceptable quality regarding worst element aspect ratio and distorted element. Figure 6.6 shows the comparison of the results of analysis of the three models for an equivalent single-pass weld in terms of temperature history and residual stress profiles at the weld toe. A convergence trend can be observed between the three models from coarser mesh to the finer mesh, and the agreement between results of the “very fine” and “fine” meshes was satisfactory. The latter was used for the subsequent analyses. A convergence study on element type did not seem necessary because of the high computation cost of higher order elements they could not be used anyway.

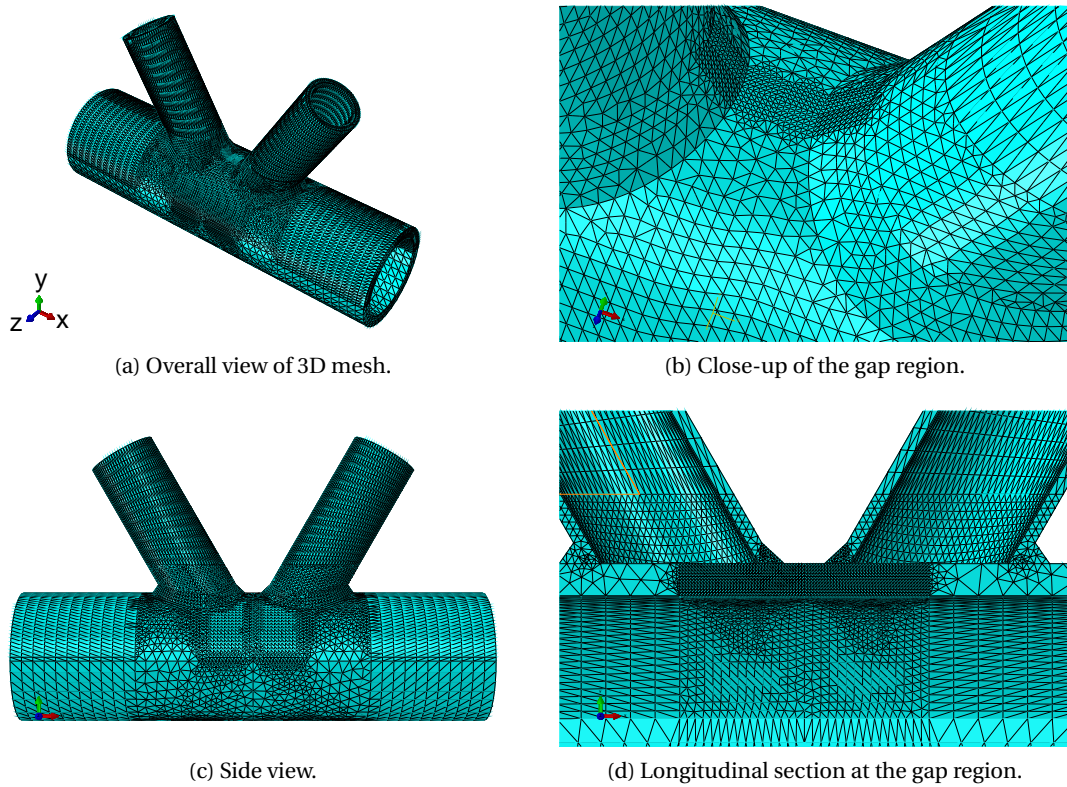


Figure 6.4: Details of FE mesh (fine mesh model).

Table 6.2: Models used in h-convergence study.

Model	Mesh size (ROI/Weld region/Far field)	$N_{element}$	$N_{node}$	Runtime [hours]
Very fine mesh	1 / 3 / 16	430226	79322	31 (4 CPUs)
Fine mesh	2 / 5 / 16	250328	51529	14 (4 CPUs)
Coarse mesh	2 / 10 / 16	132985	26818	3 (4 CPUs)

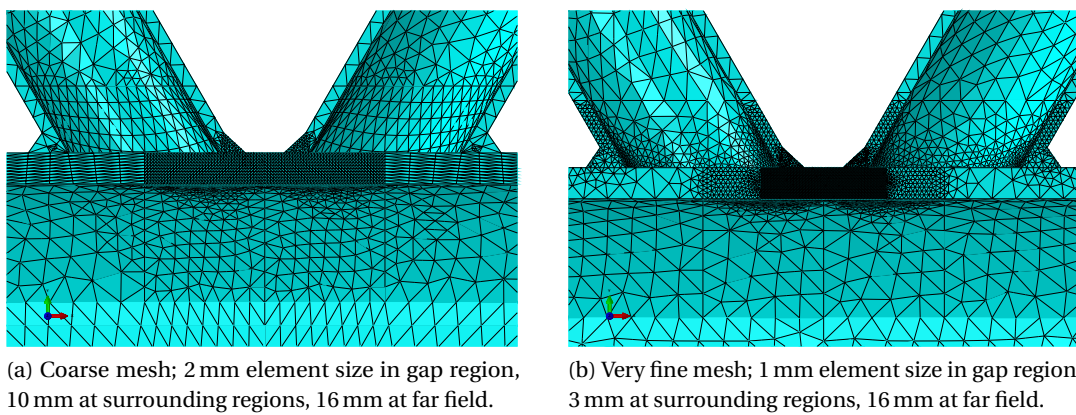


Figure 6.5: Coarse mesh and fine mesh details; Longitudinal cut at the gap region.

## 6.4. Finite element meshes

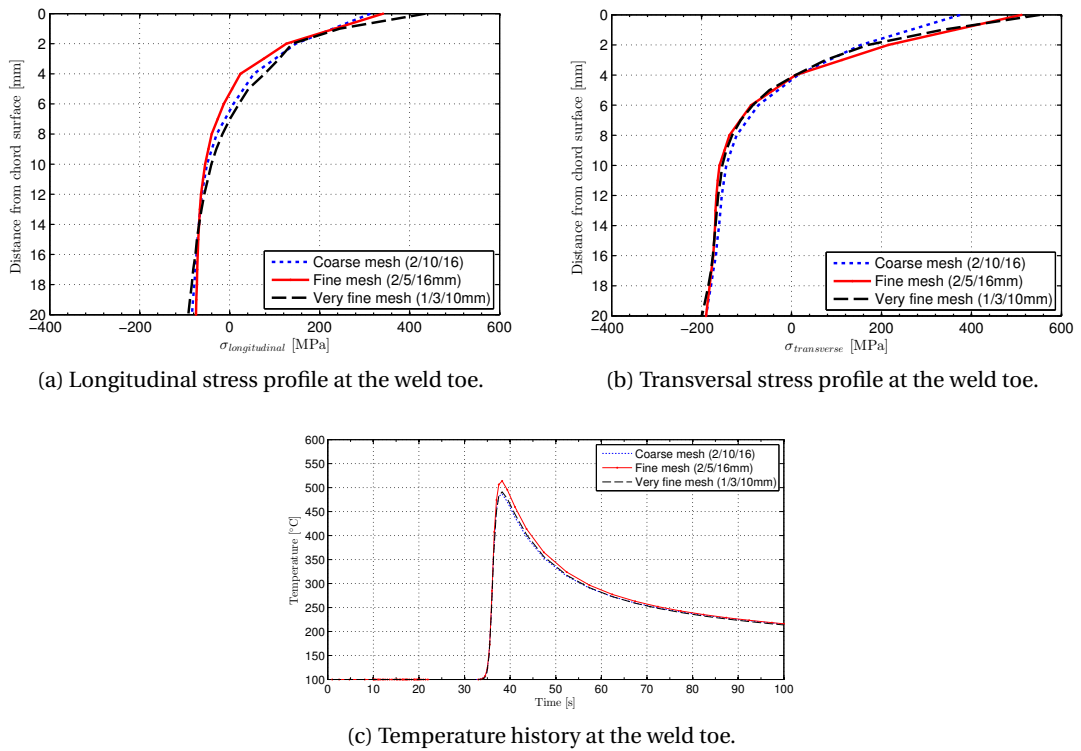


Figure 6.6: Convergence study results; Stress profiles and temperature history at the weld toe after one lumped welding pass (phase transformation effects not included).

## 6.5 Finite element analysis

Selection of proper time step size and scheme (constant or adaptive) is crucial since it affects the accuracy of the results and computation time. For the welding stage, Lindgren (2007) recommends the time step being less than the time required for the heat source to move between  $\frac{1}{3}$  and  $\frac{1}{2}$  of its dimension along trajectory. This ensures that the weld is modelled as a continuously moving heat source, not as a series of spot welds. Figure 6.7 from a study by Rohr (2013) on butt welding of two plates shows how the residual stresses start to fluctuate along the length of the weld when the time step becomes too large. The same issue may happen if adaptive time-stepping is used for the welding stage; the adaptive scheme can miss the continuity of the problem. Considering these issues, either a constant time stepping scheme or an adaptive time stepping with very small limit on maximum time step size were chosen for analyses in welding stage. The small time step in the range of 0.05 s to 0.1 s ensured the continuity of the thermal loading was implemented correctly. For the cooling stage, none of these limitations exist; Therefore, an adaptive time stepping with more relaxed time step size (0.01 s to 0.1 s) was chosen to reduce the cost of computation.

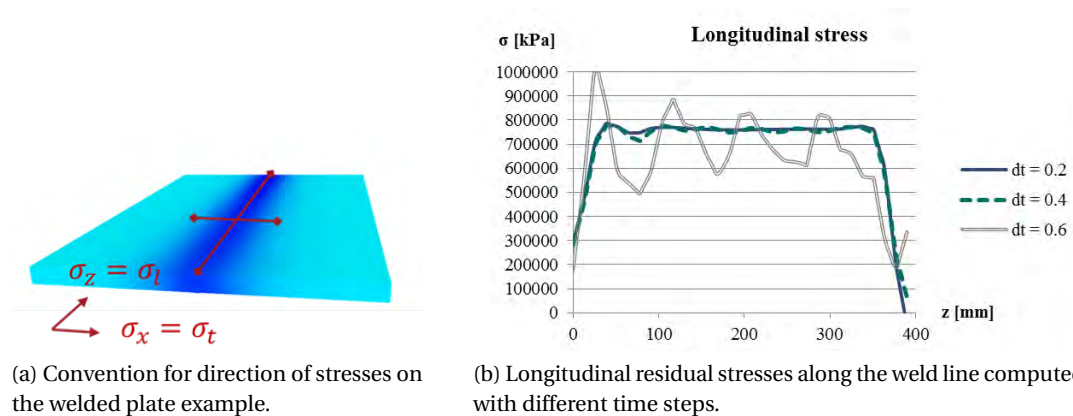


Figure 6.7: Effect of time step size on the stability of residual stress results (Rohr, 2013).

## 6.6 Thermophysical and mechanical material properties

According to Lindgren (2001b), material modelling and uncertainties in net heat input are the two main issues in welding simulation. In this section, temperature-dependent thermal, mechanical, and metallurgical material properties for S690QH together with the corresponding material characterization procedures for those properties are discussed. Same material properties for the weld and for the base metal were chosen in this study. Table 4.2 presents chemical composition of base metal.

### 6.6.1 Two approaches in modelling material behaviour

Two approaches in modelling material behaviour exist in literature (Goldak and Akhlaghi, 2005); In the first approach the multi-phase steel material is considered as homogeneous and bulk material thermo-physical properties are given as the analysis input. This approach, which comprises majority of the simulations in literature (e.g. Brickstad and Josefson (1998); Deng and Murakawa (2006)) is more suitable for thermo-mechanical analysis. Metallurgical transformations can still be included in the analysis. Volumetric change due to solid-state phase transformation is implemented by modifying thermal expansion coefficient (Deng, 2009; Yaghi and Becker, 2005). Transformation plasticity can be reproduced by reducing the yield stress of the material.

The second approach predicts the behaviour of heterogeneous metallic material based on the contributions from its various microstructure constituents by using *mixture rules*. Generally linear mixture rules are used. With this approach, the evolution of micro structure during thermal cycles is evaluated using some kinetic laws (see section 6.6.4). Knowing the phase fractions at each step of transient analysis, physical properties of the bulk material is evaluated for that step. Volume changes are computed by a linear mixture rule on a phase-by-phase basis. Transformation plasticity is modelled by adding the extra plasticity term to the total strain tensor which is a function of transformation stage and deviatoric stress (Yaghi and Becker, 2005)<sup>3</sup>.

The second modelling approach – phase related material properties – is more accurate than the first approach – bulk material properties. Its drawback is that many more material input data are required for the model. Temperature-dependent mechanical properties for each phase and kinetics of phase transformation should be known prior to analysis. Both modelling approaches are available in Morfeo/Welding software, but when considering solid-state phase transformations, exclusively second approach should be used<sup>4</sup>. Figure 6.8 depicts the analysis procedure in Morfeo when metallurgical effects are taken into account. The coupled thermal-metallurgical-mechanical problem is solved in a staggered scheme; In each step, first the thermal domain is solved. The resulting temperature field is used for prediction of phase fractions by means of various transformation kinetics models (see section 6.6.4). In the last step, mechanical field is computed based on the thermal field and phase fractions. The total strain tensor is calculated based on the following additive decomposition relation:

$$\epsilon_{tot} = \epsilon_e + \epsilon_p + \epsilon_{thm} + \epsilon_{tp} \quad (6.2)$$

<sup>3</sup>The procedure stated here is for the decoupled sequential analysis procedure. The coupling due to dependency of thermal material properties on phase transformations is not discussed.

<sup>4</sup>Bulk material properties in Morfeo are only a function of the temperature and not the temperature rate  $\dot{T}$ ; Therefore, they can not be used in a phase-transformation analysis. User defined subroutines (such as in Abaqus) do not exist in Morfeo. There are also other limitations (such as negative thermal expansion coefficient not being allowed) for the analyses of first approach type that prevent adding all the metallurgical effects to the model.

Where:

- $\dot{\epsilon}_{tot}$  : total strain rate tensor;
- $\dot{\epsilon}_e$  : elastic strain rate;
- $\dot{\epsilon}_p$  : (classical) plastic strain rate;
- $\dot{\epsilon}_{thm}$  : thermo-metallurgical strain rate (see section 6.6.3);
- $\dot{\epsilon}_{tp}$  : transformation plasticity strain rate (see section 6.6.5).

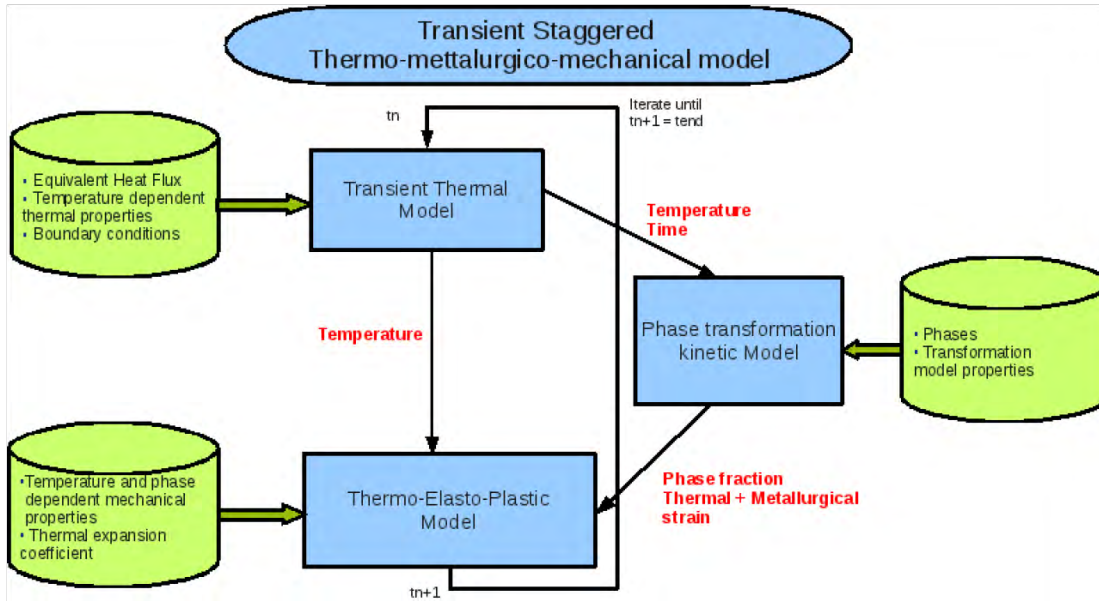


Figure 6.8: Thermal-metallurgical-mechanical simulation coupling in Morfeo 2012.

Thermal material properties are assumed the same for all constituents in Morfeo/Welding<sup>5</sup>. The program uses temperature field and the time step data to calculate phase fractions by means of kinetic laws. The elastic mechanical properties (Modulus of elasticity and Poisson's ratio) are also considered the same for all phases. All other mechanical properties – including coefficient of thermal expansion, yield stress, hardening modulus and hardening power – are phase-dependent and are evaluated with a linear mixture rule applied to phase fractions existing in each time step .

Both modelling approaches were utilised in this study; Bulk material properties were used in the models neglecting phase transformation. For models with phase transformation effects included, phase-related material data were used. The material data were acquired through experimental work at ICOM (Krummenacker, 2011; Rohr, 2013), or from the literature.

<sup>5</sup>The reason for this assumption is to de-couple the thermal and metallurgical fields and to convert the analysis into a sequential scheme.



## 6.6.2 Thermal properties

### Specific heat capacity

Mertens and Lecomte-Beckers (2012) measured the thermophysical properties of S690QH steel on unwelded tube specimens of the present study. Heat capacity was measured using Differential Scanning Calorimetry (DSC) technique on a Netzch DSC 404C instrument for the temperature range of 28 °C to 1373 °C. In this measurement method, the latent heat for solid-state phase transformation is included in the “apparent” or “equivalent” (Bergheau and Fortunier, 2008) specific heat. Heat capacity values for pure metals show a singularity at the transformation temperature ranges due to the release of latent heat. This singularity turns into a prominent maxima for the case of metal alloys (Radaj, 2003).

Since the measurements stopped at 1373 °C, the latent heat of solidus–liquidus transformation was not captured. This latent heat influences the welding temperature field by delaying melting in the way that melting front moves closer to the heat source and solidification front shifts away from the heat source. As a result, the molten pool shape becomes more stretched in the direction of moving heat source, compared to the case where latent heat is ignored.

Latent heat of fusion can not be directly handled in MORFEO. Therefore, an equivalent specific heat capacity in the mushy zone is defined using the definition of enthalpy in that zone:

$$H = \int_{T_{solid}}^{T_{liquid}} \rho c_p (T) dT + h_l \quad (6.3)$$

Where:

- $H$  : enthalpy [J m<sup>-3</sup>];
- $\rho$  : density [kg m<sup>-3</sup>];
- $c_p$  : specific heat capacity [J kg<sup>-1</sup> K<sup>-1</sup>];
- $h_l$  : latent heat of melting [J m<sup>-3</sup>].

Considering a constant equivalent specific heat ( $c_{eq}$ ) over relatively small range of ( $T_{solid}, T_{liquid}$ ) we will have:

$$c_{eq} = \frac{H}{\rho (T_{liquid} - T_{solid})} \quad (6.4)$$

With the assumption of  $c_p$  being linear function of  $T$  in the mushy zone and substituting r.h.s of equation 6.3 into equation 6.4,  $c_{eq}$  is calculated. In summary, apparent heat capacity over

whole temperature range (up to the boiling point) will be the following:

$$c_p(T) = \begin{cases} c_{p,solid} & \text{if } T < T_{solid}. \\ \frac{c_{p,solid} + c_{p,liquid}}{2} + \frac{h_l}{\rho(T_{liquid} - T_{solid})} & \text{if } T_{solid} \leq T \leq T_{liquid}. \\ c_{p,liquid} & \text{if } T > T_{liquid}. \end{cases} \quad (6.5)$$

Eurocode physical property diagrams stop at temperatures below melting temperature, because in principle they are prepared for fire-resistant design of steel structures and the thermal properties above melting point are of no interest<sup>6</sup> Solidus and liquidus temperatures were calculated according to (Thomas et al., 1987):

$$\begin{aligned} T_{Solidus} &= 1535 - 200 (\%C) - 12.3 (\%Si) - 6.8 (\%Mn) - 124.5 (\%P) - 189.3 (\%S) \\ &\quad - 4.3 (\%Ni) - 1.4 (\%Cr) - 4.1 (\%Al) \\ T_{Liquid} &= 1537 - 88 (\%C) - 8 (\%Si) - 5 (\%Mn) - 30 (\%P) - 25 (\%S) - 4 (\%Ni) \\ &\quad - 1.5 (\%Cr) - 5 (\%Cu) - 2 (\%Mo) - 2 (\%V) - 18 (\%Ti) \end{aligned} \quad (6.6)$$

Substituting the values of Table 4.2 in this equation,  $T_{Solidus}$  and  $T_{Liquid}$  are estimated as 1488 °C and 1511 °C, respectively. Figure 6.9 shows the specific heat capacity measured by Mertens and Lecomte-Beckers (2012) and modified by aforesaid method to include the latent heat effects as used in this study. Specific heat curves reported by other researchers are included in the Figure for comparison. As can be seen, values used in this study are coherent with previous studies.

The steep changes in the equivalent specific heat capacity values at mushy zone led to very small type steps at the corresponding temperatures. For future studies, obtaining convergence with a larger time step would be possible by using a Gaussian distribution instead of step function.

### Thermal Conductivity

Thermal conductivity values in the range 100 °C to 1387 °C were measured by Mertens and Lecomte-Beckers (2012). According to Goldak and Akhlaghi (2005), thermal conductivity in liquid phase should be increase to account for convective stirring at high velocities ( $\approx 1 \text{ m s}^{-1}$ ) found in the weld pool. Therefore, for temperatures above melting temperature, the conductivity values were multiplied by 3, as can be seen in Table 6.3.

<sup>6</sup>The range of heating rates in Eurocode is assumed to be between  $2 \text{ K min}^{-1}$  and  $50 \text{ K min}^{-1}$  which is much slower than typical welding heating rates.



## 6.6. Thermophysical and mechanical material properties

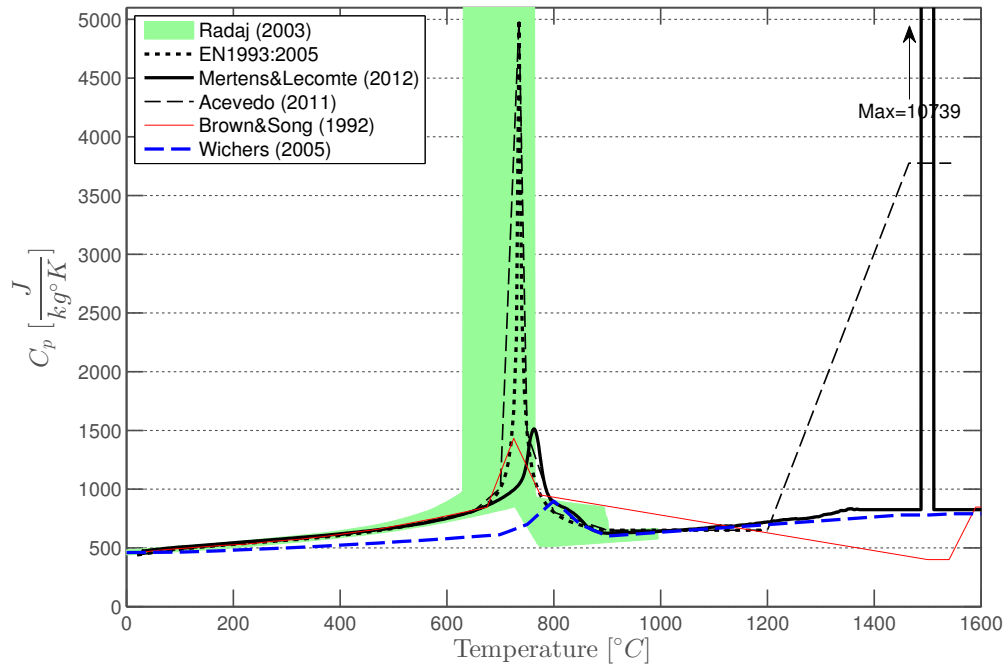


Figure 6.9: Temperature-dependent specific heat capacity values from Radaj (2003) (originally from Richter (1973)), EN1993 (2005), Mertens and Lecomte-Beckers (2012), Acevedo et al. (2013), Brown and Song (1992), and Wichers (2006). The first peak at around 750 °C corresponds to solid-state  $\alpha \rightarrow \gamma$  phase transformation. The second peak at 1500 °C denotes the *equivalent* specific heat capacity associated with melting/solidification.

Table 6.3: Thermal conductivity  $\lambda$  values for S690QH (Mertens and Lecomte-Beckers, 2012).

Temperature [°C]	100	200	300	400	500	600	700	800
$\lambda$ [ $\mu\text{W mm}^{-1} \text{K}^{-1}$ ]	4.61E+04	4.73E+04	4.63E+04	4.47E+04	4.30E+04	4.17E+04	4.26E+04	3.15E+04
Temperature [°C]	900	1000	1100	1200	1300	1387	1511	3000
$\lambda$ [ $\mu\text{W mm}^{-1} \text{K}^{-1}$ ]	2.52E+04	2.99E+04	3.28E+04	3.72E+04	3.72E+04	3.17E+04	1.00E+05	1.00E+05

### 6.6.3 Mechanical properties

Temperature dependent non-viscous mechanical properties were assumed. According to (Lindgren, 2001b) plastic deformations below half melting temperature (in kelvins) can be considered rate-independent. This does not hold when modelling liquid/mushy zones, where considerable viscosity is observed. However, mechanical properties in the high temperature range ( $T \geq 0.5T_{Liquid}$ ) is considered of minor importance for stress evaluation.

Mechanical properties at elevated temperatures were measured during this work. The detailed results can be found in Krummenacker (2011) (tests carried out in a regular tensile testing machine with an added furnace chamber) and Rohr (2013) (Gleeble tests). A summary of the hot tensile results (measured modulus of elasticity and yield stress) is presented in Figures 6.10 and 6.11. As can be seen in the figures, there is an acceptable agreement between EN 1993:2005 and the test results. Since the material characterization test data were not available for the whole temperature range, it was decided to take mechanical properties recommended by EN 1993 as input to the welding simulation analyses. Eurocode suggests two family of material constitutive laws: one with abrupt strain hardening at temperatures below 400 °C and one with a smooth linear strain hardening (Figure 6.12). The material law with linear hardening better corresponded to the measured stress-strain curves (Krummenacker, 2011; Rohr, 2013) and was used for analyses.

The temperature-dependent yield stress of various constituents (Bainite, Martensite, Ferrite, and austenite) was gathered from literature data for steels with similar composition to S690QH. Figure 6.13 shows the values suggested by different authors. The yield stress values given by Börjesson and Lindgren (2001) for bainite (Figure 6.13b) seemed unrealistically high for the steel studied in this work. Yield stresses given by Krauß (2005) were used for the phase-based numerical model in this study. Yield stress of phase-based model at ambient temperature with 84% bainite and 16% martensite gave 680 MPa (calculated using linear mixture rule) which is in agreement with Eurocode value (bulk material properties). Modulus of elasticity and Poisson's ratio were assumed to be the same for all constituents. Temperature-dependent Poisson's ratio values were taken as the values of previous study by Acevedo (2011).

#### Strain hardening behaviour

A project was initiated in 1997 by Commission X of International Institute of Welding on residual stress and distribution prediction (RSDP) for round-robin study of welding simulation of some standard weldments. Analyses carried out by various research teams using different software and methods. In their review of IIW RSDP project, Dong and Hong (2002) conclude that kinematic hardening assumption always led to lower residual stress values in the carbon steel material studied in the project. In a more recent review of the same project, Wohlfahrt et al. (2012) have reported the results of a more precise analysis of the same details as IIW RSDP and in their comparison of the two material models, higher residual stress values for isotropic hardening model is observed, compared to kinematic hardening assumption.

## 6.6. Thermophysical and mechanical material properties

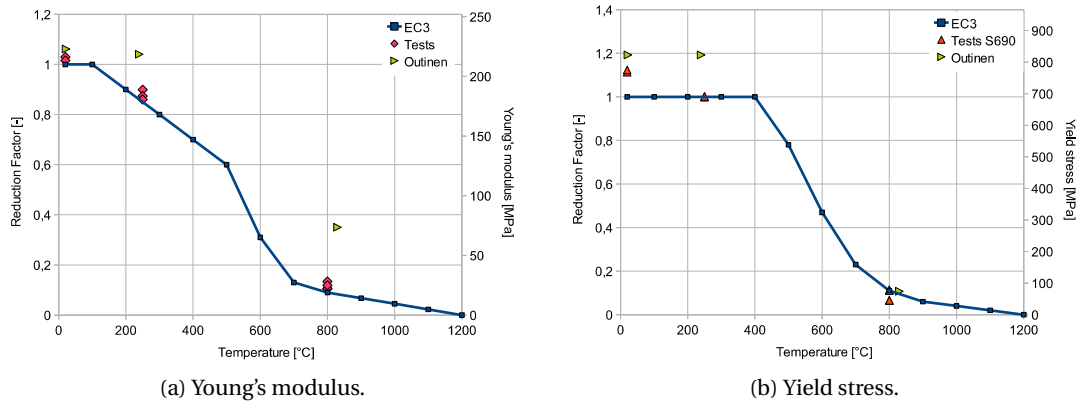


Figure 6.10: Young's modulus and yield stress of S690QH specimens measured at various temperatures (Krummenacker, 2011), compared with EN 1993:2005 curves and experimental data from Outinen (2007).

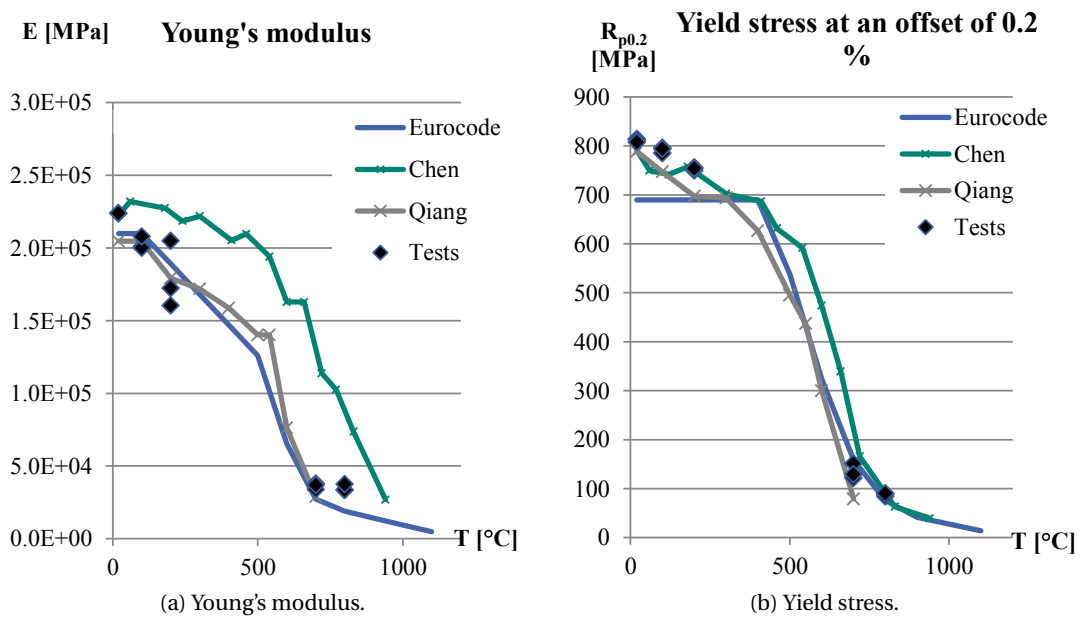


Figure 6.11: Young's modulus and yield stress of S690QH specimens measured at various temperatures (Rohr, 2013), compared with Eurocode 2005 curves.

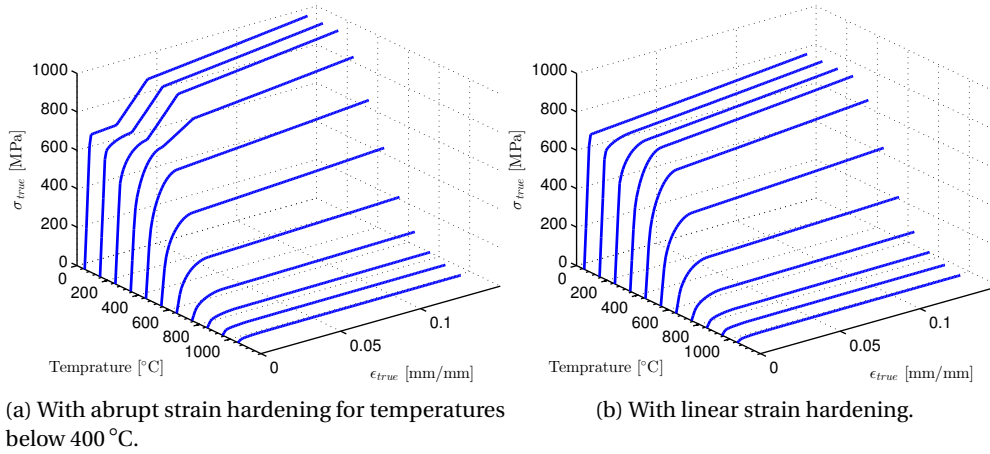


Figure 6.12: Change of stress-strain curve with temperature; Eurocode 3 (2005) part 1-2 models.

Nonetheless, choice of the strain hardening material behaviour depends on the properties of the studied metal; But with the lack of cyclic plastic behaviour data, isotropic hardening assumption is reasonable, because the residual stresses will not be underestimated.

A Ludwik-type material law (Lubliner, 2008; MORFEO, 2012) with isotropic strain hardening was used in mechanical analysis. The constitutive elasto-plastic model is formulated as:

$$\begin{cases} \sigma = C \epsilon_e \\ \epsilon_e = \epsilon_{tot} - \epsilon_p - \epsilon_{thm} \\ \epsilon_{th} = \alpha \Delta T \end{cases} \quad (6.7)$$

Where:

- $C$  : elasticity matrix;
- $\epsilon_{tot}$  : total strain tensor;
- $\epsilon_e$  : elastic strain;
- $\epsilon_p$  : plastic strain;
- $\epsilon_{thm}$  : thermo-metallurgical strain;
- $\alpha$  : coefficient of thermal expansion (see section 6.6.3).

The yield function  $\phi(\sigma, p)$  determines the elastic ( $\phi < 0$ ) or plastic state ( $\phi = 0$ ) and is defined as:

$$\phi(\sigma, p) = \sigma_{eq} - \sigma_y - H p^n \quad (6.8)$$

## 6.6. Thermophysical and mechanical material properties

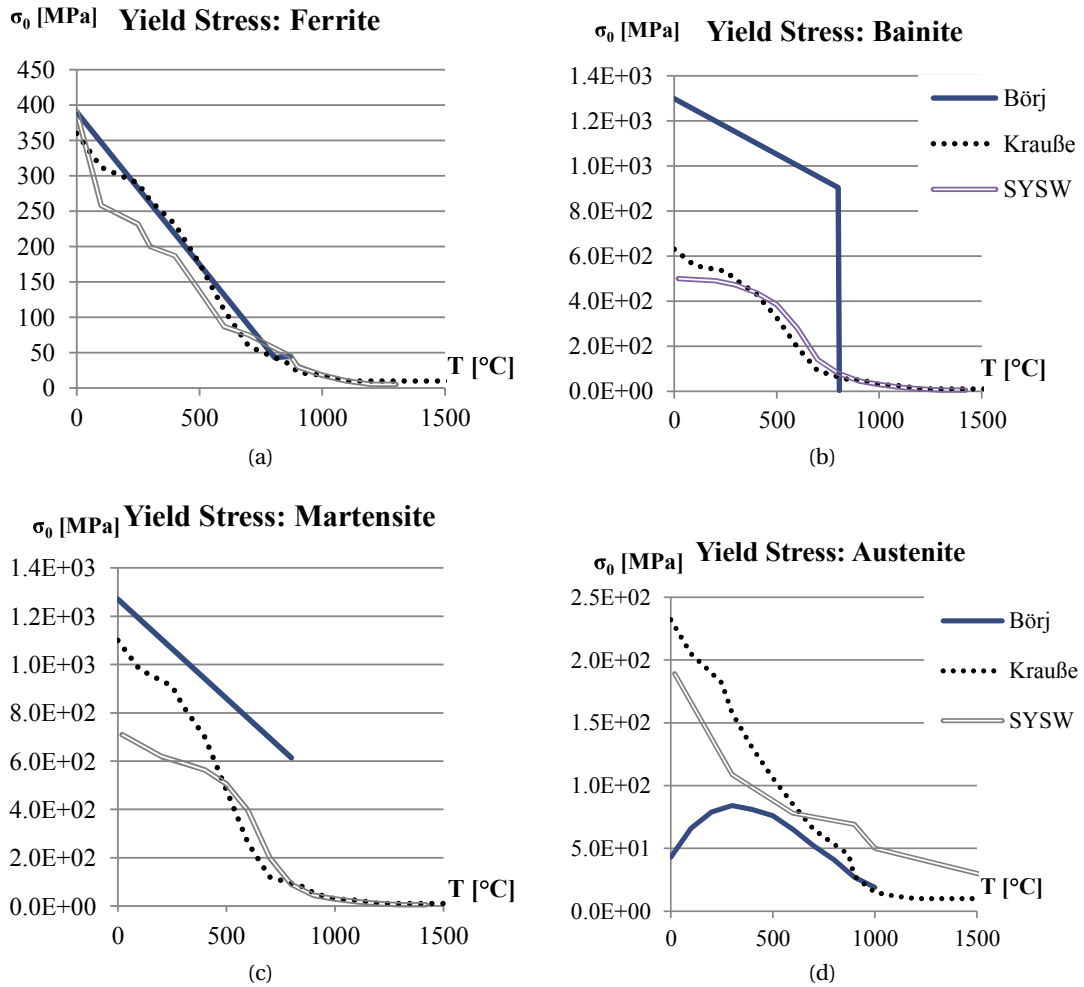


Figure 6.13: Yield limit of various phases in studied steel material (Rohr, 2013); Data from Börjesson and Lindgren (2001), Kraußé (2005), and ESI Group (2009).

Where:

- $\sigma_{eq}$  : von Mises equivalent stress;
- $\sigma_y$  : initial yield stress;
- $p$  : cumulative plastic strain;
- $H$  and  $n$  : hardening modulus and hardening exponent, respectively.

The drag stress term  $H p^n$  stands for isotropic hardening which for  $n = 1$  represents linear isotropic hardening. Finally, plastic flow rule is given by:

$$\dot{\epsilon}^p = \lambda \frac{\partial \phi}{\partial \sigma} = \lambda \frac{\sigma}{|\sigma|} \quad (6.9)$$

Where:

- $\lambda$  : non-negative plastic (Lagrangian) multiplier.

Hardening exponent was taken as one (linear hardening) and hardening modulus was calibrated using EN 1993-1-2 curves by Acevedo (2011). Figure 6.14 shows one-dimensional material response compared to Eurocode curve.

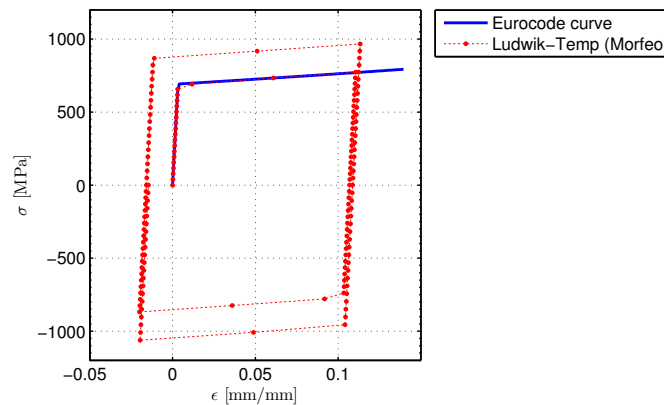


Figure 6.14: Simulated material model (Ludwik) versus Eurocode curve (room temperature).

### Coefficient of thermal expansion

Thermal expansion coefficient was determined by Mertens and Lecomte-Beckers (2012) with dilatometry test. Heating and cooling rates were  $3^\circ\text{C min}^{-1}$  for their test. The tangent (momentary) thermal expansion coefficient curve is shown in Figure 6.15 together with the curve used by Acevedo (2011). The values above austenite transformation temperature differ considerably between the two curves, but the effect on residual stresses is negligible since yield stress and modulus of elasticity are quite low at that temperature range.

## 6.6. Thermophysical and mechanical material properties

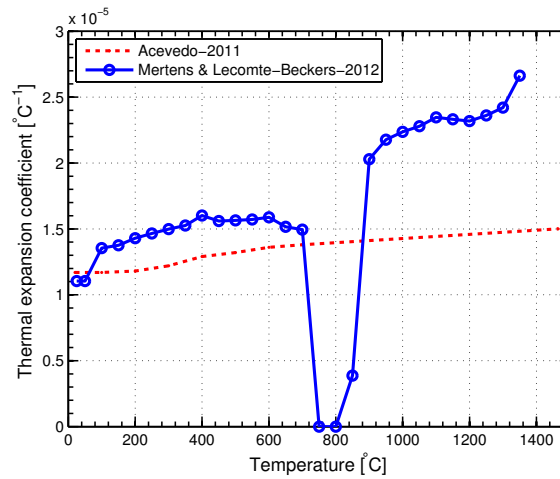


Figure 6.15: Thermal expansion coefficient used in this study (Mertens and Lecomte-Beckers, 2012) and by Acevedo (2011).

Dilatation curves for ferrite, bainite, and austenite phases were calculated from experimental dilatation curve (Figure 6.16) by linear regression on two parts of dilatation curve. The dilatation line equations are given on the figure. Bhadeshia 2002 gives similar thermal expansivity values for microstructure ( $\alpha_A = 2.1 \times 10^{-5}$ ,  $\alpha_{FPB} = 1.4 \times 10^{-5}$ ,  $\alpha_M = 1.3 \times 10^{-5}$ ). The thermal expansion coefficients are weak functions of temperature. Since the cooling rate of the test was too slow for martensitic transformation, dilatation curve for martensite was calculated by another method combining experimental data with calculated lattice parameters, as described in the following.

Thermal expansivity and lattice parameters for the two microstructures (ferrite and martensite) were calculated based on Lee et al. (2007) recommendation. They give following relations for martensite lattice parameters:

$$\begin{cases} \beta_M = (14.9 - 1.9 C_M) \times 10^{-6} \\ c_M = (0.28610 + 0.0025855 C_M) [1 + \beta_M (T - 273)] \\ a_M = (0.28610 + 0.0002898 C_M) [1 + \beta_M (T - 273)] \end{cases} \quad (6.10)$$

Where:

- $C_M$  : atomic percent of carbon in martensite;
- $\beta_M$  : thermal expansion coefficient for martensite [ $K^{-1}$ ];
- $a_M$  and  $c_M$  : martensite lattice parameters [nm].

With the assumption of atomic percent of carbon in martensite being equal to mean atomic percent of carbon in steel  $C_m = 0.694$ , the above equations give  $\beta_m = 1.36 \times 10^{-5} K^{-1}$ ,  $a_M = 0.286$  nm, and  $c_M = 0.288$  nm in room temperature.

## Chapter 6. Modelling of welding

---

Ferrite lattice parameters were calculated from following relations (Lee et al., 2007; Onink et al., 1993):

$$\begin{cases} \beta_F = 1.75 \times 10^{-5} \\ a_F = 0.28863 \times (1 + \beta_F (T - 800)) \end{cases} \quad (6.11)$$

Where:

$\beta_F$  : thermal expansion coefficient for ferrite [ $K^{-1}$ ];  
 $a_F$  : ferrite lattice parameter [nm].

There is no effect of carbon content on  $\beta_F$ , since ferrite is considered as pure iron. The equation gives  $a_F = 0.286$  nm for  $T = 20^\circ C$ .

The relative volume difference ( $\frac{\Delta V}{V}$ ) between ferrite and martensite microstructures and corresponding linear strain due to volume change ( $\epsilon^{VC}$ ) are now found by:

$$\begin{cases} \frac{\Delta V}{V} = \frac{a_M^2 c_M}{a_F^3} - 1 \\ \epsilon^{VC} = \frac{\Delta V}{3V} \end{cases} \quad (6.12)$$

Which gives  $\epsilon_{100\%FPB}^{VC} = 0.00295$ . Since the as-received studied steel was composed of 84% bainite and 16% martensite (Hildebrand, 2008), this value needs to be reduced by a factor of 0.84, i.e.  $\epsilon^{VC} = 0.00247$ . The latter value for volume change strain together with calculated  $\beta_M$  were used to draw the dilatation line for martensite in Figure 6.16.

The model presented here, is based on simplified relations for calculation of lattice parameters; The existence of other microstructure (e.g. cementite), variation of carbon content within the microstructure, and effect of alloying elements (other than carbon) on lattice parameters are neglected. These effects can be seen for example in the difference between calculated  $\beta_F = 1.75 \times 10^{-5}$  (Equation 6.11) and experimentally evaluated  $\beta_F = 1.51 \times 10^{-5}$  (Figure 6.16).

In an effort to measure the volume change due to martensitic transformation, some measurements were carried out at ICOM using a Gleeble 1500 system. Detailed report of experimental work can be found in Rohr (2013). Figure 6.17b shows the result of free dilatometry test for two specimens and Figure 6.17a shows similar schematic diagram from Deng (2009). The accuracy of the results, however, were not acceptable because the high cooling rates required for full martensitic transformation were not achieved. Future work should include more study on phase transformation behaviour – including volume change strains and transformation plasticity coefficients determination.



## 6.6. Thermophysical and mechanical material properties

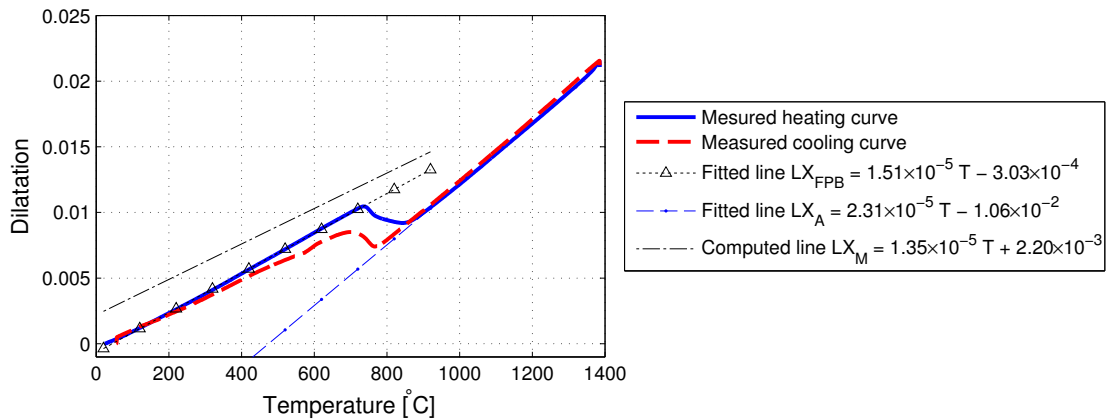
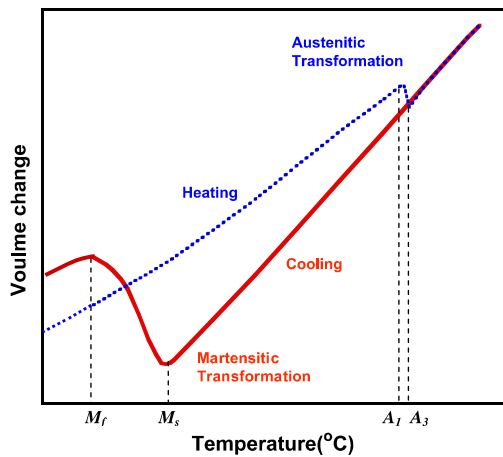
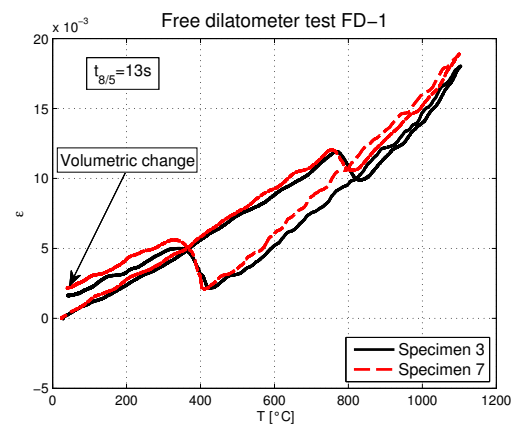


Figure 6.16: Linear dilatations of various phases; Expansion curve for Ferrite, bainite, and austenite are derived from the experiments reported by Mertens and Lecomte-Beckers (2012). Heating/cooling rate in experiments were  $3\text{ }^{\circ}\text{C min}^{-1}$ . Dilatation curve for martensite is based on calculations of lattice parameters. Indices in equations stand for various microstructures: A:austenite, F:ferrite, P:pearlite, B:bainite, M:martensite.



(a) Schematic diagram from (Deng, 2009).



(b) Measured dilatometry curves (Rohr, 2013).

Figure 6.17: Free dilatometry curves showing volume change due to phase transformation.

### 6.6.4 Phase transformation kinetics

Four phase kinetics models for diffusive or diffusionless transformations are implemented in Morfeo, including Johnson-Mehl-Avrami (JMA), Leblond (Leblond and Devaux, 1984), digitized CCT curves, and Koistinen-Marburger(KM) (Koistinen and Marburger, 1959). CCT curves from Seyffarth et al. (1992) could also be used directly in the software, but Morfeo recommends to restrict the use of CCT curve method for simple load cases as the method is not explicitly time-dependent. Therefore, it was decided to try two different phase transformation kinetic models: First using digitized CCT curves, and second, using Leblond (for diffusive transformations) and KM (for martensitic transformation). Parameters identification for Leblond model was based on the objective that the model reproduces a CCT curve similar to digitized CCT curve given by Seyffarth et al. (1992). This optimization problem was solved by manually changing Leblond model parameters and comparing the calculated CCT curve to the measured CCT curve. The governing equations for Koistinen-Marburger and Leblond models are explained in more detail in the following paragraphs.

In case of diffusionless martensitic transformation, Koistinen-Marburger model for low-alloy and non-alloy steel is written as (Koistinen and Marburger, 1959):

$$p_i = p_a(1 - e^{-\alpha(M_s - T)}) \quad (6.13)$$

Where:

- $p_i$  : martensite volume fraction;
- $p_a$  : remaining austenite volume fraction;
- $M_s$  : martensite start temperature;
- $\alpha$  : material dependent parameter.

According to Leblond method, when  $n$  different phases coexist in material, the rate of change in volume fraction of phase  $i$  ( $\dot{p}_i$ ) due to transformation of phase  $j$  into phase  $i$  can be formulated as (Boettcher et al., 2013):

$$\frac{dp_i(T, \dot{T}, t)}{dt} = \frac{p_{i,eq}^{ji}(T) - p_i(T, t)}{\tau^{ji}(T)} f_{ji}(\dot{T}) \quad (6.14)$$

Where:

## 6.6. Thermophysical and mechanical material properties

- $p_i$  : volume fraction of phase  $i$ ;  
 $p_{i,eq}^{ji}$  : equilibrium (or maximum attainable) volume fraction of phase  $i$  in  $j \rightarrow i$  transformation ( $0 \leq p_{i,eq}^{ji} \leq 1$ );  
 $\tau^{ji}$  : parameter representing characteristic time of  $j \rightarrow i$  transformation ( $\tau^{ji} > 0$ , the shorter the  $\tau^{ji}$ , the faster the transformation);  
 $f_{ij}$  : parameter for including rate-dependency into kinetics of phase transformation;  
 $T, \dot{T}$ , and  $t$  : temperature, temperature rate, and time, respectively.

Writing equation 6.14 for all phases and knowing  $\sum_{i=1}^n p_i = 1$  and  $p_i \geq 0$ , will result in (Roos et al., 2004):

$$\frac{dp_i(T, \dot{T}, t)}{dt} = - \sum_{j \neq i} A_{ij} \quad (i = 1, 2, \dots, n) \quad (6.15)$$

With:

$$A_{ij} = \begin{cases} \underbrace{\left( \frac{p_{j,eq}^{ij}(T)}{\tau^{ij}(T)} p_i(T, t) - \frac{1 - p_{j,eq}^{ij}(T)}{\tau^{ij}(T)} p_j(T, t) \right)}_{l_{ij}} f_{ij}(\dot{T}) & \forall l_{ij} > 0, (i \rightarrow j) \\ - \underbrace{\left( \frac{p_{i,eq}^{ji}(T)}{\tau^{ji}(T)} p_j(T, t) - \frac{1 - p_{i,eq}^{ji}(T)}{\tau^{ji}(T)} p_i(T, t) \right)}_{l_{ji}} f_{ji}(\dot{T}) & \forall l_{ji} > 0, (j \rightarrow i) \\ 0 & \forall l_{ij} \leq 0 \wedge l_{ji} \leq 0 \end{cases} \quad (6.16)$$

Having transformation parameters  $p_{j,eq}^{ij}(T)$ ,  $\tau^{ij}(T)$ , and  $f_{ij}(\dot{T})$  for all transformations and knowing  $\dot{T}$ , the system of first-order ODEs presented in 6.15 and 6.16 can be solved to get the evolution of volume fraction of each phase with time. A MATLAB script was written for calculations. The script is listed in Appendix D and the results of manual parameter identification for Leblond model based on experimental CCT curve from Seyffarth et al. (1992) are presented in Tables D.1 and D.2. Figure 6.18 shows the calculated phase evolution histories for three different cooling rates. Based on the cooling rate, austenite decomposes to bainite, martensite, and ferrite. For the highest cooling rate (Figure 6.18a), the resulted microstructure is exclusively martensite, while for the lowest cooling rate (Figure 6.18c), no martensite forms and the final microstructure is mostly bainite plus less than 10% ferrite. Figures 6.19 and 6.20 show measured CCT curve from literature, and calculated CCT curve after parameter identification. Because of manual parameter identification with limited number of trials and

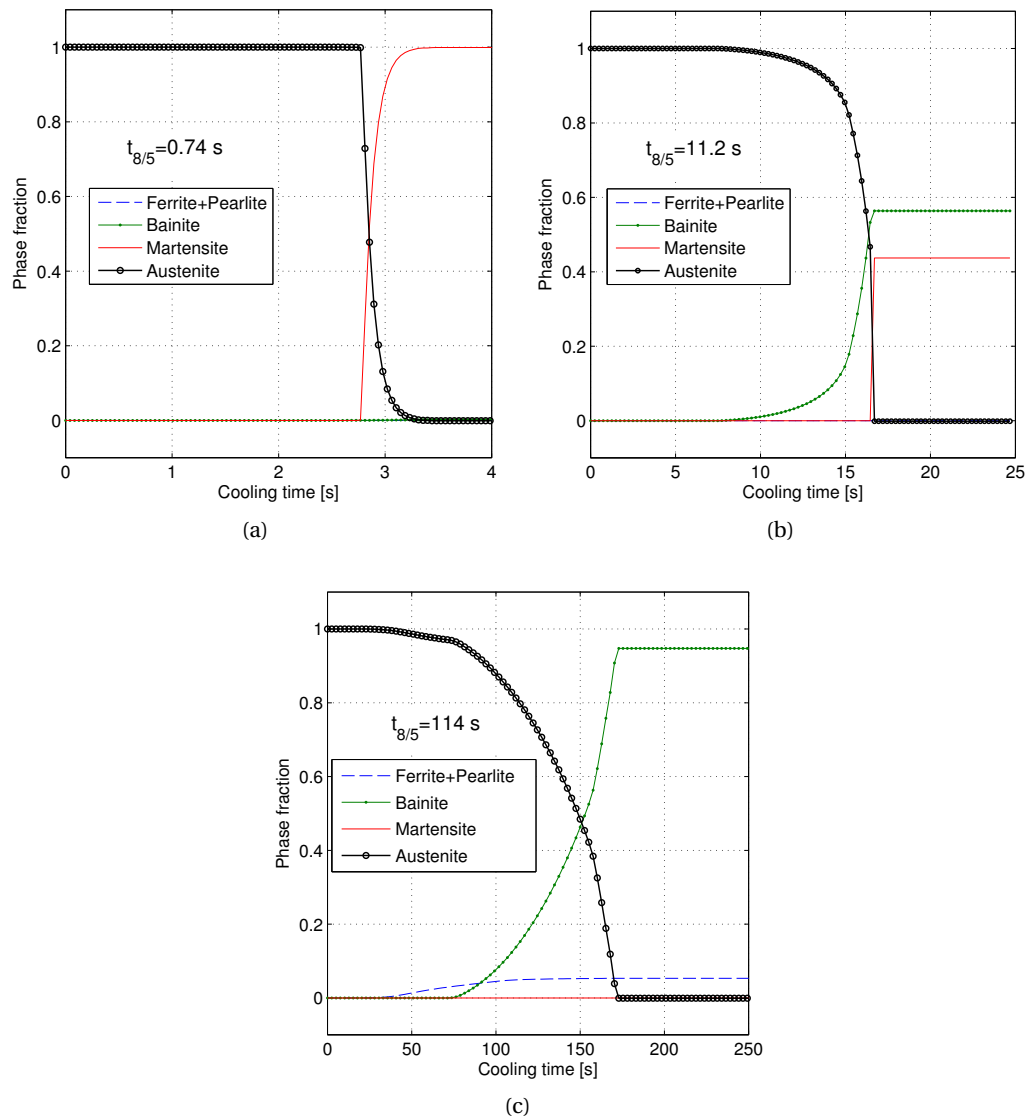


Figure 6.18: Computed austenite transformation into Ferrite+Pearlite, Bainite, and Martensite at various cooling rates.

error corrections, the experimental and computed CCT curves are not identical and some differences exist. However, the agreement between the two models is acceptable for cooling rates of practical interest for the welding simulation analyses of this study (i.e. cooling times below 20 s).

for the austenitization part of the transformation (heating part), a single Leblond model similar to values used by (Hildebrand, 2008) was used with  $T_i = 750$  °C (transformation start temperature),  $T_f = 750$  °C (transformation finish temperature), and a small characteristic time parameter ( $\tau^{ji} = 1$ ). Prior austenite grain size (pAGS) can effect martensite start temperature

## 6.6. Thermophysical and mechanical material properties

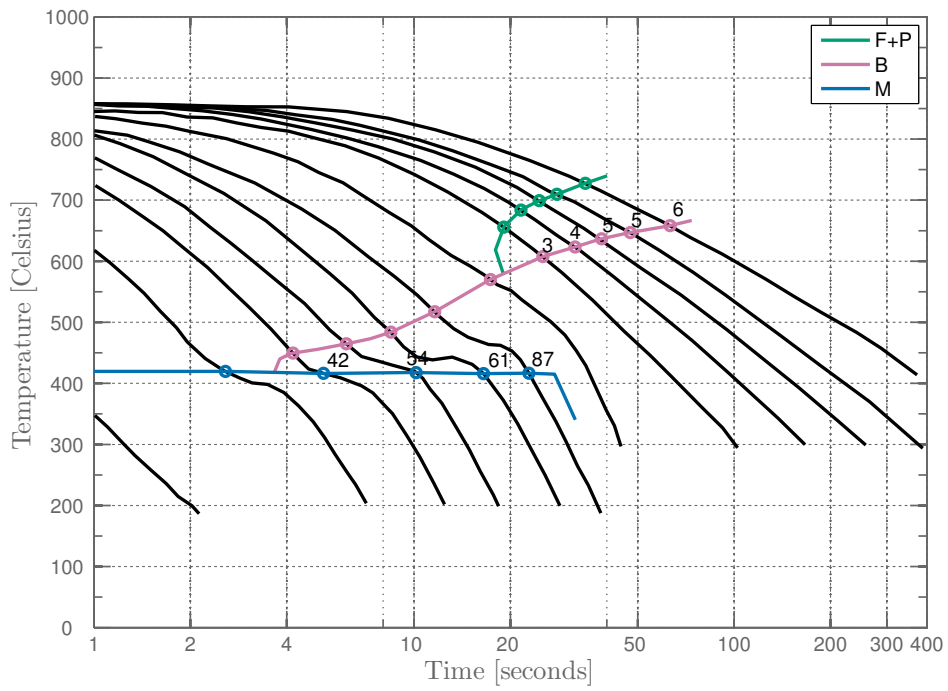


Figure 6.19: CCT curve for S690QL from Nolde and Meyer (1998); Seyffarth et al. (1992). Peak austenitization temperature: 1395 °C.

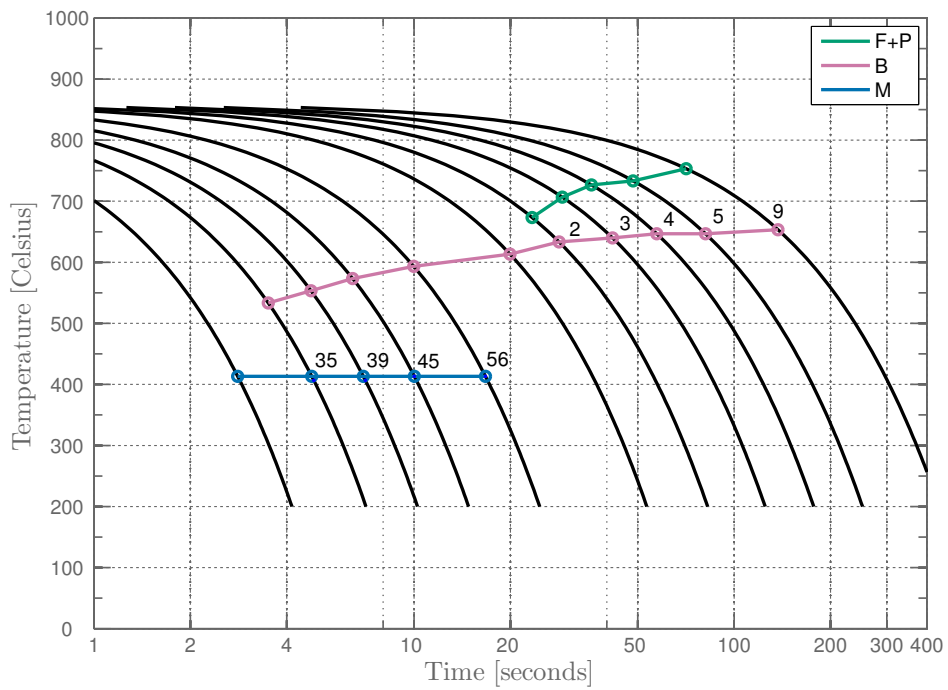


Figure 6.20: CCT curve for S690QL computed based on Leblond model with parameters shown in Tables D.1 and D.2.

(Yang and Bhadeshia, 2009). However, a recent study by Heinze et al. (2013) on welded S355J2+N welded plates with 11 wt.% martensite did not find significant change in residual stresses due to consideration of pAGS. This effect was not considered in present study. Also, martensite tempering due to multipass effects is not considered in this study.

### 6.6.5 Transformation plasticity (TRIP)

Dutta et al. (2013) give transformation plasticity coefficient for bainitic transformation as  $7.65 \times 10^{-5} \text{ MPa}^{-1}$  (c.f. Equation 2.1). Since no value for martensitic transformation plasticity coefficient was found for steel grade S690QH in published research, the value – which is in the acceptable range  $3 \times 10^{-5} \text{ MPa}^{-1}$  to  $12 \times 10^{-5} \text{ MPa}^{-1}$  given by Radaj (2003) – was used for both martensitic and bainitic transformations.

## 6.7 Boundary conditions

### 6.7.1 Initial and boundary conditions for thermal analysis

Initial conditions for heat transfer equation in diagram of Figure 2.5, were assumed as  $T_{in} = 120^\circ\text{C}$  for all nodes of the model. Ambient temperature was assumed as  $T_{ambient} = 20^\circ\text{C}$ .

### Combined effect of convection and conduction

Heat flux loss by convection  $q_{conv}$  is described by Newton's law and is a linear function of temperature (Bergheau and Fortunier, 2008):

$$q_{conv} = h_c(T)(T - T_0) \quad (6.17)$$

Where:

- $h_c$  : temperature-dependent film coefficient [ $\text{W m}^{-2} \text{K}^{-1}$ ];
- $T$  and  $T_0$  : temperature of the body and ambient temperature, respectively [kelvin or  $^\circ\text{C}$ ].

Radiation heat loss  $q_{rad}$  is governed by the Stefan-Boltzmann law:

$$q_{rad} = \epsilon_s \sigma_0 (T^4 - T_0^4) \quad (6.18)$$

Where:

- $\epsilon_s$  : surface emissivity;
- $\sigma_0$  : Stefan-Boltzmann constant  $\sigma_0 = 5.67 \times 10^{-8} \text{ W m}^{-2} \text{ K}^{-4}$ ;
- $T_0$  : reference sink temperature [in kelvin].

Equations 6.17 and 6.18 for convection and radiation can be combined into a simplified equation (Acevedo, 2011; Brown and Song, 1992). Equivalent film coefficient  $h_{eq}$  is calculated as:

$$\begin{cases} q_{rad} = \overbrace{\epsilon_s \sigma_0 (T^3 + T^2 T_0 + T T_0^2 + T_0^3)}^{h_{rad}(T)} (T - T_0) \\ q_{tot} = q_{conv} + q_{rad} = h_{eq}(T) (T - T_0) \\ h_{eq}(T) = h_c(T) + h_{rad}(T) = h_c(T) + \epsilon_s \sigma_0 (T^3 + T^2 T_0 + T T_0^2 + T_0^3) \end{cases} \quad (6.19)$$

Same values used by (Acevedo, 2011) were used in this study. Diagram in Figure 6.21 shows the values for  $h_{eq}$  compared to the work of Krauße (2005).

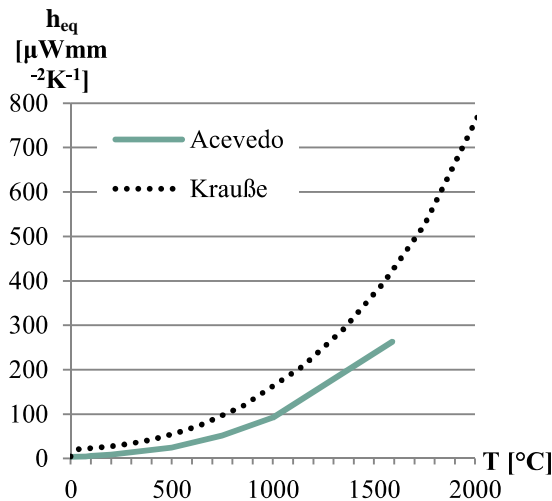


Figure 6.21: Combined coefficient for convection and radiation according to Acevedo (2011) and Krauße (2005).

### Heat source

Input heat flux for arc welding is calculated as:

$$q = \eta UI \quad (6.20)$$

Where  $q$  is net heat flux,  $U$  is the voltage, and  $I$  is the arc current.  $\eta$  is arc efficiency value

and accounts for heat losses by radiation and convection in the arc region and molten pool (Grong, 1997). With the values given in section 5.3.1 and Table 5.7 ( $I = 220 \text{ A}$ ,  $U = 28 \text{ V}$ ,  $\eta = 0.78$ ), net heat flux is equal to  $q = 4.8 \text{ kW}$  and considering 8 weld passes, total heat power input is  $Q = 38.4 \text{ kW}$ . Net heat power deposited per unit length of weld is calculated by dividing net heat flux to torch speed  $v_{average} = 7.4 \text{ mm s}^{-1}$ , which gives  $q/v = 0.65 \text{ kJ mm}^{-1}$  and  $Q/v = 5.19 \text{ kJ mm}^{-1}$ .

Heat source in Morfeo can be defined as a superposition of three heat source shapes, namely double ellipsoidal with Gaussian distribution (Goldak et al., 1984, see Figure 6.22), cylindrical with uniform distribution<sup>7</sup>, and conical shape with Gaussian and linear distributions. Heat distribution in a double-ellipsoidal volumetric heat source is given by:

$$\begin{cases} q_{vol,f} = f_f \frac{6\sqrt{3}q}{\pi\sqrt{\pi} ABC_f} \exp \left\{ -3 \left[ \left( \frac{x}{A} \right)^2 + \left( \frac{y}{B} \right)^2 + \left( \frac{z}{C_f} \right)^2 \right] \right\} \\ q_{vol,r} = f_r \frac{6\sqrt{3}q}{\pi\sqrt{\pi} ABC_r} \exp \left\{ -3 \left[ \left( \frac{x}{A} \right)^2 + \left( \frac{y}{B} \right)^2 + \left( \frac{z}{C_r} \right)^2 \right] \right\} \end{cases} \quad (6.21)$$

Where:

- $q$  : total heat flux power;
- $q_{vol,f}$  and  $q_{vol,r}$  : Heat flux in front and rear of the weld torch, respectively;
- $A$ ,  $B$ ,  $C_f$  and  $C_r$  : geometric parameters defining the shape of heat source as shown in Figure 6.22.

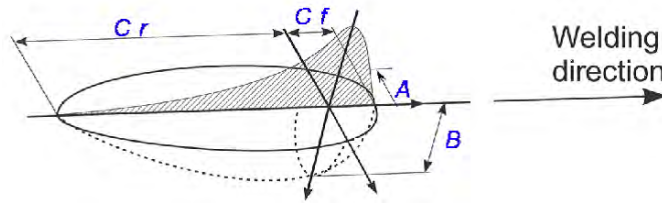


Figure 6.22: Double ellipsoid heat source model parameters (MORFEO, 2012); welding direction is considered as z-axis.

One advantage of double ellipsoid model is that it gives more steep gradient at the front of heat source and smoother gradient at the rear side, which is similar to the real arc welding condition (Goldak and Akhlaghi, 2005). Goldak and Akhlaghi (2005) recommend the size of the heat source taken as 10% less than the size of molten pool. The size of the molten pool was estimated based on dimensionless operating parameter and diagrams given by Christensen et al. (1965), Eagar and Tsai (1983). Since the lumped pass model was used in this study, the molten pool dimensions were unrealistically large. Therefore, the size of the heat source recommended by (Goldak and Akhlaghi, 2005) was used as a first try and was reduced later

<sup>7</sup>It is possible to define a linear distribution along the height of the cylinder, but with the formulation in the existing version, total heat is correctly calculated only for the case of uniform distribution. This will be fixed for the next release of the program.



during the course of calibration. In order to make a comparison for the effect of heat source, cylindrical heat source was also used for some of the models.

**Speed of welding torch** Reproduction of actual cooling rates in the thermal analysis stage are important, since the phase transformation behaviour of steel strongly depends on it. Since power of a lumped pass is a multiple of an individual real weld pass, the cooling times calculated by the model would be longer than the real weld. In order to compensate for this, the weld torch speed  $v$  was also increased proportionally in some models – models with phase transformations included – to keep the  $q/v$  ratio identical to an individual weld pass. The models can be identified in table 6.5 with suffixes *N* (normal speed) or *A* (augmented speed).

**Distribution of total heat among weld passes** Total heat input resulted by eight weld passes, was distributed between three lumped passes in the model. Two distributions were considered: (a) 20% of the power was deposited in the first pass and 40% for each of second and third passes (models with this distribution have a 244 suffix); (b) for the rest of the models, 30% of net power input was given in the first pass and 35% in each of the following passes (these models are denoted by 333). In order to model start/stop conditions of the welding more realistically, at the first 1 s and the last 1 s of each pass, both velocity and heat power of the heat source in the model were ramped from 0 to 100% and vice-versa.

**Welding sequence** Welding sequence followed the welding procedure described in section 5.3.1 and is shown in Figure 5.11. Welding and interpass waiting times were chosen similar to the average values recorded during the real welding. Table 6.4 shows the welding sequence used in the FE analysis of K-joints.

### 6.7.2 Mechanical boundary conditions

Complete clamping (all three translational DOFs restrained) at the right chord end was applied. Although the boundary conditions for K-joint in the real truss are slightly different (non-rigidly clamped in all chord and brace ends) but the effect of restraining from other truss elements on the residual stress distribution in the joint was deemed negligible and was not considered.

## 6.8 Results

A parametric study was carried out by changing some model parameters to assess their effect on calculated residual stresses. The parameters included model geometry (modelling complete K-joint or only one brace), welding start/stop positions, phase transformation parameters, welding speed (normal speed versus augmented speed which preserved the power per weld length ratio from real welding). Table 6.5 summarizes characteristics and sizes

## Chapter 6. Modelling of welding

Table 6.4: Timing of welding and cooling steps; Right side is the positive side of x-axis (shown on Figures 6.2 and 6.4), and front side is the positive z-axis. Net heat power distribution for this case was 30% for pass 1 and 35% for each of passes 2 and 3.

StepNo	Step name	Right/ Left side	Back/ Front	Start time [s]	End time [s]	Duration [s]	Heat input [kW]
1	Waiting			0	10	10	
2	Welding, QRB, pass 1	R	B	10	37	27	11.49
3	Cooling			37	100	63	
4	Welding, QLB, pass 1	L	B	100	127	27	11.49
5	Cooling			127	190	63	
6	Welding, QRE, pass 1	R	F	190	217	27	11.49
7	Cooling			217	280	63	
8	Welding, QLE, pass 1	L	F	280	307	27	11.49
9	Cooling			307	370	63	
10	Welding, QRB, pass 2	R	B	370	397	27	13.4
11	Cooling			397	460	63	
12	Welding, QLB, pass 2	L	B	460	487	27	13.4
13	Cooling			487	550	63	
14	Welding, QRE, pass 2	R	F	550	577	27	13.4
15	Cooling			577	640	63	
16	Welding, QLE, pass 2	L	F	640	667	27	13.4
17	Cooling			667	730	63	
18	Welding, QRB, pass 3	R	B	730	757	27	13.4
19	Cooling			757	820	63	
20	Welding, QLB, pass 3	L	B	820	847	27	13.4
21	Cooling			847	910	63	
22	Welding, QRE, pass 3	R	F	910	937	27	13.4
23	Cooling			937	1000	63	
24	Welding, QLE, pass 3	L	F	1000	1027	27	13.4
25	Cooling			1027	1090	63	
26	Cooling			1090	1690	600	
27	Cooling			1690	10000	8310	

of the studied models. The complexity of the geometry and size of the model led to large modelling and analysis times. To give an estimate, analysis runtimes are included in the table. For models with normal weld speed and bulk material properties, cylindrical heat source with uniform heat distribution was used. Goldak heat source with Gaussian heat distribution was used for models with augmented speed and phase-based material properties.

Table 6.5: List of models and corresponding parameters for each model.

No.	Model name <sup>a</sup>	Machine <sup>b</sup>	Run time [h]	Torch speed	Material properties.	Phase Transform. <sup>c</sup>	Power distribution	Start/Stop location
1	K-244-BLK-N-h2t	Zenobe-4cpu	105	Normal	Bulk	-	20%+40%+40%	heel → toe
2	Y-244-BLK-N-h2t	Zenobe-2cpu	20.5	Normal	Bulk	-	20%+40%+40%	heel → toe
3	Y-333-BLK-N-h2t	Zenobe-2cpu	19.5	Normal	Bulk	-	30%+35%+35%	heel → toe
4	Y-244-BLK-N-sh	Zenobe-2cpu	21	Normal	Bulk	-	20%+40%+40%	h → t shifted
5	Y-333-BLK-N-sh	Zenobe-2cpu	21	Normal	Bulk	-	30%+35%+35%	h → t shifted
6	Y-333-BLK-A-sh	Core i7-4cpu	48	Augmented	Bulk	-	30%+35%+35%	h → t shifted
7	Y-333-LEB-TP-A-sh	Zenobe-4cpu	48	Augmented	Phase-based	Leblond-TP	30%+35%+35%	h → t shifted
8	Y-333-NOL-TP-A-sh	Zenobe-4cpu	38	Augmented	Phase-based	CCT-TP	30%+35%+35%	h → t shifted
9	Y-333-NOL-VC-A-sh	Zenobe-8cpu	41	Augmented	Phase-based	CCT-VC	30%+35%+35%	h → t shifted
10	Y-333-NOL-VCTP-A-sh	Zenobe-4cpu	38	Augmented	Phase-based	CCT-VC+TP	30%+35%+35%	h → t shifted

<sup>a</sup> Abbreviations used for the model names: BLK: bulk material properties, LEB: phase-based with transformations based on Leblond model, NOL: phase-based with transformations based on digitized CCT curve given in Figure 6.19.

<sup>b</sup> Denotes the computing facility for analysis; Either a computation cluster (Zenobe) or a PC with Intel Core i7 processor was utilized.

<sup>c</sup> Abbreviations used for phase transformation assumptions: VC: only volume change effect considered, TP: only transformation plasticity considered, VCTP: both VC and TP included in phase transformation model.

### 6.8.1 Model validation

**Temperature histories** Correct estimation of thermal field is essential for prediction of residual stress with adequate accuracy. Temperature measurements carried out at the time of fabrication (see chapter 5) allows for control of peak temperatures in a point close to the weld toe. Figure 6.23 shows the temperature time histories for a point located 6 mm away from the weld toe on chord surface, approximately in the location of Thermocouples #7 and #9 in Figure 5.15b. Peak temperature evaluated by both models with either normal or augmented speed show satisfactory agreement to the measured measured peak value, although augmented speed model slightly overestimates it. However for the cooling times, the two types of models (normal speed and augmented speed) certainly give different values, because the heat input per unit length of weld is not the same for the two models. The cooling times are unreasonably large for the normal speed welds. In the next paragraph, cooling rates will be assessed only for the case of augmented speed models. The change in cooling rate has considerable impact on phase kinetics and subsequently on microstructure field.

The registered peak temperature was not high enough to calculate cooling times from 800 °C to 500 °C ( $t_{8/5}$ ). Therefore, following approxiamte formula was used for estimation of the cooling

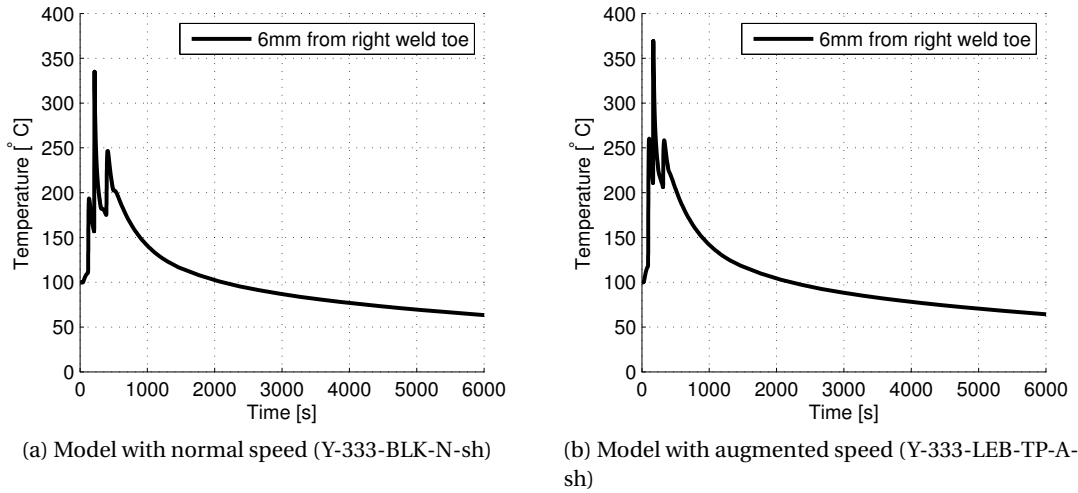


Figure 6.23: Temperature histories for a point on chord surface 6mm from the weld toe (compare to maximum for TC#7 in graphs of Figure 5.15b).

time (Seyffarth et al., 1992):

$$t_{8/5} = (6700 - 5T_0) \frac{q}{1000v} \left[ \left( \frac{1}{500 - T_0} \right) - \left( \frac{1}{800 - T_0} \right) \right] F_3 \quad (6.22)$$

Where:

- $T_0$  : preheating temperature [°C];
- $q$  : net heat flux calculated from Equation 6.20 [W];
- $v$  : welding speed [ $\text{mm s}^{-1}$ ];
- $F_3$  : weld geometry factor for three-dimensional heat flux.

Replacing  $T_0 = 120$  [°C],  $q = 5023$  [W],  $v = 7.4$  [ $\text{mm s}^{-1}$ ], and  $F_3 = 0.67$  (For T-joint welds), in the above equation will give  $t_{8/5} = 3.3$  s. Figure 6.24 shows the temperature time history and cooling times for the two points located at fusion zone and heat affected zone of the second weld pass at crown toe. Although computed cooling times of  $t_{8/5} = 5$  s to 5.5 s are longer than the value of 3.3 s given by Equation 6.22, but still they are short enough for martensite formation, according to CCT diagram of Figure 6.19. Therefore the final microstructures resulted from the theoretical  $t_{8/5}$  and calculated  $t_{8/5}$  will be similar.

**Size of fusion zone** Both FE models with normal and augmented torch speed give size of HAZ in good agreement with the weld macrograph, specially for the second and third passes (Figures 6.25 and 6.26). The size of fusion zone is slightly underestimated by the models.

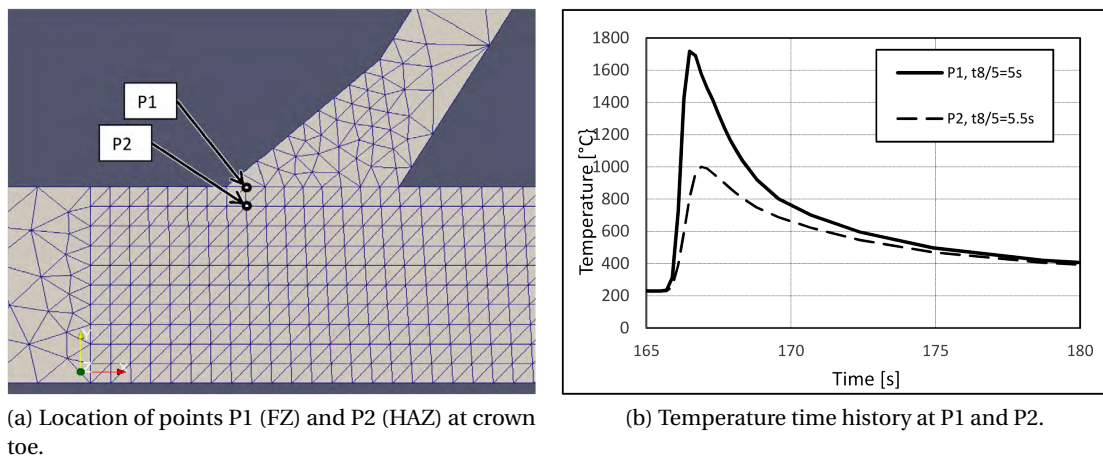


Figure 6.24: Temperature time history for two points P1 and P2 located in fusion zone and heat affected zone, respectively. the time history is shown only for the time that weld torch of pass 2 has reached the crown toe.

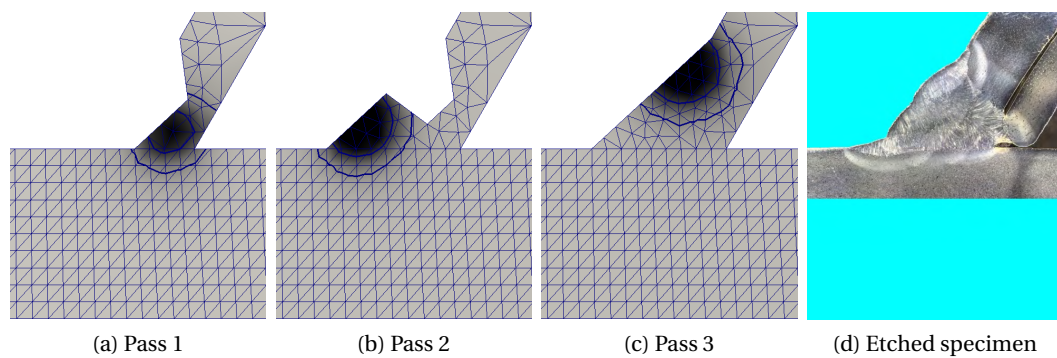


Figure 6.25: FZ and HAZ size predicted by model Y-333-BLK-N (cylindrical heat source, normal weld torch speed) compared to macrograph of weld. Contours are drawn for 650 °C and 1500 °C.

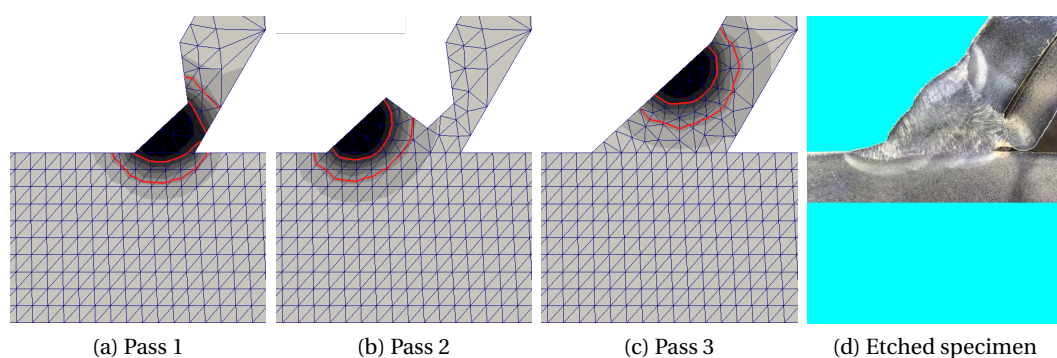


Figure 6.26: FZ and HAZ size predicted by model Y-333-LEB-TP-A-sh (double ellipsoid heat source, augmented weld torch speed) compared to macrograph of weld. Contours are drawn for 650 °C and 1500 °C.

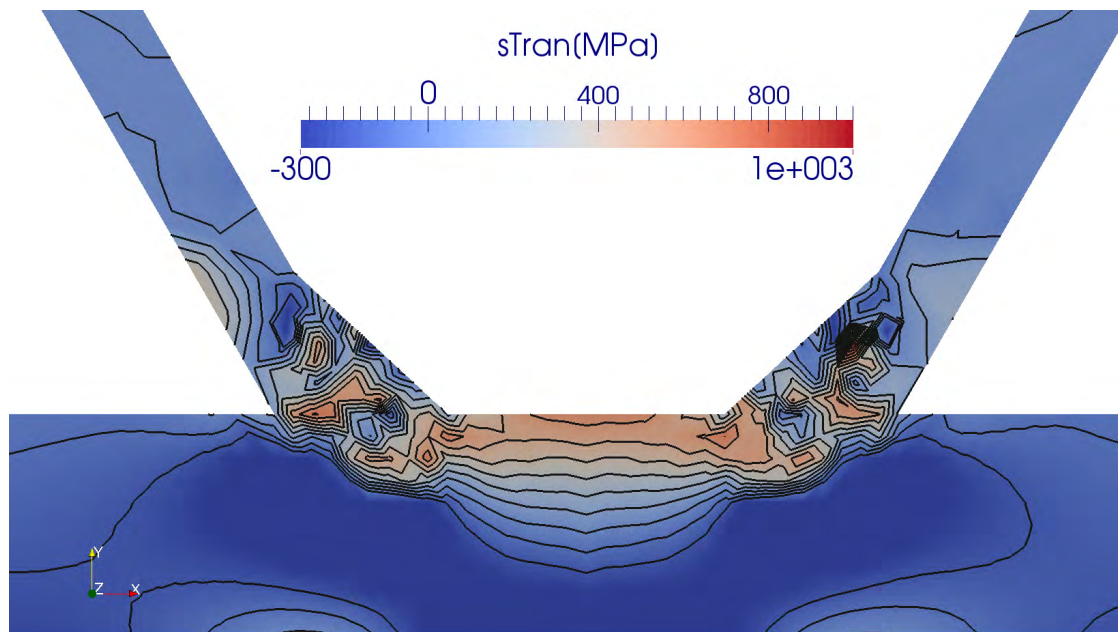
### 6.8.2 Comparison of residual stresses in K-joint and Y-joint

Comparison of transverse residual stress field at the gap region for K-joint and Y-joint models is presented in Figure 6.27. A strong restraining effect in between the braces is observed in Figure 6.27a for K-joint model which leads to high near-surface transverse residual stresses over the gap region. Calculated stresses are considerably higher than measurements (Figures 4.18 and 4.19). This is also shown in transversal and longitudinal residual stress profiles in Figure 6.28 where K-joint model with 'heel → toe' welding direction evaluates unrealistic residual stress values, especially near the chord surface ( $Depth < 3mm$ ) where longitudinal residual stress is estimated to be compressive. In contrast, the residual stress profiles for Y-joint models show acceptable agreement with measured residual stress profiles. The two Y-joint models differ only at the welding start/stop points.

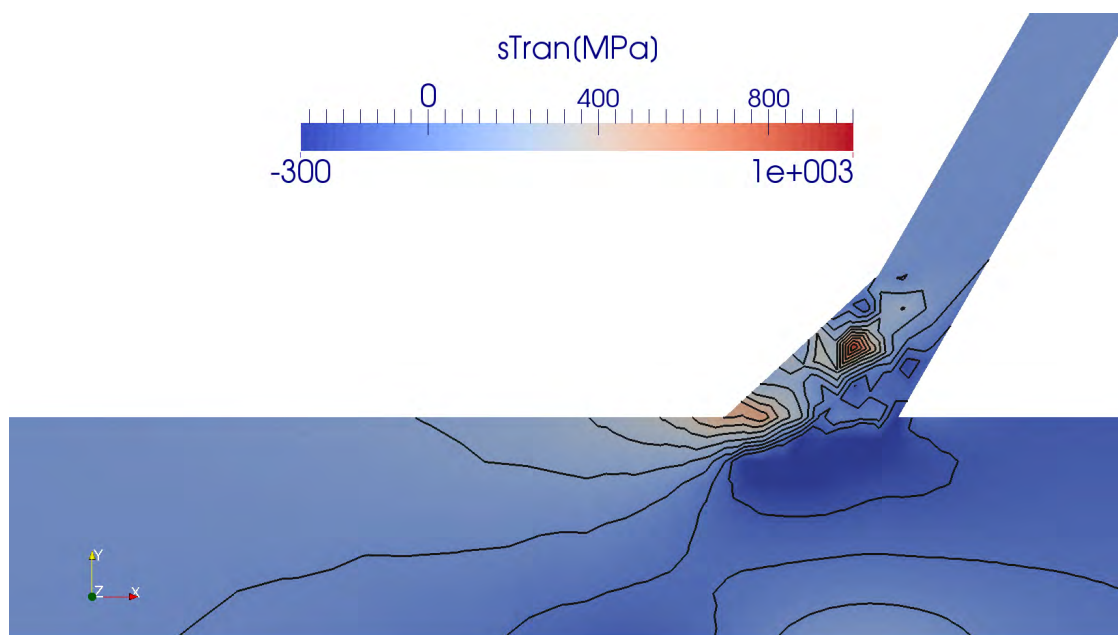
To look more closely at the behaviour of the two models, residual stress build up at the end of each welding pass is shown in Figure 6.29 for K-joint model and in Figure 6.30 for Y-joint model. For K-joint model, High input energy of the lumped passes on each brace affected a large part of the gap and when the effects from the two weld lines on the sides of the gap were combined, excessive build-up of residual stress in the gap region was produced. However, this was not the case for Y-joint model, since the interaction effect of other brace was removed from the model. Altogether, the residual stress field evaluated by Y-joint model agreed considerably better with measurements; Thus, this model was chosen as basis for subsequent analyses.

Final residual stress state in Figure 6.29 and residual stress profiles in 6.28 also show that asymmetry between residual stress profiles at the right and left weld toes are less pronounced compared to the calculations of Acevedo (2011). The reason is that weld deposition is carried out more gradually in the multipass weld model compared to single pass modelling in the study mentioned.

It should be noted that regions close to the surface and at the vicinity of the weld toe are more prone to experience stress relaxation after some loading cycles due to the notch effect at the weld toe. In this regard, the shape of residual stress profile would be more similar to the sinusoidal shape proposed by BS 7910.

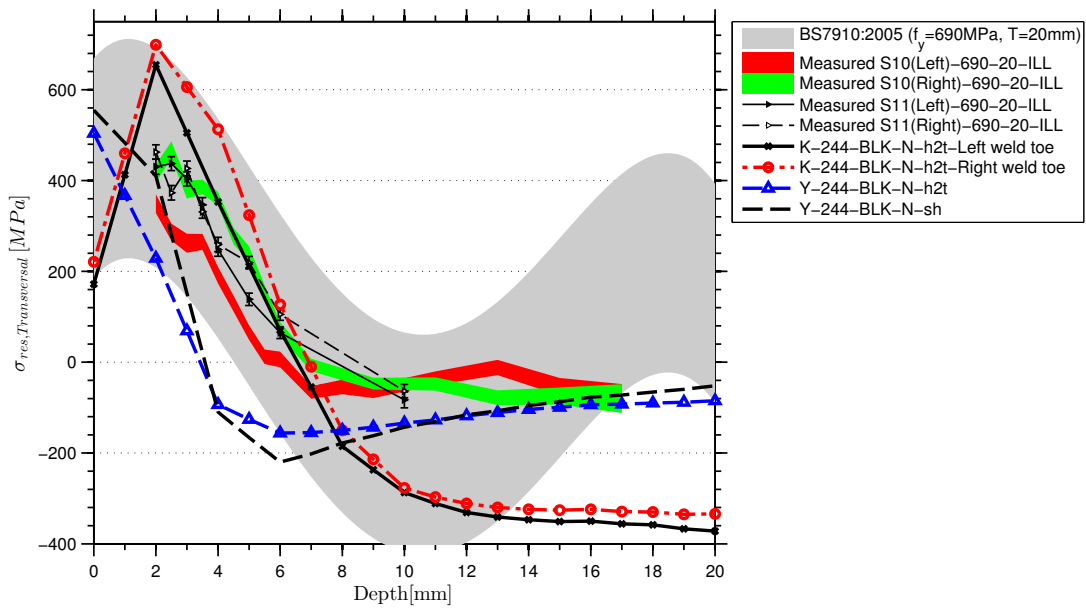


(a) K-244-BLK-N-h2t Model.

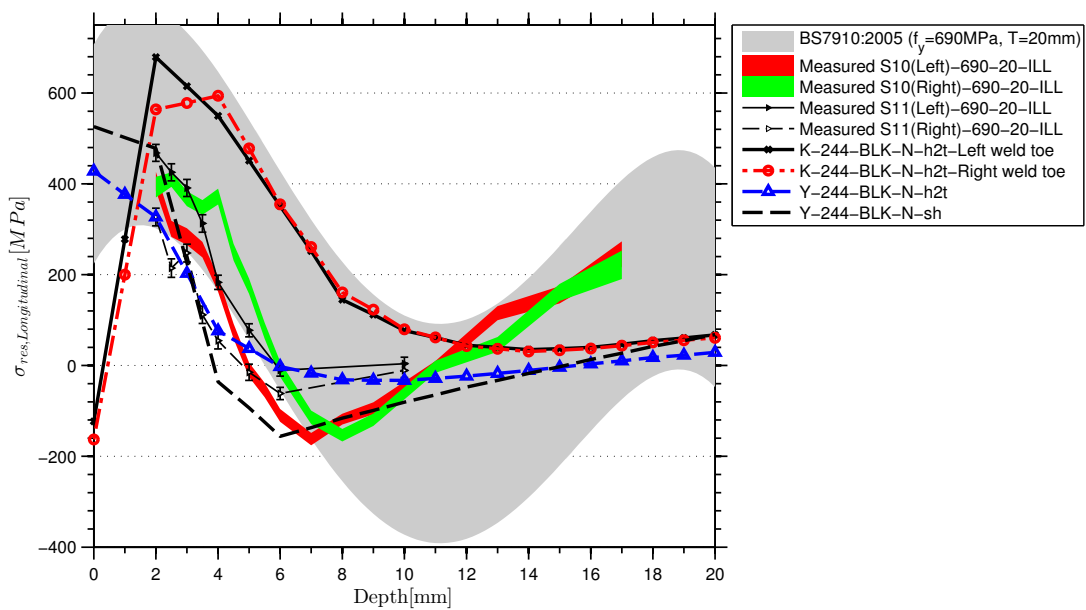


(b) Y-244-BLK-N-h2t Model.

Figure 6.27: Comparison of calculated transverse residual stress fields in the gap region between K-Joint and Y-Joint.



(a) Transverse stress profiles.



(b) Longitudinal stress profiles

Figure 6.28: Comparison of calculated stress profiles for K-Joint and Y-Joint, together with measured residual stress profiles and value ranges suggested by BS 7910 (2005).



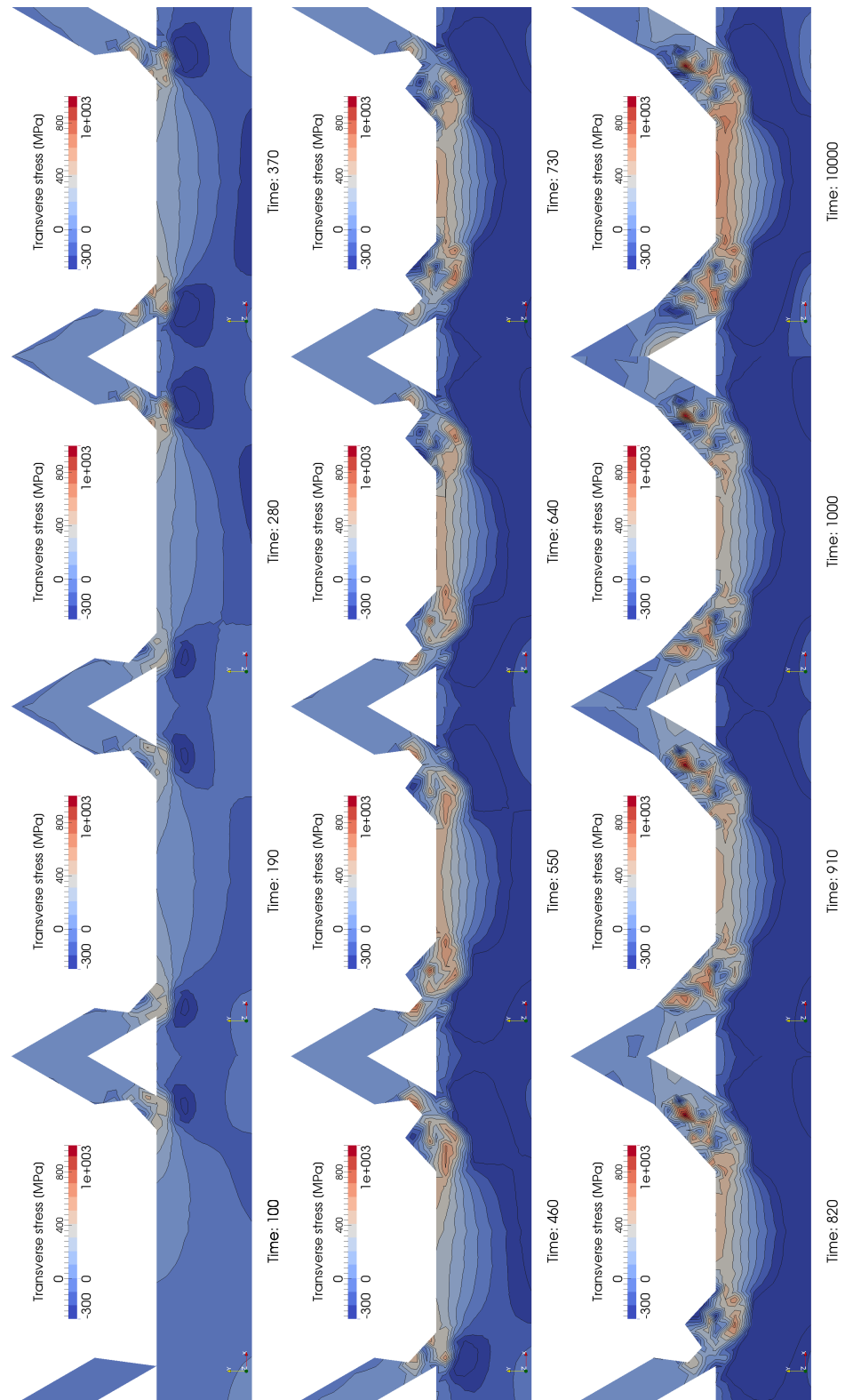


Figure 6.29: Transverse residual stress build-up in gap region of K-Joint (Model K244-BLK-N-h2t: heel-to-toe weld trajectory, No phase transformation, 20/40/40% power distribution between passes). Snapshots at the end of cooling stages.

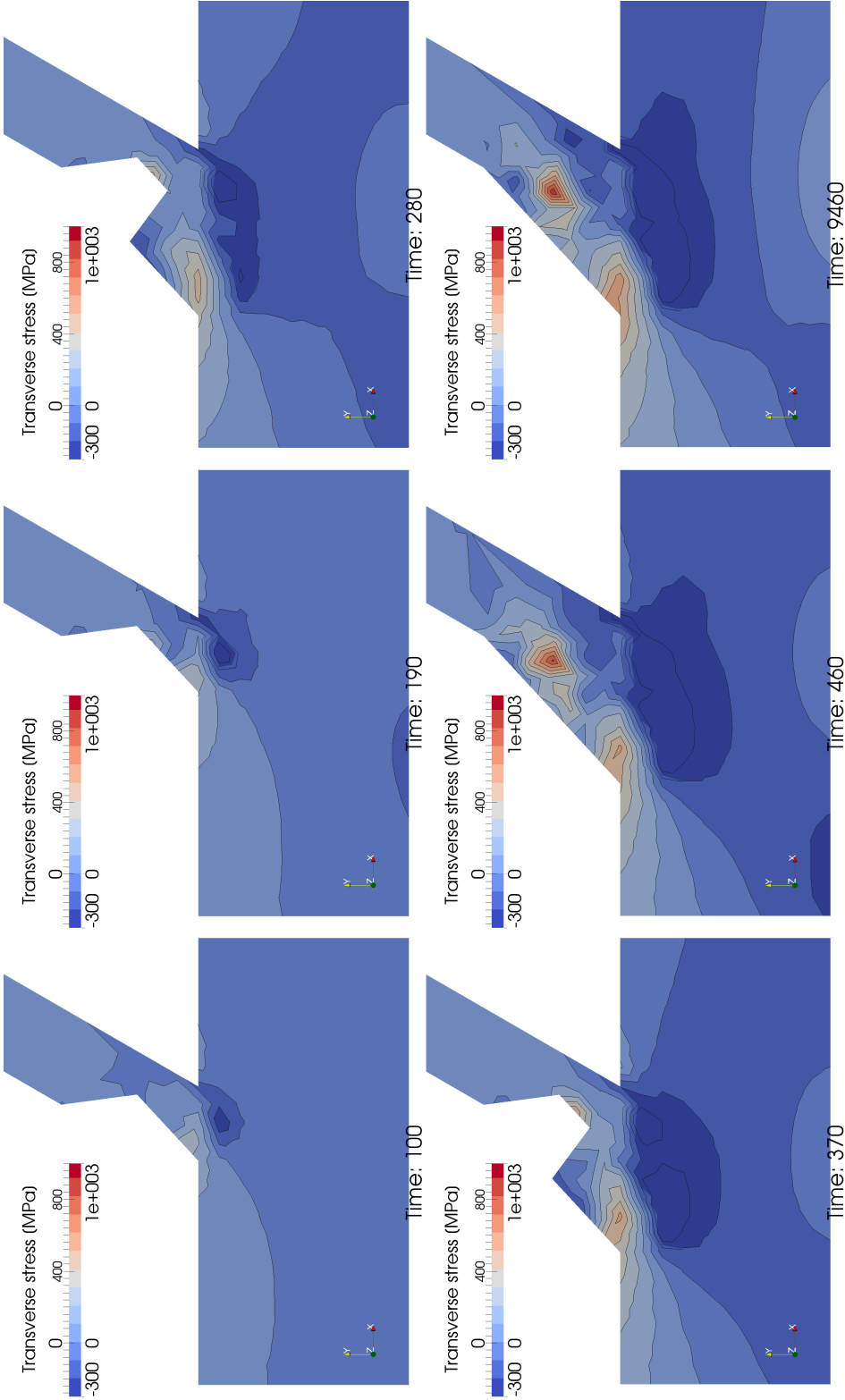


Figure 6.30: Transverse residual stress build-up in crown toe of Y-Joint (Model Y244-BLK-N-h2t: heel-to-toe weld trajectory, No phase transformation, 20/40/40% power distribution between passes). Snapshots at the end of cooling stages.

### 6.8.3 Effect of start/stop points and torch speed

As stated in section 6.3.1, two selections for welding start/stop locations were chosen in the models. One straight-forward choice was welding start at crown heel and welding stop at crown toe. In the second choice – better representative of real welding – welding start and stop points were shifted away from crown heel and crown toe locations.

Second parameter changed within the models was the distribution of heat power between the three lumped passes. Since each weld pass anneals part of residual stresses created by previous weld pass(es) in multipass welds, higher power input for the first pass in the model would improve the real welding conditions, where the residual stresses are annealed by a subsequent weld line with a lower heat input. To assess the effect of heat distribution among lumped weld passes, two different distributions 20%+40%+40% and 30%+35%+35% were examined, as described in section 6.7.1

Third parameter being adjusted was welding speed. In order to maintain the same value of heat input deposited per unit length of weld for lumped pass model compared to the real weld, the welding speed needed to be augmented; this was done for the model Y-333-BLK-A-sh with bulk material properties and for all model with phase-based material properties.

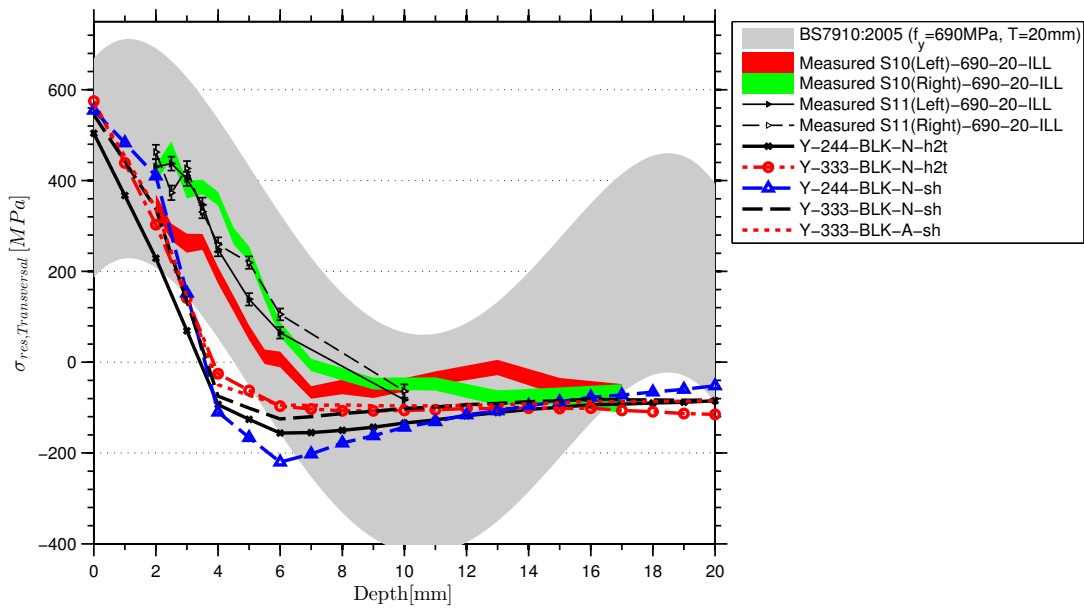
Figure 6.31 shows the impact of above parameter modifications on the residual stress profiles at the weld toe. Profiles corresponding to models with 30%+35%+35% heat source distribution have slightly smoother stress profiles compared to 20%+40%+40% models and their trend better agrees with measure profiles, specially for transversal stresses.

Stress profiles for shifted trajectory models and heel → toe models were similar. Augmented speed model Y-333-BLK-A-sh evaluated higher longitudinal residual stresses compared to normal speed model Y-333-BLK-N-sh. However, the difference of the two models for transversal residual stresses was small. For transversal residual stresses close to weld toe ( $Depth = 0$ ), all models converge to values between 505 MPa to 575 MPa. The calculated residual stress values near the surface must be interpreted with caution since no experimental stress measurements were available for the depth range of 0 mm to 2 mm.

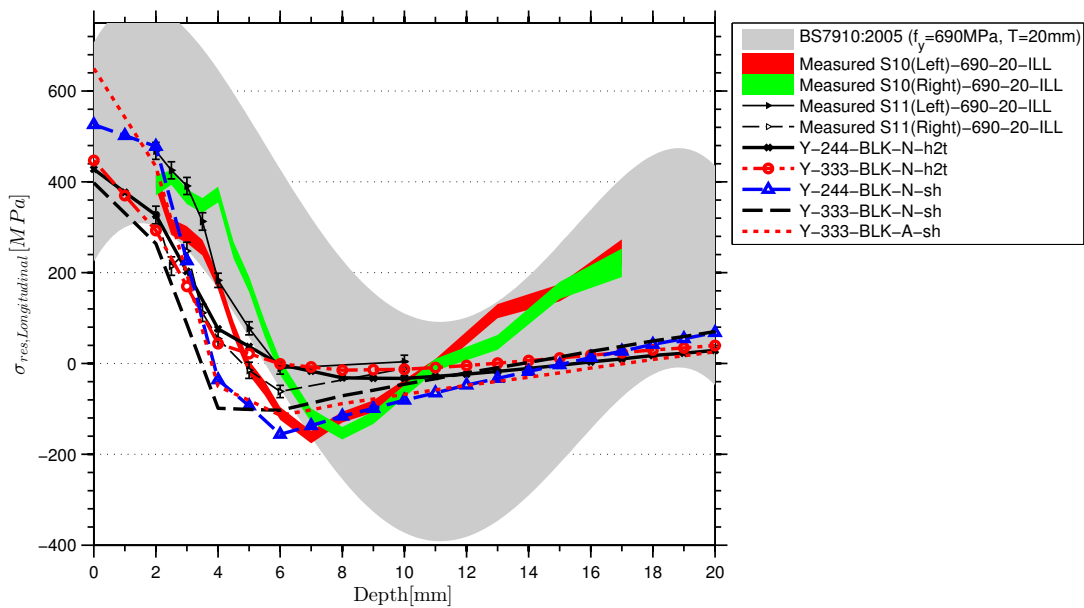
### 6.8.4 Phase transformation effects

Augmented speed model with shifted trajectory was taken from the last stage and various transformation models with phase-based material properties were added to this model. Microstructure of parent and weld metal at the beginning of simulation was set to 84% bainite and 16% martensite, as reported by Hildebrand (2008) for similar steel grade S690QL. Figure 6.32 shows stress profiles evaluated by these models.

From explanations in Chapter 2 (Figure 2.9) it was expected that stress profiles for the models with volume change (denoted by *VC*) and TRIP included (denoted by *TP*), fall between profiles of model Y-333-NOL-VC-A-sh (only *VC* included) and model Y-333-BLK-A-sh (no phase trans-



(a) Transverse stress profiles.



(b) Longitudinal stress profiles

Figure 6.31: Comparison of calculated stress profiles for different start/stop locations, power distribution, and torch speed, together with measured residual stress profiles and value range suggested by BS 7910 (2005).

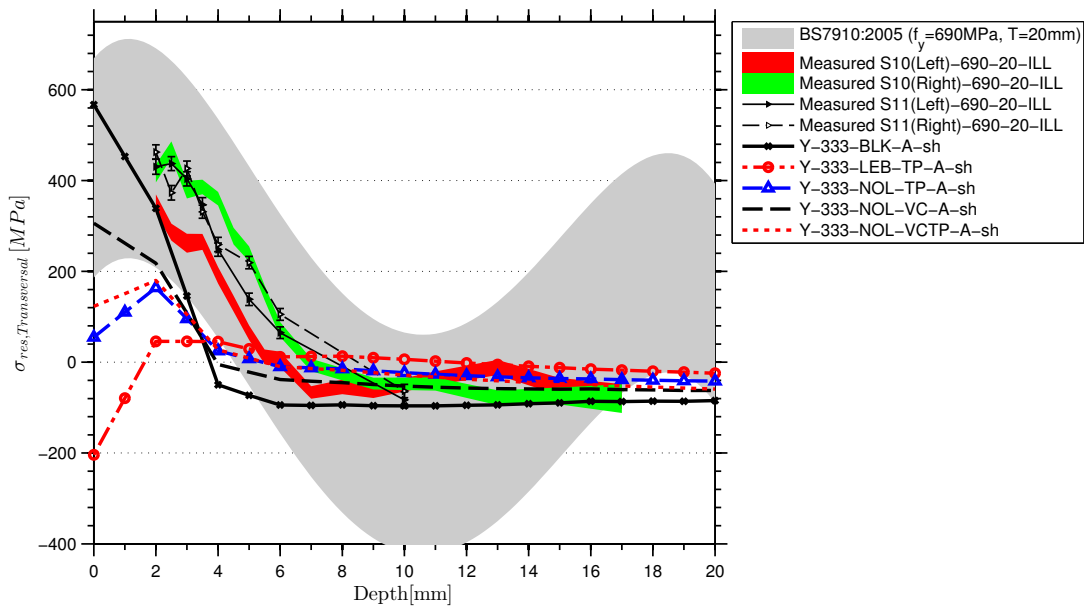
formation effects). Surprisingly, those models (Y-333-LEB-TP-A-sh, Y-333-NOL-TP-A-sh, and Y-333-NOL-VCTP-A-sh) reported lower values for near-surface stresses, compared to only VC model (Y-333-NOL-VC-A-sh) and apparently the values of Y-333-LEB-TP-A-sh model were in an unacceptable range.

Figure 6.33 shows phase fraction distributions for bainite and martensite phases at the end of simulation. From the estimated short cooling times reported in section 6.8.1, a larger martensite phase fraction was expected to form in the HAZ. The hardness measurements shown in Figure 5.32 also confirmed formation of higher martensite phase fractions at the HAZ of second weld pass. The reason for underestimation of martensite phase fraction in the model (Figure 6.33) is the implementation of algorithm for CCT-based models. The program transforms CCT diagram into a temperature-cooling rate diagram as shown in Figure 6.34 before analysis and uses the latter for phase fraction calculations. This means that there is no explicit time dependency for phase fraction calculation. This implementation gives accurate results when cooling temperature history is linear, but when the cooling curve is non-linear with time, the accuracy of microstructure prediction will decrease. For the case of studied problem, the cooling rate in temperatures below 500C is low. therefore, final predicted microstructure will overestimate bainite fraction as shown by the curve for point P1 in Figure 6.34.

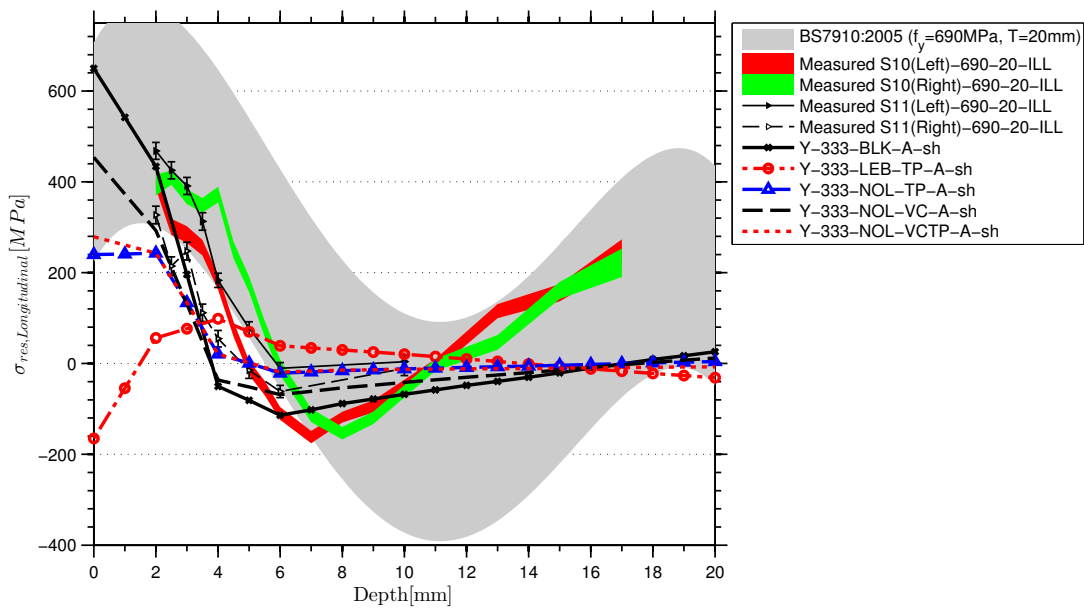
Only model with VC effects (Y-333-NOL-VC-A-sh) showed good global agreement with measured residual stresses, although it underestimated residual stress values in shallow depths. The main reasons for the discrepancy in phase-based model results are

- Implementation of phase kinetics estimation algorithm for digitized CCT curve: current implementation does not explicitly take into account the time<sup>8</sup>. This led to overestimation of final bainite phase fraction.
- Sensitivity of phase predictions to cooling times: As stated before, accurate reproduction of transient thermal field is more important for these models, compared to models without phase transformation effects. Lumping the welding passes increases heat input and shifts the cooling times towards higher values, which reduces calculated volume fraction of martensite in HAZ compared to real weld. Increasing welding speed reduces the cooling times, but this compensated only partially for the increased heat input due to weld pass lumping. Another solution for improving the estimation of cooling times with the current modelling scheme would be to modify thermal properties of material (e.g. thermal conduction coefficient).
- Lack of experimental material data: more accurate, experimentally determined, metallurgical data (volume change due to phase transformation and transformation plasticity

<sup>8</sup>A bug in the program regarding calculation of overall cooling rates was detected and reported during this investigation.



(a) Transversal stress profiles.



(b) Longitudinal stress profiles

Figure 6.32: Comparison of calculated stress profiles with and without transformation plasticity effect, together with measured residual stress profiles and value ranges suggested by BS 7910 (2005).

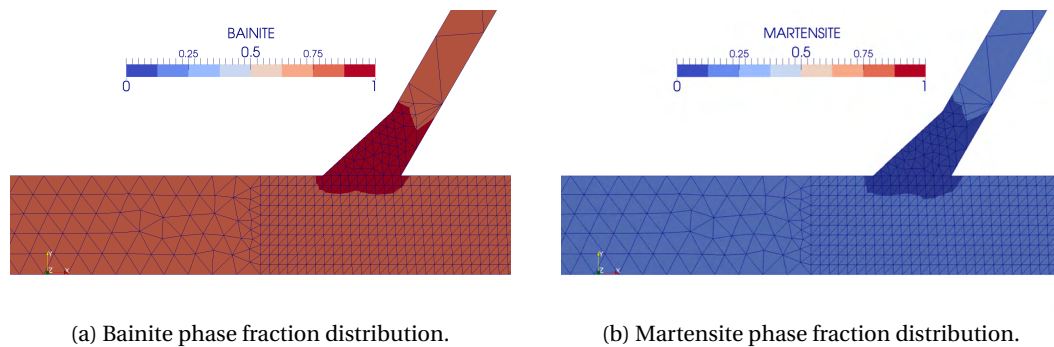


Figure 6.33: Phase fraction distributions of bainite and martensite in the weld zone at crow toe at the end of simulation (CCT-based phase kinetics with augmented speed model).

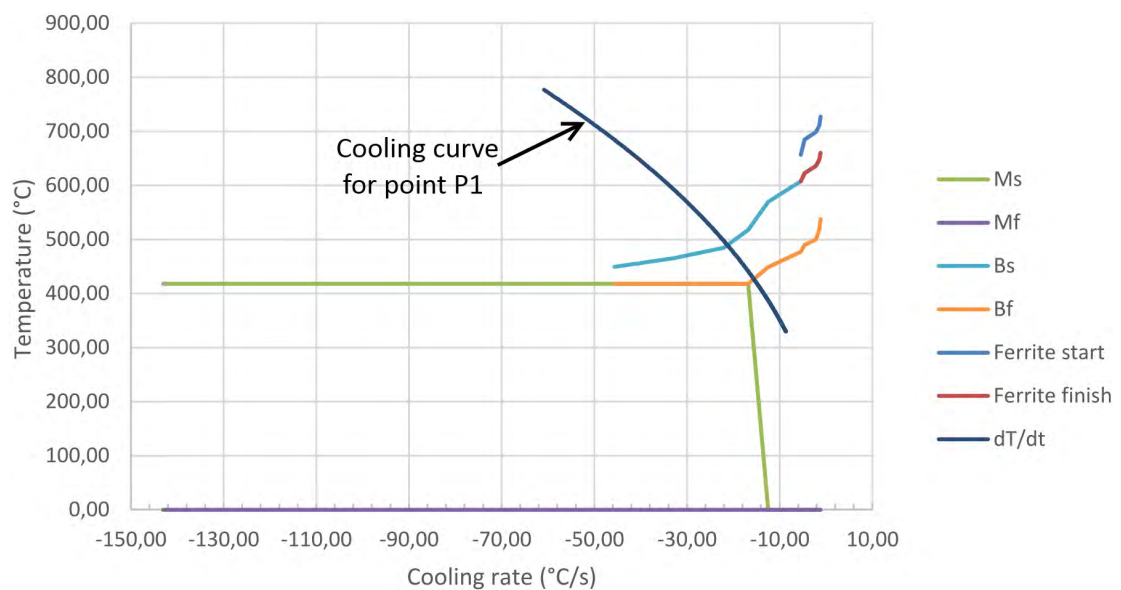


Figure 6.34: Temperature vs. cooling rate diagram derived from CCT curve of Figure 6.19 and estimated cooling curve for point P1 (see Figure 6.24a).  $M_s$  and  $M_f$  are martensite start and finish temperatures respectively;  $B_s$  and  $B_f$  are bainite start and finish temperatures respectively (GeonX S.A., 2014).

coefficient for martensitic transformation) should increase the accuracy of residual stress predictions.

Finally, model Y-333-BLK-A-sh arguably overestimates the stresses at surface and shallow depths; It is on the safe side to use this model for life-cycle analysis purpose. Model Y-333-BLK-N-h2t is as good for estimation of transversal stresses, but less good for longitudinal residual stresses.

### 6.9 Conclusion

Three-dimensional weld modelling of tubular K-joint is carried out in this chapter in order to evaluate residual stress field in the gap region. Modelling assumptions, input data, and analysis procedure are described. Parameters of the model have been changed to observe their effect on final residual stress state. Main analysis topics and findings are presented below:

- A staggered thermal-metallurgical-mechanical analysis scheme was used in this study. Two types of material properties were introduced for the models: phase-based mechanical properties for models with phase transformation included; and bulk material properties for other models. Weld metal deposition was modelled with time-based element activation. Number of real weld passes was reduced (lumped) into three equivalent weld passes. Preheating was considered in initial conditions of thermal field.
- Restraining effect observed by Acevedo (2011) is a function of heat input and gap distance. The simulations in this chapter involved lumping of several passes into three equivalent passes. This led to an overestimation of restraining effect, given that the real welding was done with several low power weld passes. Modelling of Y-joint, resulted in more realistic residual stress values and had the added benefit of reducing modelling and computation costs.
- Calculated transversal and longitudinal peak residual stresses did not reach yield stress. Models with phase-based material data reported smaller peak residual stresses compared to other models. All Y-joint models reported the location of peak values at the surface, which is not in agreement with BS 7910 prediction. It predicts that the peak of residual stresses happens in approximately 10% below surface. However, it should be noted that as-welded residual stresses on the surface are more prone to undergo relaxation due to notch effect at the weld toe after fatigue loading and become more similar to the profiles given by the code.
- Y-joint models slightly underestimated the location of minimum  $\sigma_{transversal}$  and  $\sigma_{longitudinal}$  profiles at  $0.3T_{ch}$  ( $T_{ch}$  being chord thickness) below weld toe, compared to  $0.35T_{ch}$ –



$0.4T_{ch}$  from measurements. BS 7910 gives sinusoidal through-thickness residual stress profiles for both transversal and longitudinal directions. It predicts that  $\sigma_{transversal}$  and  $\sigma_{longitudinal}$  will increase at higher depths (measured from chord surface) once they reach their minima at approximately mid-thickness. However, for the case of  $\sigma_{transversal}$ , both the calculated and measured residual stresses showed only a small increase of stress with depth after the minimum was reached. Also, FEM analysis was not able to reproduce this trend for the case of  $\sigma_{longitudinal}$ .

- The asymmetry observed in previous studies (Acevedo, 2011) in the residual stress field at the gap region, was less pronounced in this study due to multipass weld modelling.
- Accurate reproduction of transient thermal field and cooling times is crucial when phase transformation effects are included in the model. For this reason, lumping of welding passes is a difficult decision. Since the last welding passes have more impact in the final residual stress (see section 6.8.3), it is advisable that for future simulations, the analysis start with a large weld pass that lumps all weld passes except for the last two or three passes, and then these last passes being modelled according to real welding conditions (i.e. without lumping). Another solution is to increase the number of weld passes in the model, given that the problem of geometric modelling of complex weld shapes can be solved by 3D scanning methods. Alternatively, modifying convection and conduction material properties to adjust the heat transfer rate and cooling times can be considered in future studies.
- More experimental material data regarding phase transformation behaviour – including volume change strains and transformation plasticity coefficients – are needed to improve the accuracy of residual stress predictions with phase-based models.
- Models with 30-35-35% heat distribution between three passes gave systematically slightly better results than other similar models (with 20-40-40% distribution).
- Models with bulk material properties (BLK) gave better results than phase-based models based on Leblond and Koistinen-Marburger (LEB) and CCT curve (NOL) phase kinetics. The models with phase transformation effects included systematically overestimates the percentage of bainite and underestimates it for martensite. For this reason, phase transformation influence is not accurately predicted. One shall improve the model with an phase kinetics estimation procedure that is explicitly time dependent.



# 7 Fatigue crack growth simulation

## 7.1 Introduction

In this chapter fatigue crack propagation using Morfeo/Crack analysis software is presented. Morfeo/Crack is a an eXtended Finite Element (XFEM) program and currently under active development. XFEM was introduced by Belytschko and Black (1999) and Moës et al. (1999). Traditional methods – such as Virtual Crack Closure Technique (VCCT) (Krueger, 2004; Shivakumar et al., 1988) – are time consuming in mesh preparation. Moreover, because of strong mesh refinement at crack tip, some degenerated elements might appear in the model. Also numerical problems may arise due to crack tip singularity. Mesh refinement at crack tip location is not necessary for extend finite element method, since it uses discontinuous shape functions to approximate the displacement field on the two side of the crack. Another important advantage of the method is that prior knowledge of crack shape or crack path is not necessary. The crack extension direction is predicted by program itself. Morfeo uses maximum tangential stress (MTS) criteria for determining crack extension direction. In this method proposed by Erdogan and Sih (1963) for mixed mode cracking, it is assumed that the crack extends at its tip in a radial direction within a plane perpendicular to the direction of maximum tension (see Section 3.4).

The crack shape is defined by two levelset functions (Mohammadi, 2008). Levelset functions are simply functions that give the distance of each point in space to a defined boundary. Two levelsets are required in order to define the crack, one to define the plane of the crack, and one to define the crack front. The method uses two series of enrichment functions to calculate the displacement field on the two side of the crack:

$$u(x) = \sum_{I \in N} \left\{ N_I(x) \left[ u_I + \underbrace{H(x) a_I}_{\text{Heaviside enrichment term}} + \underbrace{\sum_{\alpha=1}^4 F_{\alpha}(x) b_I^{\alpha}}_{\text{crack tip enrichment}} \right] \right\} \quad (7.1)$$

Where:

- $N_I$  : Conventional shape function ;
- $u_I$  : Nodal DOF for conventional shape functions;
- $H(x)$  : Heaviside distribution;
- $a_I$  : Nodal enriched DOF (jump discontinuity);
- $F_\alpha(x)$  : Crack tip asymptotic functions;
- $b_I^\alpha$  : Nodal DOF (crack tip enrichment);

Heaviside enrichment function is a discontinuous function with the value of either 1 or -1 and changes sign in the two sides of the crack face. Enrichment functions at the crack tip improve the calculation of displacement field for better estimation of Stress Intensity Factors (SIFs).

Morfeo/Crack uses maximum tangential stress criteria (see section 3.4.1) to determine the direction of crack extension.

In the following sections, the XFEM model created for the tubular K-joint is presented and the results are discussed.

### 7.2 The XFEM model

The geometry was similar to the geometry for the K-joint that was used in Chapter 6. The mesh was independent of the crack (in XFEM), but to capture more accurately the high stress gradients in vicinity of the crack, the mesh was refined in the crack region. Morfeo manual recommends having at least 5 elements across the crack front at the beginning of analysis. The tetrahedral element mesh size was changed linearly from 10mm at 100mm distance to 0.1mm at 2mm (or less) from crack center point. Figure 7.1 shows the mesh at the vicinity of crack location.

In order to properly load the model with axial forces and moment, each member's end surface was divided to two parts and uniform stresses were applied such that the resultant of the stresses on the two parts of surface, produced desired axial force and moment in the member. The moments and axial forces for joint S10-J1 were read from the results of structural analysis of the truss (Appendix B).

Residual stress field evaluated with Morfeo/Welding was defined as initial stresses in the XFEM model. Since, the meshes for the two models were different, the program automatically did the interpolation to calculate the initial stress values at nodal locations of the XFEM mesh.

External load ratio was  $R = 0.1$  and two load combinations were defined, corresponding to: (1) maximum external load+residual stresses which gave  $K_{Max}$ , and (2) minimum external load+residual stresses which gave  $K_{min}$ . The stress intensity factor range  $\Delta K = K_{Max} - K_{min}$  was then calculated by program and used for crack propagation analysis.

A semi elliptical crack with  $a_i = 0.5$  mm and  $2c_i = 2$  mm was placed at hs1. Material behaviour

was considered linear elastic and Paris law coefficients were taken as recommended by Walbridge (2005):  $m = 3$  and  $C = 3.11 \times 10^{-13} \text{ mm MPa}^{-3} \text{ mm}^{-1.5}$ .

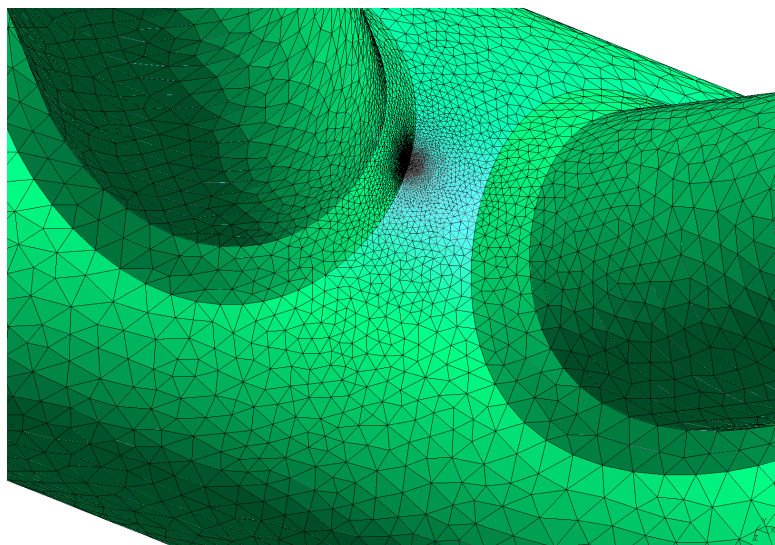


Figure 7.1: Mesh of the K-joint (joint J1 of truss) with tetrahedral elements refined at the crack location. Initial semi-elliptical crack size:  $a_i = 0.5 \text{ mm}$ ,  $2c_i = 2 \text{ mm}$ .

### 7.3 Results

Figure 7.2a shows the (magnified) deformed shape of the model, with deformations localized around crack lips. The crack shape is shown in Figure 7.2b superposed on a skeleton of the model for easier comparison. Figure 7.3 shows the stress intensity factors calculated by Morfeo/Crack for two analyses with and without residual stresses included in the calculation. It will be shown later that the SIF values reported for the case of (external load+residual stresses) were not calculated correctly by the program.

As can be seen in the crack shape, the model did not correctly predict crack propagation shape for the studied case. After conducting analyses on simpler models and discussions with Morfeo programmers, two sources of error were identified:

- Error in estimation of effect of residual stresses: Spatial gradient of the initial stress field is required for calculation of the stress intensity factors. However, this gradient is not implemented completely in the program<sup>1</sup>.
- Contact of crack faces: The contact between crack faces is not detected by Morfeo/Crack or other programs with XFEM capabilities<sup>2</sup>. This is better shown in the simple 2-

<sup>1</sup>It will be added in the next Morfeo release (v. 2.1).

<sup>2</sup>In XFEM module of Abaqus, contact between crack faces is detected, but SIF values are not calculated correctly, because of the omitted terms in computation of J contour integral corresponding to the crack faces.

dimensional center-cracked plate model in Figure 7.4b where two crack lips have overlapped (displacements are magnified to show the overlap more clearly).

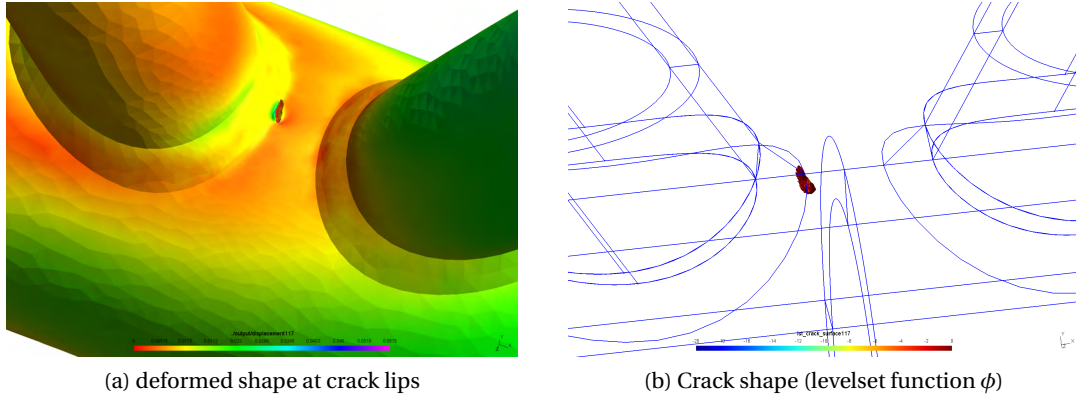


Figure 7.2: Crack shape at joint S10-J5; As can be seen, crack shape and direction are not correctly reproduced by model (c.f. Figure 5.29).

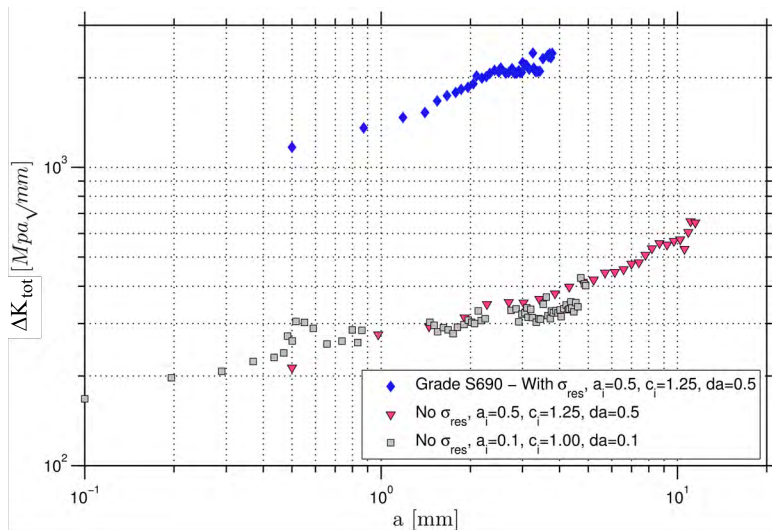


Figure 7.3: Equivalent stress intensity factors for models with, and without residual stresses.

### 7.3.1 Contact of crack faces

For the accurate prediction of crack propagation within the residual stress field, modelling of contact between crack faces is crucial. Because combination of tensile residual stresses and external compressive loads might create situations in which the crack is partially closed behind the tip, which we can call *stress-induced crack closure* in contrast to crack closure at the tip, or *plasticity-induced crack closure* (Elber crack closure). This situation is shown in Figure 7.5 for the case of a center cracked plate under external tensile loading and with compressive residual stresses which have caused the crack faces to be in contact at the middle

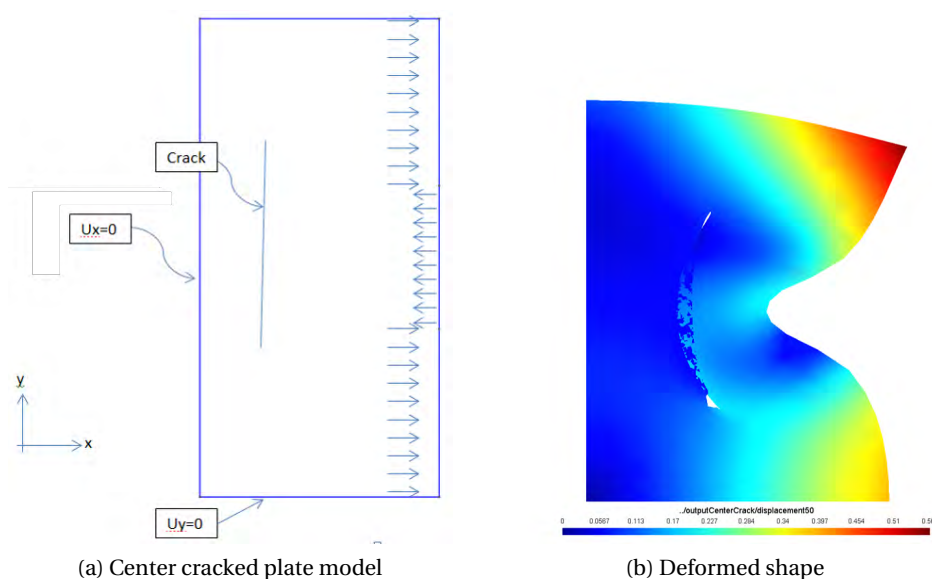


Figure 7.4: Contact of crack faces not implemented in Morfeo.

of the crack. In the presence of compressive residual stresses, total stress intensity factor  $K_{tot}$  will be smaller than the case of no or tensile residual stresses. Even when the external load is high enough (dashed horizontal line in the Figure), the rate of change of  $K_{tot}$  for a crack in compressive residual field with the change of external load is smaller than the similar rate for a crack with no (or tensile) residual stresses.

The crack faces are not stress-free any more in case of stress-induced crack closure. Therefore, the interaction integrals (Mohammadi, 2008) used for calculation of J-integral and stress intensity factors should be modified to include the effects of stresses on the crack faces. A brief investigation on Abaqus software revealed that this issue is not addressed in the XFEM module of Abaqus, neither.

It should be noted that the residual stress state is not constant during the crack propagation. Past research has shown that the residual stress field changes (McClung, 2007). Fukuda and Tsuruta (1979) measured a progressive relaxation of residual stresses during through-thickness cracking of a welded plate specimen. This relaxation due to crack growth is automatically taken into account when XFEM analysis method is used; because the cracked structure is analysed in each step under combined effect of residual stresses and external loading.

There are several methods for implementation of crack faces contact in XFEM. For the case of fatigue cracks, a simple penalty approach (Belytschko and Neal, 1991) would suffice since the nonlinearities are not large. Flowchart in Figure 7.6 is proposed for implementation of crack contact in the current analysis procedure for fatigue crack growth.

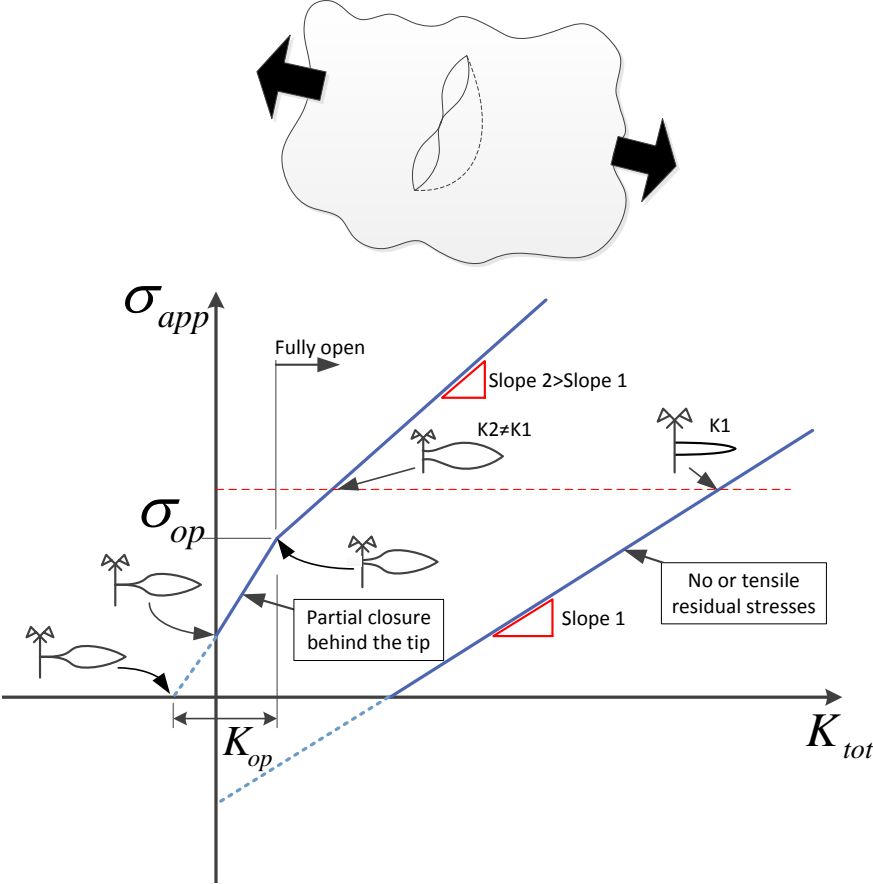


Figure 7.5: Illustration of 3D crack closure behind the tip. Schematic diagram shows total intensity factor  $K_{tot}$  versus external loading  $\sigma_{app}$  for the two cases of compressive and tensile (or none) residual stresses. Note that even if in both cases cracks are open under the same load, stress intensity factors  $K_2$  and  $K_1$  are not the same.



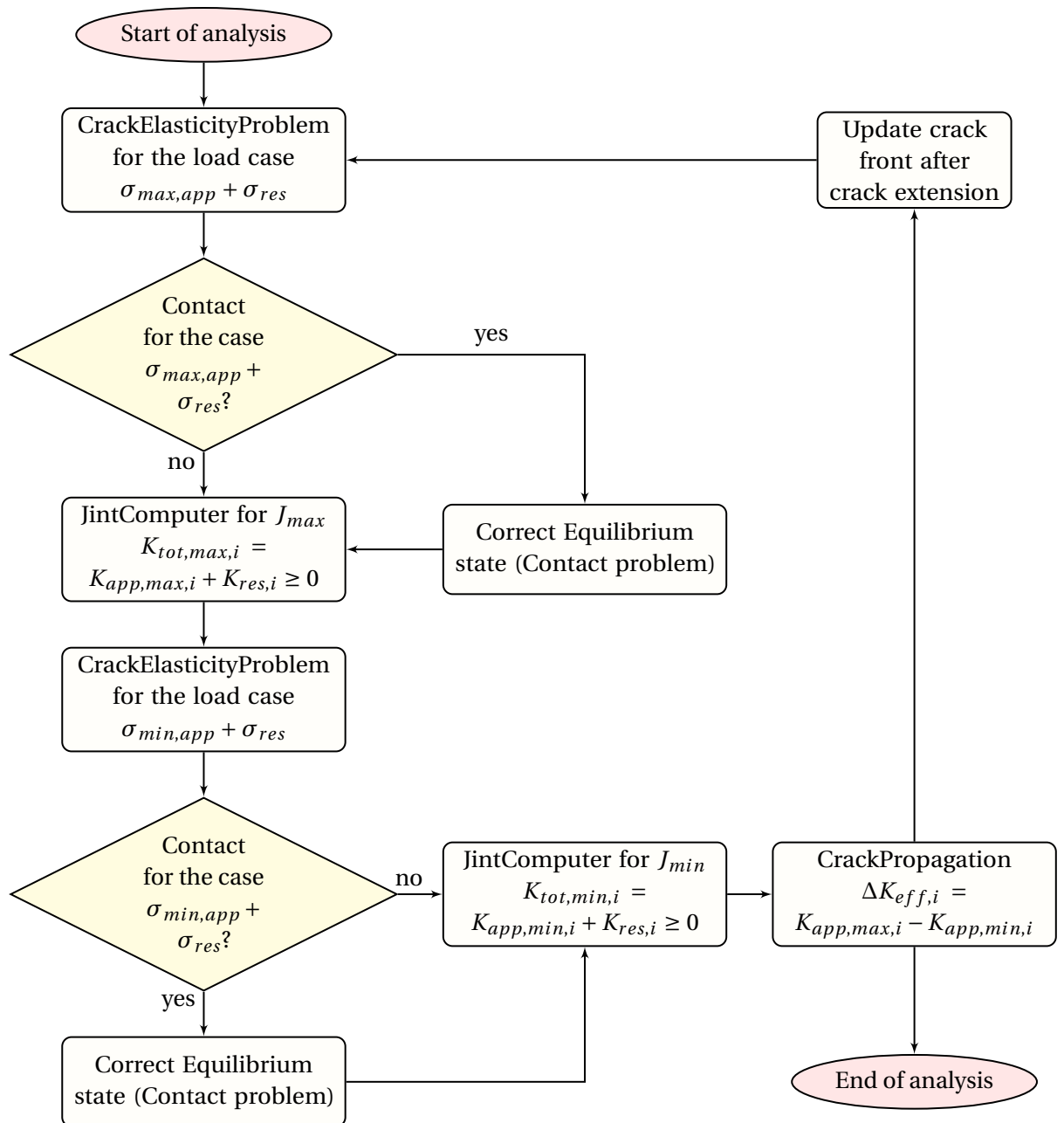


Figure 7.6: Suggestion for implementation of crack faces contact in Morfeo/Crack.

### 7.4 Conclusion

In this chapter the procedure for XFEM analysis for crack growth analysis of K-joint was explained. Shortcomings of the software tool in simulating stress-induced crack closure – which limited its use in estimation of crack growth within residual stress field – were identified and explained. In order to improve the solution, necessary modifications in the program were proposed which included modification of J-integral calculation and implementation of crack faces contact detection.

## 8 Conclusion

This research aimed at the fatigue behaviour of tubular K-joints made of HSLA construction steel grade S690QH considering the effect of welding residual stresses.

Use of high-performance steels is on one hand increasing in engineering structures, specifically in bridges, because of energy, material and cost savings. On the other hand, there is a recent interest in tubular profiles for bridge design. These profiles have been employed in offshore industry since long ago. Several road bridges, mainly located in Switzerland and in Germany, have been constructed in the past 25 years, based on the structural concept of truss bridge supporting a reinforced concrete slab. Combining this efficient structural system with the use of high strength steels can lead to more sustainable infrastructure. In this regard, this study was a necessary step towards promotion of HSLA.

Referring to the objectives stated in section 1.3, main findings of this study are summarized as follows:

### 8.1 Determination of residual stress field in high-strength tubular K-joint

#### Experimental evaluation of residual stresses using neutron diffraction

For the fatigue of welded structures, it is often postulated that the welding residual stresses are tensile and close to yield stress. One of the main outcomes of this assumption is that, regardless of the direction of applied stresses, the resultant stresses acting on the cracked welded detail are tensile. The results from neutron diffraction measurements showed that tensile residual stresses were lower than yield stress (approximately 60% of the nominal yield stress). Despite higher yield stress of specimens, the measured residual stresses in the gap region were of the same order than in the lower grade steel S355J2H studied in a previous study by Acevedo (2011). This is in contrast to residual stress profiles given by BS 7910 in which residual stress field is assumed to be a function of yield stress. The directions of principal

## Chapter 8. Conclusion

---

welding residual stresses were determined to be – with an acceptable tolerance – in alignment with longitudinal and transversal directions of weld line.

Neutron diffraction method can reliably evaluate residual stress state in the depths that other non-destructive methods can't access. However, it is costly and the cost increases rapidly when measuring residual stresses in depths that are smaller than the beam gage size. Therefore, combining in-depth measurements by neutron diffraction with surface residual stress measurements by X-rays would give a more complete image of residual stress distribution.

### **Numerical calculation of thermal residual stresses and effect of modelling parameters**

Among the phase-based models, only model with volume change (VC) effects exhibited satisfactory agreement with measured residual stresses, but underestimated residual stress values in shallow depths. The model with bulk material properties and increased torch speed also agreed well with the neutron diffraction measurements. However, as stated before, measurements of surface residual stresses are needed for validation or rejection of models.

The complex geometry of tubular K-joint resulted in a weld bead with variable cross section along the weld lines, which meant either there should be partial weld passes, or the disposition rate should have changed along the weld line by changing the weld torch speed. The torch direction angle was also variable. Facing these complexities, following simplification of the problem were applied:

- **Weld pass reduction:** total weld section was divided into three lumped weld passes;
- **Y-joint modelling:** since the real welding was executed with low heat input, the restraining effect was small and Y-joint model gave acceptable results. Residual stresses calculated by K-joint model with lumped pass welds highly overestimated the measured values.
- **Time-based element activation:** Time-based element activation was used. It is less accurate than temperature-based activation but gives better numerical stability during analysis;
- **Heat source simplifications:** constant weld torch speed was assumed. Trajectory definition and weld torch orientation were determined in relation to lumped pass weld geometry;

## 8.2 Fatigue life assessment of welded high-strength tubular K-joints

### Experimental assessment of fatigue life of welded K-joints and CHS–cast nodes

Fatigue cracking occurred at either hot-spot 1 or 1c, as was observed in previous fatigue tests on S355J2H steel. Fatigue cracking at full compressive brace side (hs1c) occurred due to presence of tensile residual stresses in the cracking region. No root cracking was observed. No visible cracking in CHS–Cast nodes was registered.

Fatigue strength of the S690 trusses was similar to the S355 trusses tested previously at ICOM. Their strength can be estimated as satisfying CIDECT fatigue category 114. Alternatively, the recommended hot spot design S-N curve for the K-joints is FAT 100, to be used with SCF values given by Schumacher (2003).

### Calculation of crack growth in residual stress field

Partial crack closure, or crack faces contact problem which was discussed in Chapter 7, is not still implemented in the Morfeo/Crack XFEM software. For the case of fatigue cracks the implementation can be done by a penalty procedure, which is simple and accurate enough for most of the cases (Mohammadi, 2008).

## 8.3 Future work

### Low transformation temperature welding

Low transformation temperature welding (LTTW) wires have been introduced in recent years as a promising solution for fatigue life improvement of high strength steel welds (Ohta et al., 2003; Ooi et al., 2014). The wires are steel alloys with high content of Nickel and Chrome and feature reduced martensitic start temperature and large transformation strains. The resulting welding residual stresses are compressive which leads to improved fatigue performance of the detail. The concept of *residual stress engineering* (Farajian et al., 2013) is an interesting topic for research on fatigue life improvement, specifically for modern high strength steels.

### Application of High Frequency Impact Treatment (HFMI) to weldments

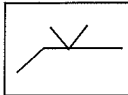
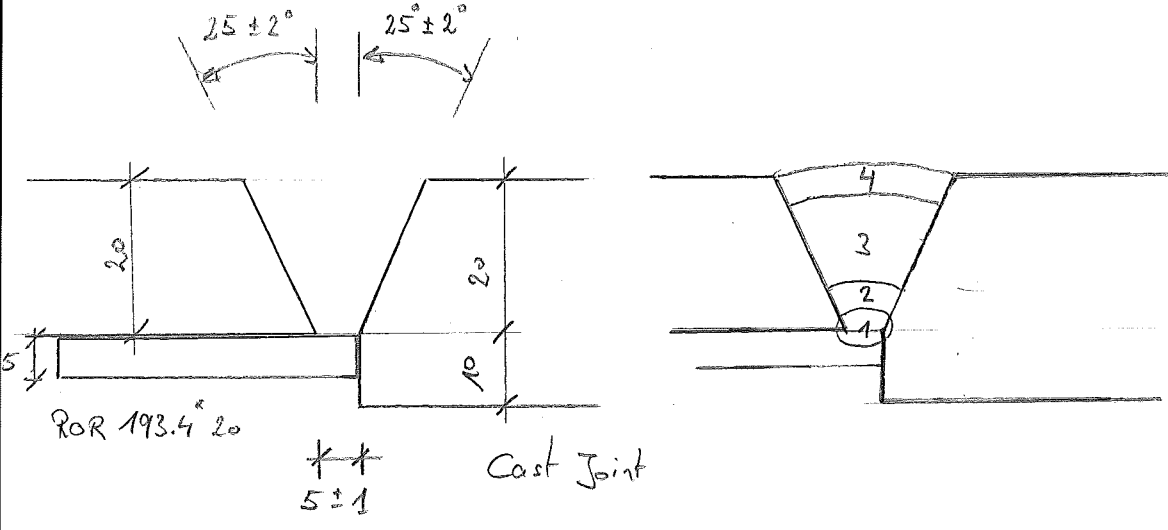
As-welded residual stresses were considered in this study. The resulting residual stress profiles can then be used as the baseline state for the cases where High Frequency Impact Treatment methods (or other post-weld treat methods) are investigated. One can imagine simulating by FEM both welding and the HFMI and account for multiple potential crack locations.

Simulation of partial crack closure discussed in previous section, is essential for these cases where large compressive stresses exist in the cracked region.

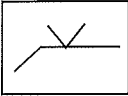
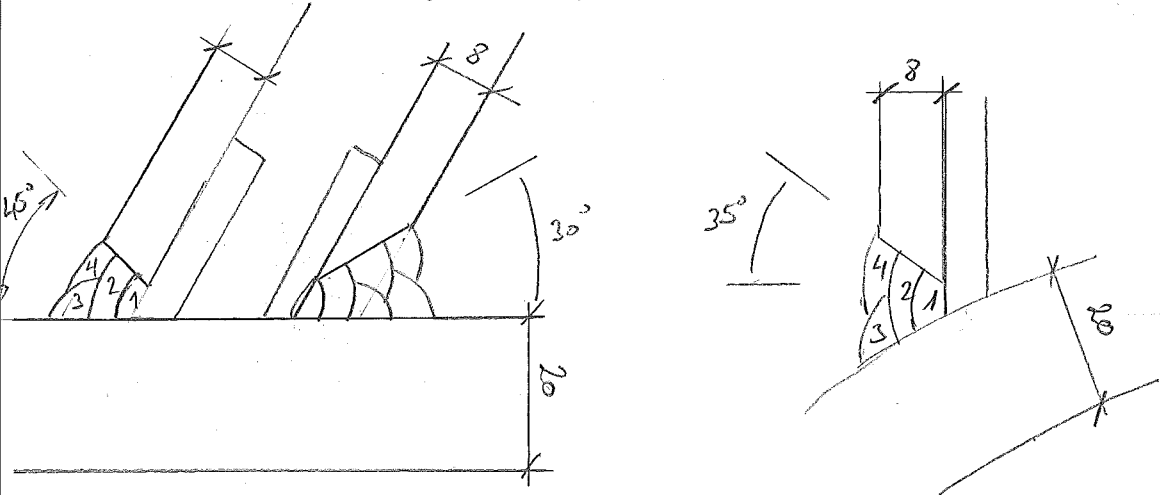
### **Welding simulation of unmatched welds**

Numerical evaluation of residual stresses in CHS–cast joints involves the added difficulty of welding unmatched steel grades. In this case, more effort is needed for material characterization. Registered temperatures of CHS–cast node reported in Chapter 5 can be used for validation of thermal model. The results of welding simulation will be useful in determining residual stress state at the weld root in the inside face of the tube wall, which according to previous fatigue tests (Haldimann-Sturm, 2005) is the crack start location for cast node connections.

# **A Fabricator's welding procedure specifications for trusses**

Référence	Spécification 816.1		Symbole du joint 	
Description :	Soudure à pénétration totale en V avec support			
Matériau de base :	S690 QH	épaisseurs :	20mm / 30mm	
Procédé :	MAG 136	QMOS N° :		
<b>Préparation et séquences de soudage</b>				
				
<b>Procédé de soudage</b>	Racine MAG 136		Remplissage MAG 136	
Passe n°	premières		remplissage	
Matière d'apport	OK Tubrod 15.09		OK Tubrod 15.09	
Type gaz / poudre	1.2 mm		1.2 mm	
Débit gaz	Argon / Co2 ( M 21 )		Argon / Co2 ( M 21 )	
Position de soudage	16 / 20 litres / minutes		16 / 20 litres / minutes	
Polarité	PF		PF	
Mode de transfert	DC +		DC +	
<b>Zone</b>	pulvérisation axiale		pulvérisation axiale	
<b>n°</b>	<b>1</b>	<b>2</b>	<b>3</b>	<b>4</b>
Ampères	(±10%) 180	175	A	185
Volts	(±10%) 24	26	V	26
Vitesse fil	(±10%) 7.5	7	m/min	7.5
Vitesse d'avance	(±10%) 20	20	cm/min	20
Apport de chaleur	(±25%) 12.96	13.65	kJ/cm	14.43
Pré - chauffage	120°C		--	
Temp. entre passes	< 250°C		< 250°C	
Remarques :				
Établi par :	NMO	Contrôlé par :	Contrôlé par :	
Date :	01.06.2011	Date :	Date :	
Version N°	0			



Référence	Spécification 816.2		Symbole du joint 				
Description :	Soudure à pénétration totale en V avec support						
Matériau de base :	S690 QH	épaisseurs :	8mm / 20mm				
Procédé :	MAG 136	QMOS N° :					
<b>Préparation et séquences de soudage</b>							
							
<b>Procédé de soudage</b>	Racine MAG 136		Remplissage MAG 136				
<b>Passé n°</b>	premières		remplissage				
<b>Matière d'apport</b>	OK Tubrod 15.09		OK Tubrod 15.09				
	1.2 mm		1.2 mm				
<b>Type gaz / poudre</b>	Argon / Co2 ( M 21 )		Argon / Co2 ( M 21 )				
<b>Débit gaz</b>	16 / 20 litres /minutes		16 / 20 litres /minutes				
<b>Position de soudage</b>	PA / PC		PA / PC				
<b>Polarité</b>	DC +		DC +				
<b>Mode de transfert</b>	pulvérisation axiale		pulvérisation axiale				
<b>Zone</b>	<b>n°</b>	<b>1</b>	<b>2</b>	<b>3</b>	<b>4</b>		
<b>Ampères</b>	(±10%)	215	230	A	230	220	A
<b>Volts</b>	(±10%)	28	28	V	28	28	V
<b>Vitesse fil</b>	(±10%)	9	9	m/min	9	9	m/min
<b>Vitesse d'avance</b>	(±10%)	19	22	cm/min	22	25	cm/min
<b>Apport de chaleur</b>	(±25%)	19.01	17.56	kJ/cm	17.56	14.78	kJ/cm
<b>Pré - chauffage</b>		100°C		--			
<b>Temp. entre passes</b>		< 250°C		< 250°C			
<b>Remarques :</b>							
<b>Établi par :</b>	NMO		<b>Contrôlé par :</b>	Contrôlé par :			
<b>Date :</b>	01.06.2011		<b>Date :</b>	Date :			
<b>Version N°</b>	0						



## **B Dimensions and instrumentation of test trusses**

**Appendix B. Dimensions and instrumentation of test trusses**

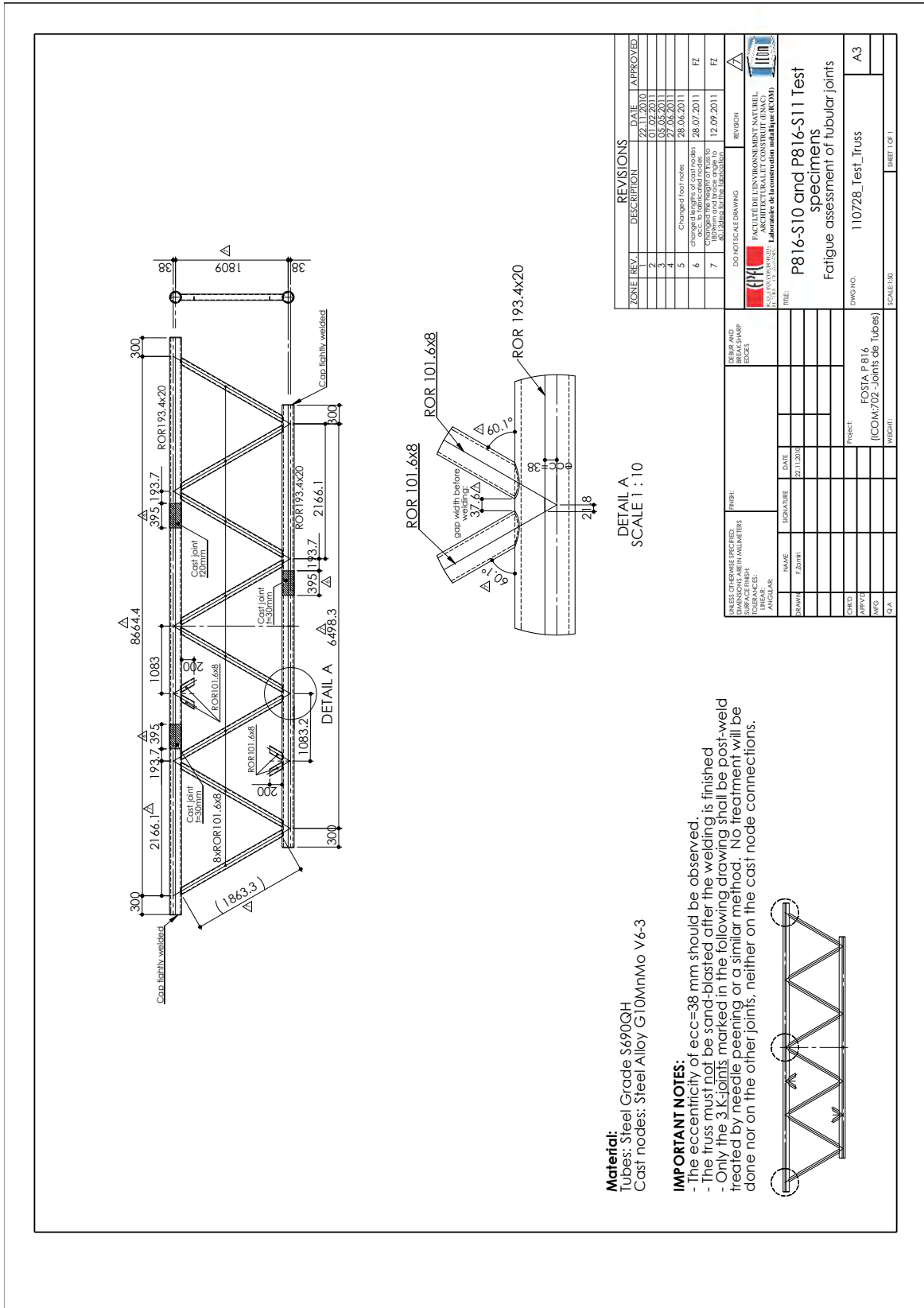


Figure B.1: As-built dimensions of test truss S10.

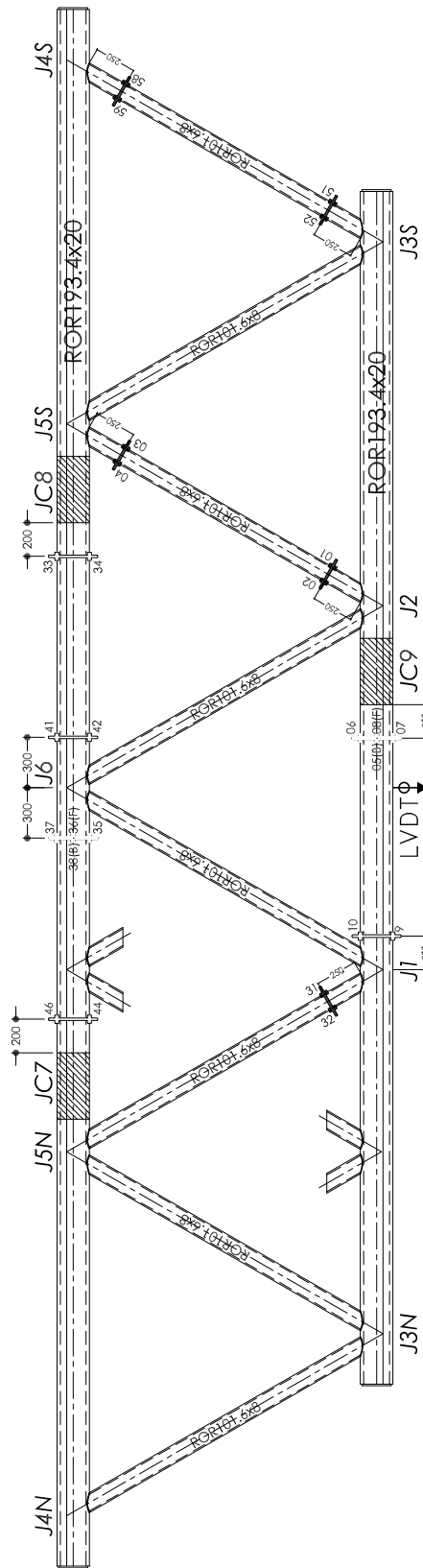


Figure B.2: Locations of strain gages and LVDT transducer for truss S10-690.



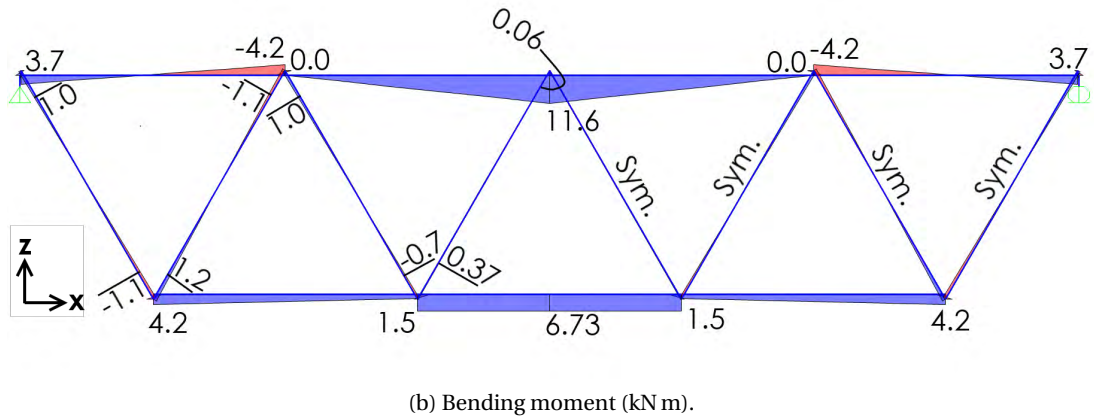
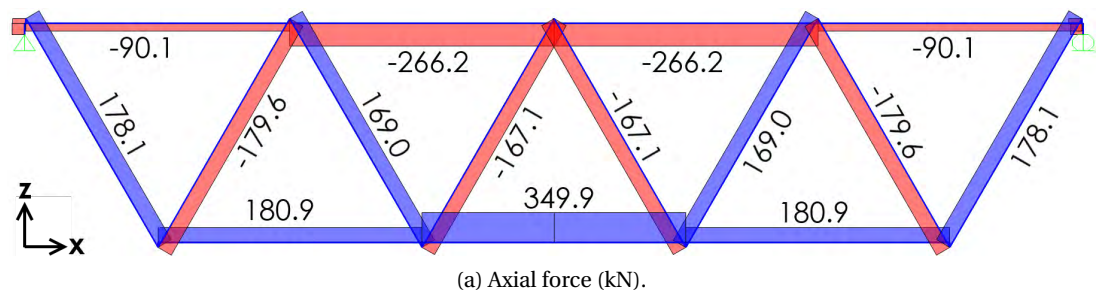


Figure B.4: Calculated normal force and bending moment range diagrams for truss S10-690 ( $\Delta Q = 300$  kN).

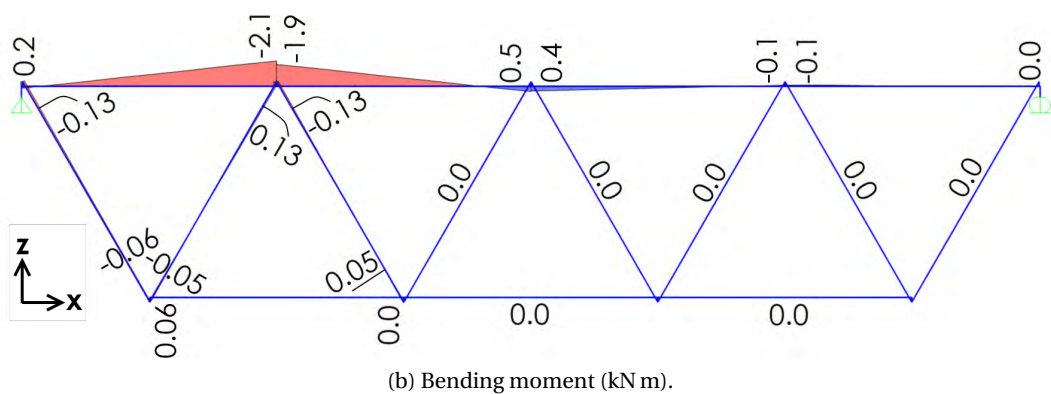
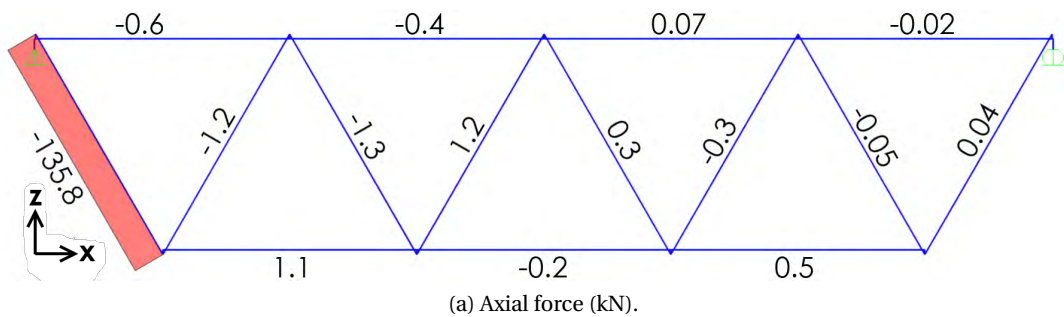


Figure B.5: Calculated normal force and bending moment diagrams due to post-tensioning truss S11-690 ( $T_{PS} = 137$  kN).





## **C** Summary of S-N data

## Appendix C. Summary of S-N data

Table C.1: Summary of fatigue test data for the full-scale truss tests carried out at ICOM; The last column is hot-spot stress with CIDECT thickness correction factor included.

Truss/Joint	$N_f$	$S_{r,hs}$	$T$	$S_{r,hs,corrected}$
S1-1	2324400	114	20	124
S1-2	3427000	114	20	124
S1-3	2086000	114	20	124
S1-4	1639000	114	20	124
S2-1	1862500	140	20	152
S2-2	2547900	140	20	153
S2-3	1211072	140	20	151
S2-4	972672	139	20	150
S3-1	938700	187	12.5	171
S3-2	1564500	187	12.5	171
S3-3	1192000	196	12.5	179
S3-4	1490000	196	12.5	179
S5-1	302470	211	20	227
S5-2	406770	211	20	227
S6-J3S+	360000	163	30	201
S6-J3N+	393000	163	30	201
S6-J1+	440000	173	30	214
S6-J2+	425000	173	30	214
S7-J3S+	165000	263	20	282
S7-J3N+	206000	263	20	283
S7-J1+	247000	281	20	302
S7-J2+	235000	281	20	302
S10-J3S+	1292000	107	20	116
S10-J3N+	1949000	107	20	116
S10-J1+	1949000	113	20	123
S10-J2+	1840000	113	20	123
S11-J3S+	516000	160	20	173
S11-J3N+	421000	160	20	173
S11-J1+	516000	169	20	182
S11-J2+	516000	169	20	182

Table C.2: Summary of nominal stresses acting on CHS–Cast joints; No visible cracking was found in these joints.

Truss	Joint	Load	$\sigma_{ax}$	$\sigma_{ipb}$	$\sigma_{nom}$
S10	JC9 (Bottom)	300	32.1	$\pm 31.4$	63.5
S10	JC7 (Top)	300	-24.4	$\pm 4.7$	-29.1
S10	JC8 (Top)	300	-24.4	$\pm 4.7$	-29.1
S11	JC9 (Bottom)	450	48.2	$\pm 47.1$	95.2
S11	JC7 (Top)	450	-36.6	$\pm 7.1$	-43.7
S11	JC8 (Top)	450	-36.6	$\pm 7.1$	-43.7

## **D Transformation kinetics calculations and input metallurgy data files**

In this appendix, MATLAB scripts to generate CCT curves from Leblond model parameters are listed. Furthermore, the results of parameter identification for Leblond model based on digitized CCT curves given by Seyffarth et al. (1992) are presented in Tables D.1 and D.2. Finally, material data files (.mdf) used as input to Morfeo/Welding analyses are given.

```

function EvaluatedCCT = LeblondModelSimplifiedv3(Transformations, Tstart, ✓
Tend, TdotVector)
% Evaluates the CCT curve based on the Leblond model. Cooling rates are
% considered constant and are passed to the function by the vector
% TdotVector (Tdot values should be entered negative, i.e. cooling). DeltaT
% is a positive value.
% Number of phases in considered to be 4: 1:F+P, 2:B, 3:M, 4:A
% Farshid Zamiri A. / EPFL-ICOM / 12.09.2013
% - Version 3: Changed the solver to MATLAB's ode45 solver. The leblond
%   function now does not do the solution and only prepares the input for
%   ode45 and reformats the output to the required structure.
%
% - Version 2: Replaced constant time stepping with adaptive time stepping

% Transform.#  Desc    i  j
% -----  -
%      1      A>F+P  4  1
%      2      A>B    4  2
%      3      A>M    4  3
%      4      F+P>A  1  4
%      4      B>A    2  4
%      4      M>A    3  4
% Peq(i) an tau(i) in the transformations(i) structure are
% corresponding to phase i

% Threshold value of phase fraction to consider as the start of ✓
transformation
StartThreshold = 0.01;

NCurves = max(size(TdotVector));
NPhases = 4;
PhaseNames = {'Ferrite+Pearlite' 'Bainite' 'Martensite' 'Austenite' };
PhaseShortNames = {'F+P' 'B' 'M' 'A'};
PhaseColor = ['grbk']; % Determines in which color each phase should be ✓
plotted.

% Initial conditions
P0 = [0 0 0 1];
% Options for the ODE solver
options = odeset('RelTol',1e-5,'AbsTol',1e-5 , 'OutputFcn',@odeplot);

for curve = 1:NCurves
    Tdot = TdotVector(curve);
    StartTime = 0;
    EndTime = (Tend - Tstart)/Tdot;
    nPoints = 100;
    timeSpan = linspace(StartTime,EndTime,nPoints);

    windowTitle = sprintf('Cooling curve number %i - dT/dt=%6.3f',curve, ✓
Tdot);

```

```

figure('name',windowTitle);

% Solve the system of equations
[time,PhaseFraction] = ode45(@(t,p) pdot(t,p, Tdot, Tstart,✓
Transformations, NPhases) ...
, timeSpan, P0, options);
Temp = Tdot*(time-StartTime) + Tstart;

EvaluatedCCT.Curves(curve).time = time;
EvaluatedCCT.Curves(curve).Temperature = Temp;

% Write the start and end temperatures for each transformation
for phase = 1:NPhases-1 % The last phase is Austenite
    ind = find((PhaseFraction(:,phase)>=StartThreshold),1,'first');
    k = curve;
    if ind>1
        EvaluatedCCT.Phases(phase).StartTime(k) = time(ind);
        EvaluatedCCT.Phases(phase).StartTemp(k) = Temp(ind);
        EvaluatedCCT.Phases(phase).StartTimeNew(k) = time(ind);
        EvaluatedCCT.Phases(phase).StartTempNew(k) = Temp(ind);
        maxfraction = 0.99*max(PhaseFraction(:,phase));
        ind2 = find((PhaseFraction(:,phase) >= maxfraction),1,'first');
        EvaluatedCCT.Phases(phase).EndTime(k) = time(ind2);
        EvaluatedCCT.Phases(phase).EndTemp(k) = Temp(ind2);
        EvaluatedCCT.Phases(phase).EndTimeNew(k) = time(ind2);
        EvaluatedCCT.Phases(phase).EndTempNew(k) = Temp(ind2);
        EvaluatedCCT.Phases(phase).Endfraction(k) = PhaseFraction(ind2,✓
phase);
    else
        EvaluatedCCT.Phases(phase).StartTime(k) = 0;
        EvaluatedCCT.Phases(phase).StartTemp(k) = 0;
        EvaluatedCCT.Phases(phase).StartTimeNew(k) = 0;
        EvaluatedCCT.Phases(phase).StartTempNew(k) = 0;
        EvaluatedCCT.Phases(phase).EndTime(k) = 0;
        EvaluatedCCT.Phases(phase).EndTemp(k) = 0;
        EvaluatedCCT.Phases(phase).EndTimeNew(k) = 0;
        EvaluatedCCT.Phases(phase).EndTempNew(k) = 0;
        EvaluatedCCT.Phases(phase).Endfraction(k) = 0;
    end
end
end

% Assign names and colors data to phases (for plotting)
for i = 1:NPhases
    EvaluatedCCT.Phases(i).Name = cell2mat(PhaseNames(i));
    EvaluatedCCT.Phases(i).ShortName = cell2mat(PhaseShortNames(i));
    EvaluatedCCT.Phases(i).Color = PhaseColor(i);
end

EvaluatedCCT.NumCurves = NCurves;

```

```
EvaluatedCCT.NumPhases = NPhases;
```

```
end
```

```

function dpdt = pdot(t,p, Tdot, StartTemp, Transformations, NPhases)
% This function calculates the right-hand-side of the phase evolution
% equations given by Leblond & Devaux (1984)
%
% Farshid Zamiri A. - EPFL/ENAC/ICOM - 12.09.2013
%
% If you get NaN results from this function, most probably the range of
% values you have given for Peq, tau, or F(thetadot) does not include the
% values calculated in here. Re-check your values for above parameters.

Temp = Tdot*t + StartTemp;
dpdt = zeros(NPhases,1); % Output should be a column vector

for i = 1:NPhases-1
    SumAij = 0;
    for j = 1:NPhases
        if j ~= i
            Aij = 0;
            pjeq = interp1(Transformations(j).Peq(1,:),Transformations(j).Peq(
(2,:),Temp);
            tauij = interp1(Transformations(j).tau(1,:),Transformations(j).
tau(2,:),Temp);
            fij = interp1(Transformations(j).F(1,:),Transformations(j).F(
(2,:),Tdot);
            kij = pjeq/tauij;
            lij = (1 - pjeq)/tauij;
            A1 = kij*p(i) - lij*p(j);
            if A1 > 0
                Aij = A1*fij;
            end
            pieq = interp1(Transformations(i).Peq(1,:),Transformations(i).Peq(
(2,:),Temp);
            tauji = interp1(Transformations(i).tau(1,:),Transformations(i).
tau(2,:),Temp);
            fji = interp1(Transformations(i).F(1,:),Transformations(i).F(
(2,:),Tdot);
            kji = pieq/tauji;
            lji = (1 - pieq)/tauji;
            A2 = kji*p(j) - lji*p(i);
            if A2 > 0
                Aij = -A2*fji;
            end
            SumAij = SumAij + Aij;
        end
    end
    dpdt(i) = -SumAij;
end

dpdt(end) = -sum(dpdt(1:end-1));

```

```
for i = 1:NPhases
    if (p(i) > 1) || (p(i) < 0)
        dpdt = [0 0 0 0]';
    end
end

% Un-comment the following row for debugging
%fprintf ('%5.3f + %5.3f + %5.3f + %5.3f = %5.3f \n', dpdt, sum(dpdt))

end
```



Table D.1: Parameters  $p_{j,eq}^{ij}(T)$  and  $\tau^{ij}(T)$  of Leblond and Devaux (1984) model for transformations derived from CCT curve of Figure 6.19 and corresponding to the CCT curve of Figure 6.20

Austenite→Ferrite+Pearlite			Austenite→Bainite			Austenite→Martensite		
T [ $^{\circ}$ C]	$P_{eq}$	$\tau_{eq}$ [s]	T [ $^{\circ}$ C]	$P_{eq}$	$\tau_{eq}$ [s]	T [ $^{\circ}$ C]	$P_{eq}$	$\tau_{eq}$ [s]
0	1	100000	0	1	0.5	0	1	0.05
580	1	2000	340	1	0.5	416	1	0.1
730	0.5	500	350	1	0.5	420	0	0.05
800	0	500	410	1	0.5	1500	0	0.05
1000	0	500	450	0.6	2			
1500	0	500	660	0.1	50			
			670	0	100			
			1000	0	100			
			1500	0	100			

Table D.2: Parameter  $f_{ij}(\dot{T})$  of Leblond and Devaux (1984) model for transformations derived from CCT curve of Figure 6.19 and corresponding to the CCT curve of Figure 6.20

$\dot{T}$ [ $^{\circ}$ /s]	Austenite → Ferrite+Pearlite	Austenite → Bainite	Austenite → Martensite
	$F(\dot{T})$	$F(\dot{T})$	$F(\dot{T})$
-1.0E+5	0	0	1
-159	0	0	1
-93	0	1	1
-64.4	0	1	1
-44.6	0	1	1
-26.7	0	1	1
-12.4	0	1	0
-8	1	1	0
-5.3	1	1	0
-3.7	1	1	0
-2.62	1	1	0
-1.51	1	1	0
0	1	1	0

```

1  Material 1 metallurgy
2
3  PHASES
4  1 ferrite          PR0=0.0
5                    LX=(2,1.51E-5,-3.03-4)
6                    NU=Table(21)
7                    YIELD=Table(31)
8                    Hv=168
9                    Ep=Table(41)
10                   Np=Table(51)
11  2 bainite        PR0=0.86
12                   LX=(2,1.51E-5,-3.03-4)
13                   NU=Table(21)
14                   YIELD=Table(32)
15                   Hv=313
16                   Ep=Table(41)
17                   Np=Table(51)
18                   K=7.65e-8
19  3 martensite     PR0=0.14
20                   LX=(2,1.35E-5,+2.20e-3)
21                   NU=Table(21)
22                   YIELD=Table(33)
23                   Hv=428
24                   Ep=Table(41)
25                   Np=Table(51)
26                   K=7.65e-8
27  4 austenite      PR0=0.0
28                   LX=(2,2.31E-5,-1.06E-2)
29                   YIELD=Table(34)
30                   Ep=Table(41)
31                   Np=Table(51)
32
33  TRANSFORMATIONS
34  1 4 F2A Ti=750 Tf=905 Ym=(3,750.0,0.0,905.0,1.0)
35  2 4 B2A Ti=750 Tf=905 Ym=(3,750.0,0.0,905.0,1.0)
36  3 4 M2A Ti=750 Tf=905 Ym=(3,750.0,0.0,905.0,1.0)
37  4 1 A2F Ti=TABLE(463) Tf=TABLE(473) Ym=TABLE(483)
38  4 2 A2B Ti=TABLE(464) Tf=TABLE(474) Ym=TABLE(484)
39  4 3 A2M Ti=TABLE(465) Tf=TABLE(475) Ym=TABLE(485)
40
41  TABLES
42  1/ 20 0.000000 100 0.000959 200 0.002306 300 0.003778 400
0.005218 500 0.006935 600 0.008600 1200 0.016800 1400 0.019650
43
44  3/ 20 -0.008000 360 0.000000 400 0.000720 500 0.002720 600
0.004720 1250 0.019500 1440 0.022780 1500 0.025330
45
46  21/ 20 0.28 200 0.285 400 0.295 600 0.31 1000 0.33 1400 0.335
47
48  31/ 20 360000 200 312000 300 289600 400 26500 500 231400 600
175800 700 110200 800 59000 900 33000 1000 22000 1100 10000 1200
10000 1300 10000 1420 10000 5000 10000

```

49  
50 32/ 20 630000 200 558000 300 532000 400 496000 500 432000 600  
326000 700 195000 800 90000 900 45000 1000 53000 1100 30000 1200  
25000 1300 10000 1420 10000 5000 10000  
51  
52 33/ 20 1100000 200 980000 300 910000 400 830000 500 700000 600  
480000 700 260000 800 120000 900 75000 1000 53000 1100 30000  
1200 25000 1300 10000 1420 10000 5000 10000  
53  
54 34/ 20 232000 200 205000 300 182000 400 4158000 500 130000 600  
106000 700 85000 800 65000 900 45000 1000 28000 1100 15000 1200  
12000 1300 10000 1420 10000 5000 10000  
55  
56 41/ 20 352848.69500 100 352795.03503 200 347594.29370 300  
340434.88282 400 314964.32663 500 274307.27627 600 199222.01925  
700 99347.53143 800 67903.48881 900 47104.41734 1000 29867.00813  
1100 18114.14913 1200 10860.70971 1300 9054.42858 1400 9054.42858  
57  
58 51/ 20 0.21529 100 0.21482 200 0.21549 300 0.21559 400 0.21524  
500 0.21548 600 0.21557 700 0.21456 800 0.21558 900 0.21878 1000  
0.21569 1100 0.21540 1200 0.21553 1300 0.21677 1400 0.21677  
59  
60 463/ -143.04 0.0 -68.006 0.0 -45.655 0.0 -32.854 0.0 -22.035  
0.0 -16.783 0.0 -12.481 0.0 -5.425 656.98 -4.644 684.79 -2.1782  
698.61 -1.4559 710.08 -1.194 727.3  
61  
62 464/ -143.04 0.0 -68.006 0.0 -45.655 449.22 -32.854 465  
-22.035 484.38 -16.783 517.76 -12.481 569.68 -5.425 607.64  
-4.644 622.48 -2.1782 636.21 -1.4559 647.58 -1.194 660.05  
63  
64 465/ -143.04 418 -68.006 418 -45.655 418 -32.854 418 -22.035  
418 -16.783 418 -12.481 0.0 -5.425 0.0 -4.644 0.0 -2.1782 0.0  
-1.4559 0.0 -1.194 0.0  
65  
66 473/ -143.04 0.0 -68.006 0.0 -45.655 0.0 -32.854 0.0 -22.035  
0.0 -16.783 0.0 -12.481 0.0 -5.425 607.64 -4.644 622.48 -2.1782  
636.21 -1.4559 647.58 -1.194 660.05  
67  
68 474/ -143.04 0.0 -68.006 0.0 -45.655 418 -32.854 418 -22.035  
418 -16.783 418 -12.481 448.74 -5.425 477.38 -4.644 489.74  
-2.1782 499.87 -1.4559 518.14 -1.194 537.49  
69  
70 475/ -143.04 0.0 -68.006 0.0 -45.655 0.0 -32.854 0.0 -22.035  
0.0 -16.783 0.0 -12.481 0.0 -5.425 0.0 -4.644 0.0 -2.1782 0.0  
-1.4559 0.0 -1.194 0.0  
71  
72 483/ -143.04 0.0 -68.006 0.0 -45.655 0.0 -32.854 0.0 -22.035  
0.0 -16.783 0.0 -12.481 0.0 -5.425 0.03 -4.644 0.04 -2.1782 0.05  
-1.4559 0.05 -1.194 0.06  
73  
74 484/ -143.04 0.0 -68.006 0.0 -45.655 0.42 -32.854 0.54  
-22.035 0.81 -16.783 0.97 -12.481 1.0 -5.425 0.97 -4.644 0.96 185

-2.1782 0.95 -1.4559 0.95 -1.194 0.97  
75  
76 485/ -143.04 1.0 -68.006 1.0 -45.655 0.58 -32.854 0.46  
-22.035 0.19 -16.783 0.03 -12.481 0.0 -5.425 0.0 -4.644 0.0  
-2.1782 0.0 -1.4559 0.0 -1.194 0.0  
77  
78

```
1 Material 1 metallurgy
2
3 PHASES
4 1 ferrite      PR0=0.0
5                LX=(2,1.51E-5,-3.03-4)
6                NU=Table(21)
7                YIELD=Table(31)
8                Hv=168
9                Ep=Table(41)
10               Np=Table(51)
11 2 bainite     PR0=0.86
12               LX=(2,1.51E-5,-3.03-4)
13               NU=Table(21)
14               YIELD=Table(32)
15               Hv=313
16               Ep=Table(41)
17               Np=Table(51)
18               K=7.65e-8
19 3 martensite  PR0=0.14
20               LX=(2,1.35E-5,+2.20e-3)
21               NU=Table(21)
22               YIELD=Table(33)
23               Hv=428
24               Ep=Table(41)
25               Np=Table(51)
26               K=7.65e-8
27 4 austenite   PR0=0.0
28               LX=(2,2.31E-5,-1.06E-2)
29               YIELD=Table(34)
30               Ep=Table(41)
31               Np=Table(51)
32
33 TRANSFORMATIONS
34 1 4 FerAus Ti=750 Tf=905 Ym=(3,750.0,0.0,905.0,1.0)
35 2 4 BaiAus Ti=750 Tf=905 Ym=(3,750.0,0.0,905.0,1.0)
36 3 4 MarAus Ti=750 Tf=905 Ym=(3,750.0,0.0,905.0,1.0)
37 4 1 AusFer Ym=TABLE(61) Tau=TABLE(71) F=TABLE(301)
38 4 2 AusBai Ym=TABLE(62) Tau=TABLE(72) F=TABLE(302)
39 4 3 AusMar Ym=TABLE(303) Ms=416 Alpha=0.11 kYm=1.0
40
41
42 TABLES
43 1/ 20 0.000000 100 0.000959 200 0.002306 300 0.003778 400
44 0.005218 500 0.006935 600 0.008600 1200 0.016800 1400 0.019650
45
46 3/ 20 -0.008000 360 0.000000 400 0.000720 500 0.002720 600
47 0.004720 1250 0.019500 1440 0.022780 1500 0.025330
48
49 21/ 20 0.28 200 0.285 400 0.295 600 0.31 1000 0.33 1400 0.335
50
51 31/ 20 360000 200 312000 300 289600 400 26500 500 231400 600
52 175800 700 110200 800 59000 900 33000 1000 22000 1100 10000 1200 87
```

10000 1300 10000 1420 10000 5000 10000  
50  
51 32/ 20 630000 200 558000 300 532000 400 496000 500 432000 600  
326000 700 195000 800 90000 900 45000 1000 53000 1100 30000 1200  
25000 1300 10000 1420 10000 5000 10000  
52  
53 33/ 20 1100000 200 980000 300 910000 400 830000 500 700000 600  
480000 700 260000 800 120000 900 75000 1000 53000 1100 30000  
1200 25000 1300 10000 1420 10000 5000 10000  
54  
55 34/ 20 232000 200 205000 300 182000 400 4158000 500 130000 600  
106000 700 85000 800 65000 900 45000 1000 28000 1100 15000 1200  
12000 1300 10000 1420 10000 5000 10000  
56  
57 41/ 20 352848.69500 100 352795.03503 200 347594.29370 300  
340434.88282 400 314964.32663 500 274307.27627 600 199222.01925  
700 99347.53143 800 67903.48881 900 47104.41734 1000 29867.00813  
1100 18114.14913 1200 10860.70971 1300 9054.42858 1400 9054.42858  
58  
59 51/ 20 0.21529 100 0.21482 200 0.21549 300 0.21559 400 0.21524  
500 0.21548 600 0.21557 700 0.21456 800 0.21558 900 0.21878 1000  
0.21569 1100 0.21540 1200 0.21553 1300 0.21677 1400 0.21677  
60  
61 61/ 0 1 580 1 730 0.5 800 0 1000 0 1500 0  
62  
63 62/ 0 1 340 1 350 1 410 1 450 0.6 660 0.1 670 0 1000 0  
1500 0  
64  
65 71/ 0 100000 580 2000 730 500 800 500 1000 500 1500 500  
66  
67 72/ 0 0.5 340 0.5 350 0.5 410 0.5 450 2 660 50 670 100  
1000 100 1500 100  
68  
69 301/ -1.00E+05 0 -159 0 -93 0 -64.4 0 -44.6 0 -26.7 0 -12.4 0 -8  
1 -5.3 1 -3.7 1 -2.62 1 -1.51 1 -0.0001 1  
70  
71 302/ -1.00E+05 0 -159 0 -93 1 -64.4 1 -44.6 1 -26.7 1 -12.4 1 -8  
1 -5.3 1 -3.7 1 -2.62 1 -1.51 1 -0.0001 1  
72  
73 303/ -1.00E+05 1 -159 1 -93 0.58 -64.4 0.46 -44.6 0.39  
-26.7 0.13 -12.4 0 -8 0 -5.3 0 -3.7 0 -2.62 0 -1.51 0  
-0.0001 0  
74  
75  
76  
77  
78  
79

**E Results of principal residual stress measurements using neutron diffraction (S355J2H sample)**

Table E.1: Residual strain measurement directions (scattering vectors) and resulted principal residual stresses and principal residual stress axes for point M0 (Note: coordinate system is shown in the following figure. The coordinate system is different with the CSYS used in Chapter 4).

Scattering vectors			Principal dir. 1			Principal dir. 2			Principal dir. 3			Error	
vx	vy	vz	vx	vy	vz	vx	vy	vz	vx	vy	vz	$\sigma_{res}$ [Mpa]	Error [Mpa]
1.000	0.000	0.000	0.90	0.44	0.00	0.00	0.00	-1.00	-0.44	0.90	0.00	522.7	18.7
0.000	0.000	1.000	-1.00	0.09	-0.01	-0.02	0.00	1.00	-0.09	-1.00	-0.01	379.5	20.1
0.000	1.000	0.000	-0.96	-0.27	0.01	0.01	0.02	1.00	0.28	-0.96	0.02	420.9	22.2
0.957	0.208	0.203	-0.95	0.32	-0.06	0.33	0.94	0.01	-0.04	0.01	1.00	222.6	23.1
0.246	0.948	-0.203	0.12	0.99	-0.08	0.02	0.03	1.00	-0.99	0.12	0.02	116.7	21.3
1.000	0.000	0.000	0.34	0.94	0.00	-0.10	0.01	-1.00	-0.93	0.34	0.09	138.1	21.1
0.000	0.000	-1.000											
0.000	1.000	0.000											
0.957	0.208	-0.203											
0.246	0.948	0.203											

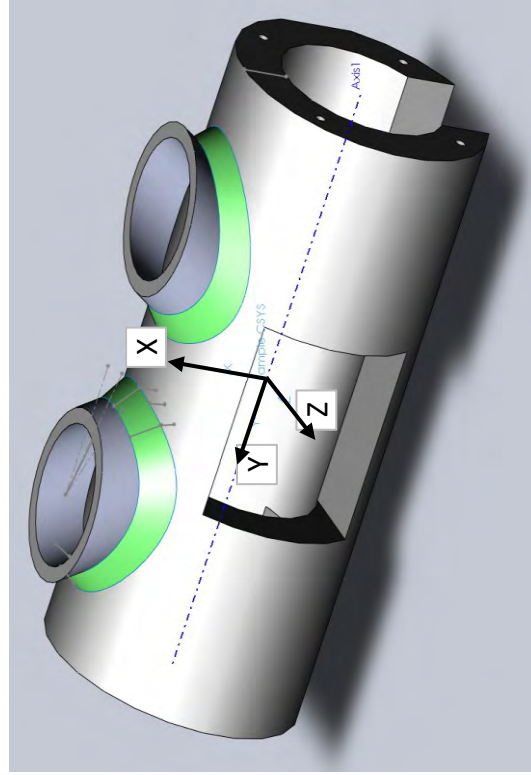




Table E.2: Residual strain measurement directions (scattering vectors) and resulted principal residual stresses and principal residual stress axes for point M1 (Note: coordinate system is shown in the following figure. The coordinate system is different with the CSYS used in Chapter 4).

Scattering vectors			Principal dir. 1			Principal dir. 2			Principal dir. 3			$\sigma_{res}$	
vx	vy	vz	vx	vy	vz	vx	vy	vz	vx	vy	vz	$\sigma_{res}$ [Mpa]	Error [Mpa]
1.000	0.000	0.000	0.78	-0.01	0.62	0.37	-0.80	-0.48	344.4	39.4	-0.50	430.8	44.5
0.000	0.000	1.000	-	-	-	-	-	-	-	-	-	-	-
0.982	0.000	0.187	0.76	-0.05	0.65	0.30	-0.86	-0.41	307.0	36.7	-0.58	403.5	53.8
0.000	1.000	0.000	-0.73	0.11	-0.68	-0.31	-0.93	0.18	149.5	29.9	0.61	338.5	50.8
-0.187	0.000	0.982	-0.71	-0.15	-0.69	0.20	0.90	-0.40	63.9	26.5	-0.68	250.1	39.5
-0.161	-0.203	0.966	0.57	0.27	0.77	0.14	-0.96	0.24	10.4	22.3	-0.81	124.9	34.6
0.957	0.208	0.203											
0.246	0.948	-0.203											

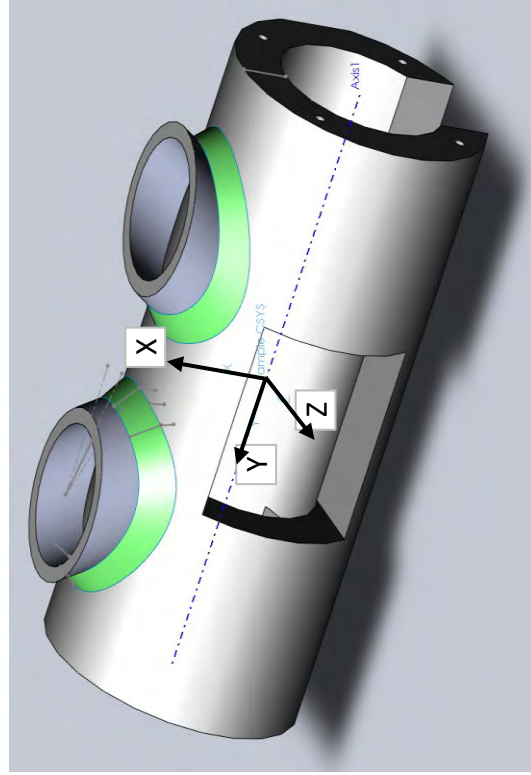
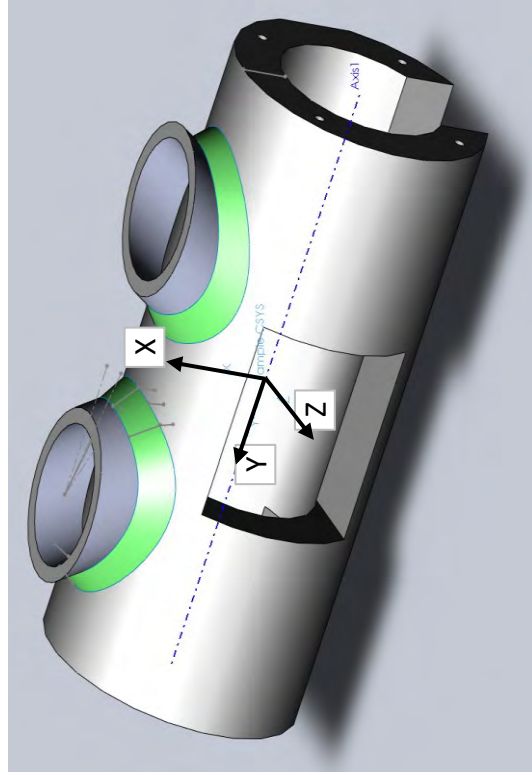


Table E.3: Residual strain measurement directions (scattering vectors) and resulted principal residual stresses and principal residual stress axes for point M2 (Note: coordinate system is shown in the following figure. The coordinate system is different with the CSYS used in Chapter 4).

Scattering vectors			Principal dir. 1			Principal dir. 2			Principal dir. 3			$\sigma_{res}$	Error
vx	vy	vz	vx	vy	vz	vx	vy	vz	vx	vy	vz	[Mpa]	[Mpa]
0.932	0.000	0.362	0.64	-0.17	-0.75	0.77	0.22	0.61	0.06	-0.96	0.27	409.2	113.4
0.000	1.000	0.000	-0.9	0.2	0.4	0.23	-0.52	0.82	0.31	0.84	0.45	435.8	116.1
-0.362	0.000	0.932	-0.92	0.24	-0.32	-0.33	0.01	0.94	-0.23	-0.97	-0.07	366.2	94.3
-0.161	-0.203	0.966	0.54	0.31	0.78	-0.09	0.95	-0.31	-0.84	0.10	0.54	408.8	124.5
0.957	0.208	0.203	0.78	-0.61	0.17	-0.51	-0.45	0.74	0.37	0.66	0.66	317.7	109.1
0.246	0.948	-0.203	0.58	-0.56	0.59	-0.68	-0.73	-0.03	-0.44	0.38	0.81	169.2	133.1



# Bibliography

- ABAQUS (2012). *ABAQUS Analysis: User's Manual, Version 6.12*. Dassault systèmes.
- Acevedo, C. (2011). *Influence of Residual Stresses on Fatigue Response of Welded Tubular Joints (Thesis No. 5056)*. Ph. D. thesis, EPFL, Lausanne.
- Acevedo, C. & Drezet, J.-M. & Nussbaumer, A. (2012). Simulation of welding stresses for fatigue design of welded tubular connections. In *Mathematical Modelling of Weld Phenomena 10*, Seggau, Austria.
- Acevedo, C. & Drezet, J. M. & Nussbaumer, A. (2013). Numerical modelling and experimental investigation on welding residual stresses in large-scale tubular k-joints. *Fatigue & Fracture of Engineering Materials & Structures* 36(2), 177–185.
- Acevedo, C. & Evans, A. & Nussbaumer, A. (2012). Neutron diffraction investigations on residual stresses contributing to the fatigue crack growth in ferritic steel tubular bridges. *International Journal of Pressure Vessels and Piping* 95, 31–38.
- Alberg, H. (2005). *Simulation of welding and heat treatment modelling and validation*. Ph. D. thesis, Luleå University of Technology, Luleå, Sweden.
- Albrecht, P. & Lenwari, A. (2008). Design of prestressing tendons for strengthening steel truss bridges. *Journal of Bridge Engineering* 13(5), 449–454.
- Belytschko, T. & Black, T. (1999). Elastic crack growth in finite elements with minimal remeshing. *International journal for numerical methods in engineering* 45(5), 601–620.
- Belytschko, T. & Neal, M. O. (1991). Contact-impact by the pinball algorithm with penalty and lagrangian methods. *International Journal for Numerical Methods in Engineering* 31(3), 547–572.
- Bergheau, J.-M. & Fortunier, R. (2008). *Finite element simulation of heat transfer*. Great Britain: ISTE Ltd. ; J. Wiley.
- Bhadeshia, H. K. D. H. (2002). Material factors. In G. E. Totten, M. A. Howes, and T. Inoue (Eds.), *Handbook of residual stress and deformation of steel*, pp. 3–10. ASM international.

## Bibliography

---

- Boettcher, S. & Böhm, M. & Wolff, M. (2013). A comprehensive model of thermo-elasto-plasticity with phase transitions in steel. Technical Report Report 13-01, Zentrum für Technomathematik, Universität Bremen, Bremen, Germany.
- Börjesson, L. & Lindgren, L.-E. (2001). Simulation of multipass welding with simultaneous computation of material properties. *Journal of Engineering Materials and Technology* 123(1), 106.
- Brandt, D. A. & Warner, J. C. (2009). *Metallurgy Fundamentals: Ferrous and Nonferrous* (5th ed.). Goodheart-Willcox Co.
- Brickstad, B. & Josefson, B. L. (1998). A parametric study of residual stresses in multi-pass butt-welded stainless steel pipes. *International Journal of Pressure Vessels and Piping* 75(1), 11–25.
- Brown, S. & Song, H. (1992). Finite element simulation of welding of large structures. *Journal of engineering for industry* 114(4), 441–451.
- BS 7910 (2005). *BS 7910:2005: Guide to methods for assessing the acceptability of flaws in metallic structures*. British Standards Institution.
- Callister, W. D. (2005). *Fundamentals of materials science and engineering: an integrated approach* (2nd ed ed.). Hoboken, NJ: John Wiley & Sons.
- Christensen, N. & Davies & Gjermundsen, K. (1965). Distribution of temperatures in arc welding. *British Welding Journal* 12(2), 54–75.
- Costa Borges, L. A. (2008). *Size effects in the fatigue behaviour of tubular bridge joints* (Thesis No. 4142). Ph. D. thesis, EPFL, Lausanne.
- Dai, H. & Francis, J. A. & Withers, P. J. (2010). Prediction of residual stress distributions for single weld beads deposited on to SA508 steel including phase transformation effects. *Materials Science and Technology* 26(8), 940–949.
- Deng, D. (2009). FEM prediction of welding residual stress and distortion in carbon steel considering phase transformation effects. *Materials & Design* 30(2), 359–366.
- Deng, D. & Murakawa, H. (2006). Numerical simulation of temperature field and residual stress in multi-pass welds in stainless steel pipe and comparison with experimental measurements. *Computational Materials Science* 37(3), 269–277.
- Deng, D. & Murakawa, H. (2013). Influence of transformation induced plasticity on simulated results of welding residual stress in low temperature transformation steel. *Computational Materials Science* 78, 55–62.
- Dong, P. & Hong, J. K. (2002). Recommendations for determining residual stresses in fitness-for-service assessment. *Welding Research Council Bulletin* (476).

- Dover, W. D. & Holdbrook, S. J. (1980). Fatigue crack growth in tubular welded connections. *International Journal of Fatigue* 2(1), 37–43.
- Dover, W. D. & Monahan, C. C. (1994). The measurement of surface breaking cracks by the electrical systems ACPD/ACFM. *Fatigue & Fracture of Engineering Materials & Structures* 17(12), 1485–1492.
- Dutta, R. K. & Amirthalingam, M. & Hermans, M. J. M. & Richardson, I. M. (2013). Kinetics of bainitic transformation and transformation plasticity in a high strength quenched and tempered structural steel. *Materials Science and Engineering: A* 559, 86–95.
- DYWIDAG (2009). DYWIDAG prestressing steel threadbar system. Technical report, DYWIDAG-Systems International (DSI).
- E28 Committee (2009). Standard test method for determining residual stresses by the hole-drilling strain-gage method. Technical report, ASTM International.
- Eagar, T. W. & Tsai, N. S. (1983). Temperature fields produced by traveling distributed heat sources. *Welding Journal* 62(12), 346–355.
- Easterling, K. E. (1992). *Introduction to the physical metallurgy of welding* (2nd ed ed.). Oxford ; Boston: Butterworth Heinemann.
- EN 10025-6 (2004). *Hot rolled products of structural steels. Part 6: Technical delivery conditions for flat products of high yield strength structural steels in the quenched and tempered condition*. European Standard.
- EN 10027-2 (1992). *Designation systems for steels. Steel numbers*. European Standard.
- EN 10210-1 (2006). *Hot finished structural hollow sections of non-alloy and fine grain steels. Part 1: Technical delivery conditions*. European Standard.
- EN 10293 (2005). *Steel castings for general engineering uses*. European Standard.
- EN1993 (2005). *Eurocode 3: Design of steel structures - Part 1-2:General rules - Structural fire design*. Brussels: European Committee for Standardization.
- EN1993 (2007). *Eurocode 3: Design of steel structures - Part 1-12:General - High strength steels*. Brussels: European Committee for Standardization.
- Erdogan, F. & Sih, G. C. (1963). On the crack extension in plates under plane loading and transverse shear. *Journal of Basic Engineering* 85(4), 519.
- ESI Group (2009). *SYSWELD*.
- Farajian, M. (2013, March). Welding residual stress behavior under mechanical loading. *Welding in the World* 57(2), 157–169.

## Bibliography

---

- Farajian, M. & Barsoum, Z. & Kromm, A. (2013, September). Residual stress engineering in fatigue resistant welds. *Materials Science Forum* 768-769, 613–619.
- Fischer, F. D. & Sun, Q.-P. & Tanaka, K. (1996). Transformation-induced plasticity (TRIP). *Applied Mechanics Reviews* 49(6), 317–364.
- Fitzpatrick, M. E. & Lodini, A. (2003). *Analysis of residual stress by diffraction using neutron and synchrotron radiation*. London; New York: Taylor & Francis.
- Francis, J. A. & Withers, P. J. (2011). Modelling the effects of phase transformations on welding stress and distortion. In P. Michaleris (Ed.), *Minimization of Welding Distortion and Buckling: Modelling and Implementation*, pp. 78–98. Woodhead Publishing.
- Fukuda, S. & Tsuruta, Y. (1979). A preliminary study of the influence of welding residual stress upon fatigue crack propagation. *Recent Research on Mechanical Behavior of Solids*, 401419.
- GeonX S.A., . (2014). Personal correspondence.
- Goldak, J. & Chakravarti, A. & Bibby, M. (1984). A new finite element model for welding heat sources. *Metallurgical Transactions B* 15(2), 299–305.
- Goldak, J. A. & Akhlaghi, M. (2005). *Computational welding mechanics*. Springer Verlag.
- Greenwood, G. W. & Johnson, R. H. (1965). The deformation of metals under small stresses during phase transformations. *Proceedings of the Royal Society of London. Series A. Mathematical and Physical Sciences* 283(1394), 403–422.
- Grong, O. (1997). *Metallurgical Modelling of Welding (2nd Edition)*. Materials modelling series. Maney Publishing.
- Haldimann-Sturm, S. & Nussbaumer, A. (2008). Fatigue design of cast steel nodes in tubular bridge structures. *International Journal of Fatigue* 30(3), 528–537.
- Haldimann-Sturm, S. C. (2005). *Ermüdungsverhalten von Stahlgussknoten in Brücken aus Stahlhohlprofilen*. Ph. D. thesis, École Polytechnique Fédérale de Lausanne, Lausanne.
- Heinze, C. & Pittner, A. & Rethmeier, M. & Babu, S. S. (2013, March). Dependency of martensite start temperature on prior austenite grain size and its influence on welding-induced residual stresses. *Computational Materials Science* 69, 251–260.
- Hensel, J. & Nitschke-Pagel, T. & Dilger, K. (2013). On the effects of austenitic phase transformation on welding residual stresses in longitudinal stiffeners. Technical Report XIII-2478-13, International Institute of Welding (IIW).
- Hildebrand, J. (2008). *Numerische Schweißsimulation: Bestimmung von Temperatur, Gefüge und Eigenspannung an Schweißverbindungen aus Stahl- und Glaswerkstoffen*. Number 18 in Schriftenreihe des Instituts für Konstruktiven Ingenieurbau, Bauhaus-Universität Weimar. Weimar: Verl. der Bauhaus-Univ.

- Hirt, M. A. (1985). Recommendations for the fatigue design of steel structures (1st edition). Technical report, ECCS Technical committee 6–Fatigue, Lausanne.
- Hobbacher, A. (2013). Recommendations for fatigue design of welded joints and components IIW document XIII-2460-13. Technical report, International Institute of Welding (IIW).
- Hughes, D. J. & Bruno, G. & Pirling, T. & Withers, P. J. (2006). Scientific review: First impressions of SALSA: the new engineering instrument at ILL. *Neutron News* 17(3), 28–32.
- Hughes, D. J. & Webster, P. J. & Mills, G. (2002). Ferritic steel Welds—A neutron diffraction standard. In *Materials science forum*, Volume 404, pp. 561–566.
- Husset, J. & Lieurade, H. P. & Maltrud, F. & Truchon, M. (1985). Fatigue crack growth monitoring using a crack front marking technique. *Welding in the World* 23(11/12), 276–283.
- Hutchings, M. & Withers, P. & Holden, T. & Lorentzen, T. (2005). *Introduction to the Characterization of Residual Stress by Neutron Diffraction* (1 ed.). CRC Press.
- IIW (2008). *Static Design Procedure for Welded Hollow Section Joints - Recommendations (IIW XV-1281r2-08)*. International Institute of Welding.
- ISO 6947 (2011). *Welding and allied processes - Welding positions*. International Organization for Standardization (ISO).
- Josat, O. (2010). Sustainable bridge Constructions—Elegant arches—filigree structures—cost effective design. In *Proceedings of ARCH'10-the 6~(th) International Conference on Arch Bridges*.
- Karlsson, L. (1986). Thermal stresses in welding. In R. B. Hetnarski (Ed.), *Thermal stresses*, Volume 1, pp. 300. Elsevier Science Publishers.
- Koistinen, D. & Marburger, R. (1959). A general equation prescribing the extent of the austenite-martensite transformation in pure iron-carbon alloys and plain carbon steels. *Acta Metallurgica* 7(1), 59–60.
- Kranz, B. & Neubert, J. & Wetzels, G. (2013). Einflussfaktoren auf die Festigkeit von laserstrahl-MSG-hybridgeschweißten Verbindungen bei Blechdicken bis zu 40 mm. *Stahlbau* 82(9), 652–656.
- Krauß, B. (2005). *Numerische Untersuchung zu Temperaturfeldern und Eigenspannungen an einer Schweißnahtverbindung bei WIG-Nachbehandlung*. Ph. D. thesis, Bauhaus-Universität Weimar, Germany.
- Krueger, R. (2004). Virtual crack closure technique: History, approach, and applications. *Applied Mechanics Reviews* 57(2), 109.
- Krummenacker, J. (2011). Simulation of the welding process of steel tube joints made of S355 and S690. Master's thesis, Karlsruher Institut für Technologie/École Polytechnique Fédérale de Lausanne.

## Bibliography

---

- Lassen, T. & Recho, N. (2006). *Fatigue life analyses of welded structures*. London, UK: ISTE.
- Leblond, J. & Devaux, J. (1984). A new kinetic model for anisothermal metallurgical transformations in steels including effect of austenite grain size. *Acta Metallurgica* 32(1), 137–146.
- Leblond, J. B. & Mottet, G. & Devaux, J. C. (1986). A theoretical and numerical approach to the plastic behaviour of steels during phase transformations I. derivation of general relations. *Journal of the Mechanics and Physics of Solids* 34(4), 395–409.
- Lee, S. J. & Lusk, M. T. & Lee, Y. K. (2007). Conversional model of transformation strain to phase fraction in low alloy steels. *Acta Materialia* 55(3), 875–882.
- Lindgren, L.-E. (2001a). Finite element modeling and simulation of welding part 1: Increased complexity. *Journal of Thermal Stresses* 24(2), 141–192.
- Lindgren, L. E. (2001b). Finite element modeling and simulation of welding. part 2: Improved material modeling. *Journal of thermal stresses* 24(3), 195–231.
- Lindgren, L.-E. (2001c). Finite element modeling and simulation of welding. part 3: Efficiency and integration. *Journal of Thermal Stresses* 24(4), 305–334.
- Lindgren, L. E. (2007). *Computational Welding Mechanics: Thermomechanical and Microstructural Simulations* (1st ed.). CRC Press.
- Lu, J. (1996). *Handbook of measurement of residual stresses*. Fairmont Press Lilburn, GA.
- Lubliner, J. (2008). *Plasticity Theory*. Dover Publications.
- Lugg, M. C. & Shang, H. M. & Collins, R. & Michael, D. H. (1988). The measurement of surface crack inclination in metals using AC electric fields. *Journal of Physics D: Applied Physics* 21(12), 1814.
- Macherauch, E. & Wohlfahrt, H. (1978). Different sources of residual stress as a result of welding. In *Proc. Conf. on Residual Stresses in Welded Construction and Their Effects*, pp. 267–282.
- Macherauch, E. & Wohlfahrt, H. & Wolfstieg, U. (1973). Zur zweckmäßigen definition von eigenspannungen. *Härterei-Technische Mitteilungen* 28(3), 201–211.
- Mackerle, J. (2002, May). Finite element analysis and simulation of welding - an addendum: a bibliography (1996-2001). *Modelling and Simulation in Materials Science and Engineering* 10(3), 295.
- Maddox, S. J. (1991). *Fatigue strength of welded structures* (Second edition ed.). Cambridge, England: Woodhead Publishing.
- Marsh, K. & Smith, R. & Ritchie, R. (1991). *Fatigue Crack Measurement: Techniques and Applications*. Engineering Materials Advisory Services Ltd.



- Marshall, P. W. & Wardenier, J. (2005). Tubular versus non-tubular hot spot stress methods. In *Proceedings of The Fifteenth (2005) International Offshore and Polar Engineering Conference, Seoul, Korea, The international Society of Offshore and Polar Engineers*.
- McClung, R. (2007). A literature survey on the stability and significance of residual stresses during fatigue. *Fatigue & Fracture of Engineering Materials & Structures* 30(3), 173–205.
- Mertens, A. & Lecomte-Beckers, J. (2012). Rapport d'essais: Caractérisation thermophysique de 2 chantillons d'acier. Technical report, Université de Liège-Department A&M-Science of Metallic Materials (MMS), Liège, Belgium.
- Mirshekar-Syahkal, D. & Collins, R. & Michael, D. H. (1982). The influence of skin depth on crack measurement by the ac field technique. *Journal of Nondestructive Evaluation* 3(2), 65–76.
- Mitter, M. (1987). Umwandlungsplastizität und ihre berücksichtigung bei der berechnung von eigenspannungen. *ZAMM - Journal of Applied Mathematics and Mechanics / Zeitschrift für Angewandte Mathematik und Mechanik* 68(12), 656–656.
- Mochizuki, M. (2007). Control of welding residual stress for ensuring integrity against fatigue and stress–corrosion cracking. *Nuclear Engineering and Design* 237(2), 107–123.
- Mohammadi, S. (2008, April). *Extended Finite Element Method: for Fracture Analysis of Structures*. Wiley-Blackwell.
- MORFEO (2012). v1.7.5 user's manual. Technical report, Cenaero, Gosselies, Belgium.
- Moës, N. & Dolbow, J. & Belytschko, T. (1999). A finite element method for crack growth without remeshing. *International Journal for Numerical Methods in Engineering* 46(1), 131–150.
- Nitschke-Pagel, T. & Wohlfahrt, H. (1992, January). Residual stress distributions after welding as a consequence of the combined effect of physical, metallurgical and mechanical sources. In L. Karlsson, L.-E. Lindgren, and M. Jonsson (Eds.), *Mechanical effects of welding : IUTAM Symposium*, International Union of Theoretical and Applied Mechanics, Luleå, Sweden, pp. 123–134. Springer Berlin Heidelberg.
- Nolde, P. & Meyer, B. (1998). Einfluß der tiefenschwefelung auf die kaltrißsicherheit hochfester stähle. *Schiffbauforschung* 37(2), 68.
- Nuismer, R. J. (1975, April). An energy release rate criterion for mixed mode fracture. *International Journal of Fracture* 11(2), 245–250. Cited by 0283.
- Nussbaumer, A. & Costa Borges, L. A. (2008). Size effects in the fatigue behavior of welded steel tubular bridge joints. *Materialwissenschaft und Werkstofftechnik* 39(10), 740–748.
- Nussbaumer, A. & Herion, S. & Veselcic, M. & Dietrich, R. (2010). New s-n curves for details in bridges with steel truss tubular superstructure. In *Proceedings of the 13th International Symposium on Tubular Structures*, Tubular structures, ISTS 13, Hong Kong. CRC Press/Balkema, Taylor & Francis group.

## Bibliography

---

- Nussbaumer, A. & Schumacher, A. & Haldimann-Sturm, S. C. & Walbridge, S. & Hirt, M. A. & Vollmar, T. (2004). Fatigue design of bridges with welded circular hollow sections. Technical Report ICOM 489E-OFROU 88-98, École Polytechnique Fédérale de Lausanne (EPFL), Laboratoire de la construction métallique (ICOM), Lausanne.
- Ohta, A. & Matsuoka, K. & Nguyen, N. T. & Maeda, Y. & Suzuki, N. (2003). Fatigue strength improvement of lap joints of thin steel plate using low-transformation-temperature welding wire. *WELDING JOURNAL-NEW YORK-* 82(4), 78–S.
- Onink, M. & Brakman, C. M. & Tichelaar, F. D. & Mittemeijer, E. J. & Van der Zwaag, S. & Root, J. H. & Konyer, N. B. (1993). The lattice parameters of austenite and ferrite in Fe-C alloys as functions of carbon concentration and temperature. *Scripta metallurgica et materialia* 29(8), 1011–1016.
- Ooi, S. W. & Garnham, J. E. & Ramjaun, T. I. (2014, April). Review: Low transformation temperature weld filler for tensile residual stress reduction. *Materials & Design* 56, 773–781.
- Outinen, J. P. (2007). *Mechanical properties of structural steels at high temperatures and after cooling down*, Volume 68.
- Pijpers, R. J. M. (2011, October). *Fatigue strength of welded connections made of very high strength cast and rolled steels*. Ph. D. thesis, Delft University of Technology, Delft.
- Pirling, T. & Bruno, G. & Withers, P. J. (2006). SALSA—A new instrument for strain imaging in engineering materials and components. *Materials Science and Engineering: A* 437(1), 139–144.
- Ponge, D. (2005). Structural materials - steels.
- Puthli, R. (2008). High strength steels and cast steel nodes for tubular structures—investigations, applications and research results. *Tubular Structures XII: Proceedings of Tubular Structures XII, Shanghai, China, 8-10 October 2008*, 3.
- Radaj, D. (1996, April). Review of fatigue strength assessment of nonwelded and welded structures based on local parameters. *International Journal of Fatigue* 18(3), 153–170.
- Radaj, D. (2003). *Welding residual stresses and distortion: Calculation and measurement*. DVS-Verlag.
- Radaj, D. & Sonsino, C. & Fricke, W. (2009, January). Recent developments in local concepts of fatigue assessment of welded joints. *International Journal of Fatigue* 31(1), 2–11.
- Richard, H. A. & Fulland, M. & Sander, M. (2005). Theoretical crack path prediction. *Fatigue & Fracture of Engineering Materials & Structures* 28(1-2), 3–12.
- Richter, F. (1973). Die wichtigsten physikalischen eigenschaften von 52 eisenwerkstoffen. *Stahleisen-Sonderberichte, Duesseldorf: Verlag Stahleisen, 1973* 8.

- Rohr, K. (2013). Evaluation of weld-induced residual stresses in s690 steel. Master's thesis, Karlsruher Institut für Technologie/École Polytechnique Fédérale de Lausanne, Lausanne.
- Romeijn, A. (1994). *Stress and strain concentration factors of welded multiplanar tubular joints*. Ph. D. thesis, Delft University of Technology, The Netherlands.
- Romeijn, A. & Karamanos, S. & Wardenier, J. (1997). Effects of joint flexibility on the fatigue design of welded tubular lattice structures. In *Proceedings of the 7th Offshore and Polar Engineering Conference*, Volume 4, pp. 90–97. International Society of Offshore and Polar Engineers.
- Roos, D. & Groth, C. & Junk, A. & Brinkmann, D. (2004). Optimierung und sensitivitätsanalyse zur parameteridentifikation in der numerischen simulation der gefügekinetik im schweißprozess. *Tagungsband zum 22*.
- Rosenthal, D. (1946). The theory of moving sources of heat and its application to metal treatments. In *Transactions of ASME*, Volume 68, pp. 849.
- Rykalin, N. N. (1974). Energy sources used for welding. *Soudage et Techniques Connexes I (12)*, 471–485.
- Saguy, H. & Rittel, D. (2005). Bridging thin and thick skin solutions for alternating currents in cracked conductors. *Applied Physics Letters* 87(8), 084103–084103.
- Samuelsson, A. & Schröter, F. (2005). *Use and application of high-performance steels for steel structures*. IABSE.
- Scharff, A. (2012). Development of innovative and efficient welding technologies for plates and profiles made of high strength steels using the example of the production of mobile cranes. *Materials Science Forum* 706-709, 2296–2301.
- Schijve, J. (2001). *Fatigue of structures and materials*. Springer.
- Schumacher, A. (2003). *Fatigue behaviour of welded circular hollow section joints in bridges*. Ph. D. thesis, École Polytechnique Fédérale de Lausanne, Lausanne.
- Schumacher, A. & Borges, L. & Nussbaumer, A. (2009). A critical examination of the size effect correction for welded steel tubular joints. *International Journal of Fatigue* 31(8-9), 1422–1433.
- Schwenk, C. & Tikhomirov, D. & Esser, G. & Rethmeier, M. (2011). General standard for welding simulation. Technical Report IIW C-Auto-44-11, International Institute of Welding (IIW).
- Seyffarth, P. & Meyer, B. & Scharff, A. (1992). *Großer Atlas Schweiß-ZTU-Schaubilder*. Deutscher Verlag für Schweißtechnik DVS-Verlag GmbH.
- Shivakumar, K. N. & Tan, P. W. & Jr, J. C. N. (1988, March). A virtual crack-closure technique for calculating stress intensity factors for cracked three dimensional bodies. *International Journal of Fracture* 36(3), R43–R50.

## Bibliography

---

- SIA (2003). Swisscodes: Concrete structures. Technical Report SIA 262:2003, Swiss society of engineers and architects(SIA), Zurich, Switzerland.
- SIA (2013). SIA 263/1 - steel structures – supplementary specifications. Technical Report SIA 263/1:2013, Swiss society of engineers and architects(SIA), Zurich, Switzerland.
- Sih, G. C. (1974). Strain-energy-density factor applied to mixed mode crack problems. *International Journal of Fracture* 10(3), 305–321.
- Stockie, J. M. (1998). The geometry of intersecting tubes applied to controlling a robotic welding torch. *Mapel Tech* 19(2), 2.
- Taleb, L. & Cavallo, N. & Waeckel, F. (2001). Experimental analysis of transformation plasticity. *International Journal of Plasticity* 17(1), 1–20.
- Thomas, B. G. & Samarasekera, I. V. & Brimacombe, J. K. (1987). Mathematical model of the thermal processing of steel ingots: Part i. heat flow model. *Metallurgical Transactions B* 18(1), 119–130.
- Troitsky, M. S. (1990). *Prestressed steel bridges: theory and design*. Bridgeseries. New York, N.Y.: Van Nostrand Reinhold.
- Ueda, Y. & Murakawa, H. & Ma, N. & 0123948045 & 978-0123948045 (2012). *Welding Deformation and Residual Stress Prevention* (1 edition ed.). Butterworth-Heinemann.
- van Straalen, I. & Dijkstra, O. (1993). Prediction of the fatigue behaviour of welded steel and aluminium structure with the fracture mechanics approach. *Journal of Constructional Steel Research* 27(1-3), 69–88.
- Van Wingerde, A. M. (1992). The fatigue behaviour of t- and x-joints made of square hollow sections. *HERON* 37(2).
- Voss, O. & Decker, I. & Wohlfahrt, W. (1997). Consideration of microstructural transformations in the calculation of residual stresses and distortion of larger weldments. In H. Cerjak (Ed.), *Mathematical modelling of weld phenomena 4*, pp. 584596.
- Walbridge, S. (2005). *A probabilistic study of fatigue in post-weld treated tubular bridge structures* (Thesis No. 3330). Ph. D. thesis, École Polytechnique Fédérale de Lausanne, Lausanne.
- Wardenier, J. & Kurobane, Y. & Packer, J. A. & van der Vegte, G. & Zhao, X.-L. (2008). *Design guide for circular hollow section (CHS) joint under predominantly static loading* (2nd ed.). Number 1 in Construction with hollow steel sections. CIDECT, Comité International pour le Développement et l'Etude de la Construction Tubulaire.
- Webster, G. (2001). Polycrystalline materials: Determination of residual stresses by neutron diffraction, ISO/TTA 3. *International Organization for Standardization, Geneva, Switzerland*.

- Weich, I. & Ummenhofer, T. & Nitschke-Pagel, T. & Dilger, K. & Eslami Chalandar, H. (2009, November). Fatigue behaviour of welded high-strength steels after high frequency mechanical post-weld treatments. *Welding in the World* 53(11-12), R322–R332.
- Weman, K. & Lindén, G. (2006). *MIG welding guide*. Cambridge, England: Woodhead.
- Wichers, M. (2006). *Schweißen unter einachsiger, zyklischer Beanspruchung Experimentelle und numerische Untersuchungen (Welding under uniaxial cyclic loads – Experimental and numerical research)*. Ph. D. thesis, Universitätsbibliothek Braunschweig.
- Withers, P. & Turski, M. & Edwards, L. & Bouchard, P. & Buttle, D. (2008). Recent advances in residual stress measurement. *International Journal of Pressure Vessels and Piping* 85(3), 118–127.
- Withers, P. J. & Bhadeshia, H. K. D. H. (2001). Residual stress. part 1 – measurement techniques. *Materials Science and Technology* 17(4), 355–365.
- Withers, P. J. & Bouchard, P. (2006). Symposium on residual stress and its effects on fatigue and fracture. Springer.
- WMB (2009). MIG-MAG lassen (<http://bit.ly/17x7JdU>). Technical report, Waack Metaalbewerking (WMB), Eindhoven, The Netherlands.
- Wohlfahrt, H. & Nitschke-Pagel, T. & Dilger, K. & Siegele, D. & Brand, M. & Sakkietitbutra, J. & Loose, T. (2012). Residual stress calculations and measurements - review and assessment of the IIW round robin results. *Welding in the World* 56(9-10), 120–140.
- Yaghi, A. & Becker, A. A. (2005). State of the art review - weld simulation using finite element methods. Technical Report FENET-UNOTT-DLE-08, University of Nottingham, United Kingdom.
- Yaman, M. & Kriz, R. & Harting, M. (2007, June). Visualization of stress tensors determined by neutron diffraction. *Journal of Neutron Research* 15(3), 267–274.
- Yang, H.-S. & Bhadeshia, H. K. D. H. (2009, April). Austenite grain size and the martensite-start temperature. *Scripta Materialia* 60(7), 493–495.
- Zamiri, F. & Nussbaumer, A. & Acevedo, C. (2012). Numerical investigation of welding residual stresses in planar bridge trusses made of CHS steel profiles. In *Tubular Structures XIV: Proceedings of the 14th International Symposium on Tubular Structures, London, Uk, 12-14 September 2012*, pp. 219.
- Zamiri Akhlaghi, F. (2009). Fatigue life assessment of welded bridge details using structural hot spot stress method. Master's thesis, Chalmers University of Technology.
- Zhao, X. L. & Herion, S. & Packer, J. A. & Puthli, R. S. & Sedlacek, G. & Wardenier, J. & Weynard, K. & Van Wingerde, A. M. & Yeomans, N. F. (2000). *Design guide for circular and rectangular hollow section joints under fatigue loading* (CIDECT, Comité International pour le

## **Bibliography**

---

Développement et l'Etude de la Construction Tubulaire ed.). Number 8 in Construction with hollow steel sections. Köln, Germany: TÜV-Verlag.

# Farshid ZAMIRI AKHLAGHI

Chemin des Peupliers 1 • 1028, Prévèrenge • Switzerland  
+41 (76) 787 15 88 • farshid.zamiri@a3.epfl.ch

---

## Education

- **PhD Structural Engineering** **Lausanne, Switzerland**  
*École Polytechnique Fédérale de Lausanne (EPFL)* 2010 – 2014(Exp.)
    - Dissertation: “Welding simulation and fatigue assessment of tubular K-joints in high strength steel”.
  - **MSc Structural Engineering and Building Performance Design** **Guthenburg, Sweden**  
*Chalmers University of Technology* 2007 – 2009
    - Thesis: “Fatigue Life Assessment of Welded Bridge Details Using Structural Hot Spot Stress Method”.
  - **MSc Earthquake Engineering** **Tehran, Iran**  
*University of Tehran* 1997 – 2000
    - Thesis: “Seismic Damage Assessment of Existing Steel Bridges by Quantitative Methods”.
  - **BSc Civil Engineering** **Mashhad, Iran**  
*Ferdowsi University of Mashhad* 1994 – 1997
- 

## Work experience

- **Steel Structures Laboratory (ICOM), EPFL** **Lausanne, Switzerland**  
*Doctoral assistant* 2010 – Present
    - Experimental and numerical residual stress measurement and fatigue assessment of tubular truss joints. My work was part of FOSTA P816 project financed by German Research Association for Steel Application. I worked extensively with numerical tools for welding simulation and fatigue crack growth. For the experimental part, I conducted residual stress measurements using neutron diffraction, large-scale fatigue tests with crack monitoring using ACPD, and material characterizations using Gleeble. I collaborated with several project partners from both academy and industry.
  - **Rah-Tarh Consulting Engineers** **Mashhad, Iran**  
*Structural design control engineer* 2004 – 2007
    - Shohada Square Rehabilitation and Development Project. I worked in a team of architects and engineers from different disciplines to coordinate and optimize the structural design of various structures including new building for main office of Mashhad municipality, Mashhad city hall, underground and multi-story parkings, and 2km of vehicle underpasses.
  - **Hexa Consulting Engineers** **Tehran & Mashhad, Iran**  
*Structural design engineer & Site engineer* 2000 – 2004
    - Underground section (9.5km) of Route No. 1 of Mashhad Light Rail Transit (LRT). I contributed to the design of the structure which was first of its kind in the country in terms of construction technique (an innovative method inspired by Berlin method). During the construction phase, I proposed modifications to improve the design, solved the issues arised in the construction phase, and resolved design conflicts with several urban utility service providers.
- 

## Teaching experience

- **Tutor for Master’s thesis projects** **2011-2014**
  - Simulation of the welding process of steel tube joints made of S355 and S690. 2011
  - Evaluation of weld-induced residual stresses in S690 steel. 2013

- CCT diagram determination and weld-induced residual stresses in S690 steel.(ongoing) 2014

- **Course assistant** **Spring 2011**

- Undergraduate course “structures en Métal”, taught by Professor Alain Nussbaumer.

- **Lecturer** **Fall 2006**

- Statics course for architecture students, Islamic Azad University of Mashhad.
- 

## Honors & Awards

- Ramböll’s annual prize for best Master’s thesis work in bridge engineering in Sweden. May 2010
  - ByggOpus:2010 prize (best Master’s thesis) in *ByggIndustrin* journal competition. May 2010
  - Ranked top 5% of undergraduate civil engineering class. September 1997
  - Ranked top 5% in Iranian nationwide universities’ entrance exam. June 1993
- 

## Computer skills

**Structural Engineering and FEA software:** Abaqus FEA, Morfeo/Welding, Morfeo/Crack, gmsh, Paraview, SAP2000, ETABS, SAFE, SCIA Engineer, Mathcad.

**Programming languages:** Python, Matlab, Fortran.

**Other:** SolidWorks, AutoCAD, L<sup>A</sup>T<sub>E</sub>X, Microsoft Project.

---

## Languages

**Persian:** mother tongue, **English:** fluent (C2), **French:** intermediate (B1), **Arabic:** basic (A2).

---

## Publications

- **Peer-reviewed conference proceedings**

- F. Zamiri Akhlaghi, A. Nussbaumer and C. Acevedo. “Numerical investigation of welding residual stresses in planar bridge trusses made of CHS steel profiles”. *Tubular Structures XIV*, CRC Press, London, 2012. ISBN 978-0-415-62137-3.

- **Conference papers**

- L. Borges, F. Zamiri, C. Acevedo, A. Nussbaumer. “Alternative stress definition and residual stress effects in fatigue design of welded tubular structures”, 2. *Darmstadter Ingenieurkongress: Bau und Umwelt*, Technische Universität Darmstadt (TUD), Darmstadt, Germany.
  - F. Zamiri Akhlaghi, C. Acevedo, A. Nussbaumer and J. Krummenacker. “Investigation of technological size effects of welding on the residual stresses and fatigue life of tubular joints made of structural steels S355 and S690”. *Fatigue design 2011*, Senlis, France, November 23-24, 2011.
  - F. Zamiri Akhlaghi, M. Al-Emrani, L. Frýba and S. Urushadze. “Fatigue Testing and Analysis of an Orthotropic Bridge Welded Detail Using Structural Hot Spot Stress Method”. *Fatigue design 2009*, Senlis, France, November 25-26, 2009.
- 

## Personal Information

Iranian, Swiss residence permit B, married, born on 24.08.1975.